Design of Static Wireless Charging System for Electric Vehicles with Focus on Magnetic Coupling and Emissions

Batra, Tushar

Publication date:
2015

Document Version
Publisher's PDF, also known as Version of record

AALBORG UNIVERSITY
DENMARK

Design of Static Wireless Charging System for Electric Vehicles with Focus on Magnetic Coupling and Emissions

Design af statisk trådløs opladningssystem til elbiler med fokus på magnetisk kobling og emissioner

PhD Thesis
by
Tushar Batra

PhD Thesis Details

Title

Design of Static Wireless Charging System for Electric Vehicles with Focus on Magnetic Coupling and Emissions

PhD Defendant

Tushar Batra

Supervisor

Associate Professor Erik Schaltz

Assessment Committee

Associate Professor Kaiyan Lu (Chairman)
Department of Energy Technology
Aalborg University
Pontoppidanstræde 101
9220 Aalborg
Denmark

Professor Subhashish Bhattacharya
Department of ECE
FREEDM Systems Center
Keystone Science Center, Suite-100
1791 Varsity Drive
Raleigh, NC 27613
USA

Senior Research Director and Professor Adel Razek
GeePs, CentraleSupelec
Plateau de Moulon
11 rue Joliot Curie
91192 Gif sur Yvette CEDEX
France

Defense Date and Place

14th December 2015

Department of Energy Technology, Aalborg University, Denmark.

Preface

This thesis is summary of research work (Nov 2012 - Oct 2015) conducted by PhD student Tushar Batra at Department of Energy Technology, Aalborg University on subject of static wireless charging of electric vehicles through resonant inductive technology. This thesis has been submitted for assessment in partial fulfillment of the PhD degree. The thesis is based on the submitted or published scientific papers which are listed on next page. Parts of the papers are used directly or indirectly in the extended summary of the thesis. As part of the assessment, coauthor statements have been made available to the assessment committee and are also available at the Faculty of Engineering and Science.

The research has been majorly supported by Danish Council for Strategic Research and Department of Energy Technology, Aalborg University. Otto Mønsteds Fond has also supported conference participations abroad and hence their role is acknowledged. Associate Professor Erik Schaltz has been the constant guiding light throughout the project in role of PhD supervisor. On personal front, he has been very friendly and supporting. Other colleagues at Department of Energy Technology, Aalborg University have also been equally supporting and helped me greatly in technical and administrative matters. Role of Bachelor students Claudiu Ionita and Ole Damm Kristensen of the same institute is also high acknowledged for their support in system construction and experiments. A special thanks to Assistant Professor Seungyoung Ahn and colleagues at KAIST, South Korea for providing valuable guidance during research stay abroad (Jan 2014 - July 2014). Last but not the least; I would like to thank my family and friends for standing behind me in all situations.

Tushar Batra
October 2015

Published Papers

{1} T. Batra, E. Schaltz, S. Ahn, “Effect of ferrite addition above the base ferrite on the coupling factor of wireless power transfer for vehicle applications”, Journal of Applied Physics, Vol. 117, pp 17D517 - 17D517-4, 2015. http://dx.doi.org/10.1063/1.4919039

{2} T. Batra, E. Schaltz, “Influence of Ferrite Grade and Thickness on System Performance of Wireless Power Transfer for Vehicle Applications”, Submitted, ECCE Asia 2016.

{3} T. Batra, E. Schaltz, “Magnetic Field Emissions for Ferrite and Non-Ferrite Geometries for Wireless Power Transfer to Vehicles”, Journal of Applied Physics, Vol. 115, no 17, pp 17E715 - 17E715-3, 2014. http://dx.doi.org/10.1063/1.4868498

{4} T. Batra, E. Schaltz, “Passive shielding effect on space profile of magnetic field emissions for wireless power transfer to vehicles”, Journal of Applied Physics, Vol. 117, pp 17A739 - 17A739-4, 2015. http://dx.doi.org/10.1063/1.4916930

{5} T. Batra, E. Schaltz, “Magnetic field emission comparison at different quality factors with series-series compensation network for inductive power transfer to vehicles", Proceedings of Wireless Power Transfer Conference (WPTC 2014), pp 13-16, 2014.

{6} T. Batra, E. Schaltz, “Magnetic field emission comparison at different quality factors with series-parallel compensation network for inductive power transfer to vehicles", Proceedings of 4th International Electric Drives Production Conference (EDPC), pp 1-4, 2014.

{7} T. Batra, E. Schaltz, S. Ahn, “Reduction of magnetic emission by increasing secondary side capacitor for ferrite geometry based series-series topology for wireless power transfer to vehicles", Proceedings of 16th European Conference on Power Electronics and Applications (EPE'14-ECCE Europe), pp 1-11, 2014.

{8} T. Batra, E. Schaltz, “Magnetic Emissions Reduction by Varying Secondary Side Capacitor for Ferrite Geometry based Series-Parallel Topology Wireless Power Transfer to Vehicles", Proceedings of International Exhibition and Conference for Power Electronics, Intelligent Motion, Renewable Energy and Energy Management (PCIM Europe 2014), Publisher: VDE Verlag, Berlin Offenbach 2014, pp 1-9, 2014.
https://www.mesago.de/en/PCIM/home.htm?ovs_tnid=0

{9} T. Batra, E. Schaltz, “Magnetic field emission comparison for series-parallel and series-series wireless power transfer to vehicles – part 1/2", Proceedings of EVTEC and APE, pp 2014435, 2014.

{10} T. Batra, E. Schaltz, “Magnetic field emission comparison for series-parallel and series-series wireless power transfer to vehicles – part 2/2", Proceedings of EVTEC and APE, pp 2014436, 2014.

Abstract

Static wireless charging using resonant inductive principle offers environmental friendly, comfortable and automatic charging solution for electric vehicles. This technology as of now is nascent with few products on the market and leading companies and universities actively engaged in research. On similar lines, a pioneer PhD project was undertaken in 2012 at Department of Energy Technology, Aalborg University with objectives of improving system design and developing high power density (weight and dimensions), low cost and low magnetic emissions power inductors for this application. This thesis summarizes the research findings of the study.

Wireless charging system as per state of art design approach consists of four major blocks: primary power electronics, inductors, secondary power electronics including load and resonant circuits (capacitors). The first contribution of this project is addition of fifth block named reflected quality factor in the system design. The fifth block similar to the resonant circuits block is dependent on the other blocks but its addition is highly beneficial in understanding and simplification of the system design in two main ways. Firstly, the system can be represented as an equivalent power source and transmission system including the load similar to other electric system like grids. Secondly, design parameters of output power, circuit efficiency and voltage or current stress across resonant components can be expressed as simple functions of the five blocks.

Inductors of wireless charging systems mostly consist of the coils and passive shielding materials and are different from inductors used in other industrial and consumer applications as majority of magnetic flux passes through air. The first objective in the inductor design is to explain effect of the shielding materials on the magnetic field path. The objective serves as base for the second objective dealing with minimization of passive shielding usage with respect to power transfer capability, weight, dimensions. There have been two major results obtained during the optimization process. The first set of results show that additional ferrite should be added in center of the inductors above base ferrite as this provides maximum increase in the power transfer per unit weight added. In the second investigation, it is shown that reducing passive shielding (ferrite and aluminum) thickness reflects comparatively lower decrease in the power transfer and efficiency in comparison to high reduction achieved in weight and dimensions of the inductors. Additionally, the same comparative analysis has been shown to be true when commonly used high ferrite grade is replaced by comparatively lower and cheaper ferrite grade.

The last objective of this project has been minimization of the magnetic emissions. For this, a semi-analytical method has been proposed for calculating ratio of the magnetic emissions at different values of the coil currents for given inductor setup. This method will help in including the emissions as a design parameter for the primary power electronics, secondary power electronics with load and capacitors in addition to the inductor design. For development of the analytical method, space variation of the magnetic emissions is studied first in the project and results show that ratio of secondary coil emission to primary coil emission is constant in the surroundings. This is utilized in introducing the analytical method and three applications have been addressed during the project. In the first application, it is shown that higher load quality factor is favorable for given

inverter current and switching frequency as it provides comparatively lower increase in the emissions compared to the output power. In the second application, a novel active shielding method of generating cancellation current in the secondary coil without using additional third coil has been proposed. This is implemented by designing the secondary capacitor bigger than its resonant value and making the secondary circuit inductive. On the negative side, the reduced emissions require higher inverter current and bigger primary capacitor to deliver the same output power. At last, two resonant topologies series-series and series-parallel are compared in term of the emissions for similar power rating. Series-parallel topology has slight advantage over its series-series counterpart on account of additional inductive secondary current component as advised by the results.

At the end, a wireless charging system has been designed and constructed as part of the project. The setup delivers output power of approximately 2 kW and 1.2 kW for vertical distance of 10 cm and 20 cm respectively. Measured resonant circuit efficiencies (primary inverter AC terminals to secondary rectifier AC terminals) for the two cases are 89% and 82% respectively. The setup has capability to deliver much higher output power subject to availability of higher current rating input power source.

Resumé

Statisk trådløs opladning ved hjælp af resonansprincippet for magnetisk induktion tilbyder en miljøvenlig, komfortabel og automatisk opladningsløsning til elbiler. Denne vordende teknologi er stadig begrænset udbredt med kun få produkter på markedet og førende virksomheder og universiteter er derfor aktivt engageret i forskning og udvikling inden for området. Aalborg Universitet er også aktive på området, hvorfor et ph.d. projekt i 2012 blev iværksat ved Institut for Energiteknik med formålet at forbedre systemdesignet og effekttætheden (mht. vægt og størrelse), samt at reducere omkostningerne og de magnetiske emissioner til denne applikation. Denne afhandling sammenfatter forskningsresultaterne af ph.d. projektet.

Trådløse opladningssystemer består af fire store blokke: primær effektelektronik, spoler, sekundær effektelektronik inklusiv belastning og resonanskredse (kondensatorer). Det første videnskabelige bidrag i projektet er tilføjelsen af en femte blok i systemdesignet kaldet reflekteret godhedsfaktor. Den femte blok er i lighed med resonanskredsløbsblokken afhængig af de øvrige blokke, men dens tilføjelse er yderst gavnlig i forståelsen og forenklingen af systemdesignet på to måder: For det første kan systemet repræsenteres som en ækvivalent strømkilde og transmissionssystem, med belastningen inkluderet, der minder om andre elektriske systemer, såsom el-nettet. For det andet kan designparametrene udgangseffekt, effektivitet og spændings- eller strømstress af resonans-komponenterne udtrykkes som simple funktioner af de fem blokke.

Induktorerne i trådløse opladningssystemer består for det meste af spolerne og passive afskærmningsmaterialer og er forskellige fra induktorerne, der anvendes i andre industrier og forbrugerapparater, da størstedelen af den magnetisk flux passerer gennem luften. Det første mål i induktordesignet er at forklare virkningen af afskærmningsmaterialernes indflydelse på magnetfeltets vej. Dette mål fungerer som base for det andet mål, der beskæftiger sig med minimering af passiv afskærmning i forhold til effektroverførelseskapaciteten, vægten og de fysiske dimensioner. Der er opnået to store resultater under optimeringsprocessen. Det første sæt resultater viser, at yderligere ferrit bør tilføjes i midten af spolerne over base-ferritpladen, da dette giver maksimal stigning i effektoverførelsen per vægtenhed tilføjet. I den anden undersøgelse er det vist, at reduktion af tykkelsen af passiv afskærmning (ferrit og aluminium) medfører forholdsvis lavere reduktion i effektoverførsel og effektivitet i forhold til den høje reduktion af vægt og dimensioner af induktorerne, der opnås. Derudover har den samme analyse vist sig at være sand, når almindeligt anvendt ferrit af høj kvalitet erstattes af en forholdsvis lavere og billigere kvalitet.

Det sidste formål med dette projekt er minimering af de magnetiske emissioner. Til dette er en semi-analytisk metode blevet foreslået til beregning af forholdet mellem de magnetiske emissioner ved forskellige værdier af spolestrømme for en given opsætning. Som en tilføjelse til induktordesignet vil denne metode vil hjælpe ved at inkludere emissioner som en designparameter for den primære effektelektronik, sekundære effektelektronik med belastning og kondensatorer. Til udviklingen af analysemetoden er rumvariation af de magnetiske emissioner først undersøgt, og resultaterne viser, at forholdet mellem sekundærspole emissionerne til primærspole emissionerne er konstant i omgivelserne. Dette udnyttes i analysemetoden, og tre applikationer er blevet behandlet i

løbet af projektet. I den første applikation er det vist, at højere belastningskvalitetsfaktor er gunstigt for en given inverter-strøm og frekvens, da det giver en forholdsvis lavere stigning i emissionerne i forhold til udgangseffekten. I den anden applikation, er en ny afskærmningsteknik blevet foreslået, der kan generere en mod-strøm i sekundærspolen uden brug af en tredje spole. Dette implementeres ved at designe den sekundære kondensator større end dens resonansværdi og gøre den sekundære kreds induktiv. På den negative side kræver de reducerede emissioner højere inverter-strøm og større primære kondensator for at levere den samme udgangseffekt. Endeligt er emissionerne af to resonanskredse (serie-serie og serie-parallel) sammenlignet for den samme effekt. Serie-parallel kredsen har en lille fordel i forhold til serie-serien kredsen på grund af en ekstra induktiv sekundær komponent.

Til sidst er et trådløst opladningssystem blevet designet og konstrueret som en del af projektet. Systemet leverer en udgangseffekt på ca. 2 kW og 1,2 kW med en vertikal afstand på henholdsvis 10 cm og 20 cm. Den målte resonanskredsløbseffektivitet (primær inverter AC terminaler til sekundær ensretter AC terminaler) for de to situationer er henholdsvis 89% og 82%. Opstillingen har kapacitet til at levere meget højere udgangseffekt på grund af den højere mærkestrøm af inputstrømkilden.

Table of Contents

Electric symbols

Electrical symbols used in the thesis are summarized first in Table 1.

Table 1. Electric symbols description

Symbol	Name		Symbol	Name
V_{grid}	Grid Rms voltage		$C_{i\text{-}dc}$	Primary DC link capacitance
$V_{i\text{-}dc}$	Inverter voltage (dc side)		V_i	Inverter voltage (ac side)
$V_{l\text{-}dc}$	Load voltage (dc side)*		$I_{l\text{-}dc}$	Load current (dc side)**
$C_{l\text{-}dc}$	Secondary DC link capacitance*		$L_{l\text{-}dc}$	Secondary DC link inductor**
V_l	Load Rms voltage (ac side)*		I_l	Load Rms current (ac side)**
V_p	Primary inductor Rms voltage		V_s	Secondary inductor Rms voltage
I_p	Primary coil Rms current		I_s	Secondary coil Rms current
L_p	Primary self-inductance		L_s	Secondary self-inductance
M	Mutual Inductance		k	Coupling factor
C_p	Primary capacitance		C_s	Secondary capacitance
R_{lp}	Primary inductor resistance		R_{ls}	Secondary inductor resistance
R_{cp}	Primary capacitor resistance		R_{cs}	Secondary capacitor resistance
R_p	Primary internal resistance		R_s	Secondary internal resistance
Q_p	Primary loss quality factor		Q_s	Secondary loss quality factor
R_r	Reflected resistance		R_l	Load resistor
Q_r	Reflected load quality factor		Q_l	Secondary load quality factor
P_i	Input or inverter AC side power		P_l	Output or load AC side power
η_p	Primary circuit efficiency		η_s	Secondary circuit efficiency
H	Net circuit efficiency		f	Frequency
ω_i	Inverter angular switching frequency		f_i	Inverter switching frequency

* @ Series-series resonant topology

**@ Series-parallel resonant topology

Note – Square, curl and round brackets are used to represent reference papers (other authors), paper written during PhD (PhD papers) and equations respectively in the thesis.

1. Introduction

Wireless charging has potential to revolutionize the world of electric power transmission. As the name suggests, this technology provides transmission of power without use of wires or cables and hence offers comfortable and automatic charging process. This technology was discovered [1-2] back in early 1900 by Nikolas Tesla. However it never picked up momentum for everyday applications and has mostly been used for two major applications: biomedical [3-5] and induction heating [6-7] in the last century. In later part of 20^{th} century, big problem of global warming by greenhouse gases came into picture. To reduce transport sector's share in the problem, there was a strong push for development of electric vehicles and hence their charging technologies. Wireless charging on account of its automatic and comfort features was seen as a possible solution to enable mass deployment of the electric vehicles. As a result, some pioneer studies [8-11] were conducted to study feasibility of wireless charging for electric vehicles. However, this technology came into limelight through breakthrough paper [12] by researchers of Massachusetts Institute of Technology. Since then, this technology is being actively pursued by leading companies and universities as an improved solution for various consumer and industrial applications. On the commercial side, this technology as of today is on nascent stage with few products [13-14] available in the market.

Wireless power transfer is possible using different scientific principles such as resonant inductive, capacitive, microwave etc. A good overview of these principles and applications can be found in [15]. This work is focused on wireless charging by resonant inductive principle only and is explained in detail in Chapter 2. This technology can be used in mainly two forms for vehicle applications. In the first form, the vehicles are charged on the move by placing the primary and secondary coils below the earth and vehicle respectively. As a result, this form is known as dynamic wireless charging [9, 16-19] and has capability to reduce transport sector dependence on fossil fuels. Practical application of this technology requires massive infrastructure investment and major policy changes by national governments. Other form of this technology involves charging vehicles when they are parked and is referred as static charging [20-28]. This form requires comparable lesser investments compared to the dynamic charging and is more consumer oriented. Combination [29] of these two forms by installing wireless charging platforms below the road at traffic signals etc. where vehicles are stationary temporarily have also been proposed. From broad technical point of view, the two forms differ in respect that both area and magnetic field are varying with time in dynamic wireless charging compared to only magnetic field variation with time in the static wireless charging. For this particular project, static wireless charging is under consideration and term wireless charging is synonymous with static wireless resonant inductive charging in rest of the thesis. Before going into depth of the system and inductor design, a brief description of the system is provided next.

1.1. System description

Block diagram of wireless charging system for vehicles applications is provided in Figure 1.

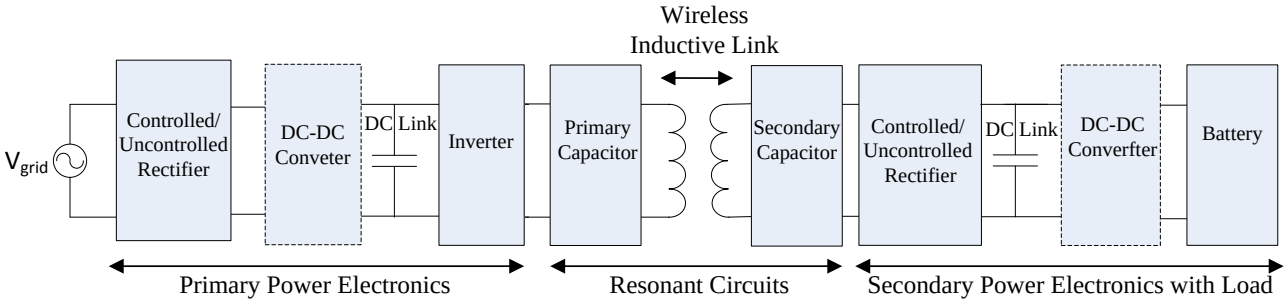

Figure 1. Block diagram wireless charging system

There are four major system blocks: primary power electronics, inductors (wireless inductive link), secondary power electronics and resonant circuits. The blocks are explained in detail in following sections.

1.1.1. Primary power electronics

The first block of primary power electronics is similar to power supply block used in most electric drives. Both single [30-33] and three [19, 34] phase solutions for power electronics have been proposed for vehicle charging. The single phase solution provided in Figure 2 feeding a single primary coil is preferred for smaller vehicles (2-3 kW). The three phase solution is better solution for charging of heavy vehicles and feeding three primary coils during operation.

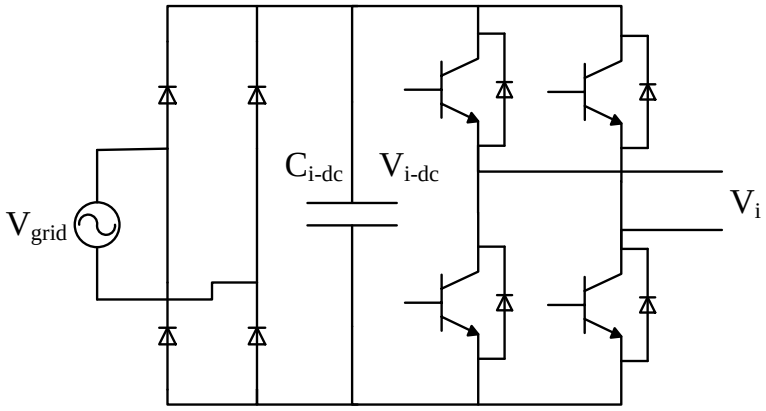

Figure 2. Primary power electronics

In this block, first 50 or 60 Hz grid voltage is rectified and smoothen in DC-link capacitor. There are two more variations (Figure 1) apart from the uncontrolled rectifier as shown in Figure 2. In the first variation, a DC-DC converter is inserted in between the uncontrolled rectifier and DC-link capacitor and is shown with dashed rectangular block in Figure 1. This provides control of DC-link voltage and as a result of the output power. Main advantage with the additional converter is that the inverter can be fully soft switched compared to partial soft switching achieved with power control through phase shifting of inverter legs (Figure 2). These two variations have been discussed in detail in [35]. The last variation is fully controlled switches for rectifier to provide bidirectional flow of power and enabling the vehicles to be an active player in the electric grid. At end of the

rectification process, constant DC-voltage is converted into medium frequency (20 kHz - 85 kHz) [20, 26-27, 35] square wave voltage by an inverter as shown in Figure 2.

1.1.2. Inductor design

Power is transferred from the primary to secondary inductor using principle of electromagnetic induction. Inductors of wireless charging system consists of three main components: coil, ferrite and aluminum. The last two are also together categorized as passive shielding. Also, there are active shielding methods [20, 36] proposed in literature for reduction of the emissions. The active shielding consists of an additional third coil having current and hence magnetic field designed in opposite phase to cancel the primary or secondary coil field. The active shielding methods have disadvantages of requirement of additional power supply and extra space required for its installation. The first problem was solved by researchers at KAIST by powering the third coil via the primary coil [20]. Active shielding method by inducing opposite phase current in the secondary coil and eliminating requirement of the third coil has been proposed during PhD project {7-8}. The inductor design is the major focus area of the thesis and is explained dedicatedly in Chapter 3.

1.1.3. Secondary power electronics load including battery

On the secondary side power electronics, uncontrolled rectifier bridge converts high frequency AC into DC to be stored in DC-link capacitor which in turn feeds the load (battery). The DC-link capacitor provides stable DC-voltage and hence voltage at AC terminals of the rectifier is of square wave nature. The uncontrolled rectifier scheme is provided in Figure 3.

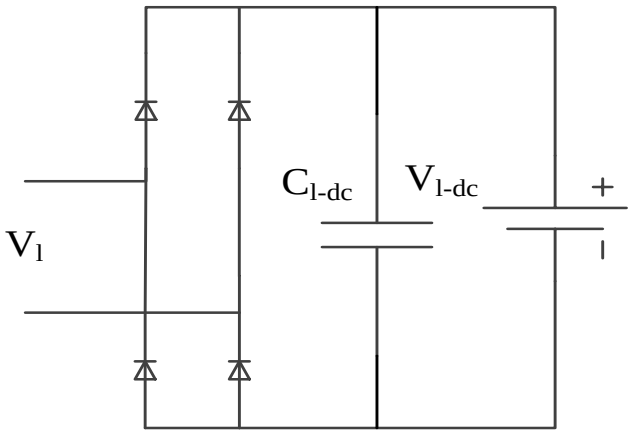

Figure 3. Secondary power electronics with battery

Similar to the primary power electronics, both single [30-33] and three [34] phase solutions have been considered for the secondary side power electronics. Also, solutions vary from active switches providing bidirectional power flow, incorporating additional DC-DC converter (dashed rectangular block in Figure 1) for independent secondary side control [25-27] and primary side controller [37] only. The battery (with or without additional DC-DC converter) can be represented as an equivalent

load and is the approach followed in the thesis as design of the power electronics is not the major focus.

1.1.4. Resonant circuits

Resonance capacitor is required in combination with the secondary inductor to cancel its reactance and boost output power. On the other hand, capacitor on the primary side is designed to cancel effective inductive reactance on the primary side and provide unity power factor operation from input side. The capacitors can be arranged in series or parallel combination with the respective inductors and leads to four resonant circuit topologies: series-series (SS), series-parallel (SP), parallel-series (PS) and parallel-parallel (PP) [23]. The four topologies are provided in Figure 4 with their comparison presented later in Section 2.2.4.

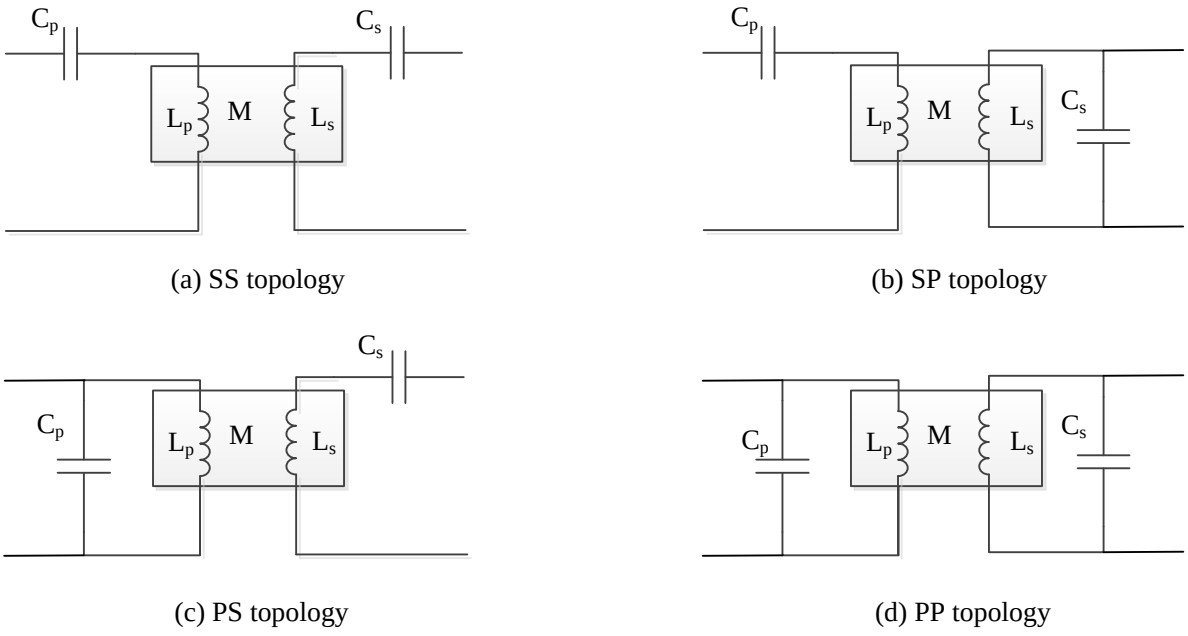

(a) SS topology

(b) SP topology

(c) PS topology

(d) PP topology

Figure 4. Resonant topologies

1.2. Project objectives

This PhD project at Department of Energy Technology, Aalborg University was started in November 2012 with the following objectives to be accomplished.

1) The first objective is to evaluate existing system design methodologies and provide modifications if required. This has been explained in detail in Chapter 2.

2) Inductors of wireless charging are different from traditional power inductors as majority of magnetic path is not closed by magnetic material. Hence, the second objective of the project is to explain magnetic field flow and effect of passive shielding materials on it. This has been explained in Chapter 3 and is of high importance in optimization of the passive shielding discussed in later part of the chapter.

3) Passive shielding addition to the coils provides increase and decrease in the power transfer and magnetic emissions respectively. On the other hand, their usage also significantly increases the inductor weight, cost, dimensions and losses. This objective deals with finding best compromise for the inductor design by weighing advantages against the disadvantages. This part is provided at end of Chapter 3 with help of two PhD papers {3-4}.

4) Design and construction of a wireless charging system in the laboratory environment is the next objective of the project. Details of the constructed system along with practical challenges with construction are discussed in Chapter 4.

5) The last objective of the project is focused on minimizing the magnetic emissions to the surroundings. The first step taken in this direction is to study space variation of the magnetic emissions. Based on the results, a semi analytical method has been proposed that includes the emissions in design of the primary power electronics, secondary power electronics and capacitors in addition to the inductors. Chapter 5 has been dedicated to this objective including the published papers and experimental verification.

2. System design and analysis

Design and analysis of wireless charging system is done using Fundamental Mode Approximation (FMA) analysis [23, 25-27, 37-39]. Strength of the analysis lies in fact that it converts the two complex power electronics blocks into equivalent AC voltage sources and phasor theory is applicable. Before going into the depth of the design, FMA analysis is provided below. The analysis and design are explained with help of SS resonant topology. The remaining three resonant topologies comparison with SS topology is provided in Section 2.4.

2.1. Fundamental mode approximation (FMA) analysis

Electric schematic of unidirectional wireless charging system is provided in Figure 5.

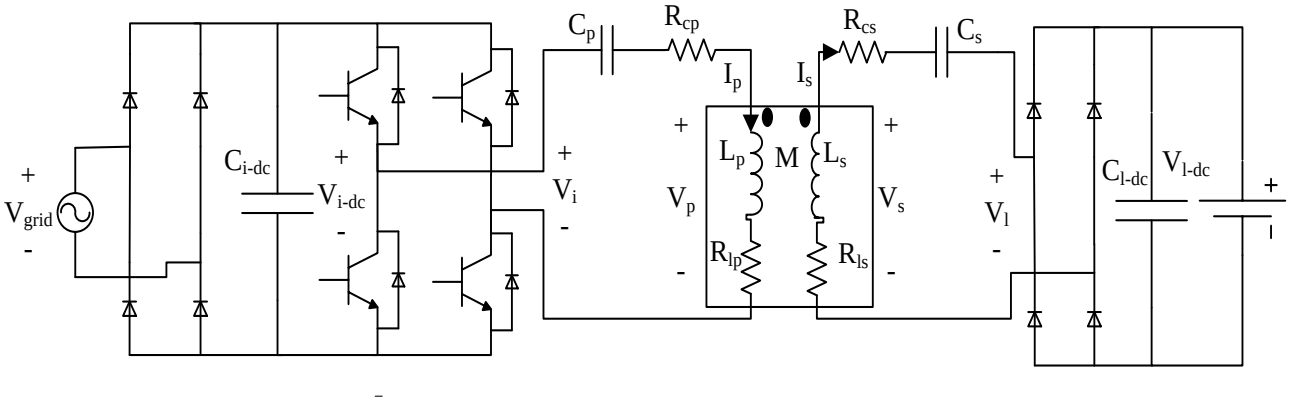

Figure 5. Electrical schematic wireless charging system

The complex system can be greatly simplified with help of FMA analysis as follows. Rectifier combined with DC–link capacitor provides constant DC voltage ($V_{i,l\text{-}dc}$) on both sides at steady state conditions. As a result, voltage at AC terminals of the inverter and load rectifier is of square wave nature. It is assumed in the last statement that an additional DC-DC converter is present between the primary rectifier and inverter for controlling DC-link voltage. The two resonant circuits are tuned at fundamental of inverter switching frequency and hence only fundamental current harmonic is present on both sides. This leads to simplification of the two power electronics blocks into equivalent voltage sources whose effective Rms voltage is given by

$$\left(V_{i,l}\right)_{FMA} = \frac{4}{\pi\sqrt{2}}\left(V_{i,l}\right)_{Square}. \quad (1)$$

The inverter AC voltage wave will consists of peaks and zeros when phase shifting control is used in place of additional DC-DC converter on the primary side. This leads to equivalent first harmonic inverter voltage to be multiplication of first harmonic inverter voltage in (1) by factor $\sin(\alpha/2)$, where α is overlap angle. The angle and resultant waveforms are presented in [34] for reference and are not presented here. For simplification, this section is presented for the angle equal to 180°. Also, the battery (with or without additional secondary side DC-DC converter) of electric vehicle

can be equated to an equivalent resistor (R_l) as it consumes active power only. This can be further simplified to an equivalent FMA resistor using conservation of power and is given by

$$(R_l)_{FMA} = \frac{8}{\pi^2}(R_l)_{Square}. \tag{2}$$

Using the above two approximations for the power electronics blocks, FMA equivalent circuit of the system is provided in Figure 6. The inverter switching frequency is the frequency of the electric system.

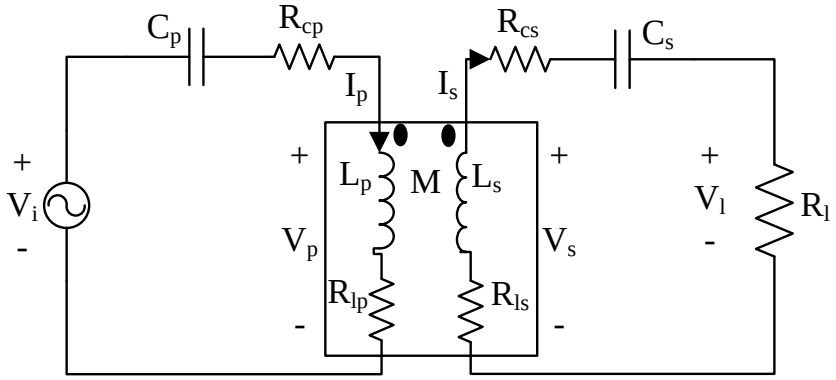

Figure 6. FMA equivalent circuit

Kirchoff's voltage equations for the system are

$$\left(j\omega_i L_p + \frac{1}{j\omega_i C_p} + R_p\right) I_p - j\omega_i M I_s = V_i \tag{3}$$

$$\left(j\omega_i L_s + \frac{1}{j\omega_i C_s} + R_s + R_l\right) I_s = j\omega_i M I_p. \tag{4}$$

Sum ($R_{p,s} = R_{lp,ls} + R_{cp,cs}$) of internal resistance of the inductor and capacitor on both sides is equated to internal resistance of each side. The secondary circuit is referred (5) to the primary side using (4) in (3).

$$\left(\left(j\omega_i L_p + \frac{1}{j\omega_i C_p}\right) + \left(\frac{-(\omega_i M)^2\left(j\omega_i L_s + \frac{1}{j\omega_i C_s}\right)}{\left(\omega_i L_s - \frac{1}{\omega_i C_s}\right)^2 + (R_s + R_l)^2}\right) + R_p + \left(\frac{(\omega_i M)^2 (R_s + R_l)}{\left(\omega_i L_s - \frac{1}{\omega_i C_s}\right)^2 + (R_s + R_l)^2}\right)\right) I_p = V_i \tag{5}$$

As a result, the reflected resistor on the primary side is given by (6).

$$R_r=\frac{(\omega_i M)^2(R_s+R_l)}{\left(\omega_i L_s-\frac{1}{\omega_i C_s}\right)^2+(R_s+R_l)^2}. \quad (6)$$

Also, resistors on the primary and secondary sides in resonant systems are represented in terms of quality factors given by (7) and (8).

$$Q_{p,r}=\frac{\omega_i L_p}{R_{p,r}} \quad (7)$$

$$Q_{s,l}=\frac{\omega_i L_s}{R_{s,l}} \quad (8)$$

Resonant circuit efficiency [38] of the system using (6) is given by (9).

$$\eta=\frac{R_r}{R_r+R_p}\frac{R_l}{R_l+R_s} \quad (9)$$

The circuit efficiency can further be decoupled (10) into primary and secondary circuit efficiency.

$$\eta=\eta_p\eta_s \quad (10)$$

The primary and secondary circuit efficiencies are in turn given by (11) and (12).

$$\eta_p=\frac{R_r}{R_r+R_p} \quad (11)$$

$$\eta_s=\frac{R_l}{R_l+R_s} \quad (12)$$

The logic behind this decoupling is that the primary circuit has reflected load resistor as its load and primary resistor as its internal resistance which matches the traditional definition of efficiency in electric circuits. An analogues statement is true for the secondary circuit.

2.2. State of art design approach

Wireless power transfer for vehicle applications is a developing technology and limited literature is available discussing the complete system design. University of Auckland is one of the pioneers of this technology and hence their design methodology [26-28] is taken as state of the art approach. As per the approach, firstly the system is designed at operation point with both sides in resonance (13).

$$\omega_i=\sqrt{L_p C_p}=\sqrt{L_s C_s}. \quad (13)$$

System design has been decoupled [26-27] into three blocks: primary coil VA rating, coupling factor and load quality factor based on the foremost design criterion of output power. The output power is derived using (3) to (8), (13) and is given by

$$P_l \approx V_p I_p k^2 Q_l \tag{14}$$

where square of the coupling factor is provided in (15).

$$k^2 = \frac{M^2}{L_p L_s}. \tag{15}$$

First of all, the decoupling between the coupling factor (inductances) and current is valid as magnetic (ferrite) core of wireless charging inductors do not saturate [25] in design range of current some tens of amperes and frequency below 100 kHz. This is mostly due to the reason that majority of magnetic flux path is in air and leads to linear magnetic characteristics as reported in [25]. First block in this decoupling is VA rating (V_pI_p) of the primary coil and is different from first block of primary power electronics mentioned in Chapter 1. The secondary block of inductor design is represented by square of coupling factor (k^2) and the final block of secondary power electronics with load is represented in term of load quality factor (Q_l). Detailed explanation of the blocks along with improvements has been provided in next Section 2.3 and is not provided here. Also, values of the capacitors (fourth block) are dependent on the remaining three blocks and hence they are not considered as an independent design blocks. However, selection of the resonant topology affects the system performance and has been discussed separately in Section 2.4. As per this approach, increase in value of one of the blocks would increases the output power rating of wireless power transfer system. This approach serves as good starting point for the design but has the following shortcomings:

1) This approach is not totally decoupled as the first and second block both are dependent on the primary inductor. The voltage across the primary inductor is dependent on the primary inductance and similar is true for the coupling factor. This is mainly due to reason that two blocks have been coupled into a single first block. Out of these two blocks, one is the primary power electronics and second is reflected quality factor introduced in the thesis. It is discussed in detail in next Section 2.3.

2) The static charging solution is under consideration in this project. Hence, low voltage limit [25] of 1 kV also needs to be followed for voltage stresses on the resonant components. Selection of the secondary quality factor provides linear relation (13) to increase in the voltage stress across the secondary resonant components.

$$|V_s| \approx |Q_l V_l| \tag{16}$$

However, there is no such parameter available which provides measure of increase in the voltage stress across the primary resonant components. This parameter is the reflected quality factor introduced as the new block in the thesis.

3) The circuit efficiency (9) is dependent on the load, reflected load and internal resistances of both sides. However in the standard approach, increase in the efficiency has only being considered by lowering of the internal resistances through improved inductor design. The circuit efficiency also needs to be considered in selection of the load quality factor and reflected quality factor.

2.3. Improved design approach

The standard design decoupling approach has been improved in this project by introducing reflected quality factor as fifth block in expression of the output power (14). The reflected quality factor similar to the capacitors is dependent on the remaining blocks but should be considered during the system design and is explained in this section. The first advantage with this addition is that the system design can be represented in similar way to other electrical systems using concept of energy source and transmission system (including load). The modified expression for output power is

$$P_l \approx V_i I_p Q_r k^2 Q_l \tag{17}$$

with the reflected quality factor and reflected resistor provided in (18) and (19).

$$Q_r = \frac{\omega_i L_p}{R_r} \approx \frac{1}{k^2 Q_l} \tag{18}$$

$$R_r \approx \frac{\omega_i M^2 Q_l}{L_s}. \tag{19}$$

Using (17), the system design can be analyzed as follows: The input power represented by first part $(V_i I_p)$ in (17) is the power to be transferred. The losses have been ignored in (17) (also in standard approach (14)) and hence remaining part of expression $\left(Q_r k^2 Q_l\right)$ represents a lossless transmission system. The transmission system cannot consume or produce power and hence its value is equal to one (18). There are three parts: reflected quality factor, coupling factor and load quality factor in the transmission system. Out of these three, the last two are independent design blocks and similar to standard approach are the second and third design blocks of system design. The first term of the reflected quality factor is dependent on the last two terms as provided in (18). Design of the second and third blocks hence determines nature (efficiency, voltage stress and emissions) of the power transmission. As a simple design rule, the transmission system needs to be designed for higher voltage and lower current (higher reflected resistance) solution similar to what is done in electric grids for higher system efficiency. In addition, lower current and high voltage solution provides lower magnetic emissions to the surroundings on account of lower current and is explained in detail in Chapter 3.

2.3.1. Primary power electronics

The first block needs to be designed for VA rating and switching frequency of the inverter switches. Due to loosely magnetic coupled nature of wireless charging inductors for vehicle applications (low reflected resistance) the current is the limiting factor in VA design of the inverter. Hence as discussed above, desirable higher voltage and lower current solution through transmission system design would provide higher reflected resistance on the primary side and higher power can be transferred for given maximum inverter current [25]. This is provided using rearranged output power expression [25] in (20).

$$P_l \approx I_p^2 R_r \approx \omega_i I_p^2 \frac{M^2}{L_s} Q_l \tag{20}$$

The switching frequency on the other hand is dependent on number of factors. The output power and reflected resistance increases linearly with the switching frequency for given inverter current (20). As a result, higher switching frequency is favored on account of the output power and reflected resistance (16). However, losses in the inductors and capacitors also increase with the switching frequency. Exact nature of the function cannot be generalized and depends on the inductor and capacitor design. As a result, generalization of primary circuit efficiency behavior with frequency is also not possible.

Secondary circuit efficiency has a similar story to the primary circuit frequency. The load resistor value increases linearly for given set of inductors (self-inductance) and load quality factor as per (8). On the other hand, the secondary internal resistance increases with frequency with mathematical function depending on the component design. As an example, the internal resistances variation with frequency has been presented for constructed geometry in Section 4.2.1.The resultant efficiency which is product of the two circuit efficiencies (9) to (12) has a similar response as the primary and secondary circuit efficiency. Also, the switching losses in the power electronics increase with the switching frequency. Hence, the switching frequency selection is compromise between the losses in various components and output power. Different design solutions varying from 20 kHz to 85 kHz have been proposed in literature promising best compromise between the losses and output power. This area is out of scope of this project.

2.3.2. Inductor design

The inductor design is done using Finite Elements Method (FEM) simulations and is discussed in detail in Chapter 3. In this section, impact of inductor output quantities: coupling factor and internal resistance on the system performance will be discussed. The coupling factor as figure of merit for inductor design of wireless charging system stands for maximum coupled flux with lowest leakage flux for both the coils. First of all, effect of the coupling factor on the primary circuit efficiency is discussed (21). The modified expression for the primary circuit efficiency (21) has been obtained using (7) and (11).

$$\eta_p = \frac{Q_p}{Q_p + Q_r} \tag{21}$$

Increase in the coupling factor reduces the primary quality factor (18) for given load quality factor. This leads to increase in the primary circuit efficiency (11). A point needs to be mentioned here regarding number of coil turns. The self-inductance of each coil is approximate proportional to square of number of coil turns for the same coil. On the other hand, the mutual inductance is roughly proportional to number of turns of both coils. From the above two statements it can be inferred that the coupling factor is practically independent of the number of turns. Ferrite is added below the coils in the inductor design to increase the coupling factor and is explained in Chapter 3. Meanwhile, the number of turns are normally kept equal [23, 25-26] on both sides for static wireless charging applications. Also, lower reflected quality factor due to higher coupling factor stands for lower voltage stress across the primary resonant components for given load quality factor as provided below in (22).

$$|V_p| \approx |Q_r V_i| \tag{22}$$

Increases in efficiency and lower voltage stress are main reasons for high interest of researchers to achieve higher coupling factors through inductor design.

2.3.3. Load quality factor

First factor to be considered in selection of the load quality factor is voltage stress on the resonant components on the secondary side. The voltage stress on resonant components is much higher than on the load as per principle of series resonance and hence lower quality factors are suitable. Another factor advocating for low load quality factor is the secondary circuit efficiency provided in (23).

$$\eta_s = \frac{Q_s}{Q_s + Q_l} \tag{23}$$

However, the reflected quality factor is inversely proportional to the load quality factor (18). Hence, lower load quality factor or higher reflected quality factor will reduce the primary circuit efficiency and increase the voltage stress on the primary side for given amount of power to be transferred. Selection of the secondary quality factor is hence a tradeoff between the efficiency and voltage stress on both sides.

2.4. Resonant circuits

Value of the capacitors is dependent on the remaining three blocks and is the reason for not taking them into consideration as independent design blocks. The load and capacitance values for the four topologies are provided in Table 2. The primary capacitance value is calculated for each topology to provide unity power factor from input side using FMA analysis. On the other hand, the secondary capacitor is made to resonate with the secondary inductors in all the topologies.

Table 2. Load and capacitors values for four resonant topologies

Topology	SS	SP	PS	PP
Load	$\frac{\omega_i L_s}{Q_l}$	$\omega_i L_s Q_l$	$\frac{\omega_i L_s}{Q_l}$	$\omega_i L_s Q_l$
Secondary Capacitor	$\frac{1}{\omega_i^2 L_s}$	$\frac{1}{\omega_i^2 L_s}$	$\frac{1}{\omega_i^2 L_s}$	$\frac{1}{\omega_i^2 L_s}$
Primary capacitor	$\frac{1}{\omega_i^2 L_s}$	$\frac{1}{\omega_i^2\left(L_p - \frac{M^2}{L_s}\right)}$	$\frac{1}{\omega_i^2\left(L_p + \frac{\omega_i^2 M^4}{L_p R_l^2}\right)}$	$\frac{1}{\omega_i^2\left(\left(L_p - \frac{M^2}{L_s}\right) + \frac{\frac{M^4}{L_s^4} R_l^2}{\omega_i^2\left(L_p - \frac{M^2}{L_s}\right)}\right)}$

As well known, series and parallel resonance provide higher voltage and current stress on the resonant components. Apart from these, dependency of the primary capacitor on the coupling factor (mutual and self-inductance) and load is of high importance as also discussed in [23]. The primary capacitor of SS topology is independent both of the load and inductances and theoretically is the best topology as also pointed out in [23]. On the other hand, primary capacitor of SP topology is dependent on the inductances but can be taken care by designing the primary capacitor as per Table 2. Secondary parallel compensated topologies of SP and PP has favorable current source characteristic towards the load compared to voltage source characteristics for secondary series compensation (SS and PS). The primary capacitor of parallel compensated topologies (PS and PP) is dependent on both the inductances and load. An additional DC-DC converter is used on the secondary side in this case [27] which reflects constant load on the primary side and primary capacitor can be designed as per Table 2. Also, these topologies require a current source on the primary side and are practically implemented using LCL topology on the primary side as explained in [23]. This topology provides higher current for given inverter current in the primary coil on account of parallel resonance and seems to be a better solution than series compensated primary topologies (SS and SP). However, DC-link voltage becomes the limiting factor for these topologies as explained in [27].

3. Inductor design

Materials used for the three components: coils, ferrite and aluminum are discussed first before going into details of the design. Additional active shielding coils [20, 36] can also be present in the magnetic environment as also discussed in Section 1.1.2. However for simplifying the inductor design explanation, discussion in this chapter is limited to the three components.

3.1. Materials

The materials used in wireless charging system for vehicle applications are summarized in this section. Values of material properties used in laboratory setup constructed at Department of Energy Technology, Aalborg University are provided in Chapter 4.

3.1.1. Coils

Operational frequency (20 kHz - 85 kHz) of the system requires Litz wire with multiple parallel strands. Two major parameters of Litz wire to be selected are radius of each parallel strands and number of parallel strands. Removal of skin effect is basis of selection for the first part and is done by selecting radius of indivual strand lower than the skin depth. Current density of approximately 4 A/mm^2 [27] is used for this application and is used to linearly calculate number of parallel strands required for given maximum current.

3.1.2. Ferrite

High grade of ferrite with high real relative permeability in range of some thousands is used in the inductor design. The high grade also offers very low imaginary permeability (losses) which is important to deliver output power with good efficiency. Also commercially available high grade ferrite has much smaller dimensions than required for fabricating wireless charging inductors for vehicle applications. Hence, smaller ferrite plates or bars need to be put together in order to fabricate required base ferrite {1}.

3.1.3. Aluminum

Common grade aluminum with low resistivity is used in the inductor design. No special grade of aluminum has been reported in design of the wireless charging inductors to best of my knowledge.

3.2. Design

Inductor design is done using Finite Element Method (FEM) simulations as analytical solutions [40-42] are mathematical intensive and are not highly accurate. The design consists of designing shape, size and placement of the three components: coils, ferrite and aluminum. Major design parameters to be achieved are low internal resistance, high coupling factor, and low magnetic emissions. The first parameter of internal resistance requires different FEM model than the remaining two parameters. This distinction is explained in detail below along with design of the three parameters.

3.2.1. Coupling factor and magnetic emissions

The two design parameters of the coupling factor and magnetic emissions are calculated using 3D FEM model. In the model, the multiple parallel conductors of Litz wire are modelled as single conductor having similar outer dimensions. FEM solver used in this project is Comsol and has in built-in uniform current distribution function in the single conductor coil and external magnetic fields [43] can be calculated using this model. Term external is in respect to the coil as this model is not able to simulate the current distribution inside the coil. This practical FEM model provides solution with good accuracy for the coupling factor and emissions and has been used in other research works [25] for this application.

Different inductor designs [11, 17, 25-27] with variations of the three components have been proposed in literature but all of them can be narrowed into a general design. The general design consists of a layer of ferrite placed below the coil on opposite side of the other coil and has been termed as base ferrite {1}. The coil diameter is kept approximately 60% of the overall inductor diameter as suggested in [25] for providing this short circuit path. The base ferrite is followed by another layer of aluminum. Purpose of the three components can be understood with help of two set of results for four geometries: only coils, aluminum, ferrite and full provided in Figure 8 and 9. The two set of results are at constant current (23 A) and constant output power (1.58 kW) at 20 kHz. The sample geometry is taken from PhD papers {4} with the full geometry representing the general design introduced earlier in the paragraph.

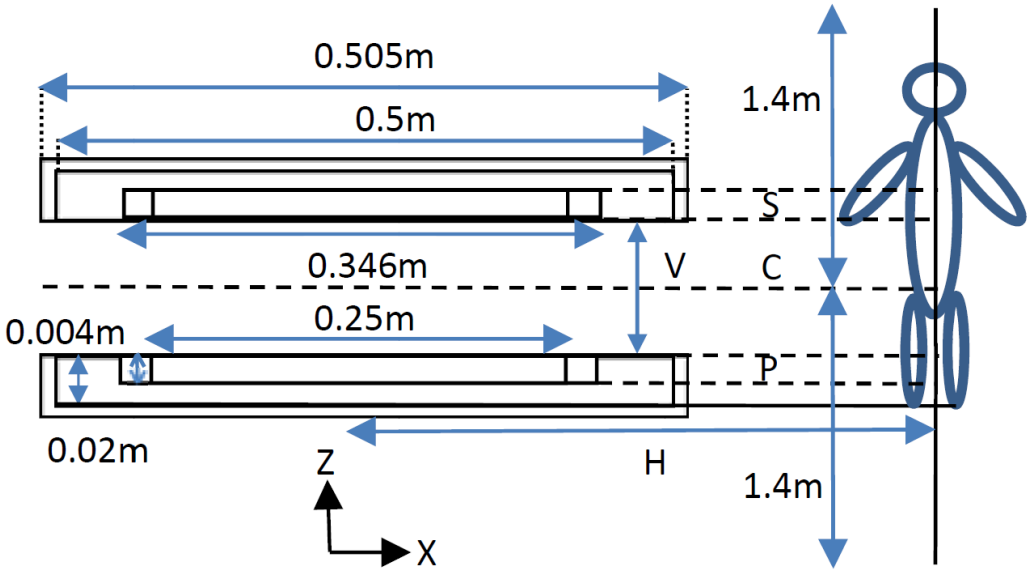

Reproduced with permission from [T. Batra, E. Schaltz, "Passive shielding effect on space profile of magnetic field emissions for wireless power transfer to vehicles", Journal of Applied Physics, Vol. 117, pp 17A739 - 17A739-4, 2015]. Copyright [2015], AIP Publishing LLC.

Figure 7. Side view sample geometries

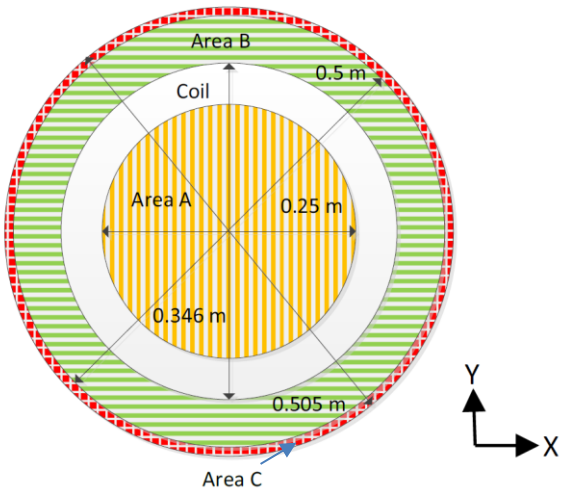

Geometry	Area A	Area B	Area C
No-shielding	Air	Air	Air
Aluminum	Air	Air	Aluminum
Ferrite	Ferrite	Ferrite	Air
Full	Ferrite	Ferrite	Aluminum

Figure 8. Top view sample geometries

The four geometries are constructed in FEM solver (Comsol). The two set of results for V=10 cm and H=60 cm are provided below followed by discussion of results. A few words here about magnetic emissions measurement guidelines provided by International Commission on Non-Ionising Radiation Protection (ICNIRP) [25-27, 48]. The guidelines state that body average of Rms flux densities should be below 62.5 mG in frequency range 0.8 kHz – 125 kHz. However, region or points in the surroundings where the measurements needs to be made are not clarified [25] in the guidelines for this application. The measurement method for emissions is again adopted using research papers [25-27] from University of Auckland. For horizontal distance (X-axis), the emissions are measured at least 50 cm away from center of the inductors. Logic behind this is that smallest electric vehicle on the shorter side is assumed to be around 100 cm wide and centrally placed wireless charging system would be 50 cm away from first human contact. On the other hand for the vertical direction (Z-axis), the emissions are highest in region between the primary (P) and secondary (S) coils {3-10} and is measured up to certain distance on both sides from center (C).

3.2.1.1. Constant primary current

The primary coil is activated with sinusoidal current of 23 A Rms at 20 kHz with the secondary coil open circuited. The self-inductance, mutual inductance and coupling factor of the four geometries

are provided in Table 3. The magnetic field emissions (H=60 cm) and magnetic field arrow plot (normalized) for the four geometries are provided in Figure 9 to 12.

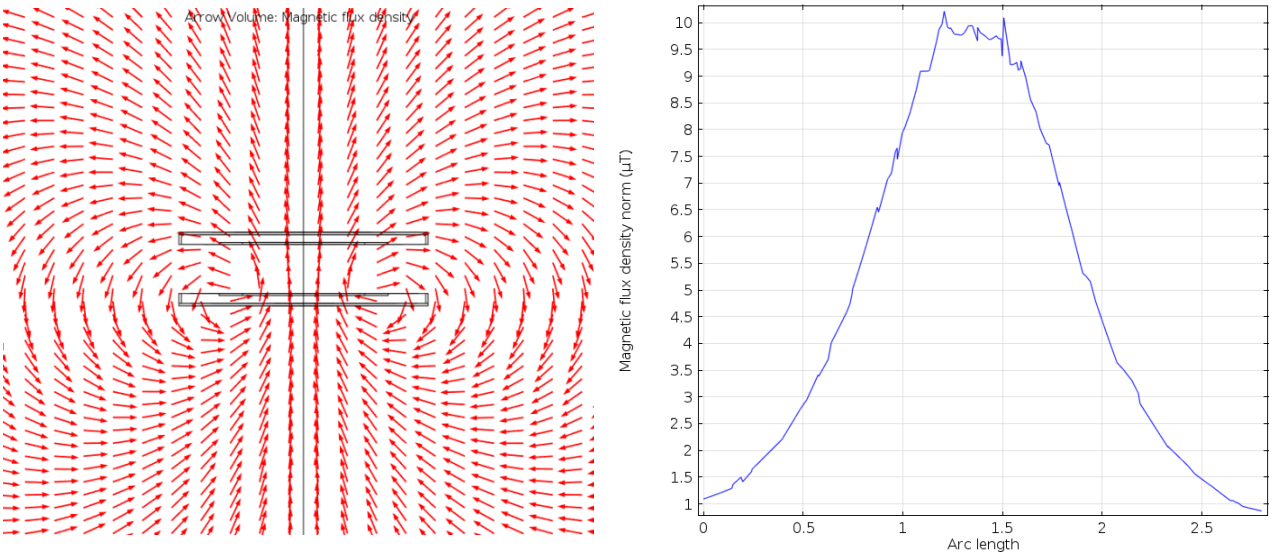

(a) Magnetic field arrow plot - Normalized scale (b) Magnetic emissions (μT) versus Z-axis

Figure 9. Only coils geometry

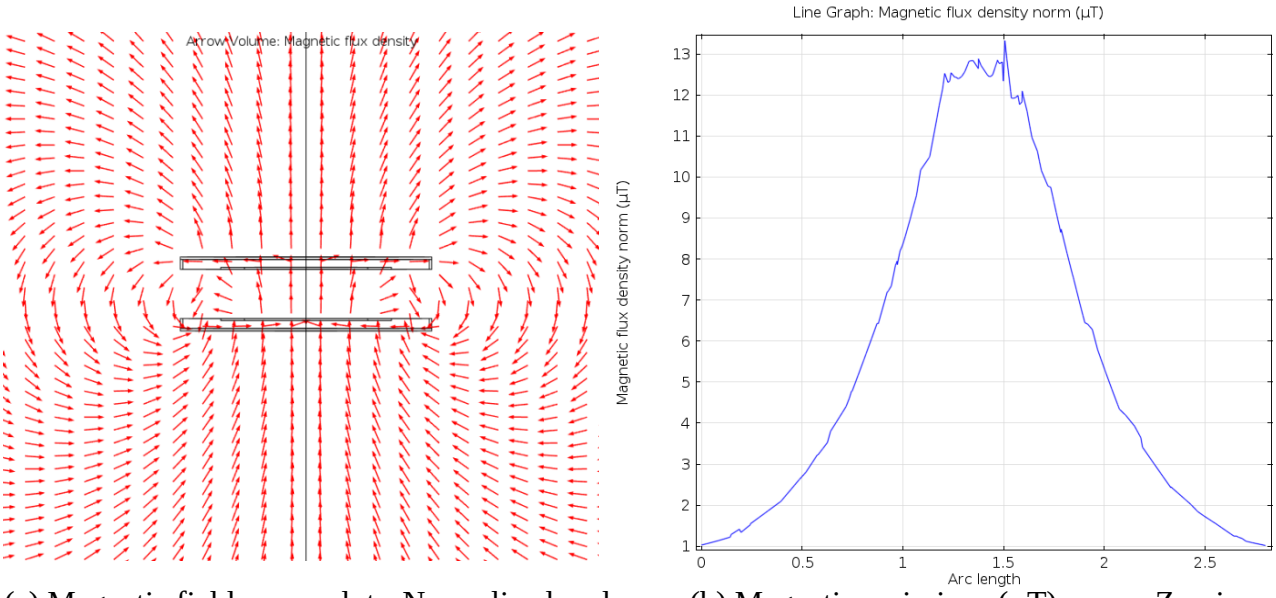

(a) Magnetic field arrow plot - Normalized scale (b) Magnetic emissions (μT) versus Z-axis

Figure 10. Ferrite geometry

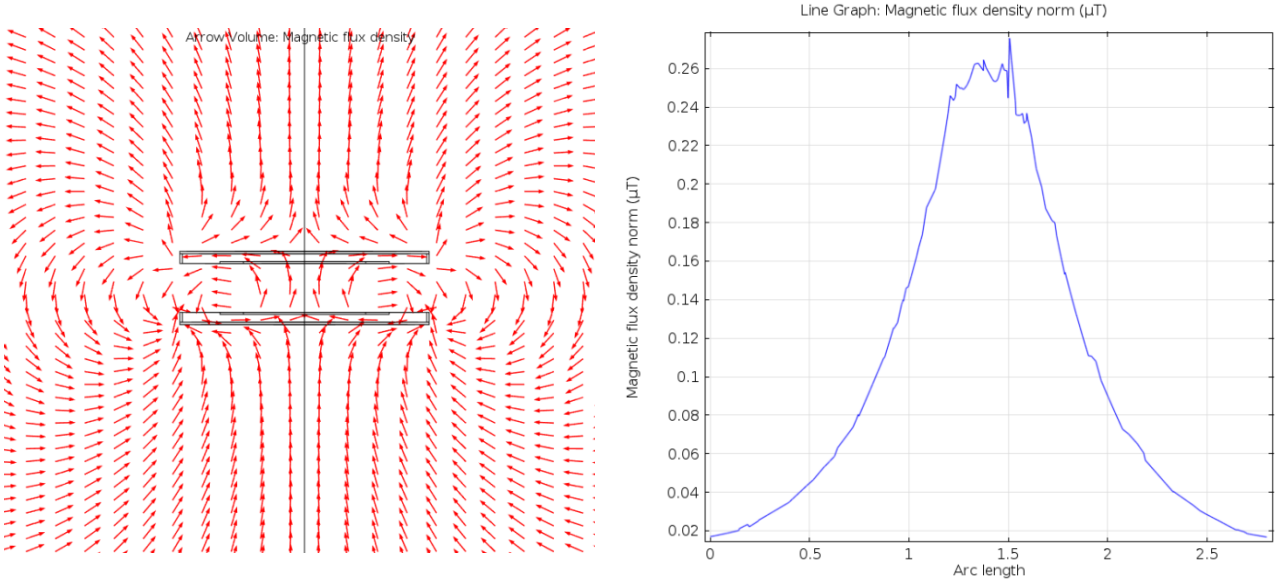

(a) Magnetic field arrow plot - Normalized scale (b) Magnetic emissions (μT) versus Z-axis

Figure 11. Aluminum geometry

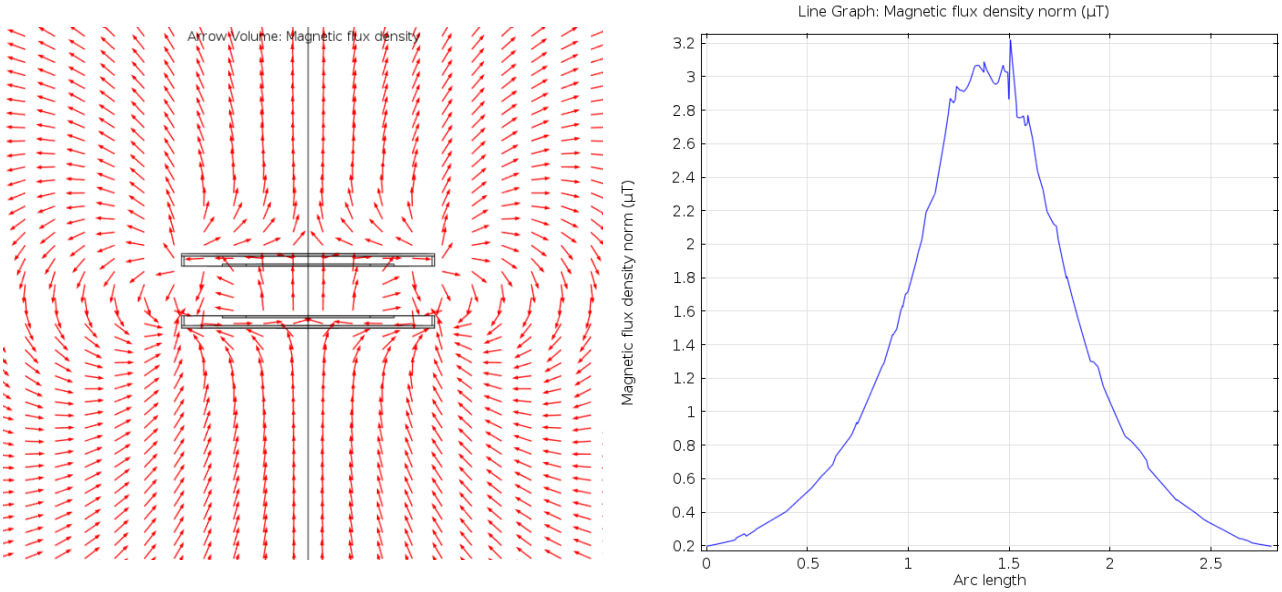

(a) Magnetic field arrow plot - Normalized scale (b) Magnetic emissions (μT) versus Z-axis

Figure 12. Full geometry

Table 3. Inductances and coupling factor

Geometry	**M (μH)**	**L_p=L_s (μH)**	**k**
Only Coils	17	71	0.23
Ferrite	60	158	0.38
Aluminum	2	32	0.06
Full	50	147	0.34

3.2.1.2. Constant output power

Firstly in this section, the output power is calculated using (15) for the only coils geometries with primary current of 23 A Rms at 20 kHz and assuming load quality factor of 10 {4}. The value comes out to be 1.58 kW and is taken as reference value. The primary current for the remaining three geometries is calculated using (15) for similar reference power and load quality factor. The primary coil is energized with current provided in Table 4 for the four geometries. The secondary coil similar to Section 3.2.1.1 is open circuited and the magnetic emissions for similar horizontal distance (H=60 cm) are provided in Figure 13. The emissions plot for the only coil geometry is provided again (Figure 9b) in Figure 13a for comparison with the other geometries.

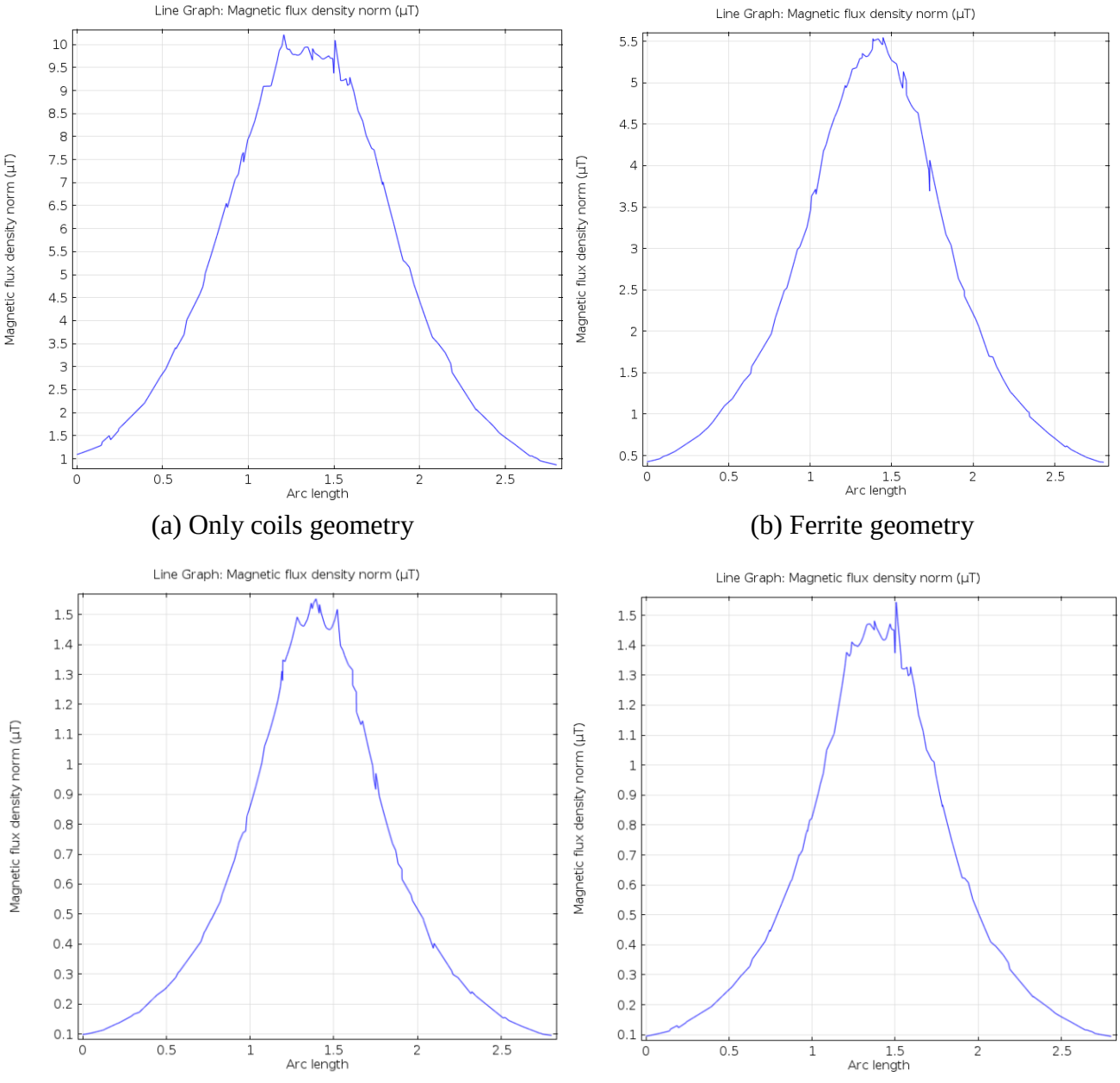

(a) Only coils geometry

(b) Ferrite geometry

(c) Aluminum geometry

(d) Full geometry

Figure 13. Magnetic emissions (µT) versus Z-axis

Table 4. Primary current and coupling factor

Geometry	k	I_p Rms (A)
Only Coils	0.23	23
Ferrite	0.38	9.52
Aluminum	0.06	131.24
Full	0.34	11.03

3.2.1.3. Discussion

The two set of results provided in Section 3.2.1.1 and 3.2.1.2 are discussed in this section.

3.2.1.3.1. Only coils geometry

This is the simplest possible inductor geometry with no passive shielding present. The coupling factor and emissions for this geometry are taken as reference and will be used for comparison with the remaining three geometries.

3.2.1.3.2. Ferrite geometry

High grade ferrite is used below the coil in form of spokes [25], plate [11] and other forms [17, 27]. In all the forms, similar idea of providing short circuit path to the magnetic flux from inner to outer side of the coil is basis for the design. This is also visible in Figure 10a where the magnetic field rotates and passes through the primary base ferrite on the return path. This is different from magnetic field behavior of the only coils geometry in Figure 9a. The magnetic flux as well known flows in closed loops closing the coil (primary). Due to lower magnetic resistance offered by ferrite, the magnetic flux magnitude increases and as a result both the self and mutual inductance increases. Increase in the mutual inductance dominates increase in the self-inductance and as a result the coupling factor increases. The last statement can be explained with help of magnetic flow arrow diagram of Figure 10a. As wireless charging systems have weak magnetic coupling, most of the primary magnetic flux does not couple with the secondary coil. Hence, the self-inductance has major contribution from leakage flux loops which only have short circuit magnetic path through the primary base ferrite. On the other hand, the mutual inductance is integration of flux loops which pass through both the primary and secondary ferrite base. Hence the mutual flux loops have comparably lower magnetic resistance and provide comparably higher increase in the mutual inductance compared to increase in the self-inductance provided by leakage flux loops.

Apart from the coupling factor, the magnetic emissions also increase for the ferrite geometry compared to the only coils geometry for same primary current and is visible by comparing Figure 9b and 10b. Part of the magnetic emission loop path also finds short circuit path through one or both ferrite bases and results in higher emission value for the ferrite geometry. However with increase in the coupling factor, lower current compared to the only coil geometry is required for transferring the same output power as provided in Table 4. This reduces the emissions for given output power and can be verified by comparing Figure 13a and 13b. Summarizing the above, it can be concluded

that ferrite increases the coupling factor and on account of lower current required for transferring the same power also reduces the emissions. On the negative side, there are magnetic losses in the ferrite that reduce the efficiency. The losses are reduced to minimum by using high grade of ferrite as already discussed in Section 3.2.1. Also, ferrite being a compound of heavy metal iron has significant effect on the weight of the inductor.

3.2.1.3.3. Aluminum geometry

Aluminum reduces the magnetic emissions through means of eddy currents. Mechanism of reduction of the emissions can be understood with help of magnetic field arrow diagram of Figure 11a. The magnetic flux goes in parallel with surface of the aluminum on its outer side as it is not able to penetrate the aluminum thickness. Aluminum is used in thickness range of some millimeters which is much higher than skin depth of aluminum for the design frequency range (20 kHz to 85 kHz). As a result, aluminum increases the length of the magnetic flux loop by not allowing the loops to pass through them. This results in increased value of the magnetic resistance and reduces the magnetic flux value (emissions). The last set of statements can be verified from the emissions value for the aluminum geometry (Figure 11b) which is much lower than the values for the only coil (Figure 9b) and ferrite (Figure 10b) geometries.

However, aluminum plate on the secondary side acts as an infinite magnetic resistance again on account of eddy currents and hence the magnetic flux does not effectively couple the secondary coil. This results in huge drop in the mutual inductance and coupling factor as provided in Table 3. This point can also be seen with help of constant power results in Table 4. Very high primary current is required to provide similar output power compared to the only coils and ferrite geometries. This is not practical and refers to fact that aluminum cannot be alone used in inductor design of wireless charging system. A layer of ferrite must be placed in between the coil and aluminum for practical system design as also pointed in [20]. This brings the discussion to the full geometry discussed next.

3.2.1.3.4. Full geometry

Practical inductor design of wireless charging system combines the increased coupling factor from ferrite usage and reduction of emissions from combined usage of ferrite and aluminum. Aluminum has slight negative effect on the coupling factor even with introduction of ferrite layer as seen by comparing the coupling factors of the ferrite and full geometry in Table 3. In other words, slightly higher primary current is required to provide similar output power in the full compared to the ferrite geometry and is provided in Table 4. This reduction in the coupling factor needs to be accepted in the inductor design with aluminum usage as it also provides high reduction in the emissions which can be seen by comparing Figure 10b and 12b. The emissions reduction works in similar way as explained for the aluminum geometry by elongation of the field path and is provided for this geometry in Figure 12a.

3.2.2. Internal resistance

The internal resistance has contributions from DC resistance, skin effect, proximity effect, hysteresis loss in ferrite and eddy current losses in both ferrite and aluminum. Calculating the internal resistance using 3D FEM model would demand all hundreds parallel strands of Litz wire to be modelled separately. This approach is not practical as it needs immense computation power and has already been reported in literature [43-44]. For the internal resistance calculation, first the external magnetic field is calculated using 3D single conductor model discussed in Section 3.2.1. This external magnetic field is used as input for 2D FEM model [43] where all the parallel strands can be modelled separately and internal resistance can be computed with reasonably good accuracy. This part has not been deeply focused during PhD project due to lack of time and will be considered in future works. Alternatively, there are analytical formulas [45-47] also available for calculation of the internal resistance with the parallel conductors included. The internal resistance has been modeled as discrete resistor in 3D FEM model (discussed in 3.2.1) used in the project.

3.3. Passive shielding optimization

Passive shielding as discussed in Section 3.2 increases the power transfer capability and reduces emissions of wireless charging system. On the downside, their addition to the coils increases weight, dimensions, losses and cost of the inductors. Two investigations (papers) have been made during the project for optimization of the passive shielding by weighing their advantages to disadvantages. Of all the considered quantities, only the coupling factor and emissions are electro-magnetic in nature and have been already discussed in detail. The remaining quantities (weight, dimensions, losses and cost) are self-explanatory and need not be explained further. Hence, in this section only a short summary of the investigation (paper) followed by the published/submitted paper is provided.

3.3.1. Investigation 1

Base ferrite is used in variety of shape and size: spokes, disk and others in the inductor design of wireless charging systems as also discussed in Section 3.2.2.3. However it was observed that extra ferrite can be placed parallel to the coil surface and above the base ferrite. Advantage of this addition is increase in the coupling factor with no increase in the outer dimensions of the inductor. This extra ferrite being closer to the other coil in comparison to the base ferrite has potential of providing relative higher increase in the coupling factor. In this paper, best physical location for placement of extra ferrite is investigated w.r.t increase in the coupling factor and weight added by ferrite. It is deduced from the results that ferrite placed in center of the coil provides highest increase in the coupling factor for per unit weight added. The full paper along with the discussion and results is provided next in Section 3.3.1.1.

3.3.1.1. PhD paper 1

This paper was originally published with following details.

{1} T. Batra, E. Schaltz, S. Ahn, “Effect of ferrite addition above the base ferrite on the coupling factor of wireless power transfer for vehicle applications”, Journal of Applied Physics, Vol. 117, pp 17D517 - 17D517-4, 2015.
http://dx.doi.org/10.1063/1.4919039

AIP Journal of Applied Physics

Effect of ferrite addition above the base ferrite on the coupling factor of wireless power transfer for vehicle applications

T. Batra, E. Schaltz, and S. Ahn

Citation: Journal of Applied Physics **117**, 17D517 (2015); doi: 10.1063/1.4919039
View online: http://dx.doi.org/10.1063/1.4919039
View Table of Contents: http://scitation.aip.org/content/aip/journal/jap/117/17?ver=pdfcov
Published by the AIP Publishing

Effect of ferrite addition above the base ferrite on the coupling factor of wireless power transfer for vehicle applications

T. Batra,[1,a)] E. Schaltz,[1] and S. Ahn[2]
[1]Department of Energy Technology, Aalborg University, Aalborg 9220, Denmark
[2]EMC Lab, CCS Graduate School for Green Transportation, KAIST, Daejeon 305-701, South Korea

(Presented 6 November 2014; received 22 September 2014; accepted 4 January 2015; published online 23 April 2015)

Power transfer capability of wireless power transfer systems is highly dependent on the magnetic design of the primary and secondary inductors and is measured quantitatively by the coupling factor. The inductors are designed by placing the coil over a ferrite base to increase the coupling factor and reduce magnetic emissions to the surroundings. Effect of adding extra ferrite above the base ferrite at different physical locations on the self-inductance, mutual inductance, and coupling factor is under investigation in this paper. The addition can increase or decrease the mutual inductance depending on the placement of ferrite. Also, the addition of ferrite increases the self-inductance of the coils, and there is a probability for an overall decrease in the coupling factor. Correct placement of ferrite, on the other hand, can increase the coupling factor relatively higher than the base ferrite as it is closer to the other inductor. Ferrite being a heavy compound of iron increases the inductor weight significantly and needs to be added judiciously. Four zones have been identified in the paper, which shows different sensitivity to addition of ferrite in terms of the two inductances and coupling factor. Simulation and measurement results are presented for different air gaps between the coils and at different gap distances between the ferrite base and added ferrite. This paper is beneficial in improving the coupling factor while adding minimum weight to wireless power transfer system. © *2015 AIP Publishing LLC*. [http://dx.doi.org/10.1063/1.4919039]

I. THEORY

Wireless Power Transfer (WPT) by resonant inductive coupling has shown great promise for charging of electric vehicles. The main advantages of WPT charging are comfort and possibility of power transfer, while the vehicle is moving.[1] Providing high power transfer capability with minimum inductor size and weight is one the biggest challenges in design of WPT inductors. The power transferability of WPT is highly dependent on the coupling factor between the inductors and is given[2] by $P = V_1 I_1 k^2 Q$. P is the power transferred to the secondary side, V_1 and I_1 are the voltage and current for the primary coil, k is the coupling factor, and Q is the secondary side quality factor in the above relation. The coupling factor is defined as $k = \frac{M}{\sqrt{L_1 L_2}}$, where M is the mutual inductance and L_1 and L_2 are the self-inductances of the primary and secondary coils, respectively. Top and side views of the sample geometry used in the paper are provided in Figs. 1 and 2. It is a square geometry of outer dimensions 30 cm × 30 cm. The two inductors ($L_1 = L_2 = L$) are identical and hence the coupling factor can be written as $k = \frac{M}{L}$. Litz wire is used for construction of the coils and relative permeability of the used ferrite is 3200. If no ferrite is present in Figs. 1 and 2, the resultant geometry is termed as Only Coils Geometry.

Ferrite is added in the base below the coil in the form of bars[2,3] and other forms to increase the coupling factor and concentrate the field between inductors. Ferrite base is an essential component for design of WPT for vehicle applications. For the sample geometry, Base Geometry is termed as when base ferrite plates along with the coils are present in the inductors. Statements and results in the paper are presented with help of the primary field (inductor), and analogues results are applicable for the secondary field (inductor). Area above the base ferrite and limited to upper end of the primary coil (marked as Primary Air in Fig. 2) is mostly having air in the inductor design.[2,3] Hence, addition of ferrite in Primary Air does not increase (desired) outer dimensions of the inductor but can be used to increase the coupling factor relatively higher than the base ferrite, as it is closer to the other inductor. Investigating physical locations (Zones) in Primary and Secondary Air where highest increase in coupling factor is achieved per unit weight addition of ferrite is the main theme of this paper. The term "addition of ferrite" stands for extra addition of ferrite in Primary and Secondary Air of Base Geometry throughout the paper. Also, zones touching and away from the base plate are referred to as "Touch" and "Far" zones, respectively, in Figs. 1 and 2. In other publications,[1,4,5] geometries where ferrite was present above the base ferrite were proposed. But none of them to best of our knowledge studied placement of ferrite into two separate portions (base and above) and variation of the two inductances and coupling factor at different physical locations above the base ferrite.

Variation in the primary self-inductance practically depends only on addition of ferrite in Primary Air due to large air gap between the inductors. Magnetic field intensity at a point close (low magnetic resistance) to circumference of the primary coil is higher than at a point away (high magnetic resistance) from it in Primary Air of Base Geometry. Hence,

a)Author to whom correspondence should be addressed. Electronic mail: tba@et.aau.dk.

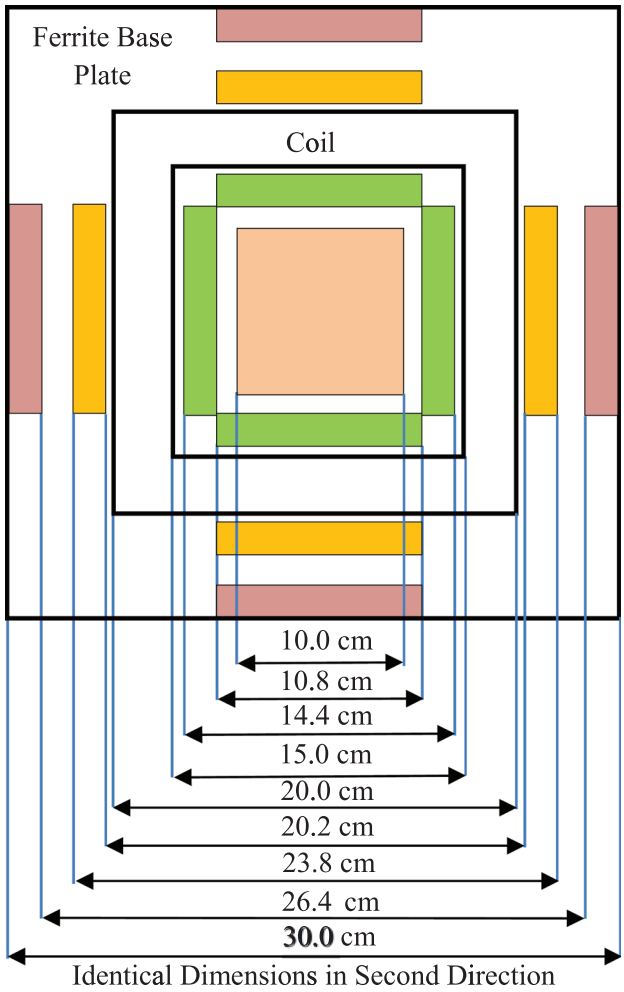

FIG. 1. Sample geometry side view.

two divisions for the self-inductance variation can be made on basis of ferrite placement from the primary coil circumference—high (close—Zones 2 and 3) and low (away—Zones 1 and 4). Further, the close zones can be subdivided as Zone 3 will have lower field compared to Zone 2 as it lies on the outer side of the coil, which has more area for returning flux as compared to starting flux. The primary magnetic field flows in closed loops closing the primary coil and flux inside the coil

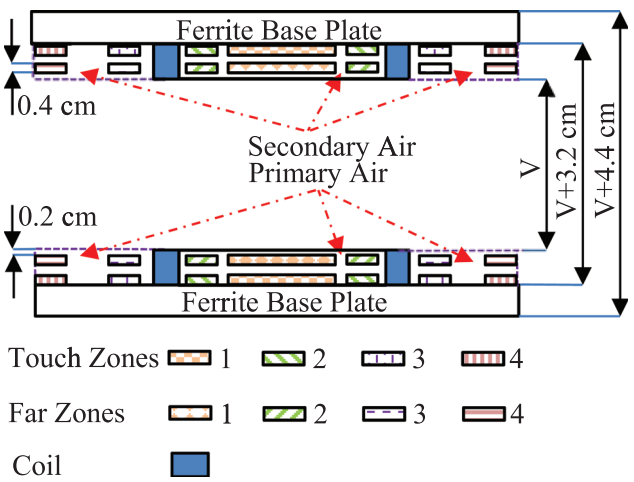

FIG. 2. Sample geometry top view.

is assumed to be the starting flux. Similar argument can be deduced for inner Zones 1 and 4 with Zone 1 having higher field. The above statements explain division of Primary Air into four zones, which show different self-inductance variation for ferrite addition. On the other hand, variation in the mutual inductance depends on added ferrite in Secondary Air only. Ferrite addition should attract more flux inside circumference of the secondary coil than Base Geometry for increase in the mutual inductance and vice versa. Two distinctions for increase (Zones 1 and 2) and decrease (Zones 3 and 4) as a result are possible for mutual inductance variation w.r.t. ferrite addition. Zones (2 or 3) closer to the secondary coil circumference will show more sensitivity towards mutual inductance variation compared to Zone (1 or 4) for ferrite addition as they are closer to path of the primary flux coming towards the secondary ferrite base plate. Highest flux in Primary Air is in Zones 2 and 3 and secondary Zones 2 and 3 lie directly above them and explains the last statement. As a result, Secondary Air similar to Primary Air is divided into four zones. The above mentioned behaviors of the inductances for the four zones along with the supporting results are provided in Sec. II. The coupling factor variation which is a byproduct of the two inductances variation is also discussed.

Distance of the zones from the primary coil circumference and zone dimensions are arbitrary selected values in the paper. They are not uniquely defined by any physical law. Concept of zones has been introduced to mark major areas (Zones), which show similar behavior towards ferrite addition. At last, change in the self-inductance, mutual inductance, or coupling factor divided by change in weight of either inductor has been used as criterion for measuring sensitivity of ferrite addition. As the ferrite material (density) is same for the base and zones, weight is replaced by volume in the last definition. They are denoted by symbols C_s, C_m, and C_k and mathematically sensitivity coefficients for zone ferrite can be written as $C_{s,m,k} = \left(\frac{(L,M,k)_{zone} - (L,M,k)_{base\ geometry}}{Zone\ ferrite\ volume\ (Volume\ Change)}\right)$ with Base Geometry as reference. The coefficients for the base ferrite plate can be defined in a similar way as $C_{s,m,k} = \left(\frac{(L,M,k)_{base\ geometry} - (L,M,k)_{only\ coils}}{Base\ ferrite\ volume\ (Volume\ Change)}\right)$. Only Coils Geometry serves as reference value for the latter coefficients.

II. RESULTS

A. No-Load plot

Theory presented in Sec. I was based on the magnetic field of individual (primary) coil. Primary magnetic field for the surrounding air of Base Geometry is provided in Fig. 3 and is obtained with a no-load simulation[5,6] on Comsol with the primary coil energized and secondary coil open-circuited. Length of an arrow represents strength of the magnetic field at that point. This plot is used to explain the results for the four zones in Subsection II B.

B. Sensitivity coefficients

Simulation and experimental results for two different air gap (V = 6 cm and 12 cm) between the inductors are presented in Tables I–IV. The inductances, C_s, C_m, and C_k are provided

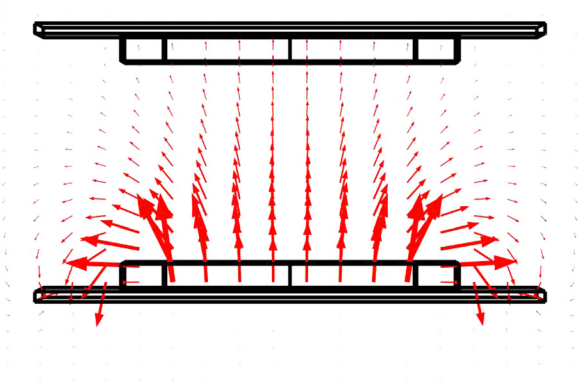

FIG. 3. Primary magnetic field arrow plot.

TABLE I. Simulations results—V = 12 cm.

Zone	Zone type	$L = L_1 = L_2$	C_s	M	C_m	$k = \frac{M}{L}$	C_k ($\times 10^{-3}$)
Only coils		180.947	N.D.	17.154	N.D.	0.0948	N.D.
Base geometry		305.839	0.231	39.527	0.041	0.1292	0.064
1	Touch	311.204	0.134	41.461	0.048	0.1332	0.100
2	Touch	317.737	0.382	41.744	0.071	0.1314	0.071
3	Touch	310.235	0.141	38.977	−0.018	0.1256	−0.120
4	Touch	306.701	0.028	39.594	0.002	0.1291	−0.003
1	Far	311.000	0.130	41.154	0.041	0.1323	0.077
2	Far	316.340	0.338	40.861	0.043	0.1292	0
3	Far	311.509	0.182	38.780	−0.024	0.1245	−0.150
4	Far	306.538	0.0225	39.464	−0.002	0.1288	−0.013

TABLE II. Simulations results—V = 6 cm.

Zone	Zone type	$L = L_1 = L_2$	C_s	M	C_m	$k = \frac{M}{L}$	C_k ($\times 10^{-3}$)
Only coils		180.976	N.D.	41.647	N.D.	0.2301	N.D.
Base geometry		319.671	0.257	102.736	0.113	0.3214	0.169
1	Touch	327.015	0.184	108.457	0.143	0.3317	0.257
2	Touch	332.916	0.426	108.747	0.193	0.3266	0.167
3	Touch	323.878	0.135	102.006	−0.023	0.3149	−0.210
4	Touch	320.602	0.030	103.251	0.016	0.3220	0.019
1	Far	326.611	0.173	107.368	0.116	0.3296	0.205
2	Far	331.254	0.372	106.264	0.113	0.3208	−0.190
3	Far	325.138	0.176	101.139	−0.051	0.3111	−0.330
4	Far	320.230	0.018	102.864	0.004	0.3212	−0.006

in μH, (μH/cm^3), (μH/cm^3), and (1/cm^3), respectively. Also, abbreviation N.D. stands for Not Defined in the tables. Using Figs. 1 and 2, ferrite volumes for the base, Zone 1, and the remaining three zones for either inductor are 540 cm^3, 40 cm^3, and 31.1 cm^3, respectively. Simulations are done on finite element solver Comsol and experimental readings for the inductances are taken with RLC meter (Agilent–U1733C). The experimental procedure is provided in Fig. 4. The operation frequency is 10 kHz for both. The simulation and experimental results are in good compliment with each other. Following observations are obtained from the results.

1. Touch and far zones

For Touch Zones, the base plate is touching the added ferrite and hence they act as one material of low magnetic resistivity. On the other hand, when ferrite is added in Far Zones, an additional magnetic resistance is present between the base plate and the added ferrite. Far Zones are closer to return path of the magnetic flux than Touch Zones; still C_k is lower for them as compared to Touch Zones due to the additional magnetic resistance. Comparing each zone number for the two zone types, i.e., Touch and Far, in all four tables validates the last statement. Hence, ferrite should be added touching rather than at a gap from the base ferrite. The behavior of self and mutual inductances is discussed in detail only for Touch Zones in the next points. The sensitivity coefficients for Far Zones are slightly different as compared to Touch Zones due to the additional magnetic resistance.

2. Zone 1

Magnetic field intensity is moderate in primary Zone 1 in Fig. 3, and hence, C_s increases moderately with addition in this zone. C_m also increases because the addition links more primary flux to the secondary coil as compared to the base geometry. C_m increases comparatively higher than C_s and hence the coupling factor (C_k) increases. Relative increase in path length (reciprocal of self-inductance) of the flux to now pass through primary Zone 1 (originally passing away from primary Zone 1 in base geometry) is much higher than relative increase in path length (reciprocal of mutual inductance) of the flux to shift to secondary Zone 1 (originally passing away from secondary Zone 1 in base geometry) and explains the last statement. The above statements can be verified by comparing rows 2 (base geometry) and 3 in the

TABLE III. Experimental results—V = 12 cm.

Zone	Zone type	L_1	L_2	$L = \sqrt{L_1 L_2}$	C_s	$L_1 + L_2 + 2M_1$	$L_1 + L_2 - 2M_2$	$M = (M_1 + M_2)/2$	C_m	$k = \frac{M}{L}$	C_k ($\times 10^{-3}$)
Only coils		172.3	183.6	177.86	N.D.	400.5	318.8	20.425	N.D.	0.1148	N.D.
Base geometry		305.7	311.2	308.4	0.242	694.2	533.8	40.100	0.074	0.1300	0.028
1	Touch	309.7	315.9	312.8	0.110	705.4	540.3	41.275	0.029	0.1320	0.050
2	Touch	316.7	321.8	319.2	0.347	720.8	552.8	42.000	0.061	0.1315	0.048
3	Touch	309.5	313.3	311.4	0.096	699.5	542.1	39.350	−0.024	0.1264	−0.116
4	Touch	306.9	310.9	308.9	0.016	695.5	536.0	39.875	−0.007	0.1291	−0.029
1	Far	310.2	314.1	312.1	0.092	703.3	539.7	40.900	0.020	0.1310	0.025
2	Far	313.9	315.8	314.8	0.206	709.6	544.0	41.400	0.041	0.1315	0.048
3	Far	308.5	312.3	310.4	0.064	692.8	541.2	37.825	−0.073	0.1220	−0.257
4	Far	306.2	310.8	308.5	0.003	693.4	535.4	39.500	−0.019	0.1280	−0.064

TABLE IV. Experimental results—V = 6 cm.

Zone	Zone type	L_1	L_2	$L=\sqrt{L_1L_2}$	C_s	$L_1+L_2+2M_1$	$L_1+L_2-2M_2$	$M=(M_1+M_2)/2$	C_m	$k=\frac{M}{L}$	C_k ($\times10^{-3}$)
Only coils		172.3	183.6	177.86	N.D.	447.3	270.7	44.150	N.D.	0.2482	N.D.
Base geometry		317.9	322.7	320.3	0.263	837.2	436.0	100.300	0.104	0.3132	0.120
1	Touch	323.7	330.5	327.1	0.170	860.9	440.9	105.000	0.117	0.3210	0.195
2	Touch	330.4	334.2	332.3	0.386	873.8	449.7	106.025	0.184	0.3191	0.189
3	Touch	320.8	325.2	323.0	0.087	846.3	445.8	99.625	−0.022	0.3080	−0.167
4	Touch	319.6	323.8	321.7	0.045	842.7	439.5	100.800	0.016	0.3132	0
1	Far	323.2	328.1	325.6	0.132	856.4	442.8	103.400	0.077	0.3175	0.107
2	Far	325.1	328.5	326.8	0.209	855.9	445.4	102.625	0.075	0.3140	0.026
3	Far	318.9	323.7	321.3	0.032	835.9	442.4	98.375	−0.062	0.3037	−0.305
4	Far	317.6	322.5	320.0	−0.010	838.7	438.4	100.075	−0.007	0.3095	−0.119

tables. At the end, it can be concluded that this is a preferred zone for ferrite addition.

3. Zone 2

In primary Zone 2, the magnetic field intensity is highest of the four zones in Fig. 3 due to shortest magnetic path and as a result increase in C_s is highest. C_m also increases with added ferrite on the secondary side with the same reason as for Zone 1. C_m is also higher for Zone 2 in comparison to Zone 1 as Zone 2 provides shorter path to the flux. C_k increases for this zone but high value of C_s forces it to be lower than C_k for Zone 1. The above comparison for Zone 1 and Zone 2 can be done by comparing rows 3 and 4 in the tables. Based on the results this zone is the next preferred area for ferrite addition after Zone 1.

4. Zone 3

Primary Zone 3 has lower field intensity than Zone 2 in Fig. 3 and as a result same is the case with C_s. Addition of ferrite to secondary Zone 3 forces some of the flux not to pass from inside the secondary coil and hence C_m is negative. In the tables, row 5 has negative C_m and C_k which validates reduction of the mutual inductance and coupling factor. Hence, this is not the preferred zone for ferrite addition.

5. Zone 4

This is the outermost zone and has least sensitivity towards both the self and mutual inductances. Magnitude of the field is reduced away from the circumference of the coils in both the primary and secondary Zone 4 and is reason for low values of C_s and C_m compared to Zone 1 and Zone 2. The results for this zone are provided in row 6 of the tables. C_k has low values compared to the first two zones and hence addition in this zone has least effect on the power transfer capability of the system.

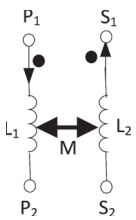

Measure (μH)	RLC Meter Terminals	Remaining Coil Terminals
L_1	P_1 and P_2	Open - S_1 and S_2
L_2	S_1 and S_2	Open - P_1 and P_2
L_1+L_2+2M	P_1 and S_2	Short - P_2 and S_1
L_1+L_2-2M	P_1 and S_1	Short - P_2 and S_2

FIG. 4. Experimental procedure.

6. Base and touch zone ferrite

Positive C_k for Touch Zones 1 and 2 appears to be small. This should, however, not be considered as not having a significant influence on the coupling factor. In order to clarify this point, sensitivity coefficients for Base Geometry are also provided. Comparing coefficients (C_k) for Zones 1 and 2 with Base Geometry from rows 1, 2, and 3 of the tables show that they are close to each other and the remaining two zones are below it. Hence, it can be concluded that base ferrite also increases the coupling factor by comparable (or even lower) numbers on a per unit weight or volume basis. Still base ferrite is necessary in the inductor design for concentrating the magnetic field in between the inductors and minimum leakage to surroundings.

III. CONCLUSIONS

Addition of extra ferrite above the base ferrite for the inductors of wireless power transfer to vehicles is under investigation in this paper. The additional ferrite being closer to the other inductor can increase the coupling factor significantly. The paper notifies four different zones which show different sensitivity in terms of the change in self-inductance, mutual inductance, and coupling factor to extra ferrite addition. Simulation and experimental results show that the central area of the inductor provides highest increase in the coupling factor per unit added weight and is most favorable for ferrite addition. Also, the results show that ferrite addition increases the coupling factor more when the added ferrite is touching rather than at a gap from the base ferrite.

[1]S. Ahn and J. Kim, "Magnetic field design for high efficient and low EMF wireless power transfer in on-line electric vehicle," in *Proceedings of the 5th European Conference on Antennas and Propagation, Rome, Italy, 11–15 April 2011* (IEEE), pp. 3979–3982.
[2]M. Budhia, G. A. Covic, J. T. Boys, and C. Y. Huang, IEEE Trans. Ind. Electron. **60**(1), 318 (2013).
[3]M. Budhia, G. A. Covic, and J. T. Boys, IEEE Trans. Power Electron. **26**(11), 3096 (2011).
[4]H. Sakamoto, K. Harada, S. Washimiya, K. Takehara, Y. Matsuo, and F. Nakao, IEEE Trans. Magn. **35**(5), 3526–3528 (1999).
[5]T. Batra and E. Schaltz, J. Appl. Phys. **115**(17), 17E715 (2014).
[6]T. Batra and E. Schaltz, "Magnetic field emission comparison at different quality factors with series-series compensation network for inductive power transfer to vehicles," in *Wireless Power Transfer Conference 2014, Jeju Islands, South Korea, 8–9 May 2014* (IEEE), pp. 13–16.

3.3.2. Investigation 2

In this section, two aspects thickness and grade of shielding materials ferrite and aluminum are under investigation. Ferrite and aluminum are used in thickness range of few centimeters and few millimeters in the system inductor design. In the first aspect, thickness of both shielding materials is reduced and an investigation is made for change in the coupling factor, inductor weight, magnetic emissions and losses. Results indicate that wireless charging inductors weight and thickness can be substantially reduced if slight higher losses and lower coupling factor are accepted. For the second aspect, the commonly used high grade expensive ferrite is replaced with relatively lower grade cheaper ferrite in terms of performance parameters: coupling factor, inductor weight, magnetic emissions and losses. The results for this case indicate that there is not much reduction in the coupling factor with the changing ferrite grade. However, the losses are more for the lower grade and can be accepted as a tradeoff with reduction in cost. This summary is followed by synopsis of submitted paper and additional results in Section 3.3.2.1 and 3.3.2.2 respectively.

3.3.2.1. PhD paper 2

This paper has been submitted with following details.

{2} T. Batra, E. Schaltz, “Influence of Ferrite Grade and Thickness on System Performance of Wireless Power Transfer for Vehicle Applications”, Submitted, ECCE Asia 2016.

Influence of Passive Shielding Grade and Thickness on System Performance of Wireless Power Transfer for Vehicle Applications

1. Introduction – Passive shielding is used in wireless power transfer (WPT) inductors for vehicle applications to boost the power transfer and provide shielding from the magnetic field emissions. On the other hand, the drawbacks of using passive shielding are increased cost, losses, dimensions and weight of the inductors. In this paper, three investigations are made for optimizing ferrite grade (Ferrite 1 and 2), ferrite thickness (T) and aluminum thickness (S) by counterweighing advantages against disadvantages. The three investigations are explained after brief introduction to the experimental inductor and power electronics setup.

2. Experimental setup – The experimental inductor and electrical setup used in the paper is provided in Figure 1 and 2 below. The magnetic emissions are measured for 16 measurement points and their average is provided in the results.

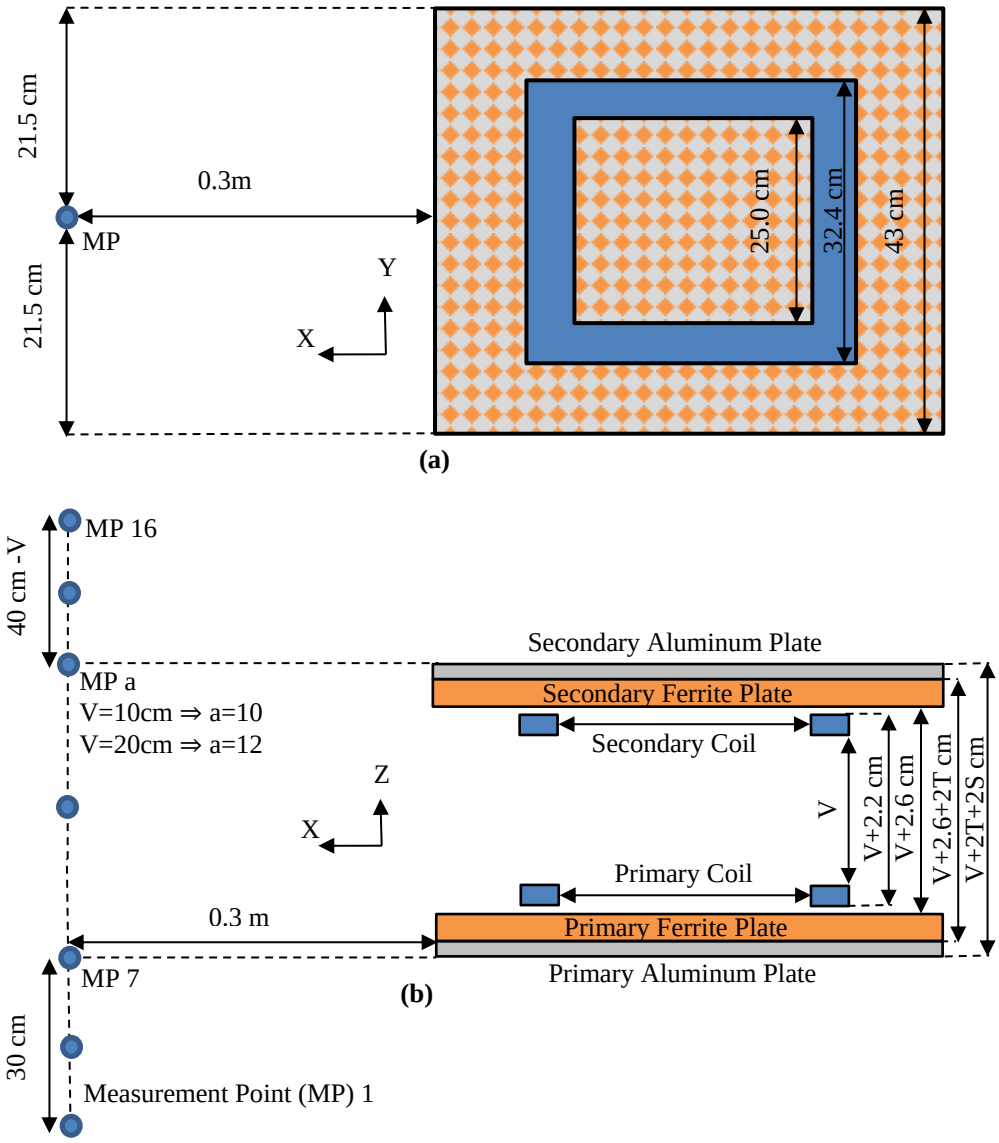

Figure 1 – Inductor setup

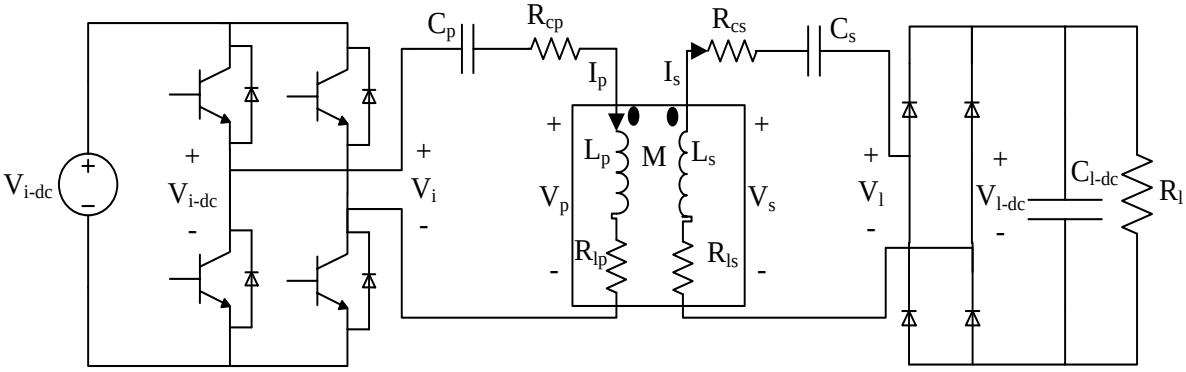

Operation point $\Rightarrow \omega_i=\sqrt{L_pC_p}=\sqrt{L_sC_s} \Rightarrow$ **Circuit efficiency**$= (V_lI_s)/(V_iI_p)$

Figure 2 – Electrical schematic diagram

3. Investigation 1 – The main motivation behind this investigation is development of low weight and low dimensions inductors. Ferrite is used in thickness range of 10 mm [1-3] in the inductor design of WPT. Hence, first of all weight of one of the identical inductor (Figure 1) and its components for ferrite thickness of 10 cm and aluminum thickness of 2 cm is provided.

1) Overall weight=11.252 Kg
2) Aluminum=0.724 Kg
3) Ferrite=8.526 Kg
4) Coil=2.001 Kg

Ferrite is the main contributor in the inductor weight as provided above. It is proposed in the first investigation that the inductor weight and dimensions can be greatly reduced by reducing ferrite thickness as this has comparatively lower effect on system performance (output power, emissions and efficiency). To prove the last statement, experiments are conducted at constant primary current (provide in Table 1), switching frequency (22 kHz) and load (R_l=4.3 Ω) for different ferrite thickness and results are summarized in Table 1. Value of the capacitors is constant and hence switching frequency is varied slightly from 22 kHz to achieve resonance in the system. The same values are used in the remaining two investigations and are not provided again. The measured current and voltage waveforms are provided for lowest ferrite thickness (T=2.5 mm) at V=20 cm in Figure 3.

Table 1. System Performance versus Ferrite Thickness

Ferrite Thickness (T)		**Output Power**		**Average Emissions**		**Circuit efficiency**	
mm	P.U. (%)	W	P.U. (%)	mG	P.U. (%)	%	P.U. (%)
V=10cm, I_p=10 A Rms, S=2 mm							
2.5	25	929	59	73	62	91	100
5	50	1246	78	96	82	89	98
7.5	75	1392	88	115	98	89	98
10	100	1588	100	117	100	91	100
V=20cm, I_p=20 A Rms, S=2 mm							
2.5	25	498	58	118	74	70	85
5	50	693	81	149	93	73	89
7.5	75	790	92	168	105	80	98
10	100	855	100	160	100	82	100

Per Unit (P.U.) % = (Value at T)/(Base values at T=10mm)×100

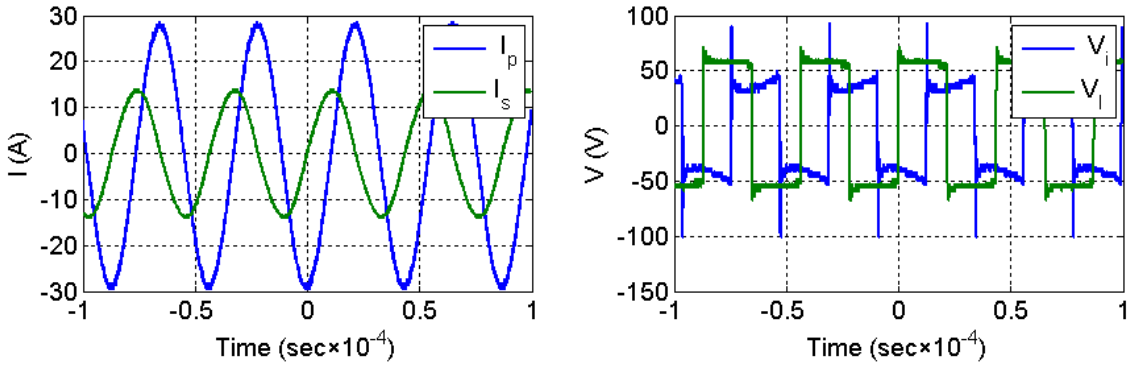

Figure 3 – Electrical waveforms at T=2.5 mm, S=2 mm and V=20 cm

4. Investigation 2 – In state of art inductor designs [1], high and expensive ferrite grade (Ferrite 1) [4] with high relative permeability (magnetic) and very low imaginary permeability (losses) is used. In this investigation, alternate cheaper and inferior magnetic properties ferrite grade [5] is compared with the high grade in terms of system performance to reduce inductor cost. Ferrite 1 is used in Investigation 1 and results are already provided in Table 1. Corresponding results for Ferrite 2 are provided in Table 3. But first, properties of the two ferrite grades are summarized in Table 2. Weight of Ferrite 2 is nearly similar to weight of Ferrite 1 provided in Investigation 1.

Table 2. Comparison ferrite grades

Ferrite	Application	Real Relative Permeability	Imaginary Relative Permeability	Cost	Availability
1	WPT	2300	≈0*	Expensive	Hard
2	Other Applications	660	20	Cheaper	Easy

* Resolution of manufacturer's graph does not allow for accurate reading at 22 kHz

Table 3. System Performance versus Ferrite 2 Thickness

Ferrite Thickness (T)		Output Power		Average Emissions		Circuit efficiency	
mm	P.U. (%)	W	P.U. (%)	mG	P.U. (%)	%	P.U. (%)
V=10cm, I_p=10 A Rms, S=2 mm							
4	40	1323	83	96	68	87	99
6	60	1460	92	114	81	89	101
8	80	1527	96	117	83	88	100
10	100	1588	100	141	100	88	100
V=20cm, I_p=20 A Rms, S=2 mm							
4	40	760	81	148	74	75	94
6	60	815	87	162	81	80	100
8	80	918	98	173	87	80	100
10	100	940	100	200	100	80	100

Per Unit (P.U.) % = (Value at T)/(Base values at T=10mm)×100

At the end, corresponding voltage and current waveforms at S=4 mm, T=2 mm and V=20 cm is provided in Figure 4.

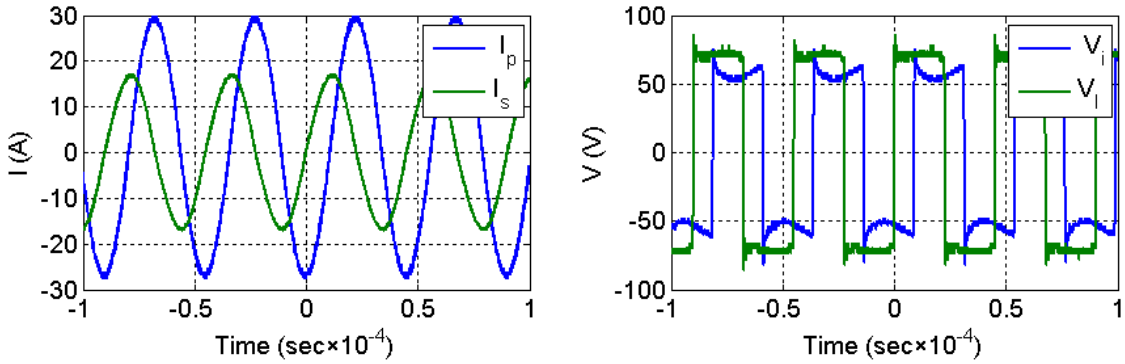

Figure 4 – Electrical waveforms at S=4 mm, T=2 mm and V=20 cm

5. Investigation 3 – This investigation is focused on finding optimized thickness for aluminum which is used in range of few millimeters in state of art designs [1-3]. For this, the aluminum thickness is varied from 0 to 4 mm for both ferrite grades and the results are summarized in Table 4. Before that, voltage and current waveforms are provided for S=0 mm, T=8 mm and V=20 cm are provided in Figure 5.

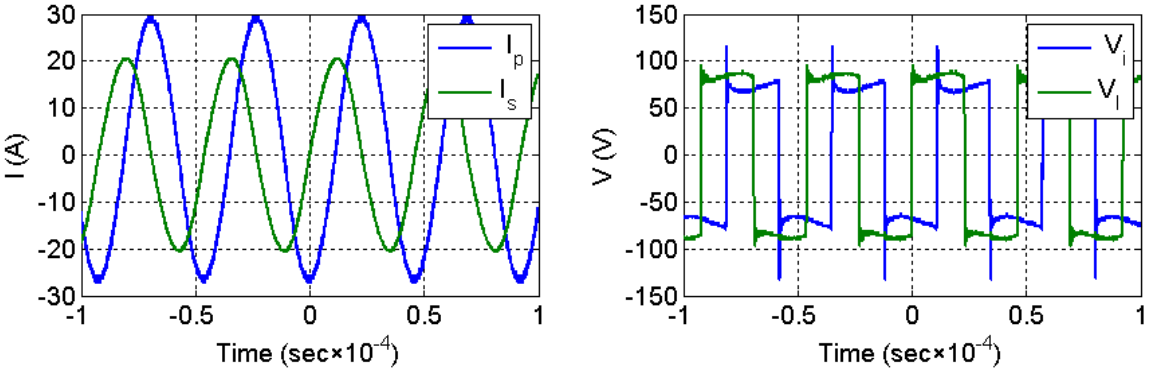

Figure 5 – Electrical waveforms for Ferrite 1 at S=0 mm, T=8 mm and V=20 cm

Table 4. System Performance versus Aluminum Thickness

Aluminum Thickness (S)		**Output Power**		**Average Emissions**		**Circuit efficiency**	
mm	P.U. (%)	W	P.U. (%)	mG	P.U. (%)	%	P.U. (%)
Ferrite 1 at V=10 cm, I_p=10 A, T=10 mm							
0	0	1779	111	218	186	90	98
2	100	1597	100	117	100	92	100
4	200	1442	90	127	109	89	97
Ferrite 1 at V=20 cm, I_p=20 A, T=10 mm							
0	0	1099	130	249	156	86	106
2	100	848	100	160	100	82	100
4	200	835	98	157	98	84	103
Ferrite 2 at V=10 cm, I_p=10 A, T=8 mm							
0	0	1805	114	216	153	87	100
2	100	1588	100	141	100	87	100
4	200	1477	93	123	87	88	100

Ferrite 2 at V=20 cm, I_p=20 A, T=8 mm							
0	0	1091	120	223	129	84	104
2	100	911	100	173	100	80	100
4	200	820	90	173	100	79	99

Per Unit (P.U.) % = (Value at S)/(Base values at S=2mm)×100

5. Results – The following results are obtained from the three investigations.

1) Investigation 1 and 2 – For both ferrite grades, decrease in the ferrite thickness (usage) is much higher than the corresponding decrease in the output power, emissions and efficiency. Hence, weight and dimensions of the inductors can be reduced by using lower thickness of ferrite.

2) Investigation 1 and 2 – The two ferrite grades have near similar performance tested under identical conditions. As a result, the lower grade ferrite can replace higher expensive ferrite grade subject to condition that slightly higher emissions and lower efficiency are acceptable.

3) Investigation 3 – First observation from the last investigation is well known and suggests that removing aluminum from inductor design will have positive impact on the efficiency and output power. However, the emissions increase significantly with removal of aluminum and hence its presence in mandatory. Second observation on the other hand is novel and suggests that aluminum thickness should be kept to minimum as higher value has very little effect on its primary function of reducing emissions.

6. Final version – In the final version, the following will be added to the present synopsis.

1) Analytical model based on magnetic circuits to explain the results.
2) RLC measurements and FEM simulations to supplement experimental results.
3) Magnetic field measurements at all 16 measurement points.
4) Experimentally measured waveforms at all ferrite and aluminum thicknesses.

References

[1] M. Budhia, G. A. Covic, J. T. Boys, "Design and Optimization of Circular Magnetic Structures for Lumped Inductive Power Transfer Systems", IEEE Transactions On Power Electronics, vol 26., no 11., pp. 3096-3108, 2011.

[2] M. Budhia, G. A. Covic, J. T. Boys, "Development of single sided flux couplers for contactless electric vehicle charging", IEEE Transactions On Industrial Electronics, vol 60., no 1., pp. 318-328, 2013.

[3] M. Budhia, G. A. Covic, J. T. Boys, Chang-Yu Hwang, "Development and evaluation of single sided flux couplers for contactless electric vehicle charging", Energy Conversion Congress and Exposition (ECCE) 2011, vol., no., pp. 614-621, 2011.

[4] http://www.digikey.com/product-detail/en/33P2098-0M0/240-2773-ND/5230555

[5] http://www.lairdtech.com/products/mp1496-000

[6] T. Batra, E. Schaltz, S. Ahn, "Effect of ferrite addition above the base ferrite on the coupling factor of wireless power transfer for vehicle applications", Journal of Applied Physics, Vol. 117, pp 17D517 - 17D517-4, 2015.

3.3.2.2. PhD paper 2 – Additional results

PhD paper 2 in Section 3.3.2.1 has been submitted as synopsis to a conference where number of pages is limited to five. In order to present better understanding of the paper, analytical explanation, RLC meter results and experimental readings are added in this section. A point needs to be mentioned here that numbering of tables and figures in this section are in continuation to the main paper {4} as this section is extension of the paper.

3.3.2.2.1. Analytical explanation

In this section, analytical explanation is provided for low dependence of thickness (ferrite and aluminum) and grade (ferrite) of the shielding materials on the self and mutual inductances for wireless charging inductors. The last statement is presented with help of two figures below. In Figure 6, magnetic equivalent circuit of the same inductor setup used in the paper {4} is provided. In the second Figure 7, FEM (Comsol) magnetic field plot for primary no-load (primary activated) test is provided.

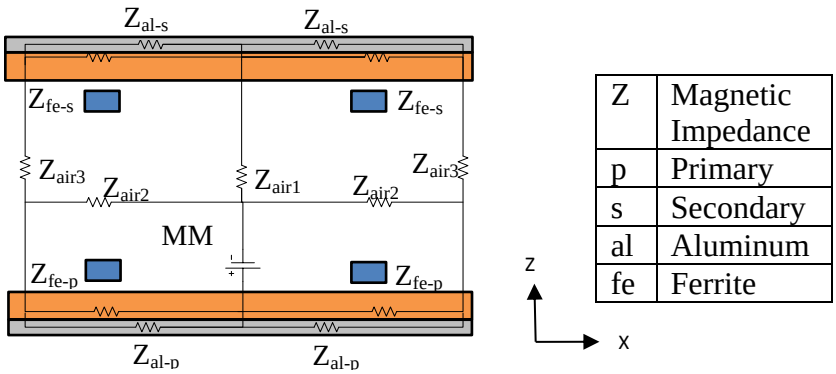

Z	Magnetic Impedance
p	Primary
s	Secondary
al	Aluminum
fe	Ferrite

Figure 6. Magnetic equivalent circuit

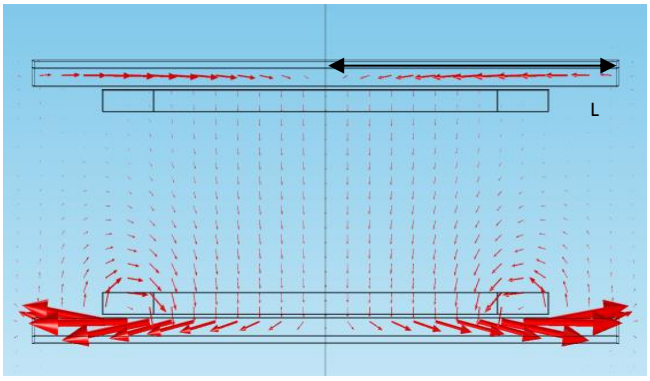

Figure 7. Primary no-load magnetic field plot

Primary magneto motive force (MMF) is AC in nature but for explanation has been taken as DC as shown in Figure 6. In other words, it can be understood in this way that in second half of the

sinusoidal cycle polarity of MMF will be reversed. As the two inductors are identical, secondary side MMF can also be used for the study. Magnetic impedance (Z=L/(μA)) of ferrite is order of magnitude lower than that of air and aluminum as per their complex permeability (Table 6). Hence even if area for magnetic flux in ferrite is reduced, high real relative permeability of ferrite still makes its impedance to act as a short circuit compared to the other impedances. Majority of flux in ferrite flows in X-direction as shown in Figure 7 and length (L) in the magnetic impedance is provided by this direction. Dimensions in Y-direction and Z-direction on the other hand are used for calculating the area. Analysis done here are 2D analysis (XZ plane) and if YZ plane is chosen instead, dimension in Y direction will become the length for the resistance formula. Hence only reducing in Z-direction (thickness) does not practically affect the inductances and hence the coupling factor, output power and emissions. On the other hand, reduction in X or Y dimensions will result in lowering of flux attraction and the inductances can have significant variation but is not considered in this investigation. Similar arguments are true for varying variation in the inductances with the ferrite grade. A lower ferrite grade still has magnetic impedance much smaller than of air and majority of flux passes through it.

Non-significance of aluminum thickness on the inductances can be explained in an opposite way to the ferrite case. Magnetic impedance of the aluminum acts as open circuit compared to other impedances in Figure 6. As a result, majority of the magnetic flux linking the two coils (mutual inductance) follows the following path: $(Z_{fe\text{-}p} \rightarrow Z_{air3} \rightarrow Z_{fe\text{-}s})_{half\ flux} \rightarrow Z_{air1}$. On the other hand, majority of flux closing only the primary coil (self-inductance) follows path: $(Z_{fe\text{-}p} \rightarrow Z_{air2})_{half\ flux}$. This can be seen with help of no-load FEM simulation in Figure 7. Ferrite impedances are negligible as compared to air impedances and the equivalent impedances for the two cases can be approximated as $(Z_{air3})_{half\ flux} \rightarrow Z_{air1}$ and $(Z_{air2})_{half\ flux}$. Hence, the magnetic flux and inductances are highly dependent on the air impedances and not on thickness of shielding materials. But side effect of the thickness reduction is that area for flux flow is reduced and this leads to increased internal impedance in both materials. The increase in resistance can be verified by RLC meter measurements in next Section 3.3.2.2.2.

3.3.2.2.2. RLC meter results

The self-inductance, mutual inductance and internal resistances at different ferrite thickness and grade and aluminum thickness are provided next in Table 5 and 6 respectively. Discussion about behavior of the inductances and resistance with variation in the three has already been discussed in last Section 3.3.2.2.1 and will not be provided again here.

Table 5. Inductor Parameters versus Ferrite Thickness and Grade

Ferrite Thickness (T)		**R_{lp}**		**L_p**		**R_{ls}**		**L_s**		**M**	
Mm	P.U. (%)	mΩ	P.U. (%)	μH	P.U. (%)	mΩ	P.U. (%)	μH	P.U. (%)	μH	P.U. (%)
Ferrite 1 at V=10 cm											

2.5	25	243	148	218	86	204	132	217	88	53	72
5	50	176	107	241	95	170	110	235	95	65.25	89
7.5	75	172	105	244	96	163	106	241	98	68.75	94
10	100	164	100	253	100	154	100	247	100	73.5	100
Ferrite 1 at V=20 cm											
2.5	25	224	147	215	88	177	132	215	90	19	72
5	50	166	109	232	95	159	119	229	96	23	87
7.5	75	164	108	239	98	144	107	235	98	24.75	93
10	100	152	100	245	100	134	100	239	100	26.5	100
Ferrite 2 at V=10 cm											
4	40	212	115	241	95	207	122	237	95	212	86
6	60	193	105	247	97	184	108	244	98	193	93
8	80	183	99	249	98	171	101	247	99	183	95
10	100	184	100	254	100	170	100	249	100	184	100
Ferrite 2 at V=20 cm											
4	40	194	118	236	96	179	122	232	96	194	87
6	60	177	108	241	98	163	111	237	98	177	93
8	80	164	100	243	99	153	104	240	99	164	96
10	100	164	100	246	100	147	100	242	100	164	100

Per Unit (P.U.) % = (Value at T)/(Base values at T=10mm)×100

Table 6. Inductor Parameters versus Aluminum Thickness

Aluminum Thickness (S)		**R_{lp}**		**L_p**		**R_{ls}**		**L_s**		**M**	
Mm	P.U. (%)	mΩ	P.U. (%)	µH	P.U. (%)	mΩ	P.U. (%)	µH	P.U. (%)	µH	P.U. (%)
Ferrite 1 at V=10 cm											
0	0	97	59	256	101	93	60	257	104	80.5	110
2	100	164	100	253	100	154	100	247	100	73.5	100
4	200	167	102	248	98	152	99	247	100	71	97
Ferrite 1 at V=20 cm											
0	0	99	65	246	100	94	70	248	104	30.25	114
2	100	152	100	245	100	134	100	239	100	26.5	100
4	200	143	94	241	98	132	99	240	100	25.5	96
Ferrite 2 at V=10 cm											
0	0	131	72	259	104	119	70	258	104	80.75	113
2	100	183	100	249	100	171	100	247	100	71.25	100
4	200	182	99	250	100	178	104	247	100	71	100
Ferrite 2 at V=20 cm											
0	0	122	74	249	102	114	100	248	103	30.75	118
2	100	164	100	243	100	153	134	240	100	26	100
4	200	170	104	243	100	158	139	240	100	25.5	98

Per Unit (P.U.) % = (Value at S)/(Base values at S=2mm)×100

3.3.2.2.3. Experimental results

The experimental waveforms which could not be provided in PhD paper {4} due to page limitation are provided in this section.

1) Results are presented in Figure 8 for varying ferrite thickness with Ferrite 1, S=2 mm and V=10 cm and correspond to upper part of Table 1 in paper {4}.

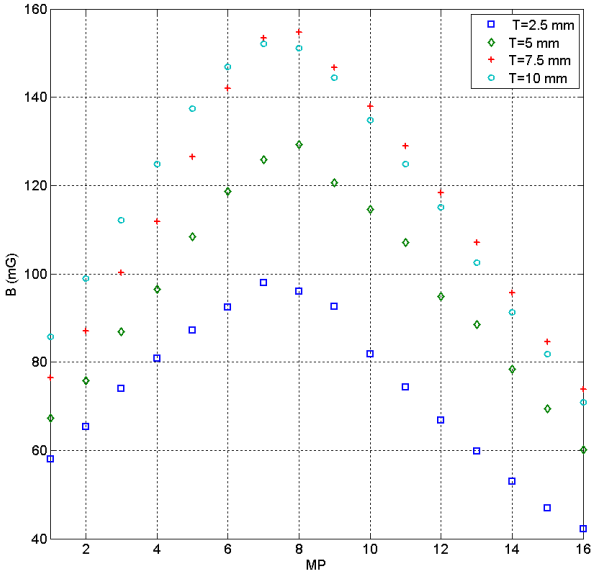

(a) Emissions

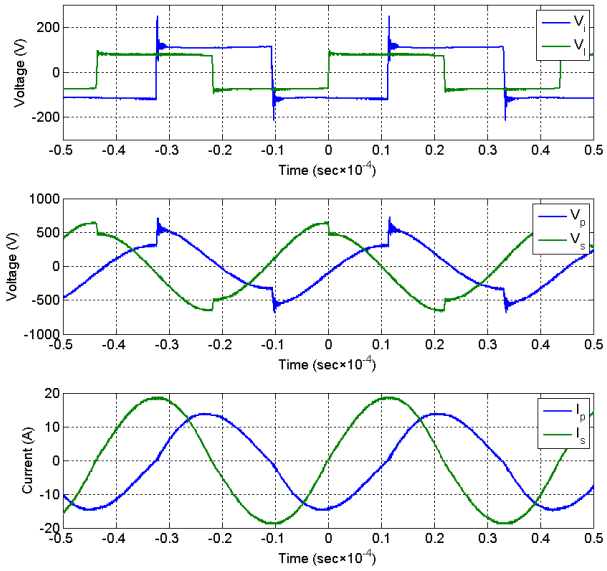

(b) Electrical quantities @ T=2.5 mm

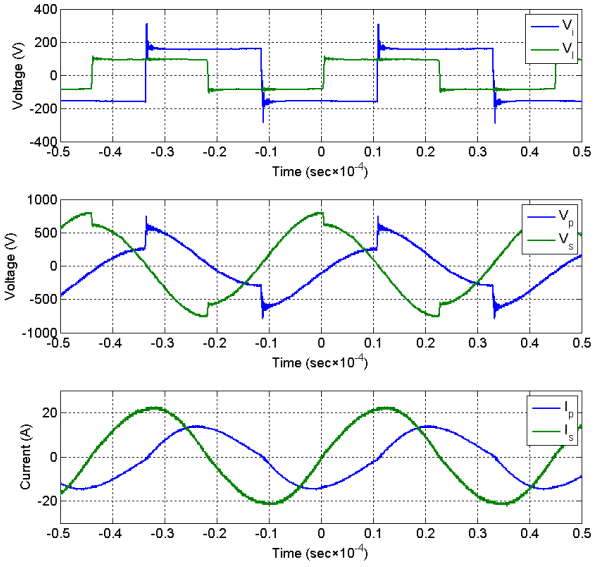

(c) Electrical quantities @ T=5 mm

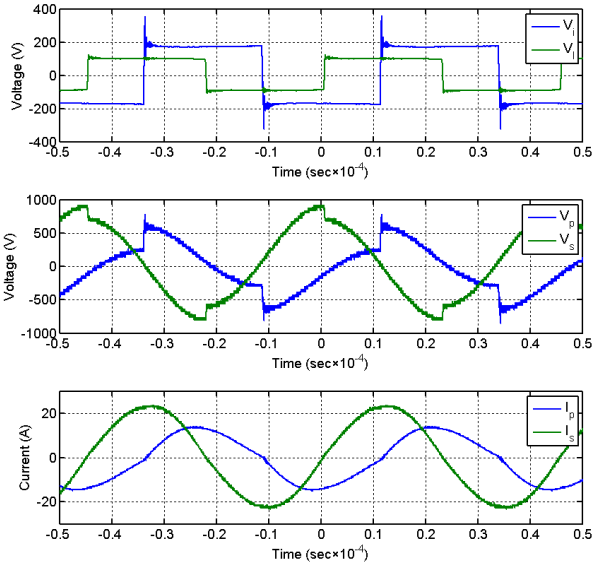

(d) Electrical quantities @ T=7.5 mm

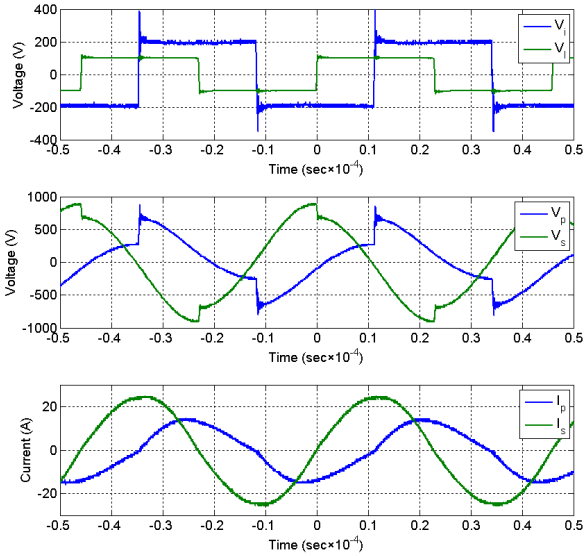

(e) Electrical quantities @ T=10 mm

Figure 8. Emissions and electrical quantities @ Ferrite 1, S=2 mm and V=10 cm

2) Results are presented in Figure 9 for varying ferrite thickness with Ferrite 1, S=2 mm and V=20 cm and correspond to lower part of Table 1 in paper {4}.

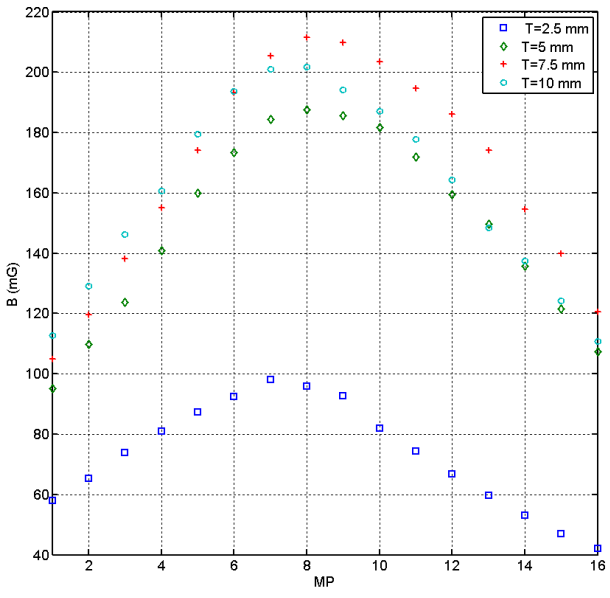

(a) Emissions

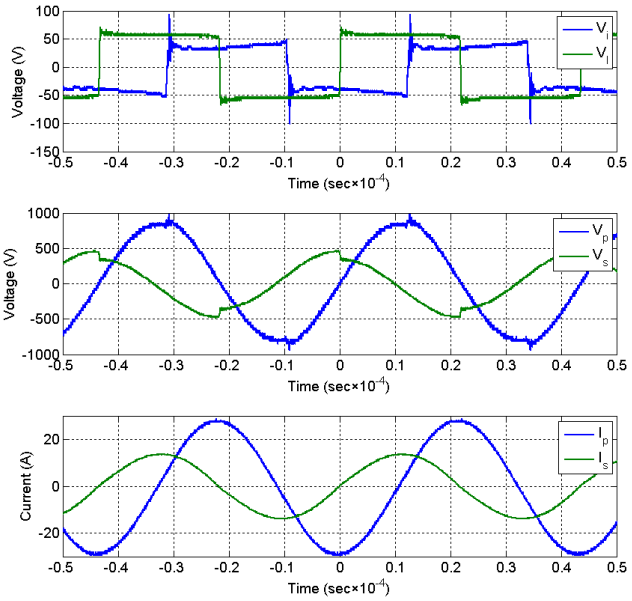

(b) Electrical quantities @ T=2.5 mm

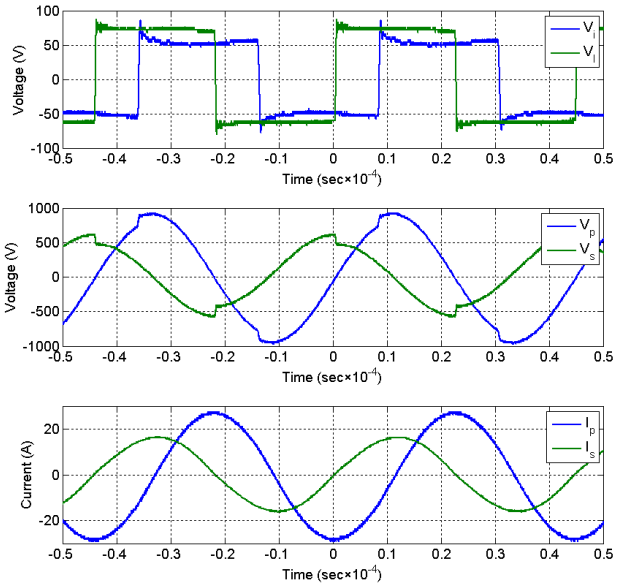

(c) Electrical quantities @ T=5 mm

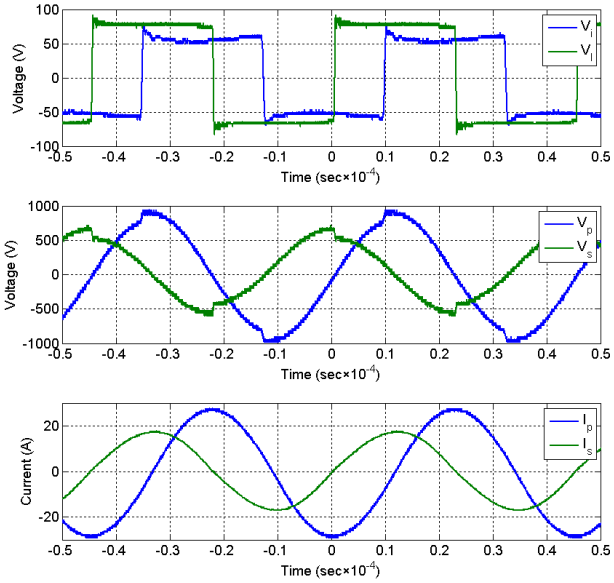

(d) Electrical quantities @ T=7.5 mm

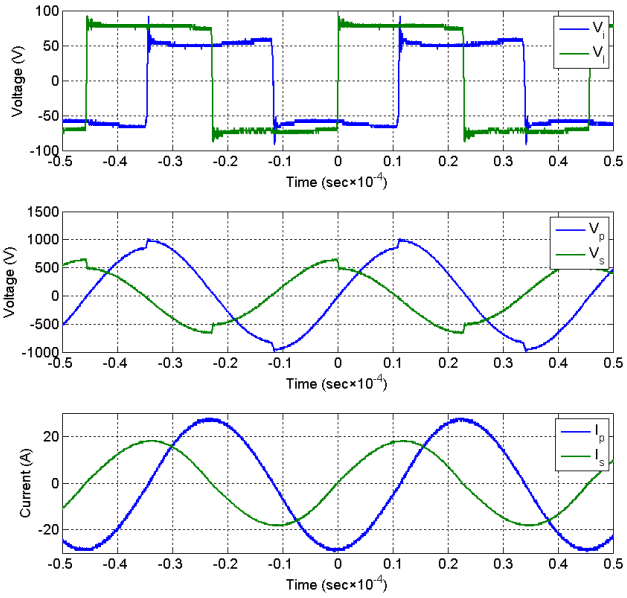

(e) Electrical quantities @ T=10 mm

Figure 9. Emissions and electrical quantities @ Ferrite 1, S=2 mm and V=20 cm

3) Results are presented in Figure 10 for varying ferrite thickness with Ferrite 2, S=2 mm and V=10 cm and correspond to upper part of Table 2 in paper {4}.

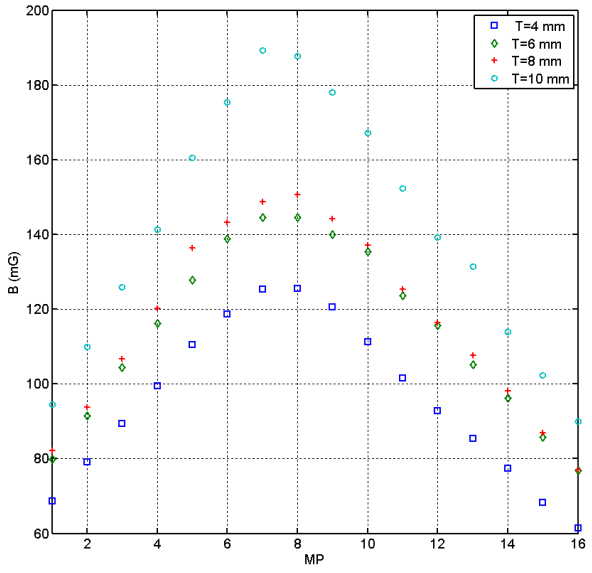

(a) Emissions

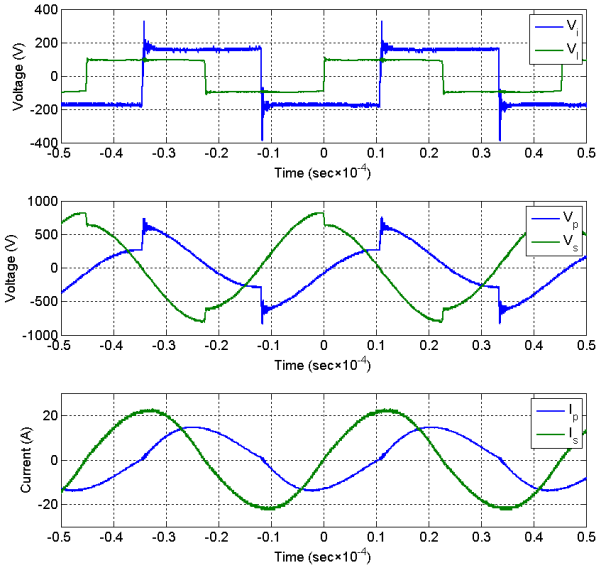

(b) Electrical quantities @ T=4 mm

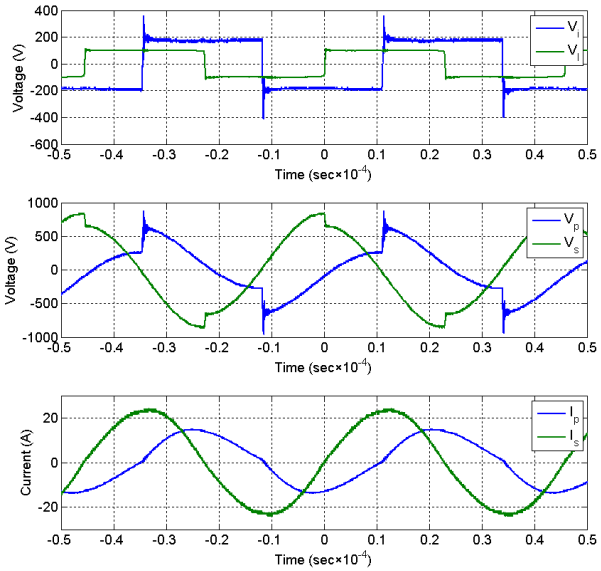

(c) Electrical quantities @ T=6 mm

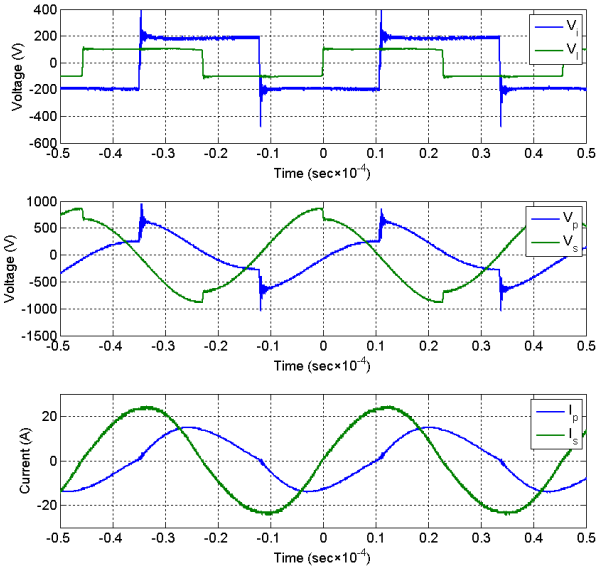

(d) Electrical quantities @ T=8 mm

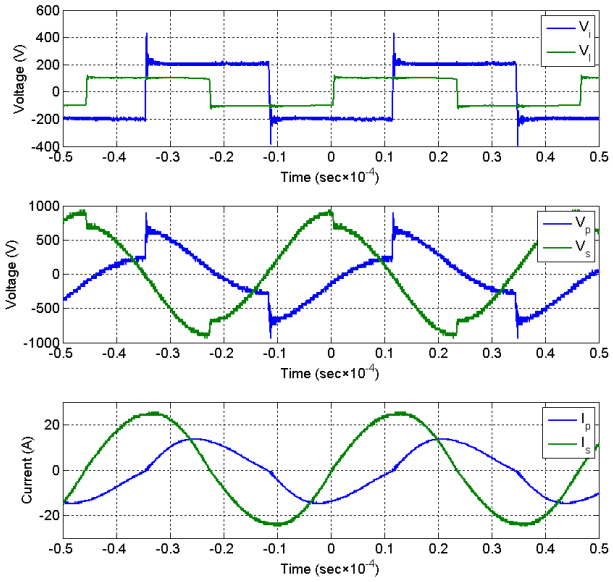

(e) Electrical quantities @ T=10 mm

Figure 10. Emissions and electrical quantities @ Ferrite 2, S=2 mm and V=10 cm

4) Results are presented in Figure 11 for varying ferrite thickness with Ferrite 2, S=2 mm and V=20 cm and correspond to lower part of Table 2 in paper {4}.

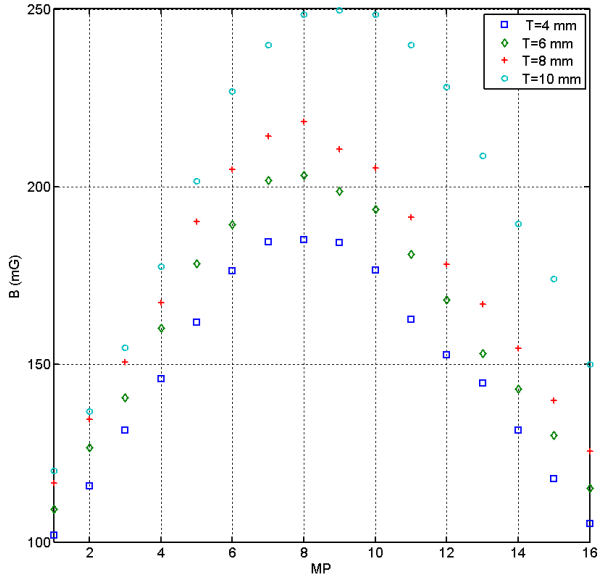

(a) Emissions

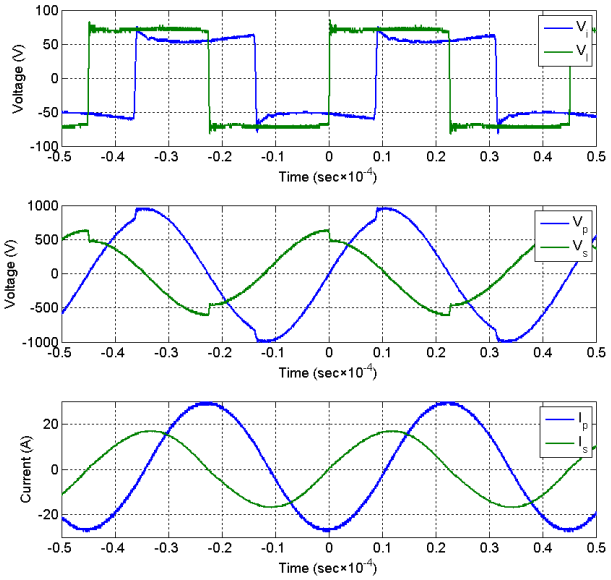

(b) Electrical quantities @ T=4 mm

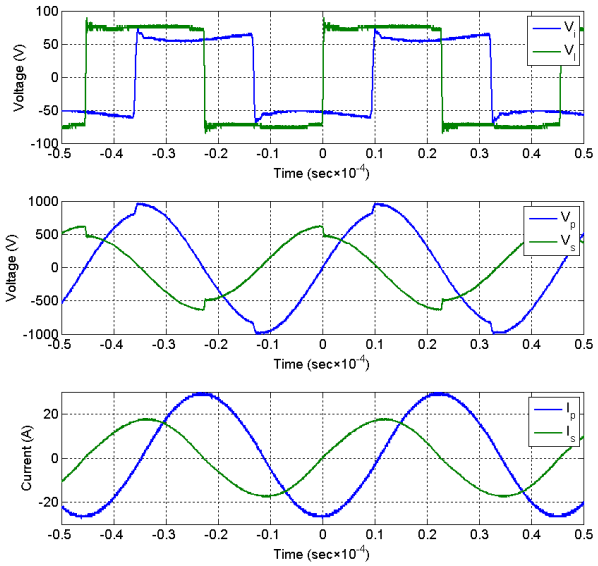

(c) Electrical quantities @ T=6 mm

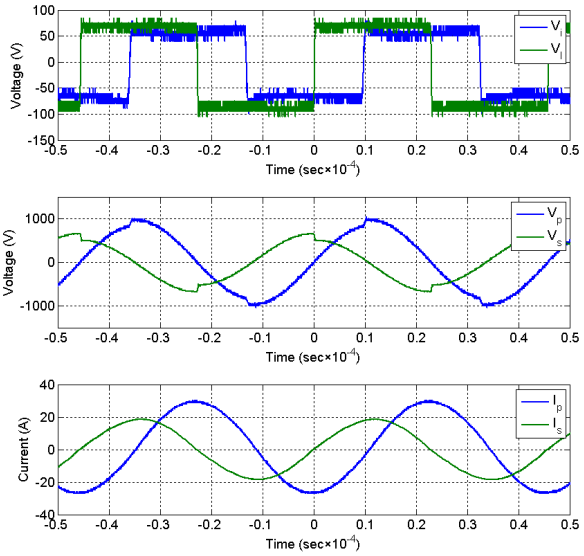

(d) Electrical quantities @ T=8 mm

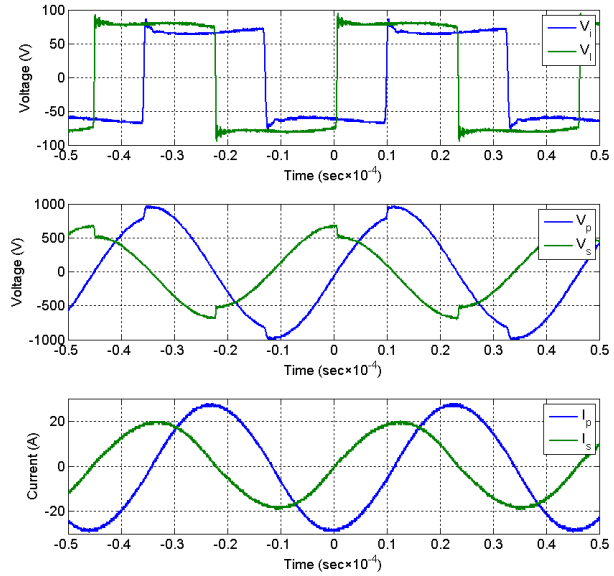

(e) Electrical quantities @ T=10 mm

Figure 11. Emissions and electrical quantities @ Ferrite 2, S=2 mm and V=20 cm

5) Results are presented in Figure 12 for varying aluminum thickness with Ferrite 1, T=10 mm and V=10 cm and correspond to upper part of Table 4 in paper {4}.

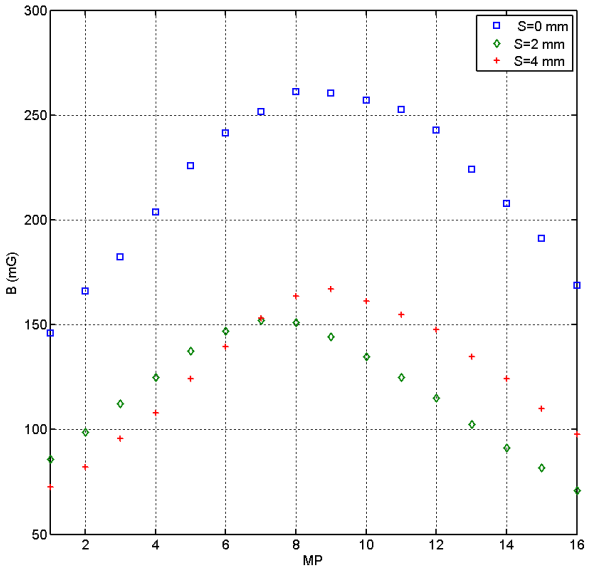

(a) Emissions

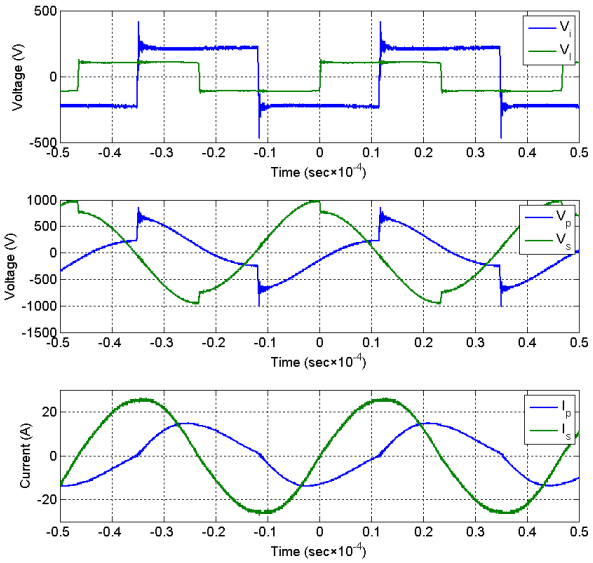

(b) Electrical quantities @ S=0 mm

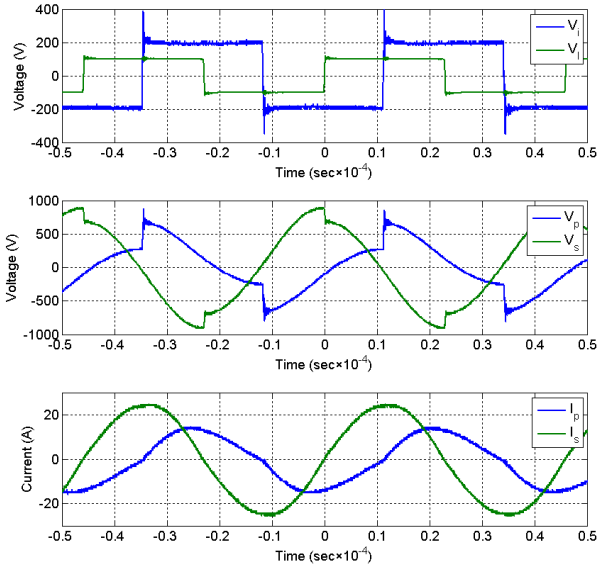

(c) Electrical quantities @ S=2 mm

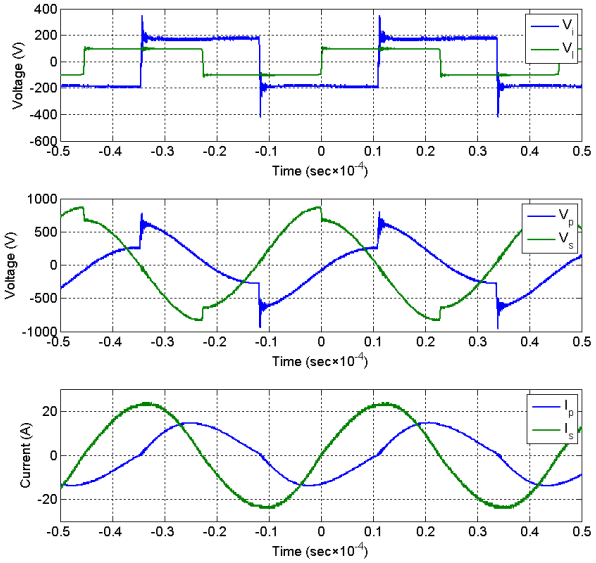

(d) Electrical quantities @ S=4 mm

Figure 12. Emissions and electrical quantities @ Ferrite 1, T=10 mm and V=10 cm

6) Results are presented in Figure 13 for varying aluminum thickness with Ferrite 1, T=10 mm and V=20 cm and correspond to upper middle part of Table 4 in paper {4}.

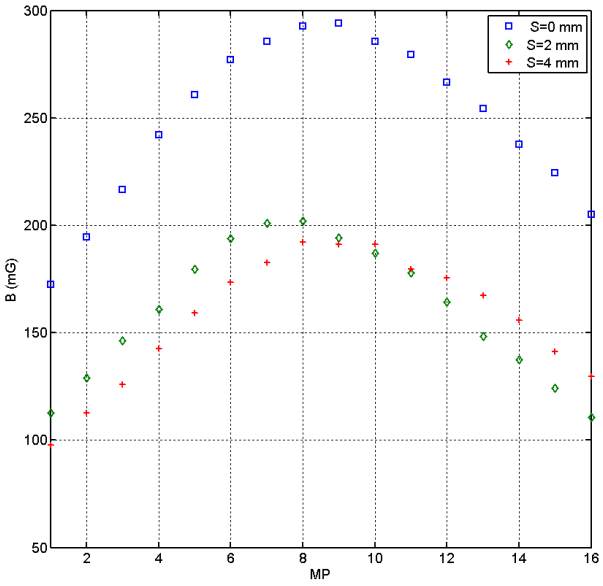

(a) Emissions

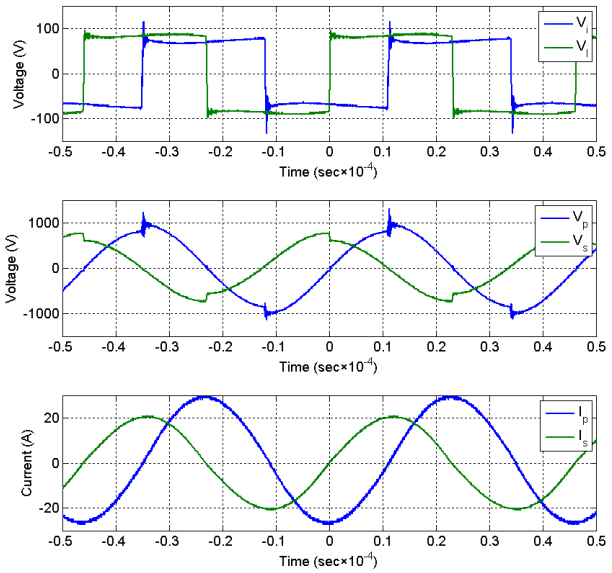

(b) Electrical quantities @ S=0 mm

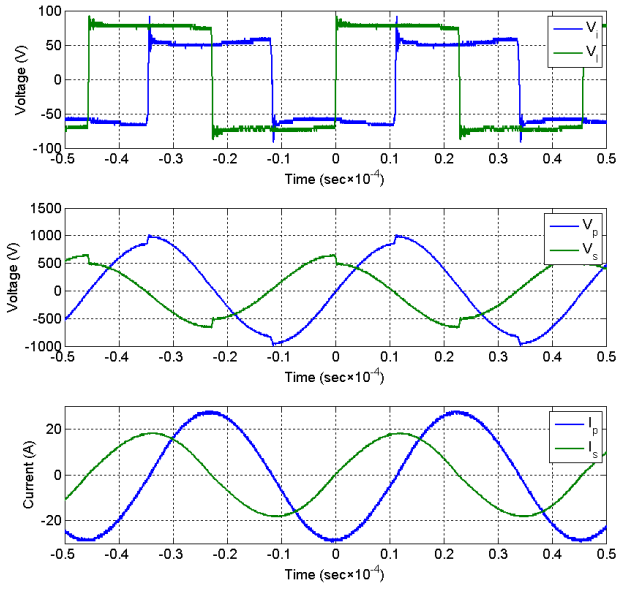

(c) Electrical quantities @ S=2 mm

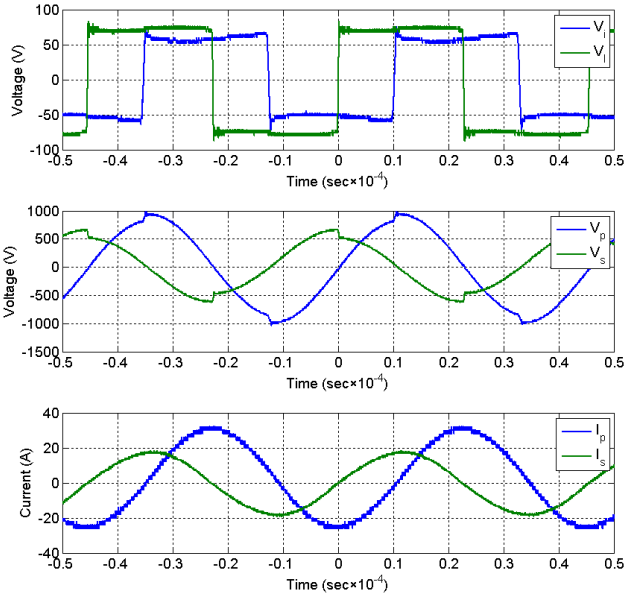

(d) Electrical quantities @ S=4 mm

Figure 13. Emissions and electrical quantities @ Ferrite 1, T=10 mm and V=20 cm

7) Results are presented in Figure 14 for varying aluminum thickness with Ferrite 2, T=8 mm and V=10 cm and correspond to lower middle part of Table 4 in paper {4}.

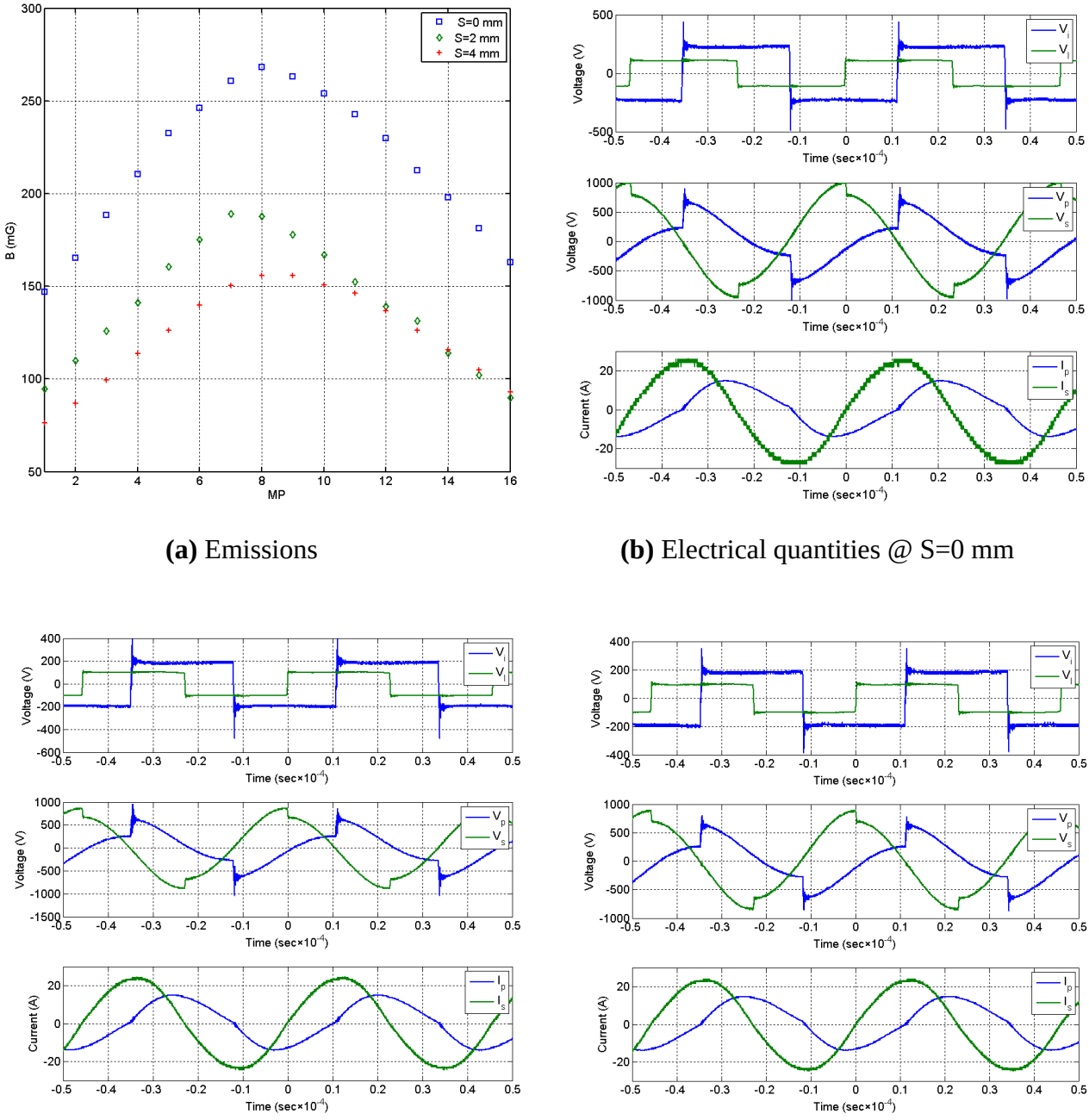

(a) Emissions

(b) Electrical quantities @ S=0 mm

(c) Electrical quantities @ S=2 mm

(d) Electrical quantities @ S=4 mm

Figure 14. Emissions and electrical quantities @ Ferrite 2, T=8 mm and V=10 cm

8) Results are presented in Figure 15 for varying aluminum thickness with Ferrite 2, T=8 mm and V=20 cm and correspond to lower part of Table 4 in paper {4}.

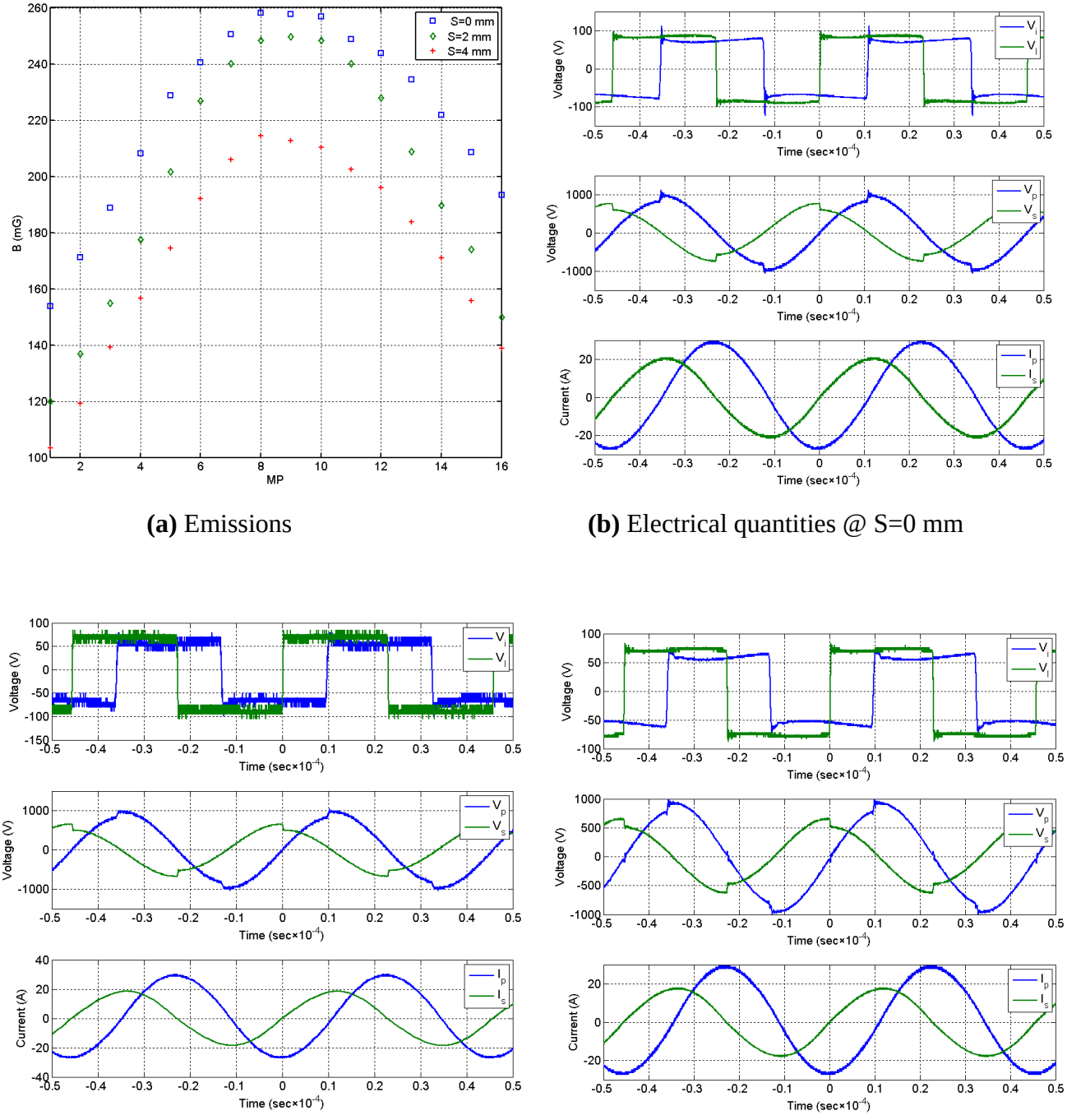

(a) Emissions

(b) Electrical quantities @ S=0 mm

(c) Electrical quantities @ S=2 mm

(d) Electrical quantities @ S=4 mm

Figure 15. Emissions and electrical quantities @ Ferrite 2, T=8 mm and V=20 cm

4. Laboratory setup

Details of the wireless charging system constructed during PhD project in lab of Department of Energy Technology, Aalborg University is provided in this section.

4.1. Power electronics

The primary and secondary power electronics blocks are simplified in the construction as they are not the focus of this study. Complete electric schematic of SS and SP topologies along with photographs of the constructed system are provided in Figure 14. The primary side rectifier combined with DC-link capacitor provides constant DC voltage ($V_{i\text{-}dc}$). Hence, they are replaced by two DC power supplies each with indivual maximum ratings of 10 A and 600 V. The supplies can be arranged in series or parallel depending on requirement of higher current or voltage. The supplies are also bottleneck for the output power with maximum current of 20 A. The other components are rated for much higher current ratings. In the future, higher current ratings power supplies will be introduced to increase output power rating of the setup. The inverter is constructed using two inverter legs manufactured by Microsemi. The inverter leg has maximum ratings of 100 A and 1200 V at 50 kHz (maximum rated frequency). There is no control system implemented in the system as focus of the project is on the inductor design and magnetic emissions. The system is operated in open loop by calculating required input voltage for given load and switching frequency using FMA analysis. On the secondary side, the rectifier bridge is again manufactured by Microsemi and is rated for 1200 V and 40 A. Value of DC-link capacitor is 112 µF and the battery is replaced by resistor bank with desired resistance set using (2). The DC link capacitor is replaced by DC link choke of value 3.9 mH for experiments for SP topology.

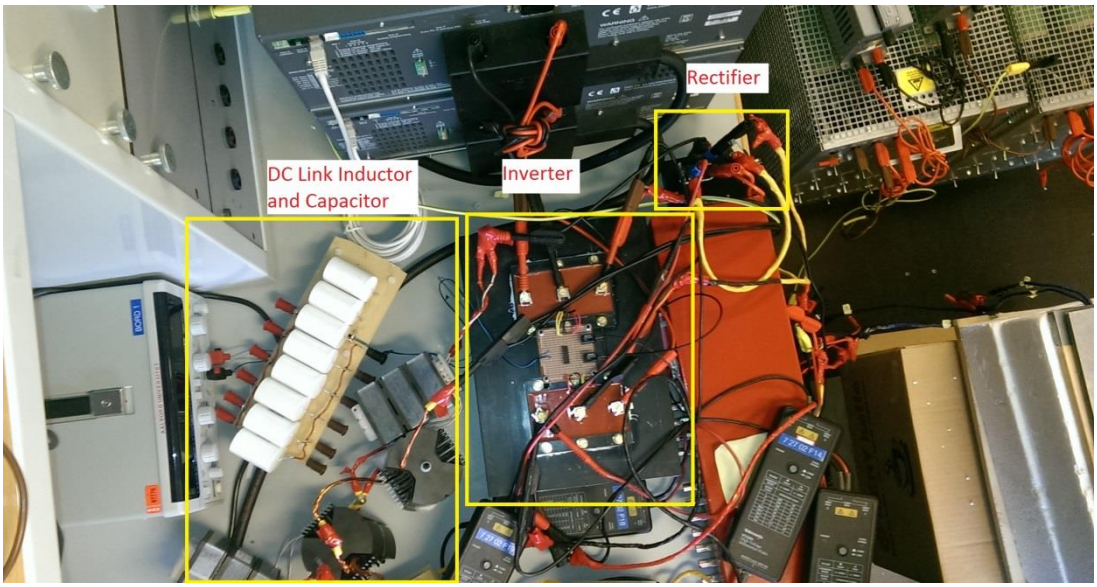

(a) Experimental setup shot 1

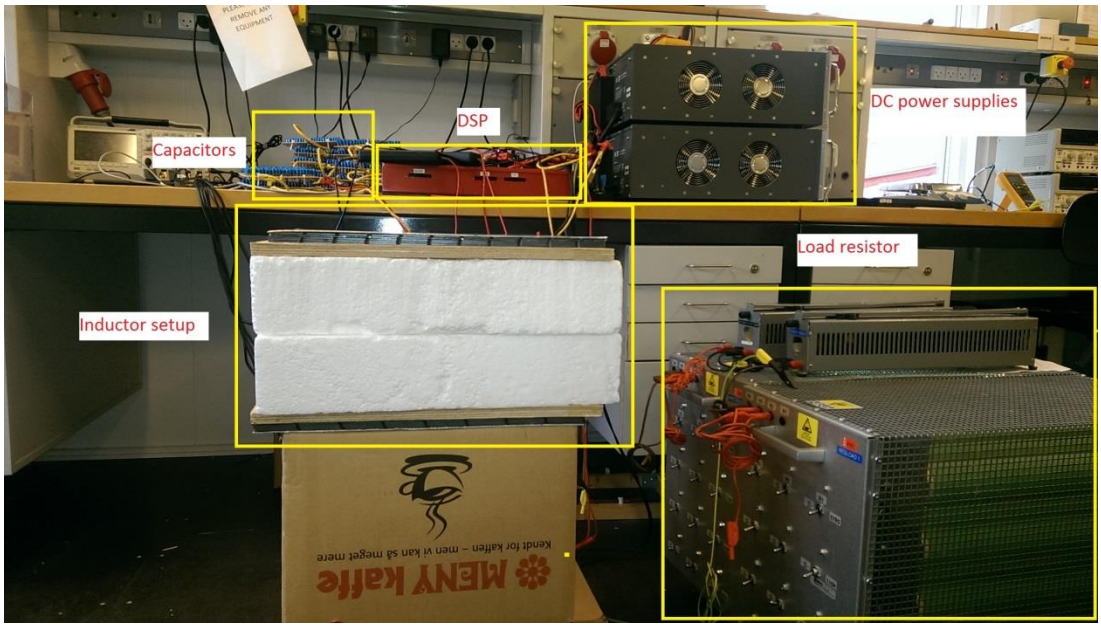

(b) Experimental setup shot 2

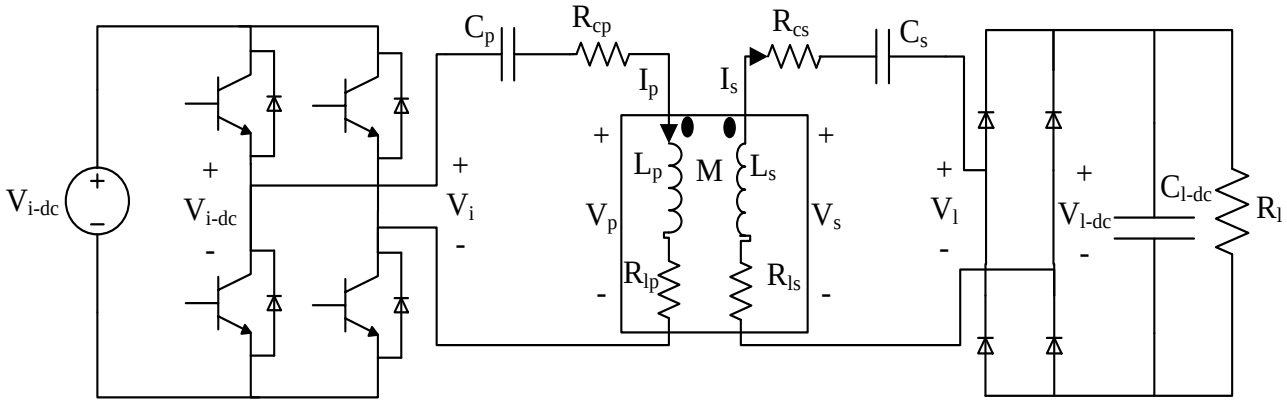

(c) SS topology electrical schematic

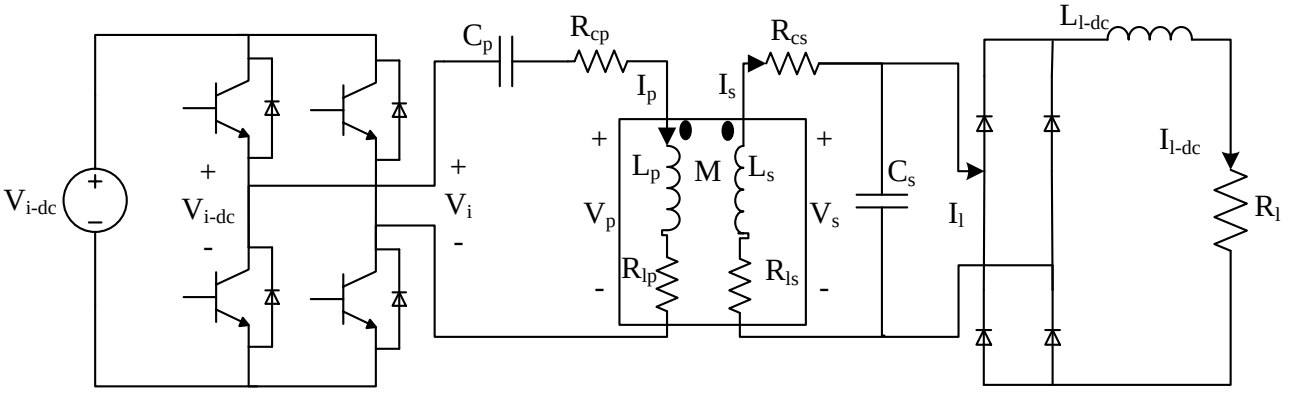

(d) SP topology electrical schematic

Figure 14 – Experimental setup

4.2. Inductor setup

The inductor setup designed and constructed during PhD project is provided in Figure 15. The first two parts of Figure 15 are photographs of the inductor components followed by three geometric views. The setup can be rearranged into four different inductor configurations with varying vertical distance (V), horizontal displacement (T) and presence of nearby vehicle (extra aluminum plate). Details of the five configurations are provided in Figure 15 (c) to (e) and Table 5.

Table 5. Inductor configurations

Configuration	V (cm)	T (cm) [Dotted Red Line]	Extra Aluminum Plate Presence [Light Green]
1	10	0	No
2	20	0	No
3	10	10	No
4	10	0	Yes

(a) Primary coil

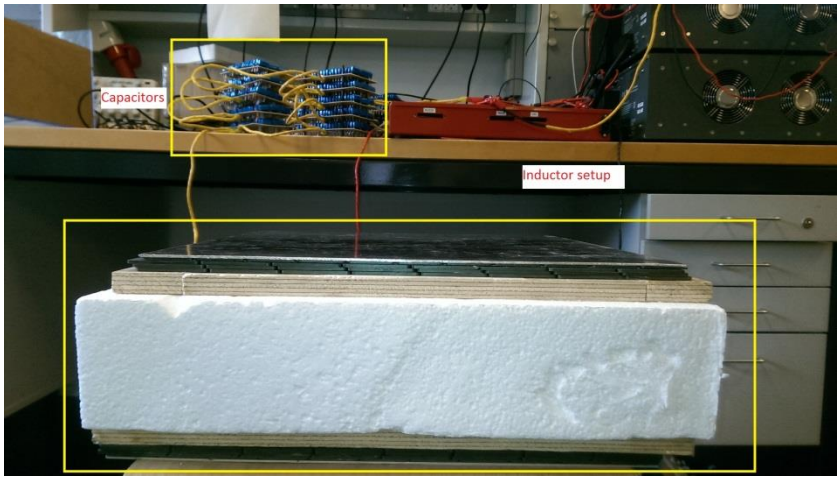

(b) Inductor setup

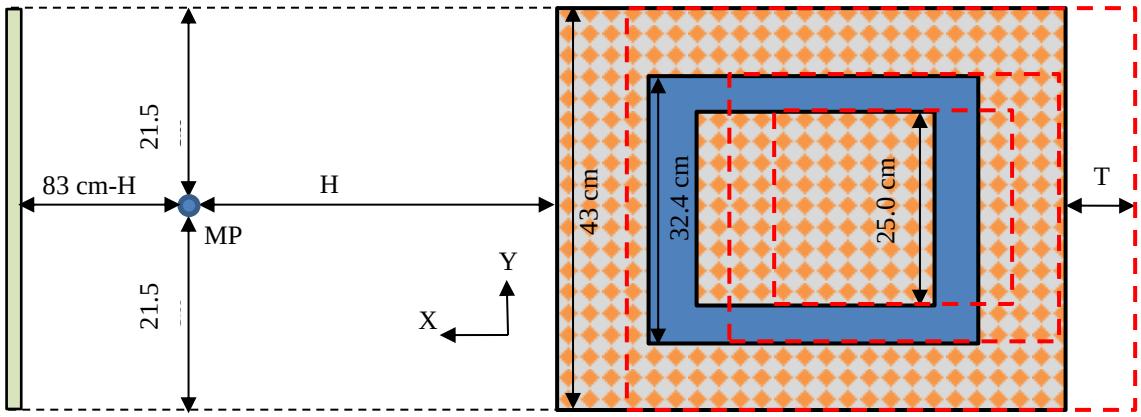

(c) View 1

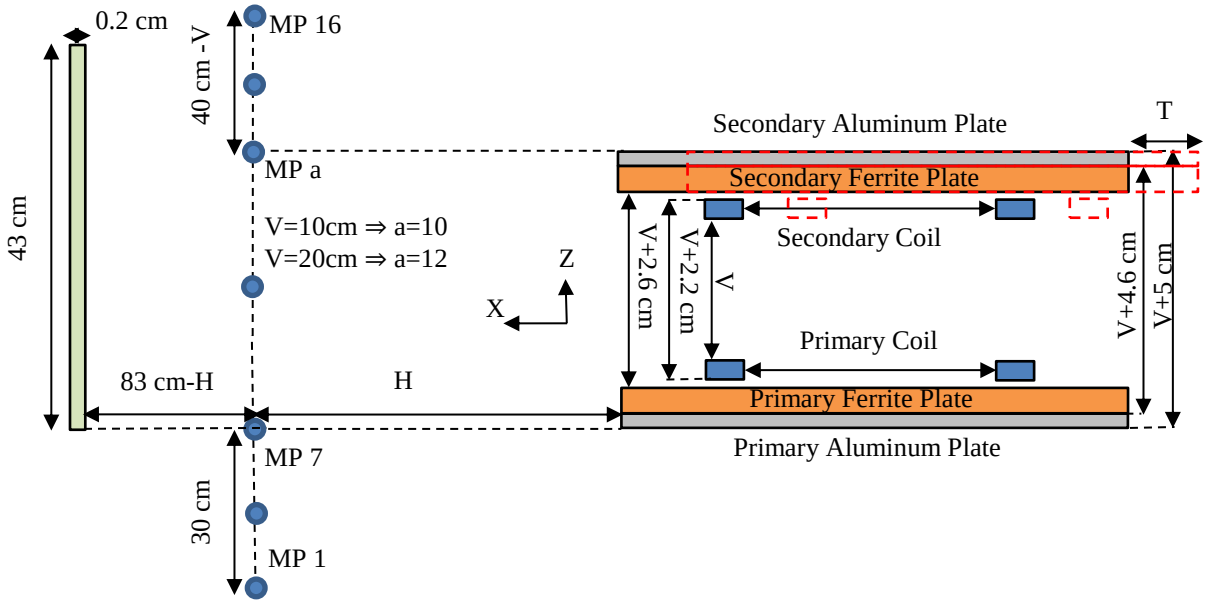

(d) View 2

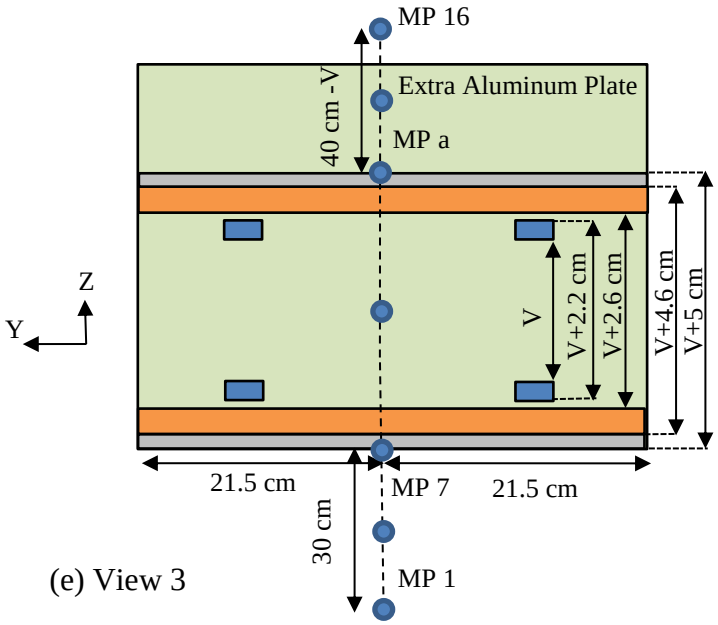

(e) View 3

Figure 15 – Inductor setup

Specification of the materials used is provided in Table 6. Ferrite is available in form of square of size 53 mm × 53 mm. These small plates are joined together to form big ferrite plates shown in Figure 15 (b).

Table 6. Material properties

Material	Property	Value
Litz wire	Number of turns	16
Litz wire	Number of strands in each turn	168
Litz wire	Diameter indivual strand	30 AWG
Litz wire	Maximum rated current	35-40 A
Litz wire	DC resistance	0.002 Ω/m
Ferrite	Real relative permeability	2300
Ferrite	Imaginary relative permeability	≈0*
Ferrite	Resistivity	5 Ω-m
Aluminum	Resistivity	5×10^{-8} Ω-m

* Resolution of manufacturer's graph does not allow accurate reading at 22 kHz.

The emissions measurements are done for 16 measurement points (MP) at two horizontal distances (H=0.3 and 0.5 m) from the vehicles. The emissions are measured using AC Milliguass Meter Model UHS2 [49] manufactured by Alpha Labs Inc. Error up to 7% has been quoted in the instruction guide with additional error due to placement of sensors at different positions in the machine if measurements are made closer than two meters from the source. This is true for the measurements in the paper and few readings have additional error on this account. Also in the guide it has been provided that values shown by the machine needs to be multiplied by 1.2 for readings above 20 kHz. Hence, all the experimental readings provided in the thesis are multiplied by this factor as all readings lie in this frequency range.

4.2.1. Inductor parameters

The inductor parameters i.e. self-inductance, mutual inductance and internal resistance for the four inductor configurations are provided below in Table 7.

Table 7. Inductor configurations inductances and internal resistances

Configuration	L_p (µH)	R_{lp} (mΩ)	M (µH)	L_s (µH)	R_{ls} (mΩ)
1	250	184	72	248	174
2	242	154	26	239	147
3	249	170	53	248	168

Configuration	L_p (µH)	R_{lp} (mΩ)	M (µH)	L_s (µH)	R_{ls} (mΩ)
4	250	180	72	247	178

Also, variation of the inductor parameters with frequency (1 kHz – 100 kHz) is provided for Configuration 1 in Figure 16. This figure has been provided to point out two things already mentioned in Chapter 2. First of all, value the inductances are practically independent of the frequency. Secondly, the internal resistance of the inductors is strong function of the frequency. The resistance increases with mostly on account of the proximity effect and increased losses in the shielding materials. This discussion is limited to this point as further research on the internal resistance will be conducted in future projects as also mentioned in Section 3.3.2.

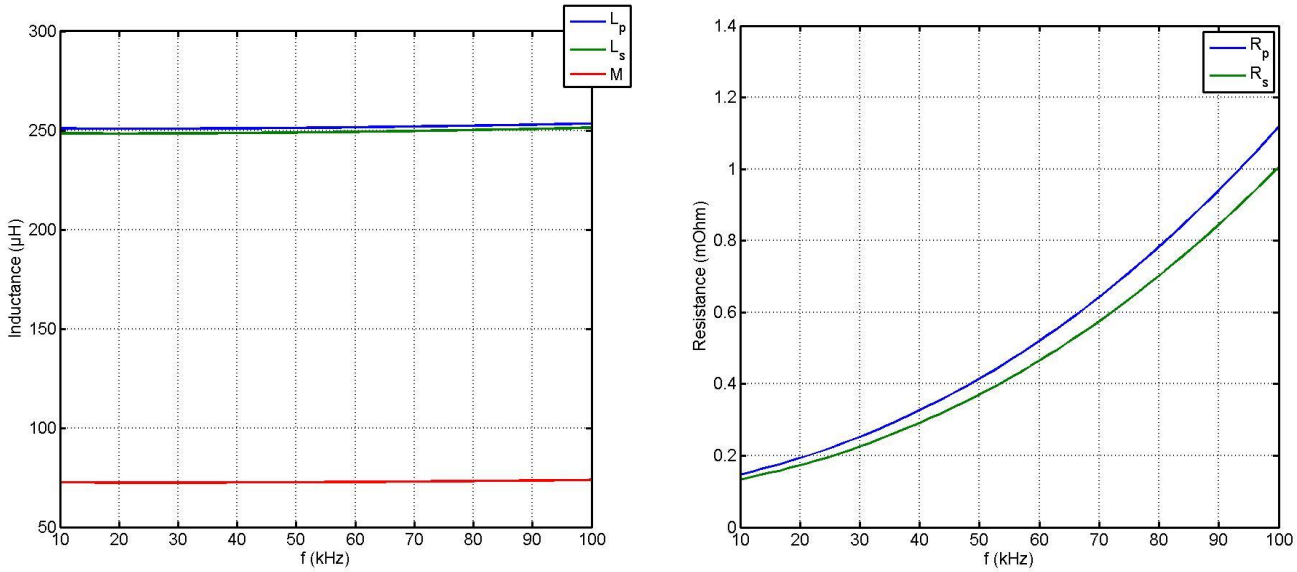

(a) Inductances (b) Internal resistances

Figure 16. Inductor parameters versus frequency

4.2.2. Inductor weight

The overall weight and weight of indivual components for one of the identical inductors (Figure 15) are as follows.

1) Overall weight=11.252 Kg
2) Ferrite=8.526 Kg
3) Aluminum=0.724 Kg
4) Coil=2.001 Kg

Ferrite is the biggest contributor in overall weight of the inductors. As a result, minimization of ferrite usage has been considered during the project and has already been presented in Section 3.3.2.

4.3. Resonance circuits

The capacitors are designed for minimum switching frequency of 22 kHz. Also, as value of the self-inductance is practically decoupled [25] from horizontal or vertical misalignment and is also provided in Table 7. This leads to the required capacitance on either side to be approximately 215 nF. There are three major objectives that need to be achieved with the capacitor design.

1) As SS topology is mainly under focus during PhD project, the capacitors should be able to withstand high voltage (18).
2) Internal resistance of the capacitors should be low to have high system efficiency.
3) As this is laboratory setup and experiments needs to be conducted with variable capacitor values {7-8}. Rearrangement should be possible to provide different net capacitance values.

Keeping the above three points in mind, three 3.3 nF capacitors having blocking voltage of 1 kV are put in series (to increase voltage limit) and then twenty such series combinations are applied in parallel (to reduce internal resistance). The combination is mounted on an isolating board providing equivalent capacitance of 22 nF. Twenty of such isolating boards are fabricated and can be connected in series or parallel to achieve desired capacitance. Most of the experiments are conducted at two switching (resonant) frequencies of approximately 22 kHz and 26 kHz. The capacitors at these frequencies are termed as capacitor combinations (CC) 1 and 2 respectively. Equivalent capacitance and internal resistance for the two capacitor combinations is provided in Table 8.

Table 8. Capacitor properties

CC	f (kHz)	C_p (nF)	R_{cp} (mΩ)	C_s (nF)	R_{cs} (mΩ)
1	22	215	32	218	29
2	26	152	36	152	29

At the end of this chapter two points needs to be mentioned regarding the measurements.

1) RLC measurements in this chapter are made with Agilent E4980A Precision LCR meter.
2) A pair of connecting wire (made of Litz wire) is connected to the inductors and capacitors and hence their values are added in the given readings.

5. Magnetic emissions

Magnetic emissions produced by wireless charging system are dependent on the coil currents and inductor design. However the emissions are minimized only by inductor (coil and passive shielding) design as discussed in Section 3.2.1. The magnetic emissions are not considered during selection of the two power electronics blocks discussed in Section 2.2. This is mainly due to reason that there are no analytical relations connecting the magnetic emissions and coil currents as are available for other design parameters voltage stress (20, 21) and output power (12, 15). In this project, semi-analytical relation between the emissions and system blocks (except inductors) is established. The relationship is explained using analytical method first followed by its verification using FEM simulations and experiments.

5.1. Analytical explanation

Analytical formulas for the magnetic emission calculations are mathematically intensive [40-42] and are not available for complicated inductor geometries. Hence, the geometry needs to be approximated to closet available standard solution and this leads to errors in the results. This is the very reason for wide usage of FEM simulations to make these calculations. Still in order to provide an analytical understanding of the emissions to the reader, the section is presented with help of non-shielded identical two coils geometry [42] with cylindrical coordinates (ρ, φ, z) as shown in Figure 17. Effect of the shielding on the emissions is added to the analytical results for the two coils geometry.

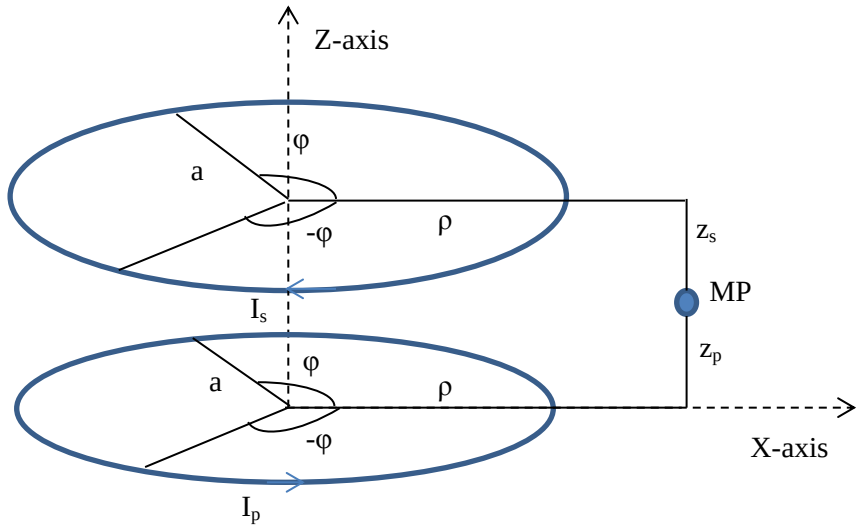

Figure 17. Two coil geometry

5.1.1. Single current coil

Analytical expression for the emission in the surroundings for a single current carrying coil (I_p) at any point and given instant of time has been presented in [42]. Two components ($B_{\rho\text{-}p}$ and $B_{z\text{-}p}$) of the primary coil field (B_p) for the same instant of time are given by (24) and (25).

$$B_{\rho\text{-}p}=\frac{\mu}{\pi}\sqrt{\frac{a}{\rho}}\frac{z_p}{k_p}\frac{K(k_p)\left((a-\rho)^2+z_p^2\right)-E(k_1)\left(a^2+\rho^2+z_p^2\right)}{\left((a-\rho)^2+z_p^2\right)\left((a+\rho)^2+z_{p)}^2\right)}I_p = K_{\rho\text{-}p}I_p \tag{24}$$

$$B_{z\text{-}p}=\frac{\mu}{\pi}\frac{\sqrt{a\rho}}{k_p}\frac{K(k_p)\left((a-\rho)^2+z_p^2\right)+E(k_p)\left(a^2-\rho^2-z_p^2\right)}{\left((a-\rho)^2+z_p^2\right)\left((a+\rho)^2+z_p^2\right)}I_p = K_{z\text{-}p}I_p \tag{25}$$

$$k_p^2=\frac{4a\rho}{\left((a+\rho)^2+z_p^2\right)}. \tag{26}$$

In (24) and (25), $K(k_p)$ and $E(k_p)$ are complete elliptic integral of the first and second kind respectively and k_p is given by (26). The two components are product of the current and their space variable ($K_{\rho\text{-}p}$, $_{z\text{-}p}$) as provided in (24) and (25). Also, the two emission components are orthogonal to each other and hence magnitude of the primary emission (B_p) is given by (27)

$$|B_p|=\sqrt{\left(B_{\varphi\text{-}p}\right)^2+\left(B_{z\text{-}p}\right)^2} \tag{27}$$

Using (24), (25) and (27), it can be concluded that the primary emission (B_p) can also be expressed in a similar way as multiplication (28) of the primary space constant (K_p) and coil current. The mathematics is not provided as analytical calculation of the space constant is not the purpose of the semi-analytical method.

$$B_p=K_pI_p \tag{28}$$

The space constants using (24) to (27) depend on the coil geometry, permeability of air and location of measurement point in space. For wireless charging inductors having shielding, it is dependent on additional factors like size, placement, permeability etc. of the shielding materials. The permeability out of these factors is connected to both inductor design and current and is discussed in more detail with following two points.

1) The coil system of Figure 17 has no shielding material and imaginary relative permeability of air is zero. Hence the space variable does not induce any phase delay between the emission and current. This is also true for shielding wireless power inductors as majority of flux path still passes through air and remaining path in ferrite whose real permeability is much higher than imaginary permeability (Table 6) [25].

2) The ferrite core is not saturated [25] for medium power applications like charging of electric vehicles due to majority of flux path in air.

Hence the linearity of emissions to the applied current is also valid for shielded wireless power inductor geometries. Another point to be noted is that the coil current unlike the space constant impact the emission at all points in the surroundings linearly with equal effect.

5.1.2. Two current coils

For system with both coils carrying current, secondary coil emission (B_s) at the same instant of time can be written in an analogues way by replacing subscript p with subscript s in (24) to (27) and is given by (29).

$$B_s=K_sI_s \tag{29}$$

As a result, space resultant emission (B_t) at the given instant of time is subtraction of the two fields as per Lenz's law and is provided in (30).

$$B_t=B_p-B_s \tag{30}$$

Also using definition of the space constants from (28) and (29), (30) is modified to (31).

$$B_t=K_pI_p-K_sI_s \tag{31}$$

The coil currents are first sinusoidal harmonic of the switching frequency and hence phasor resultant is required to calculate resultant emission (B_r). Phase angle of the primary and secondary current are taken as 0 and α respectively. The primary and secondary currents as a result at real (t=0) instant of time are I_p and I_s cosα. On the other hand, the coil currents for the imaginary time instant which is quarter cycle away are 0 and I_s sinα respectively. The space resultant at real (B_{re}) and imaginary (B_{imag}) instant of time using (31) are provided in (32) and (33).

$$B_{re}=K_pI_p-K_sI_s\cos\alpha \tag{32}$$

$$B_{imag}=-K_sI_s\sin\alpha \tag{33}$$

The phasor resultant of the emission is equal to square root sum of the two phasor components and is provided in (34). It is simplified to (35) using (32) and (33).

$$|B_r|=\sqrt{(B_{re})^2+\left(B_{imag}\right)^2} \tag{34}$$

$$|B_r|=\sqrt{\left(K_pI_p-K_sI_s\cos\alpha\right)^2+(K_sI_s\sin\alpha)^2} \tag{35}$$

Unlike linear function of single current coil emission (28), the resultant emission is non-linear function of the space constants and coil currents. Hence analytical dependence of the coil currents on the resultant emission cannot be determined analytically for given inductor design as the space constants do not have unique values in the surroundings. This problem can be solved by modifying

(35) to (36) using mathematical rearrangement and the solution is provided in Section 5.1.4 after brief discussion on space ratio (K_s/K_p) in Section 5.1.3.

$$|B_r| = K_p \sqrt{\left(I_p - \frac{K_s}{K_p} I_s \cos\alpha\right)^2 + \left(\frac{K_s}{K_p} I_s \sin\alpha\right)^2} \tag{36}$$

5.1.3. Space ratio

Constant behavior of the space ratio for shielded and non-shielded (only two coils) in region between the coils was explained with help of FEM simulations in {3-4}. It was also shown that the ratio behaves more constant for shielded geometries compared to non-shielded geometries. This can be explained analytically for the two coil geometry of Figure 17 as follows. Both radius (a) and vertical gap (z_1+ z_2) between wireless power inductors for vehicles applications are in range of around 20 cm [25, 27] and the emissions are measured in region with $\rho \geq 50$ cm (Section 3.2.1). This leads to

$$\rho > a \tag{37}$$

$$\rho > z_p \tag{38}$$

$$\rho > z_s. \tag{39}$$

The three inequalities become bigger with increase in value of ρ and terms $((a-\rho)^2 + z_1^2)$, $(a^2 + \rho^2 + z_1^2)$, $((a+\rho)^2 + z_1^2)$ and $-(a^2 - \rho^2 - z_1^2)$ for the primary emission components in (24) and (25) are dominated by ρ. Similarly, the corresponding terms for the second coil are dominated again by same distance ρ. As a result, the two coils having same current produce near similar emissions in region of highest emissions. This stands for constant value of the space ratio in the emissions measurement region. It can be explained in simpler words as that average distance of measurement point from the two coils becomes more comparable with increasing ρ. At center of the two coils (z_1=z_2) and for same magnitude of current, fields components for the two coils will be exactly equal and the space ratio is exactly one. Change in value of the space ratio lies in small bandwidth around central value (at center of coils). The central value is one for geometry of Figure 17 and selecting this central value for all points does not make a significant difference in calculation of the resultant emission. The space ratio is constant but not necessarily one and is shown for Configuration 3 later in Section 5.2.2. With different inductors, average distance of measurement point from closer say secondary inductor become bit lesser compared to the primary inductor and hence the space ratio value shows little drop. The space ratio is measured using no-load tests on FEM simulations and has been explained in {3-10}. For the primary no-load test, the secondary coil is open-circuited and vice versa for the secondary no-load test. The two no-load emissions readings are used to calculate space ratio using (40).

$$\frac{K_s}{K_p}=\frac{B_s}{B_p}\frac{I_s}{I_p} \tag{40}$$

5.1.4. Emissions ratio

Taking the space ratio to be constant using discussion in Section 5.1.3, the resultant emissions expression of (36) can be in similar terms to the single current coil emission (26) can be expressed as multiplication of two parts: space constant or inductor design part (K_p) and current dependent part $\left(\sqrt{\left(I_p-\frac{K_s}{K_p}I_s\cos\alpha\right)^2+\left(\frac{K_s}{K_p}I_s\sin\alpha\right)^2}\right)$. The first part depends on the inductor design as provided in Section 5.1.1 and FEM simulations are required to understand effect of factors like coil design, shielding materials etc. on the resultant emission. On the other hand, the second part impacts value of the emission at all points equally. Hence for a given inductor design, ratio of the emissions of wireless charging system at two different operation conditions (denoted by added subscript 1 and 2) can be calculated analytically.

$$\text{Emissions ratio}=\frac{|B_{r2}|}{|B_{r1}|}\frac{\sqrt{\left(I_{p2}-\frac{K_s}{K_p}I_{s2}\cos\alpha_2\right)^2+\left(\frac{K_s}{K_p}I_{s2}\sin\alpha_2\right)^2}}{\sqrt{\left(I_{p1}-\frac{K_s}{K_p}I_{s1}\cos\alpha_1\right)^2+\left(\frac{K_s}{K_p}I_{s1}\sin\alpha_1\right)^2}} \tag{41}$$

The space ratio multiplied by the secondary current in (41) provides effective secondary current which is present with respect to the primary current in the surroundings. The space ratio is one for geometries with similar inductors as in Figure 17 and hence the secondary current is equal to the equivalent secondary current. On the other hand, as an example for a smaller secondary inductor or the secondary inductor is shifted away from the measurement point, the space ratio and secondary effective current will reduce for the same measurement point. The space ratio is calculated using FEM simulations once and hence this method is referred as semi-analytical method. Using this method, a comparative analysis can be made analytically for different value of the system blocks (except inductors). The space ratio and proposed method is verified in the rest of the chapter using FEM simulations and experimental setup for three applications. FEM simulations validation along with detailed theory for the three applications is presented with help of published papers {3-10} for disc type inductor geometry. The experimental verification on the other hand is done using inductor and experimental setup provided in Chapter 4.

5.2. Space ratio results

First step in establishing analytical relation between the emissions and other system components is to study the emissions profile in the surroundings. This was studied in paper {3} for only two

geometries: ferrite and non-ferrite (only coils) provided in Figure 7 and 8. It was later extended to all the four geometries of Figure 7 and 8 in next paper {4}. The results from both set of papers indicate that the emissions in measurement region have nearly equal contribution from the two coils carrying similar current. The two papers with detailed theory and FEM validation are provided next in Section 5.2.1 and 5.2.2 followed by experimental verification in Section 5.2.3.

5.2.1. PhD paper 3

This paper was originally published with following details.

{3} T. Batra, E. Schaltz, “Magnetic Field Emissions for Ferrite and Non-Ferrite Geometries for Wireless Power Transfer to Vehicles”, Journal of Applied Physics, Vol. 115, no 17, pp 17E715 - 17E715-3, 2014.
http://dx.doi.org/10.1063/1.4868498

AIP Journal of Applied Physics

Magnetic field emissions for ferrite and non-ferrite geometries for wireless power transfer to vehicles

T. Batra and E. Schaltz

Citation: Journal of Applied Physics **115**, 17E715 (2014); doi: 10.1063/1.4868498
View online: http://dx.doi.org/10.1063/1.4868498
View Table of Contents: http://scitation.aip.org/content/aip/journal/jap/115/17?ver=pdfcov
Published by the AIP Publishing

Magnetic field emissions for ferrite and non-ferrite geometries for wireless power transfer to vehicles

T. Batra[a)] and E. Schaltz
Department of Energy Technology, Aalborg University, Aalborg 9220, Denmark

(Presented 7 November 2013; received 19 September 2013; accepted 17 December 2013; published online 26 March 2014)

Minimizing magnetic field emissions to surroundings are one of the most challenging design criteria for wireless power transfer to vehicles. In this paper, concept of division of the emissions into three zones (primary, secondary, and combined zone) in the vertical direction is introduced. For geometries without ferrite, these zones can be defined only on basis of distance from coils. The simulation results indicate that magnetic field profile in the surroundings is influenced for ferrite based geometries and the three zones tend to overlap. This overlapping is studied via Comsol simulations for vertical separation between the coils in range of 100–180 mm. It is observed that lower vertical separation results in higher overlapping of the zones and the coils behave as they are effectively placed close to center of air gap. The analysis in this work provides a better understanding of the space profile of magnetic field emissions (with and without ferrite) for wireless power transfer to vehicles. © *2014 AIP Publishing LLC*. [http://dx.doi.org/10.1063/1.4868498]

Wireless Power Transfer (WPT) is the transfer of energy through magnetic fields from primary coil to secondary coil using principle of electromagnetic induction. WPT is used to charge batteries of commercial devices like smartphones, consumer electronics, etc. It is also considered as a good solution for charging of Electric Vehicles (EV). Power rating and air gap between the coils of WPT for EV applications are much bigger than for the devices mentioned above. As a result, the analyses presented in this paper are applicable to EV only. Electric system (battery and power electronics) of EV is approximated by a resistive load[1] during the design process.

Ferrite is used in the inductor design to lower magnetic resistance for the fields and as a result more power can be transferred for the same set of coils. Ferrite also significantly influences space profile of the magnetic fields. The study of this influence for different vertical separations between the coils is the main theme of this paper. This influence is explained by comparing simulation results (Comsol) from two extreme case geometries: one without ferrite (non-ferrite geometry) and other having a full-ferrite disc[2] (ferrite geometry). There have been papers discussing reduction[3] of the magnetic fields for WPT but none of them to our knowledge has focused on the space profile of the magnetic fields for ferrite or non-ferrite geometry based WPT to vehicles.

Side and top views of the sample with non-ferrite geometry are shown in Fig. 1. Side view of ferrite geometry is identical to the non-ferrite geometry in Fig. 1(a). Disc of air in the non-ferrite geometry of Fig. 1(b) is to be replaced here by disc of ferrite to obtain top view of the ferrite geometry. The geometry shown above consists of two identical and perfectly aligned inductors separated by a gap distance (V). The magnetic field emissions are studied for closet human contact along vertical line at 0.5 m from center of the primary inductor. Litz wire similar to one in Ref. 4 is used in both the coils and each coil consists of 12 turns. The magnetic field profile is studied for Series-Series topology in this paper and fundamental mode analysis[5] equivalent circuit is provided in Fig. 2. The relation[1] between the two currents at resonance condition ($w = 1/\sqrt{(L_pC_p)} = 1/\sqrt{(L_sC_s)}$) for the topology is $I_s = (jwM/R_s)I_p$.

Magnetic field (B_p and B_s) at any point in surrounding will depend linearly (K_p and K_s) as $|B_p| = K_p \times |I_p|$ and $|B_s| = K_s \times |I_s|$. Hence, the net magnetic field at any point can be written as $|B| = \sqrt{(I_pK_p)^2 + (I_sK_s)^2}$.

The magnetic field emissions can therefore be divided in the space in three zones named as primary, secondary, and combined zone on basis of K_p and K_s taking the primary current equal to the secondary current. This zone division is defined only with respect to space and not time. K_p and K_s for a point depend only on distance of that point from the coils. In the primary zone, the distance of any point (point A in Fig. 1(a)) is less for the primary coil as compared to the secondary coil which stands for ratio K_s/K_p less than one. The primary coil dominates the resultant magnetic field in this zone. A similar argument is applicable for the secondary zone with point B as an example in Fig. 1(a). A very strict definition of the combined zone can be given by value of K_s/K_p equal to one and will be a point lying on center (C) in Fig. 1(a). However, for practical studies, the combined zone can be taken up to some distance on both the sides from center (C) because in this region the net magnetic field has a respectable contribution from both the coils.

Maximum field strength reached for WPT systems is much lower than saturation limit of ferrite so treating magnetic behavior as linear for ferrite geometries is a fair assumption as also reported in other papers.[3] Hence, the magnetic fields for the two coils are proportional to their respective currents for the ferrite geometry also. The magnetic flux of the primary and secondary coils is attracted by the ferrite at the other end. As a result, the maximum of the magnetic field for

[a)]Electronic mail: tba@et.aau.dk.

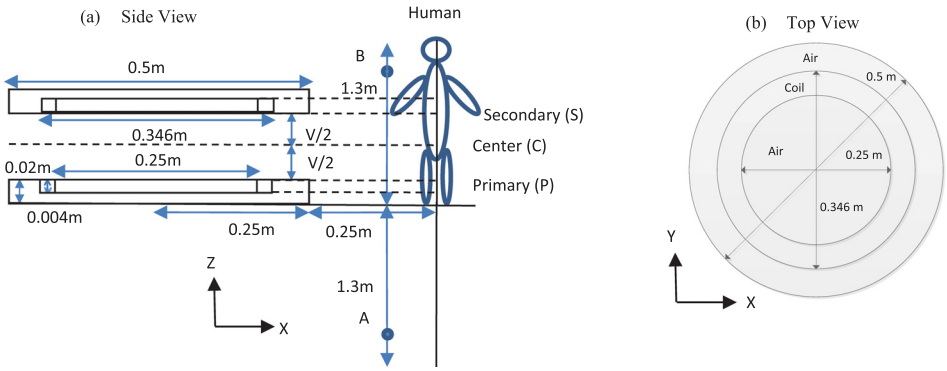

FIG. 1. Sample with non-ferrite geometry.

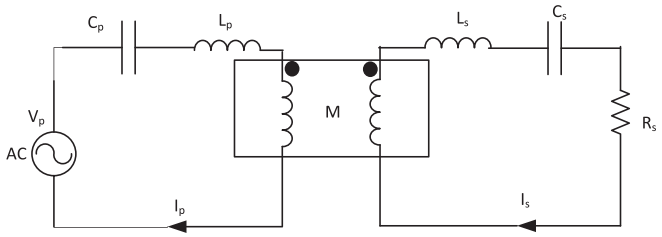

FIG. 2. FMA equivalent Series-Series topology.

the ferrite geometry coils on the vertical line of Fig. 1(a) shifts close to center (C), i.e., between P and C for the primary current and between C and S for the secondary current. The notation maximum is used here to describe maxima of magnetic field in space. For maxima in time domain (phasor) later in the result section, terminology of peak has been used to avoid confusion. The three zones tend to overlap depending on vertical separation between the two inductors. A smaller gap distance (V) stands for a bigger overlap between the zones and vice versa. For the geometry without ferrite on the other hand, this maximum on the same vertical line occurs at P for the primary current and at S for the secondary current. These points are at shortest distance to their corresponding coils. Hence, if equivalent non-ferrite geometry is made for the ferrite geometry with respect to the magnetic emissions, coils of that equivalent geometry would be closer to each other than the ferrite geometry coils.

The three zones have been defined in terms of ratio K_s/K_p. This ratio can be obtained by no-load curves for the two coils plotted at same current (23 A max at 20 kHz). Ratio of the magnetic fields will be equal to ratio of their corresponding constants and is expressed as $|B_s|/|B_p| = K_s/K_p$.

Peak magnetic field plots for the geometries at no-load conditions for gap distance (V) in range of 100–180 mm are provided in Figs. 3(a)–5(a). Plots of ratio of the peak magnetic fields are provided in Figs. 3(b)–5(b). Position of the primary inductor is fixed and the secondary inductor is shifted upwards for varying the gap distance (V) in the figures. The discussion of results is presented below for the combined and secondary zones. Analogous statements to the ones provided for the secondary zone are applicable to the primary zone.

The distance of the two coils from center (C) is identical. Therefore, center (C) is the exact combined zone with value of K_s/K_p equal to one for ferrite and non-ferrite curves in Fig. 3(b). Peak magnetic field at center (C) in Fig. 3(a) is also identical for both the coils of either geometry, which again stands for K_s/K_p equal to one. Discussions of results that is common to (a) or (b) parts of Figs. 3–5 are discussed only for Figs. 3(a) or 3(b). Values of K_s/K_p for the ferrite and non-ferrite curves in Fig. 3(b) as per the definition of the primary and the secondary zone are less and greater than one, respectively. The peak value of magnetic field for the secondary coil is above the one for the primary coil in the secondary zone for both the geometries in Fig. 3(a), which is synonymous with the last statement. Value of K_s/K_p increases in the secondary zone and then becomes nearly constant as we move away from center (C) for both the curves in Fig. 3(b).

In Fig. 3(a), maximum of the primary coil for the ferrite geometry lies between primary (P) and center (C). This

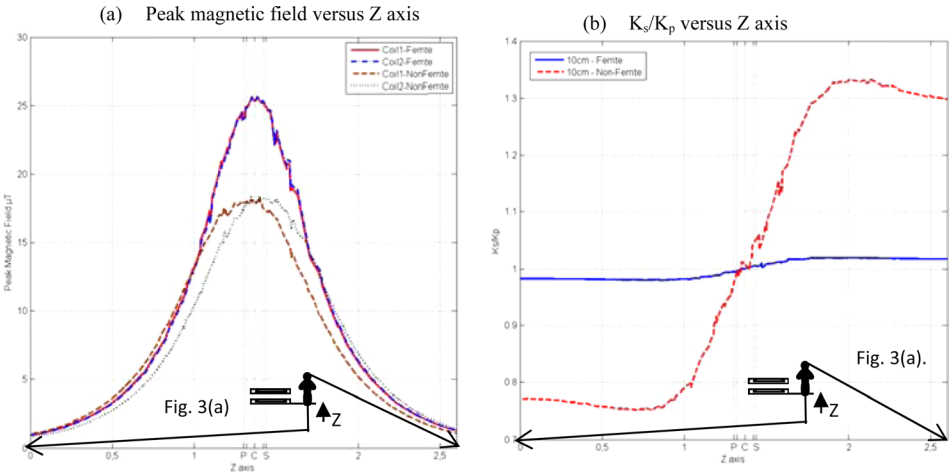

FIG. 3. Plots at V = 10 cm.

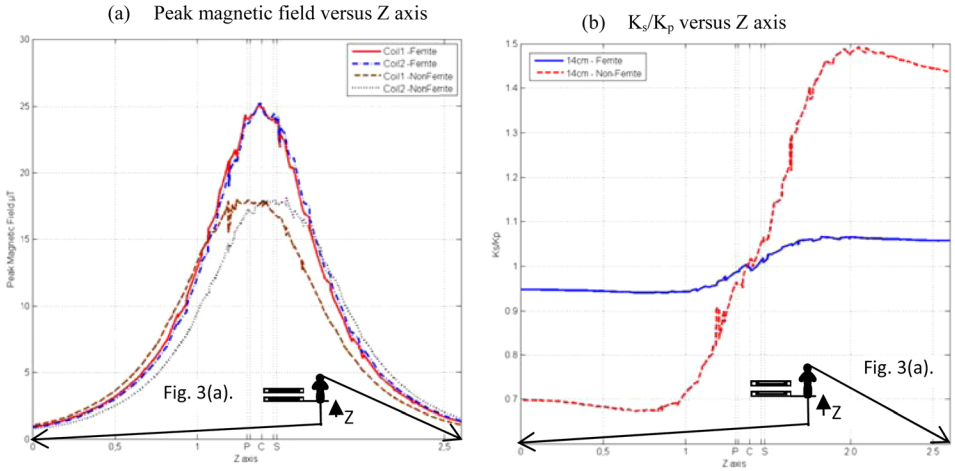

FIG. 4. Plots at V = 14 cm.

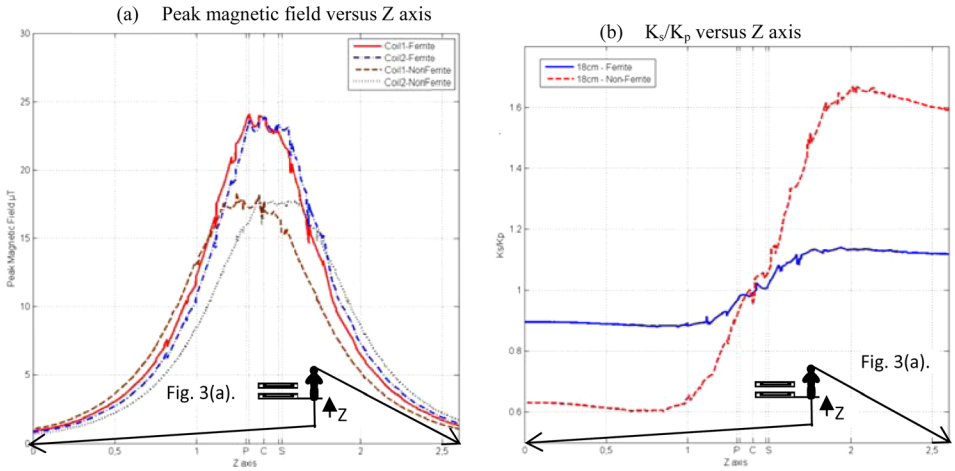

FIG. 5. Plots at V = 18 cm.

maximum is closer to center (C) as compared to maximum of the primary coil for the non-ferrite geometry which is centered at primary (P) in the same figure. This has been referred as overlapping of the primary zone into the secondary zone in this paper. This overlapping can also be seen with help of Fig. 3(b). In this figure, the ferrite curve is lower than the corresponding non-ferrite curve in the secondary zone. Also, as we move in direction of increasing gap distance (V) from Fig. 3(a) to Fig. 5(a), maximum of ferrite curves are shifting away from center (C) and the overlapping is reducing. Ferrite curves of Figs. 3(b)–5(b) when compared for any fixed point in the secondary zone again show that the overlapping reduces as value of K_s/K_p increases with the increasing gap distance (V). The non-ferrite curves show a similar behavior for the same set of figures. But changes in values of K_s/K_p are different from Fig. 3(b) to Fig. 5(b) for the two geometries due to presence of ferrite in the second geometry.

Concept of division of magnetic field emissions for Series-Series topology wireless power transfer into three zones with respect to space has been introduced in this paper. Criterion for the three zones for non-ferrite based geometries is based solely on distance, whereas for ferrite based geometries the zones overlap due to magnetic attraction of ferrite from the other end. As a result the coils appear to be closer to each other from magnetic emissions point of view. Summarizing, this work is focused on space profile of magnetic fields with and without ferrite for Series-Series topology wireless power transfer. This can be used in future works to study change in resultant magnetic field due to addition of ferrite in the system. Also, it can be used as a base for studying magnetic field profiles for the other three topologies of wireless power transfer to vehicles.

[1]W. Chwei-Sen *et al.*, IEEE Trans. Ind. Electron. **52**(5), 1308 (2005).
[2]H. Sakamoto *et al.*, IEEE Trans. Ind. Appl. **35**(5), 3526 (1999).
[3]M. Budhia *et al.*, IEEE Trans. Power Electron. **26**(11), 3096 (2011).
[4]M. Budhia *et al.*, IEEE Trans. Ind. Electron. **60**(1), 318 (2013).
[5]M. G. Egan *et al.*, IEEE Trans. Ind. Electron. **35**(4), 884 (1999).

5.2.2. PhD paper 4

This paper was originally published with following details.

{4} T. Batra, E. Schaltz, “Passive shielding effect on space profile of magnetic field emissions for wireless power transfer to vehicles”, Journal of Applied Physics, Vol. 117, pp 17A739 - 17A739-4, 2015.
http://dx.doi.org/10.1063/1.4916930

Passive shielding effect on space profile of magnetic field emissions for wireless power transfer to vehicles

T. Batra and E. Schaltz

Citation: Journal of Applied Physics **117**, 17A739 (2015); doi: 10.1063/1.4916930
View online: http://dx.doi.org/10.1063/1.4916930
View Table of Contents: http://scitation.aip.org/content/aip/journal/jap/117/17?ver=pdfcov
Published by the AIP Publishing

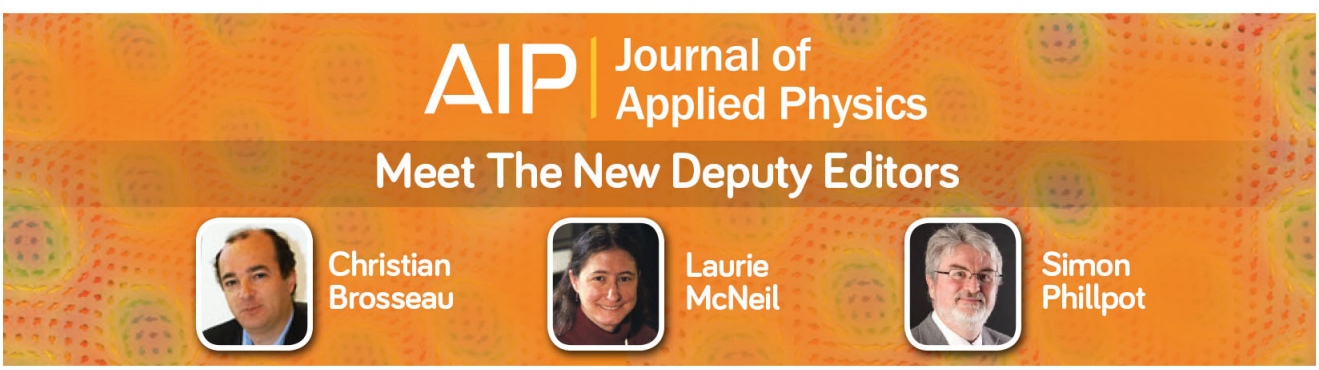

Passive shielding effect on space profile of magnetic field emissions for wireless power transfer to vehicles

T. Batra[a] and E. Schaltz
Department of Energy Technology, Aalborg University, Aalborg 9220, Denmark

(Presented 7 November 2014; received 22 September 2014; accepted 23 November 2014; published online 6 April 2015)

Magnetic fields emitted by wireless power transfer systems are of high importance with respect to human safety and health. Aluminum and ferrite are used in the system to reduce the fields and are termed as passive shielding. In this paper, the influence of these materials on the space profile has been investigated with the help of simulations on Comsol for the four possible geometries—no shielding, ferrite, aluminum, and full shielding. As the reflected impedance varies for the four geometries, the primary current is varied accordingly to maintain constant power transfer to the secondary side. Surrounding magnetic field plots in the vertical direction show that maxima's of the two coils for the no shielding geometry are centered at the respective coils and for the remaining three are displaced closer to each other. This closeness would lead to more effective addition of the two coil fields and an increase in the resultant field from space point of view. This closeness varies with distance in the horizontal direction and vertical gap between the coils and is explained in the paper. This paper provides a better understanding of effect of the passive shielding materials on the space nature of magnetic fields for wireless power transfer for vehicle applications. © *2015 AIP Publishing LLC*. [http://dx.doi.org/10.1063/1.4916930]

I. INTRODUCTION

Wireless power transfer (WPT) is contactless transfer of energy from the primary coil to the secondary coil by means of magnetic field. This technology has been used in biomedical industry for a considerable period of time. Researchers are interested in this technology for stationary[1] and on line[2] battery charging of electric vehicles (EVs) due to its safety and comfort features. The magnetic field emissions to the surroundings are an unwanted byproduct of this system. In order to minimize these emissions, active and passive shielding methods[3] are used. For passive shielding, ferrite and aluminum are added to the inductors to reduce the magnetic fields to the surroundings. In a previous publication[4] by the same authors, it was shown that ferrite has an effect of displacing magnetic field maxima's of the two coils closer to each other in the surroundings (vertical direction) of WPT. This closeness leads to a higher resultant field from space point of view as compared to the non-ferrite (or non-shielded) geometry for which the maxima's are placed at the respective coils. In this paper, it is shown that geometries with aluminum and combination of both materials termed as aluminum and full geometries also show this effect. Also, the combination shows this effect more than when one of the materials is used. Results are presented for different vertical (V) and horizontal (H) distances from the coils for the four geometries. As distance is increased and decreased in the horizontal and vertical directions, respectively, contribution of the two coils in the resultant magnetic field becomes more comparable for all the geometries. Additionally in Ref. 4, constant current was used for both the geometries and hence the ferrite geometry with higher coupling factor had higher secondary power (P) and magnetic emissions compared to the non-ferrite geometry. Comparison for the four geometries in this paper is done at constant secondary power so that the closeness effect and reduction of fields by the shielding materials and their combination can be studied together. Increasing the power rating and keeping the magnetic emissions under prescribed limits is one of the most significant challenges for the future success of this technology. This paper provides insight in the behavior of the magnetic fields in the surroundings by addition of passive shielding materials. The results can be used for better design of wireless power

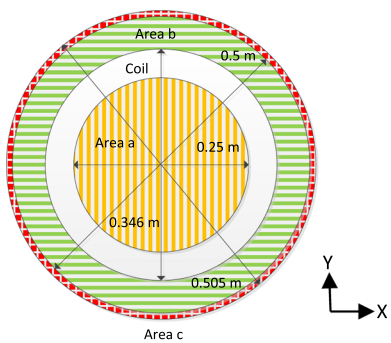

Geometry	Area A	Area B	Area C
No-shielding	Air	Air	Air
Aluminum	Air	Air	Aluminum
Ferrite	Ferrite	Ferrite	Air
Full	Ferrite	Ferrite	Aluminum

FIG. 1. Sample geometry top view.

[a]Author to whom correspondence should be addressed. Electronic mail: tba@et.aau.dk.

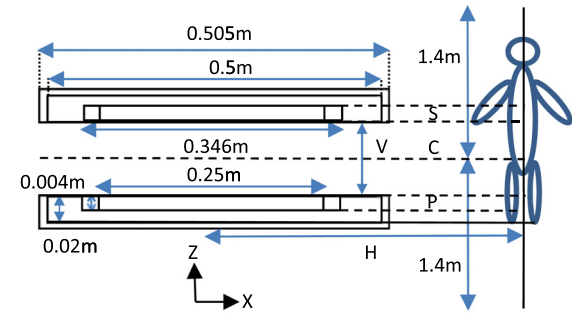

FIG. 2. Sample geometry side view.

transfer systems with respect to material use and magnetic emission reduction.

II. THEORY

First of all, side and top views of the identical inductors for the four geometries are presented in Figs. 1 and 2, respectively. Coils similar to the ones in Ref. 5 are used and relative permeability of ferrite is 2300. The primary coil (P), secondary coil (S), and center line (C) are marked in Fig. 1. Series-series topology is used in this paper out of the four topologies[6] used in WPT applications. Fundamental mode analysis (FMA)[4] equivalent circuit of the topology is presented in Fig. 3. The primary and secondary currents at resonant frequency $\left(w_r = \frac{1}{\sqrt{L_p C_p}} = \frac{1}{\sqrt{L_s C_s}}\right)$ are orthogonal to each other as[7] $I_s = \frac{jw_r M}{R_s} I_p$. For a fair comparison of the four geometries for the space nature of the fields, the secondary power $\left(P = Ip^2 \frac{w_r M^2}{L_s} Q\right)$ has been kept constant. Q is secondary quality factor and is given by $Q = \frac{w_r L_s}{R_s}$. The primary current is increased to maintain same secondary power as the reflected resistance $\left(R_r = \frac{w_r M^2}{L_s} Q\right)$ is different for the four geometries.

Due to the large air gap between the coils of WPT, maximum magnetic field reached in ferrite core is much lower[1,7] than the saturation level for ferrite. Hence, magnetic fields (B_p and B_s) emitted by the two coils at any point in the surroundings are linearly proportional to the current and are given by $|B_{p,s}| = K_{p,s}|I_{p,s}|$. K_p and K_s are space constants for the two coils for a given point in the surroundings. The resultant magnetic field with the primary and secondary currents having phase angle 0° (reference phasor) and 90° (currents relation above), respectively, can be written[4,7] as $|B| = \sqrt{(|I_p|K_p)^2 + (|I_s|K_s)^2}$. The resultant expression contains terms for both the coil currents and space constants. To investigate effect of the space constants only on the resultant magnetic field, the currents are taken as equal and the resultant field expression is modified to $|B| = |I_p| \sqrt{K_p{}^2 + K_s{}^2}$. Contribution of the two coils in the resultant field can be studied with the help of ratio K_s/K_p. Value of this ratio greater than one stands for a greater contribution from the secondary coil in the resultant magnetic field and has been referred as secondary zone[4] ($K_s/K_p > 1$). Similarly, primary zone[4] and combined zone[4] are defined as $K_s/K_p < 1$ and $K_s/K_p = 1$. The ratio can be obtained with the help of no-load tests[4,7] with the primary coil energized and secondary coil open-circuited and vice versa. The no-load test of each coil is done at same input current ($I = I_p = I_s$) and dividing the magnetic field of the two tests yields the ratio $\left(\frac{K_s}{K_p} = \frac{|B_s|}{|B_p|}\right)$. Variation of K_s/K_p for the four geometries is presented in Sec. III.

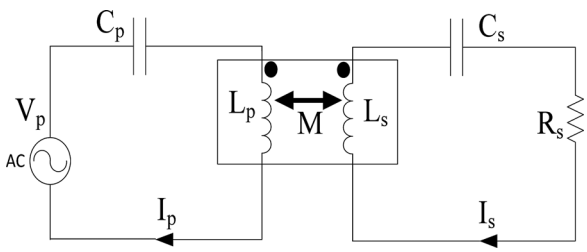

FIG. 3. FMA equivalent series-series topology.

III. SIMULATION RESULTS

Values for the reflected resistance are obtained by simulations on Comsol for different values of the horizontal and vertical distances for the four geometries. The primary inductor is at same physical position and the secondary inductor is moved to change the vertical distance in the simulations. The input current is then calculated $\left(P = Ip^2 \frac{w_r M^2}{L_s} Q\right)$ by keeping value of the secondary power constant. The secondary side power and quality factor are taken as 1 kW and 10 for calculation of the input current. Values of the input current and reflected resistance are provided in Table I. The input current from the table is used for exciting the coils for the no-load simulation tests. Rms magnetic fields and ratio K_s/K_p from the no-load tests are presented in Figs. 4 to 7. The frequency of operation is 20 kHz. Points to the left and right of center line (C) in Figs. 4 to 7 are the primary and secondary zone points, respectively. Turn ratio of 12:12 is used for all the geometries in the paper. The number of turns of the primary and secondary coils is proportional to K_p and K_s, respectively. Therefore for a turn ratio of 12:24, K_s/K_p value at C will be shifted to two from one in (c) parts of Figs. 4 to 7. The following points are to be noted from Figs. 4 to 7. Some of the points are presented only for the secondary zone. Analogous statements are applicable for the primary zone.

TABLE I. Simulation results.

	V = 10 cm		V = 20 cm	
Geometry	R_r (Ω)	I (A)	R_r (Ω)	I (A)
No-shielding	4.86	14.34	0.72	37.35
Ferrite	28.80	5.90	3.18	17.73
Aluminum	0.14	84.5	0.01	323.25
Full	21.01	6.90	1.83	23.38

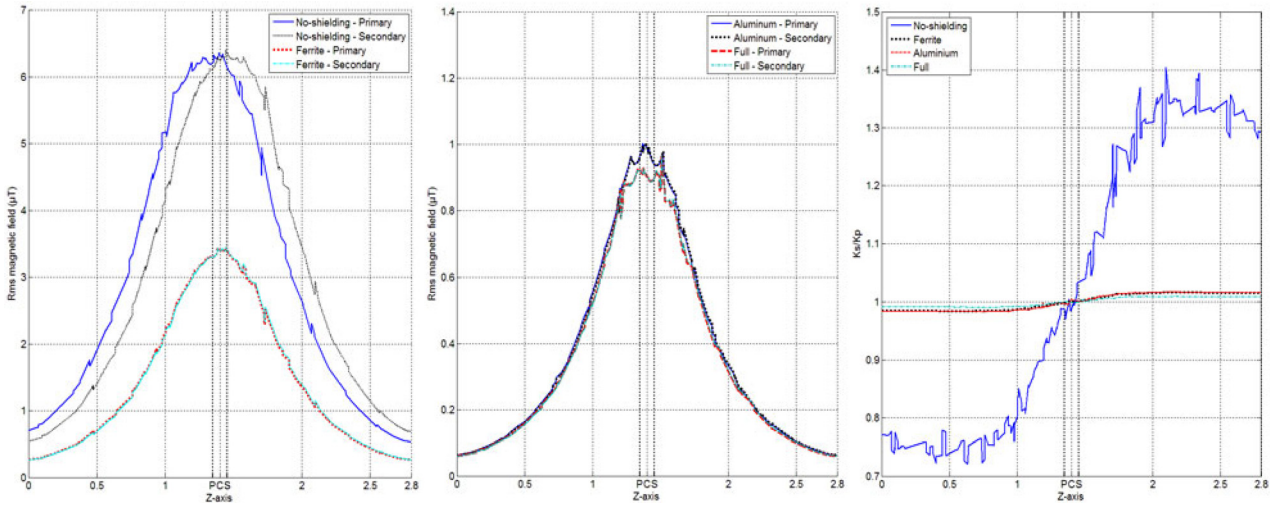

FIG. 4. (a) and (b) Rms magnetic field versus z-axis—V = 10 cm and H = 0.6 m. (c) Ratio K_s/K_p versus z-axis—V = 10 cm and H = 0.6 m.

(1) Aluminum geometry is not a practical inductor design as the reflected resistance is very low for the same coil size as provided in Table I. As a result, the primary current needs to be increased to a high value to maintain the same power transfer capability. Therefore, a layer of ferrite must be present between the aluminum and coil for a practical inductor design as also provided in Ref. 3. The full geometry is an example of such a design with combined usage of ferrite and aluminum. Results for the aluminum geometry are still provided in the paper to make a comparison with the other geometries and to understand the effect of aluminum on the space profile of the magnetic emissions.

(2) Space maxima's of the primary and secondary coils for the non-ferrite geometry are centered at point of shortest distance, i.e., at P and S, respectively, in (a) part of Figs. 4 to 7. For the remaining three geometries, the maxima's of the curves are in between P and C and P and S for the primary and secondary coils rather than at point of shortest distances in (a) and (b) parts of Figs. 4 to 7. This closeness of the curves leads to more effective addition of the primary and secondary magnetic fields as per $|B| = \sqrt{(|I_p|K_p)^2 + (|I_s|K_s)^2}$. K_s/K_p (closeness of the curves) in the secondary zone is maximum and minimum for the full and no-shielding geometries, respectively, as visible in (c) parts of Figs. 4 to 7. For the comparison between the ferrite and aluminum geometries, K_s/K_p in the secondary zone is slightly higher for the aluminum as compared to the ferrite geometry for V = 10 cm in (c) parts of Figs. 4 and 5. In (c) parts of Figs. 6 and 7, i.e., for V = 20 cm, the trend is opposite with K_s/K_p higher for the ferrite geometry. But a general consensus cannot be made that which of the two materials shows this effect more. Aluminum and ferrite are used in different forms and sizes in the inductor design of WPT and the results presented here are for a particular design only.

(3) K_s/K_p curves in the secondary zone for all the geometries show a decrease in value as H is increased and V is constant. It can be verified by comparing (c) parts of Figs. 4 and 5 or Figs. 6 and 7. For H = 0.6 m (Figs. 4(c) and 6(c)), the curves first increase in the primary zone and then become nearly constant. On the other hand, for H = 1 m (Figs. 5(c) and 7(c)) the curves just increase in the primary zone. The above statements can be explained with the help that distances of the measurement point from the two inductors become more comparable as H is increased.

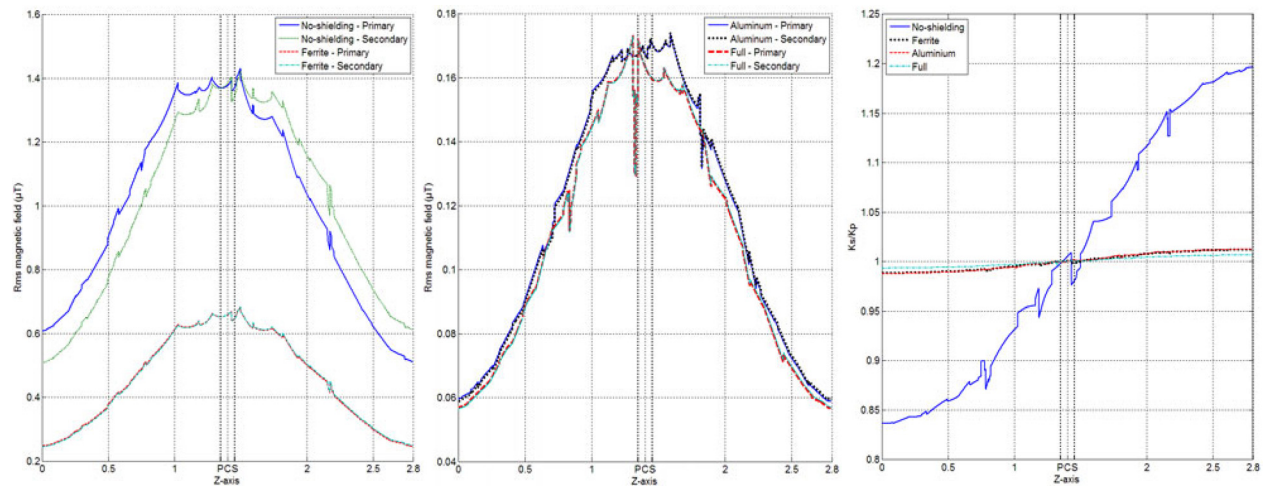

FIG. 5. (a) and (b) Rms magnetic field versus z-axis—V = 10 cm and H = 1 m. (c) Ratio K_s/K_p versus z-axis—V = 10 cm and H = 1 m.

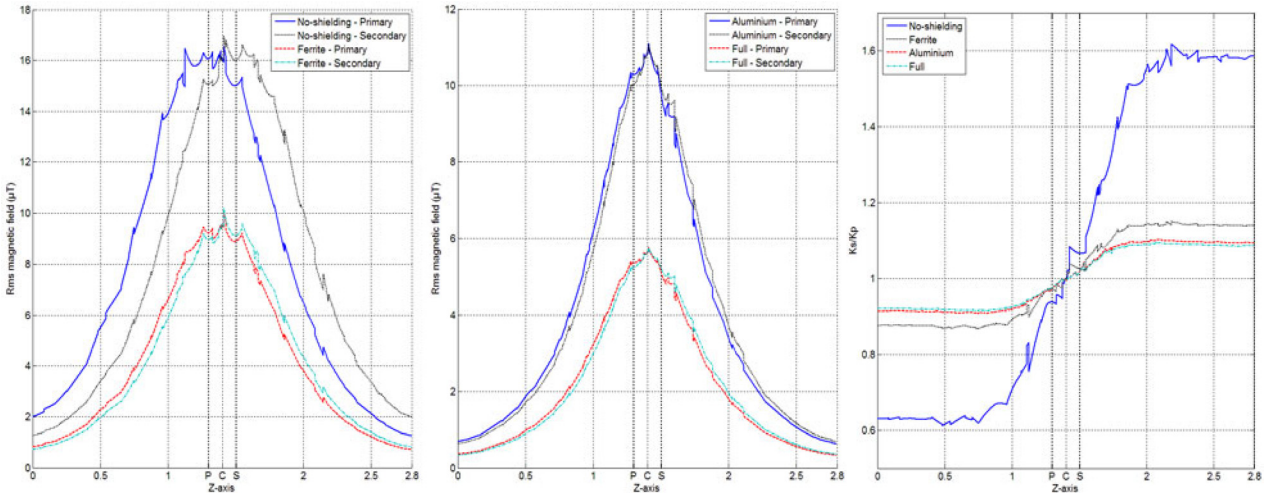

FIG. 6. (a) and (b) Rms magnetic field versus z-axis—V = 20 cm and H = 0.6 m. (c) Ratio K_s/K_p versus z-axis—V = 20 cm and H = 0.6 m.

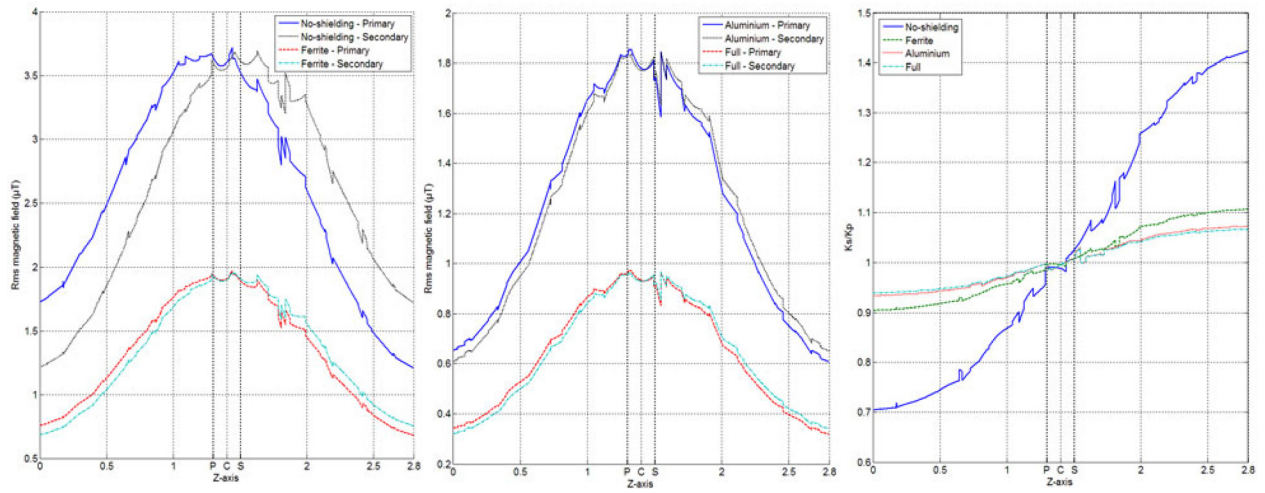

FIG. 7. (a) and (b) Rms magnetic field versus z-axis—V = 20 cm and H = 1 m. (c) Ratio K_s/K_p versus z-axis—V = 20 cm and H = 1 m.

(4) K_s/K_p is compared for varying V and constant H using set of Figs. 4(c) and 6(c) or Figs. 5(c) and 7(c). With increasing V, the curves for all geometries drift apart and the reason for this is that the magnetic attraction and repulsion by the ferrite and aluminum reduce significantly with increase in the gap distance between the inductors. Hence with increasing V, the effect reduces for both the shielding materials and their combination.

IV. CONCLUSION

This paper is focused on individual and combined effect of the two passive shielding materials aluminum and ferrite on the space profile of the magnetic emissions for wireless power transfer system for vehicle applications. Simulation results show that both the shielding materials and their combination displace the individual coil field curve closer to each other. This closeness would lead to a higher resultant field on account of more effective addition of the individual coil fields. Also, it is observed from the results that as the distance of the measurement point from the coils is increased, the two coils have a more comparable role in the resultant magnetic field for all the geometries. The role of the two coils is again more comparable with the decreasing gap distance between the two inductors for all the geometries. All the above statements are explained with the help of simulations on Comsol in this paper.

ACKNOWLEDGMENTS

This work has financially been supported by The Danish Council for Strategic Research.

[1]M. Budhia, G. A. Covic, J. T. Boys, and C. Y. Huang, IEEE Trans. Power Electron. **26**(11), 3096 (2011).
[2]S. Ahn and J. Kim, "Magnetic field design for high efficient and low EMF wireless power transfer in on-line electric vehicle," in *5th European Conference on Antennas and Propagation, Rome, Italy, 11–15 April 2011*, pp. 3979–3982.
[3]J. Kim, J. Kim, S. Kong, H. Kim, I. S. Suh, N. P. Suh, D. H. Sho, J. Kim, and S. Ahn, Proc. IEEE **101**(6), 1332 (2013).
[4]T. Batra and E. Schaltz, J. Appl. Phys. **115**(17), 17E715 (2014).
[5]M. Budhia, G. A. Covic, J. T. Boys, and C. Y. Huang, IEEE Trans. Ind. Electron. **60**(1), 318 (2013).
[6]C.-S. Wang, O. H. Stielau, and G. A. Covic, IEEE Trans. Ind. Electron. **52**(5), 1308 (2005).
[7]T. Batra and E. Schaltz, "Magnetic field emission comparison at different quality factors with series-series compensation network for inductive power transfer to vehicles," in *Wireless Power Transfer Conference 2014, Jeju Islands, South Korea, 8–9 May 2014*, pp. 13–16.

5.2.3. PhD paper 4 – Experimental verification

PhD paper {4} was presented with help of analytical and FEM results. In this chapter, experimental verification of constant nature of the space ratio is provided for the four inductor configurations presented in Chapter 4. The inductor configurations belong to category of the full geometry introduced in the paper {4}. The space ratio is calculated by performing primary and secondary no-load tests for the four inductor configurations and results are provided in Section 5.2.3.1 to 5.2.3.4.

5.2.3.1. Configuration 1

The space ratio along with the emissions are provided in Figure 18 (a) to 20 (a) at three different current values (10 A Rms, 15 A Rms, 20 A Rms). The switching frequency is 22 kHz for the three cases. Additionally, the electric quantities are also provided for the no-load tests in (b) part of Figure 18 to 20.

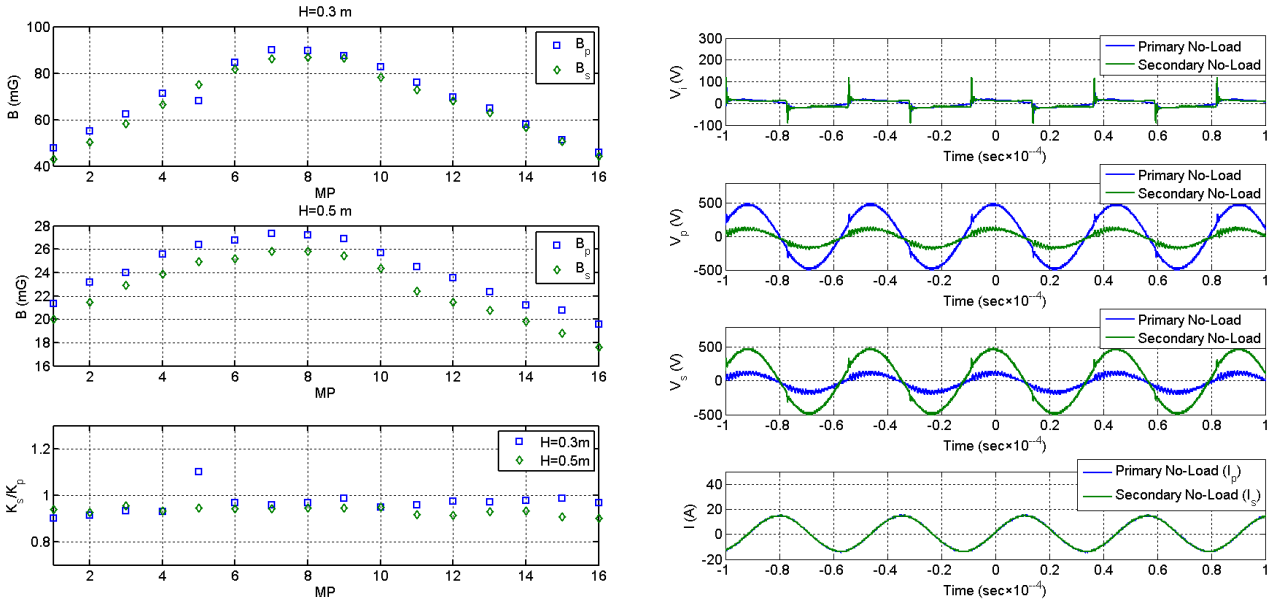

(a) Emissions and space ratio **(b)** Electrical quantities

Figure 18. Configuration 1 @ 10 A Rms

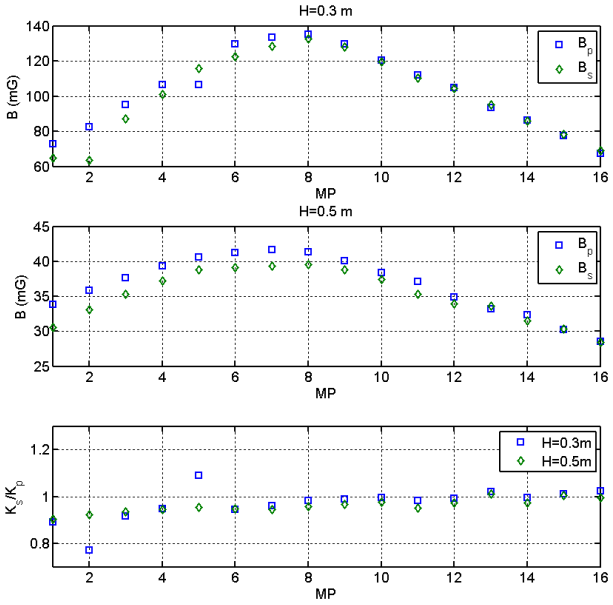

(a) Emissions and space ratio

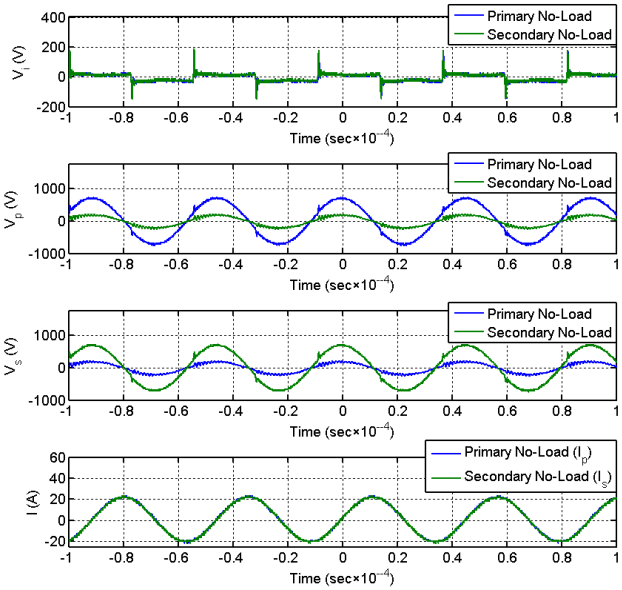

(b) Electrical quantities

Figure 19. Configuration 1 @ 15 A Rms

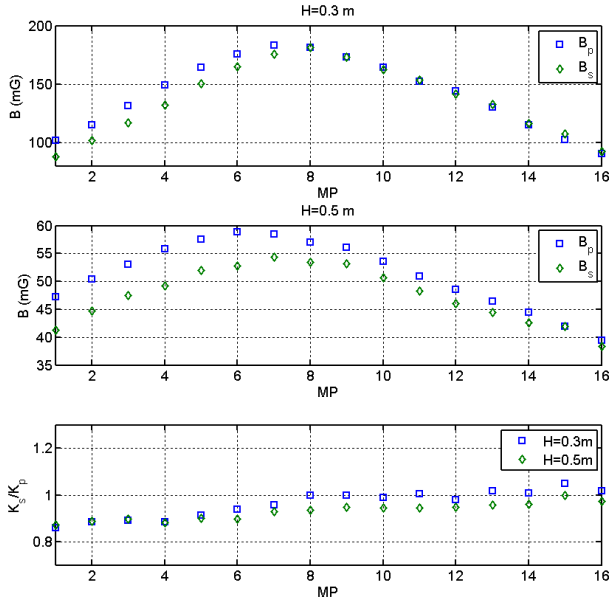

(a) Emissions and space ratio

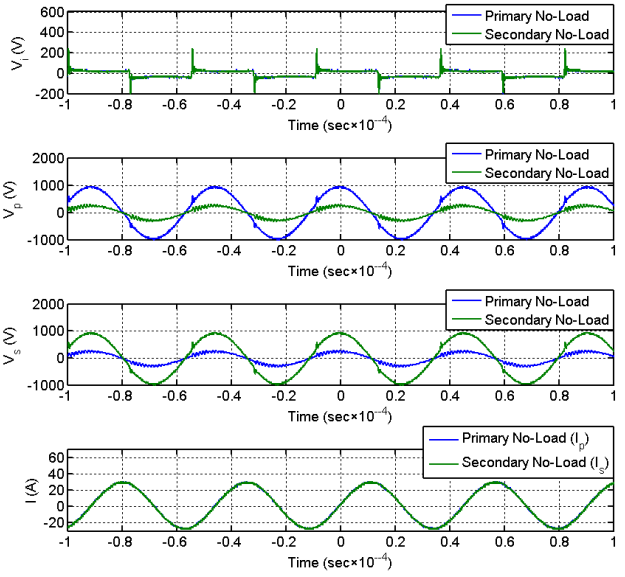

(b) Electrical quantities

Figure 20. Configuration 1 @ 20 A Rms

5.2.3.2. Configuration 2

The no-load tests results for Configuration 2 at switching frequency of 21.8 kHz are provided in Figure 21.

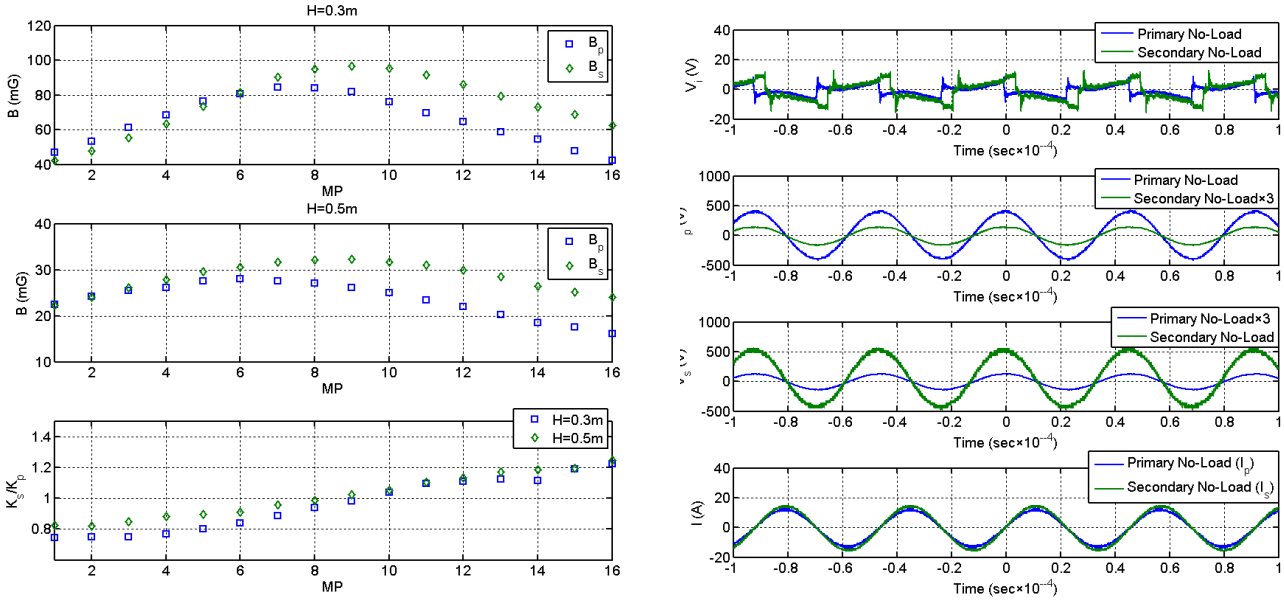

(a) Emissions and space ratio **(b)** Electrical quantities

Figure 21. Configuration 2

5.2.3.3. Configuration 3

The no-load tests results for configuration 3 at switching frequency of 21.8 kHz are provided in Figure 22.

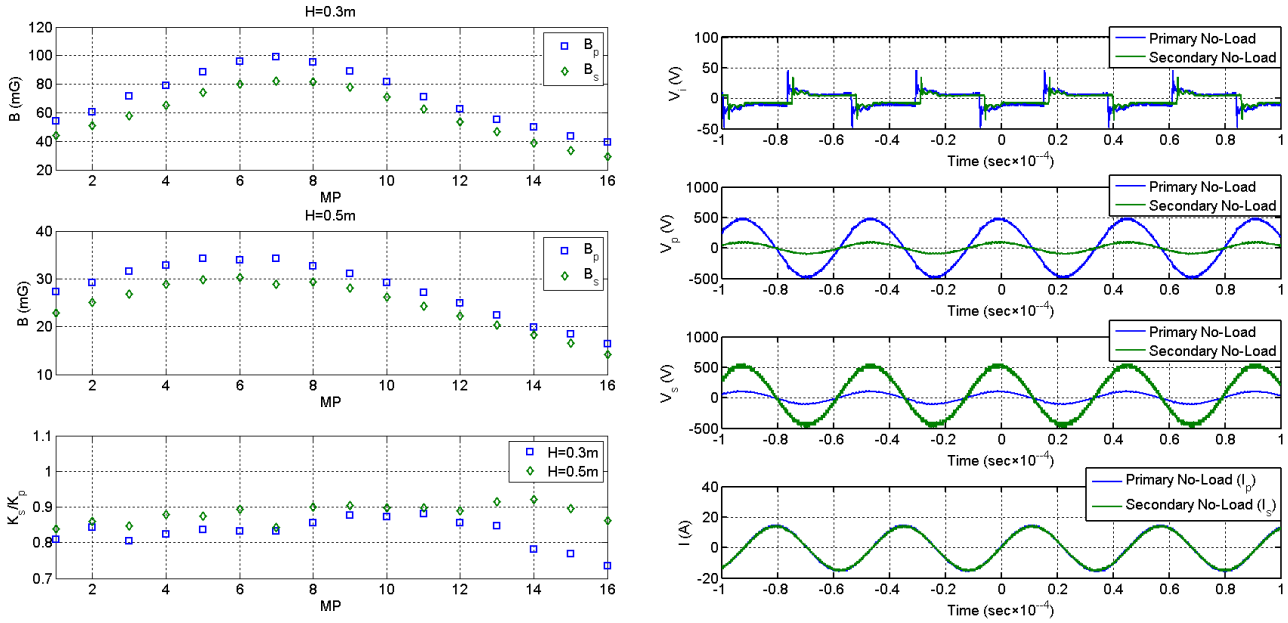

(a) Emissions and space ratio **(b)** Electrical quantities

Figure 22. Configuration 3

5.2.3.4. Configuration 4

The no-load tests results for Configuration 4 at switching frequency of 21.8 kHz are provided in Figure 23.

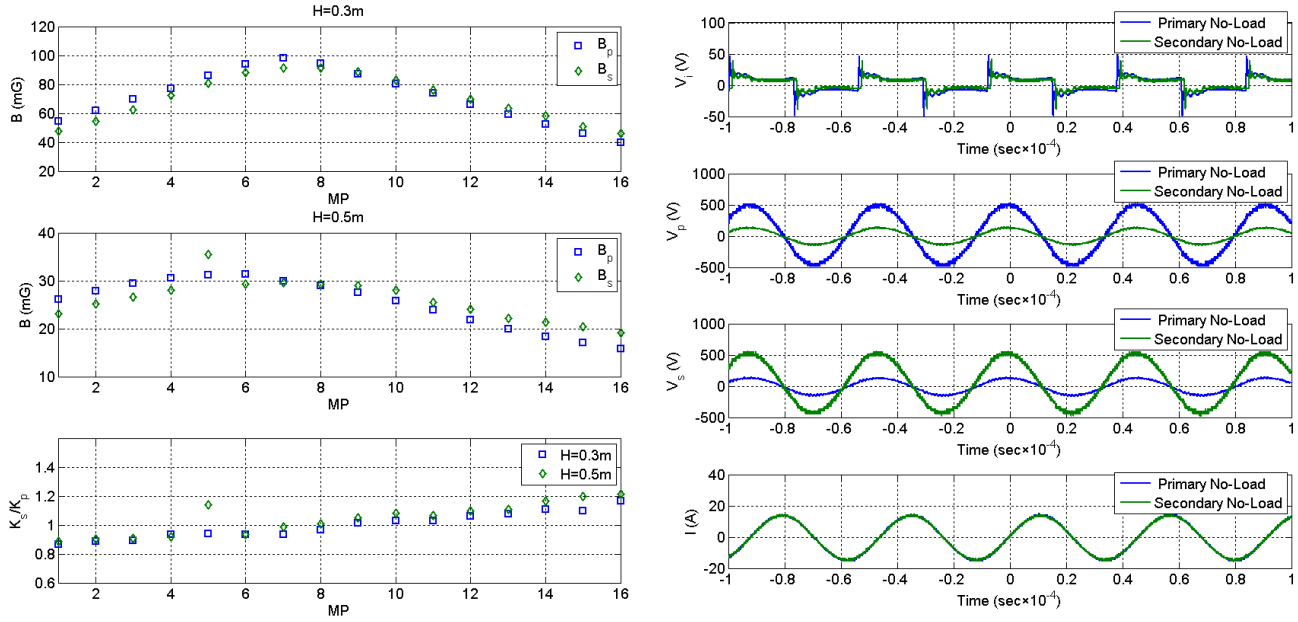

(a) Emissions and space ratio

(b) Electrical quantities

Figure 23. Configuration 4

5.3.3.5. Discussion

The following observations are made from Figure 18 to Figure 23.

1) For all configurations, the emissions are highest in between the coils or region of highest emissions (MP 6 to 10 for Configuration 1, 3 and 4 and MP 6 to 10 for Configuration 2).

2) For all configurations, the space ratio has constant value in region of highest emissions with value at the center of the coils taken as constant value. The central values using Figure 18 to 23 are 1, 1, 0.9 and 1 for Configuration 1, 2, 3 and 4 respectively. There is deviation on both sides from this central value in all configurations. The deviation is higher for points outside the highest emissions region but still these points are provided for better understanding of the reader.

3) For all configurations, the deviation from the central value is lower for horizontal distance H=0.5 m compared to H=0.3 m. Explanation for this is that average distance of the measurement points from the coils is more comparable for H=0.5 m compared to H=0.3 m. This point was had already been discussed in papers {3-4}.

4) For Configuration 1, it has been shown in Figure 18 to 20 that the emissions of the two coils increase linearly with their respective currents. As an example, the emissions at MP 8 changes from approximately 90 mG to 140 mG to 185 mG with corresponding current change of 10 A rms to 15 A rms to 20 A rms respectively. This verifies the linearity assumption taken in papers {3-10}.

5) For Configuration 1, the coil currents for the two tests are equal and hence the emissions are nearly same in region of highest emissions. This leads to value of space ratio practically equal to one and is visible in lower parts of Figure 18(a) to 20(a).

6) For Configuration 2, different currents are used for the primary no-load test (8.7 A Rms) and secondary no-load test (10.3 A Rms). Hence, the secondary field is above the primary field in Figure 21(a). This is done to validate (23) for the space ratio calculation for non-similar currents. The ratio can be approximated as one for this configuration. Also, as vertical distance between the inductors (V) increases to 20 cm for Configuration 2, variation in value of the space ratio is more from the central value compared to Configuration 1.

7) For Configuration 3, the primary inductor is closer to the measurements points compared to the secondary inductor. Hence, the primary field is higher than the secondary field for the same current value. The value of the ratio is just below 1 and is taken as 0.9 in the highest emission region as visible in Figure 22(a). This shows that the space ratio is constant in the highest emissions region but not necessarily equal to 1.

8) For Configuration 4, behavior of the coil fields and space ratio is practically similar to Configuration 1. The external metal plate has practically no impact on the emissions in the concerned area which is similar to its nearly zero effect on the inductances provided in Table 7.

5.3. Application1

Selection of load quality factor has been considered as discussed in Section 2.3.3 from point of view of output power, voltage stress (current stress for parallel resonance) across the resonant components and efficiency. In this application, selection of the load quality factor w.r.t. magnetic emissions is introduced using the semi-analytical method. General theory for the semi-analytical method has already been provided in Section 5.1.4. This theory is streamlined for this specific application in PhD papers {5} and {6} for SS and SP topologies respectively. The semi-analytical method is verified with FEM results in papers {5-6} in Section 5.3.1 and 5.3.3. Also, experimental verification of paper {5} and {6} is provided in Section 5.3.2 and 5.3.4 respectively. The results from both papers and experiments indicated that higher quality factor is favorable from the emissions point of view for given inverter current and switching frequency.

5.3.1. PhD paper 5

This paper was originally published with following details.

{5} T. Batra, E. Schaltz, “Magnetic field emission comparison at different quality factors with series-series compensation network for inductive power transfer to vehicles", Proceedings of Wireless Power Transfer Conference (WPTC 2014), pp 13-16, 2014.

Magnetic Field Emission Comparison at Different Quality Factors with Series-Series Compensation Network for Inductive Power Transfer to Vehicles

Tushar Batra and Erik Schaltz
Department of Energy Technology
Aalborg University
Aalborg, Denmark
tba@et.aau.dk, esc@et.aau.dk

Abstract— **Inductive power transfer is non-contact transfer of energy by means of magnetic fields. A higher secondary side quality factor at fixed input current ensures a linear increase in power transfer across the air gap. But also at the same time magnetic emissions to the surroundings increase. First of all in this paper an analytic expression for comparing the magnetic emissions at different quality factors is introduced. It is shown with help of simulations on Comsol that emissions have a lower increase as compared to linear increase in the power transferred with the quality factor as suggested by the analytical calculations.**

Keywords-Inductive Power Transfer, magnetic fields, resonacne.

I. INTRODUCTION

Inductive Power Transfer (IPT) uses the principle of electromagnetic induction for transferring energy from primary coil to secondary coil as in a transformer. The coils of a transformer are coupled to each other through a magnetic medium providing low reluctivity to magnetic flux. On the other hand, there is a large air gap between the coils of IPT and magnetic flux path is predominantly air. Hence, capacitors need to be added on both sides for unity power factor operation and to ensure maximum power transfer [1] across the air gap. A block diagram of a IPT system is shown below in Fig. 1.

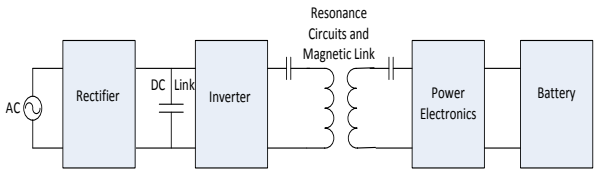

Figure 1. Block diagram inductive wireless power transfer

Power converter on the primary side enables operation at a frequency much higher than the grid frequency and hence size of the components is reduced. Current rating of this converter limits input current of the system. Power electronics for the secondary side have been proposed for both unidirectional [2] and bidirectional [3] exchange of power with battery of Electric Vehicle (EV).

Magnetic emissions to the surroundings are a significant part of design process for these systems. Active and passive shielding [1, 4] is used to minimize these emissions. The study of variation of magnetic emissions and power transferred with quality factor at fixed input current is the main theme of this paper. With help of theoretical expressions and simulations, it is shown that the magnetic emissions have a lower increase compared to the linear increase in the power with the quality factor. This paper would be helpful in forming a better understanding of the system design especially w.r.t magnetic emissions

II. SERIES-SERIES COMPENSATION NETWORK

Fundamental Mode Analysis [5] equivalent circuit diagram of the topology is shown below in Fig. 2. The secondary side power electronics and battery of EV are approximated by a resistance [6]. Also, resistance of the coils and magnetic resistance (losses) are much smaller than the load resistance and are neglected for the theoretical part.

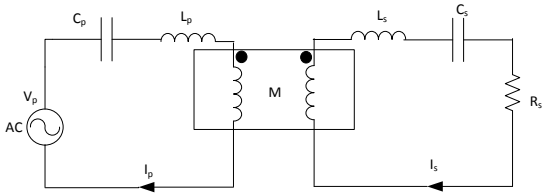

Figure 2. Fundamental mode analysis equivalent circuit [7]

Symbols used in this section are first summarized in Table I.

TABLE I. SYMBOLS

Symbol	Name	Symbol	Name
I_p	Primary current	I_s	Secondary current
V_p	Primary voltage	M	Mutual inductance
L_p	Primary self-inductance	L_s	Secondary self-inductance

The work has financially been supported by The Danish Council for Strategic Research.

Symbol	Name	Symbol	Name
C_p	Primary capacitor	C_s	Secondary capacitor
R_s	Load resistance	Q	Quality factor
w	Angular frequency	w_r	Resonance angular frequency

Voltage equations, resonance frequency and quality factor for the system are

$$\left(jwL_p+\frac{1}{jwC_p}\right)I_p - jwMI_s = V_p \quad (1)$$

$$\left(jwL_s+\frac{1}{jwC_s}\right)I_s + R_sI_s = jwMI_p \quad (2)$$

$$w_r=\frac{1}{\sqrt{L_pC_p}}=\frac{1}{\sqrt{L_sC_s}} \quad (3)$$

$$Q=\frac{w_rL_s}{R_s}. \quad (4)$$

Inserting (3) and (4) into (1) and (2) and rearranging,

$$V_p = - jw_rMI_s=\frac{w_rM^2}{L_s}QI_p \quad (5)$$

$$I_s =\frac{jw_rM}{R_s}I_p = jM\frac{Q}{L_s}I_p. \quad (6)$$

Using (5), input power (P) for the system is

$$P=V_pI_p=\frac{w_rM^2}{L_s}QI_p^2. \quad (7)$$

Peak magnetic field in ferrite core of IPT systems is much smaller than saturation field value for ferrite [8]. Hence, magnetic fields (B_p and B_s) due to the primary and secondary coils at any point in the space can be expressed as

$$|B_p|=K_p|I_p| \quad (8)$$

$$|B_s|=K_s|I_s|. \quad (9)$$

K_p and K_s are constants for the primary and secondary coils for any point in the space respectively. Using (6), (8) and (9), rms magnetic field at any point in the surroundings is given by

$$|B|=\sqrt{(|I_p|K_p)^2+(|I_s|K_s)^2}$$

$$|B|=I_p\sqrt{K_p^2+\left(K_sQ\frac{M}{L_S}\right)^2}. \quad (10)$$

Using (10), ratio K for comparing rms magnetic fields (B_a and B_b) for two different quality factors (Q_a and Q_b) at the same primary current can be expressed as

$$K=\frac{|B_a|}{|B_b|}=\frac{\sqrt{1+\left(Q_a\frac{M}{L_S}\frac{K_s}{K_p}\right)^2}}{\sqrt{1+\left(Q_b\frac{M}{L_S}\frac{K_s}{K_p}\right)^2}}. \quad (11)$$

Ratio of power (P_a and P_b) for the quality factors using (7)

$$\frac{P_a}{P_b}=\frac{Q_a}{Q_b}. \quad (12)$$

Let us assume that

$$Q_a > Q_b \quad (13)$$

Squaring both sides, adding similar term on both sides and rearranging,

$$Q_a^2+Q_a^2\left(Q_b\frac{M}{L_S}\frac{K_s}{K_p}\right)^2 > Q_b^2+Q_b^2\left(Q_a\frac{M}{L_S}\frac{K_s}{K_p}\right)^2 \quad (14)$$

$$\frac{Q_a}{Q_b} > \frac{\sqrt{1+\left(Q_a\frac{M}{L_S}\frac{K_s}{K_p}\right)^2}}{\sqrt{1+\left(Q_b\frac{M}{L_S}\frac{K_s}{K_p}\right)^2}}. \quad (15)$$

Inserting (11) and (12) in (15),

$$\frac{P_a}{P_b} > \frac{|B_a|}{|B_b|}. \quad (16)$$

Hence, the linear increase of power is higher than corresponding increase in the emissions with the quality factor at the same input current for inductive power transfer systems.

III. SAMPLE GEOMETRY

Side and top views of the sample geometry [9] is provided in Fig. 3 (a) and (b) respectively. The two inductors are identical, centered symmetrically and have a coupling ratio (M/L_s) of 0.21. Number of turns in both the coils is 12 [10]. There are 810 parallel conductors in each turn with an indivual diameter of 0.1mm. The outer diameter of the turn is 4mm. Relative permeability of the ferrite is 2300.

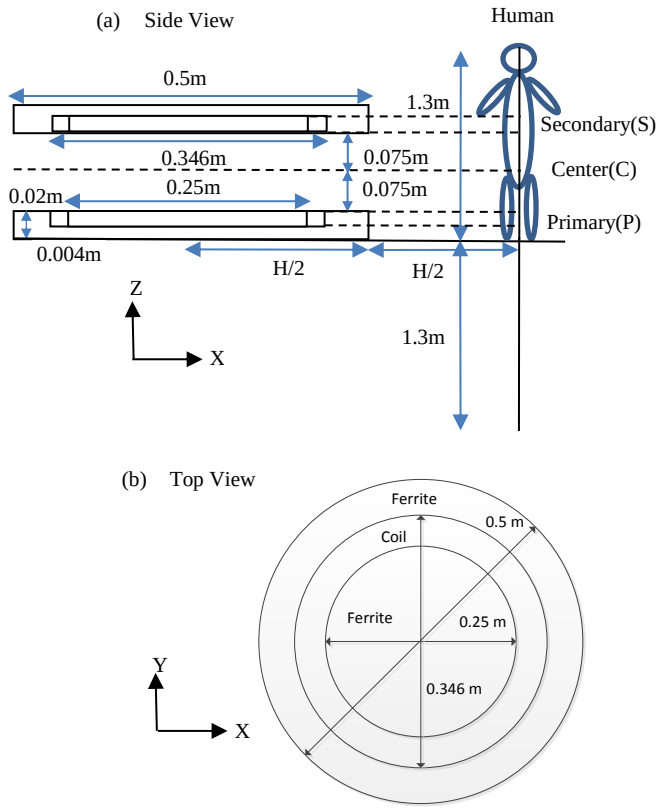

Figure 3. Side and top views sample geometry [7]

IV. RESULTS

Assuming an EV to be 1m wide, the nearest human will be at H = 0.5 m in Fig. 3(a). The results in this section are presented for two distances H = 0.5m and 1m. Primary current (I_p – 23A rms at 20 kHz) is same for all no-load and on-load simulations presented below.

A. Ratio K_s/K_p

The ratio can be found by no-load tests [7] on the two coils at same current. Using (8) and (9), for the same current

$$\frac{K_S}{K_p} = \frac{|B_S|}{|B_p|}. \tag{17}$$

Rms magnetic fields and their ratio K_s/K_p for the no-load simulations are provided in Fig. 4 and Fig. 5.

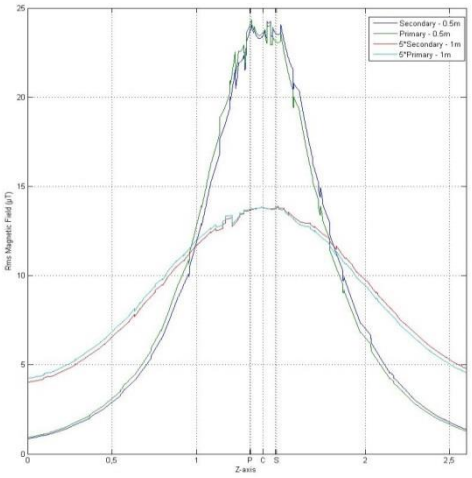

Figure 4. Rms magnetic field (μT) versus Z-axis

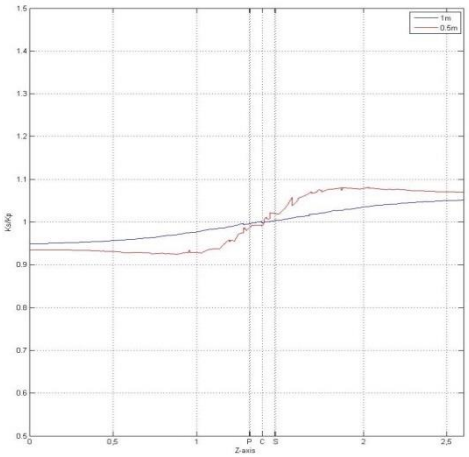

Figure 5. Ratio Ks/K_p versus Z-axis

B. Ratio K

Theoretical ratio K can be calculated by applying (11) for varying value of K_s/K_p in Fig. 5. The theoretical results and simulated results from Comsol for K are presented in Fig. 6 and 7.

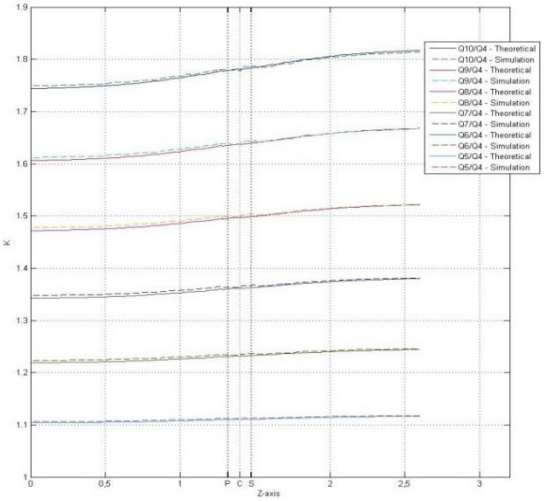

Figure 6. Ratio K versus Z-axis (H = 1m)

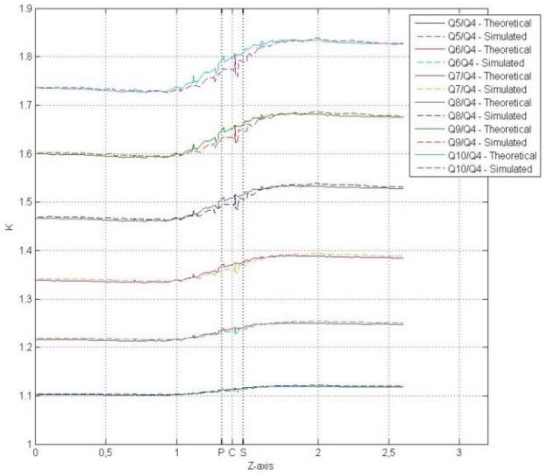

Figure 7. Ratio K versus Z-axis (H = 0.5m)

Rms magnetic field at different quality factors from simulations are presented next in Fig. 8 and 9.

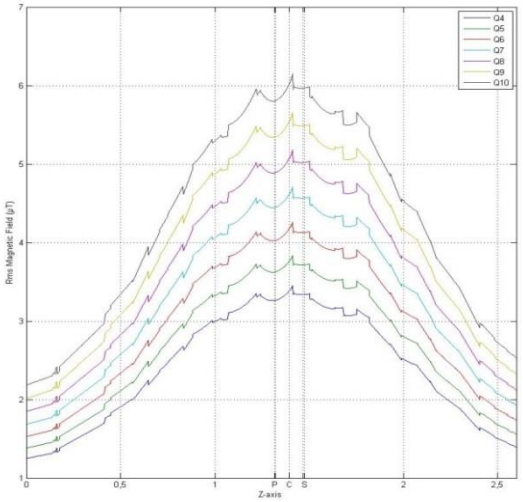

Figure 8. Rms magnetic field (μT) verus Z-axis (H = 1m)

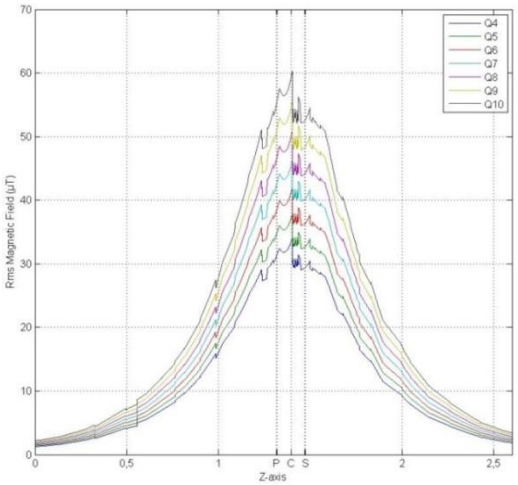

Figure 9. Rms magnetic field (μT) verus Z-axis (H = 1m)

The circuit parameters for the simulations are presented in Table II.

TABLE II. CIRCUIT PARAMETERS

Q	Is(A)	V_p(V)	P(W)=V_p*I_p (23A)
4	0.245+j20.053	82.565+j0.279	1898.995
5	0.385+j25.02	102.839-j0.283	2365.297
6	0.551+j29.971	123.039-j0.966	2829.897
7	0.748+j34.902	143.162-j1.767	3292.726
8	0.973+j39.815	163.210-j2.687	3753.83
9	1.2263+j44.709	183.180-j3.723	4213.14
10	1.508+49.585	203.075-j4.875	4670.725

V. DISCUSSION OF RESULTS

Value of ratio K_s/K_p is fairly constant as one (value at C) for both the distances H as seen in Fig. 5. The same can also be seen with help of rms magnetic fields in Fig. 4. In this plot, magnetic fields for both the coils are nearly same at all points in the space. Another point worth mentioning is here that number of turns for the primary coil is proportional to K_p and vice versa. The turn ratio used in the paper is 12:12 and hence value of K_s/K_p is close to one. If the turn ratio was 12:24, the value of K_s/K_p would be two at C.

Theoretical ratio K has been calculated in Fig. 6 and 7 by applying (11) along curve K_s/K_p of Fig. 4. It shows good compliment with the simulated results in the same figures for both the distances. Fig. 8 and 9 again show that rms magnetic fields increases with the quality factor of the system. K_s/K_p and as a result K for H = 1m has less deviation from the corresponding curves for H = 0.5m in Fig. 6 and 7. This stands for that the coils have more comparable contribution in the resultant magnetic field as the distance in horizontal direction is increased. Also, K_s/K_p varies for geometries without ferrite and with the air gap and is discussed in [7].

Ratios K in Fig. 6 and 7 have same a small deviation on both sides from value at C. By neglecting this deviation or approximation of K_s/K_p equal to one gives the advantage that theoretical ratio K can be expressed as a single number. The approximate K is most accurate for region near C as K_s/K_p is actually one there as shown in Fig. 5. The magnetic emissions are highest in region near C as seen in Fig. 8 and 9. At the end as suggested by (7), input power of the system shows a linear increase with the quality factor as shown in Table II.

VI. CONCLUSION

In this paper, first of all a theoretical ratio K for comparing inductive power transfer system with series-series compensation network at different quality factors has been developed. Simulated and theoretical results both suggest that for a fixed input current magnetic emissions have a lower increase as compared to linear increase of power with the quality factor. Moreover, ratio K has nearly constant behavior and hence can be approximated by its value at the center of the system. Both the full and approximated values of K can be calculated without performing on-load tests which is very advantageous for the initial design of the system.

REFERENCES

[1] U. K. Madawala, and D. J. Thrimawithana, "Current sourced bi-directional inductive power transfer system," IET Power Electronics, vol. 4, no. 4, pp. 471-480, 2011.

[2] A. Neves, D. M. Sousa, A. Roque, J. M. Terras, "Analysis of an inductive charging system for a commercial electric vehicle," 14th European Conference on Power Electronics and Applications (EPE 2011), pp. 1-10, Aug. 30 2011-Sept. 1 2011.

[3] U. K. Madawala, and D. J. Thrimawithana, "A Bidirectional Inductive Power Interface for Electric Vehicles in V2G Systems," IEEE Transactions on Industrial Electronics,, vol. 58, no. 10, pp. 4789-4796, 2011.

[4] J. Kim, J. Kim, S. Kong, H. Kim, I. S. Suh, N. P. Suh, D. H. Sho, "et al." ,"Coil Design and Shielding Methods for MagneticResonant Wireless Po wer Transfer System", Proceedings of the IEEE , vol. 101, no. 6, pp. 1332-1342, 2013

[5] M. G. Egan, D. L. O'Sullivan, J. G. Hayes, S. E. Schulz, J. T. Hall, "Power-Factor-Corrected Single-Stage Inductive Charger for Electric Vehicle Batteries," IEEE Transactions on Industrial Electronics, vol. 54, no. 2, pp. 1217-1226, 2007.

[6] W. Chwei-Sen, O. H. Stielau, and G. A. Covic, "Design considerations for a contactless electric vehicle battery charger," IEEE Transactions on Industrial Electronics, vol. 52, no. 5, pp. 1308-1314, 2005.

[7] T. Batra, E. Schaltz, "Magnetic Field Emissions for Ferrite and Non-Ferrite Geometries for Wireless Power Transfer to Vehicles", Journal of Applied Physics – Special Edition, in press.

[8] M. Budhia, G. A. Covic, J. T. Boys, "Design and Optimization of Circular Magnetic Structures for Lumped Inductive Power Transfer Systems," IEEE Transactions On Power Electronics, vol 26., no 11., pp. 3096-3108, 2011.

[9] H. Sakamoto, K. Harada, S. Washimiya, K. Takehara, Y. Matsuo, F. Nakao "Large air-gap coupler for inductive charger [for electric vehicles]," IEEE Transactions on Magnetics, vol. 35, no. 5, pp. 3526-3528, 1999.

[10] M. Budhia, G. A. Covic, J. T. Boys, C. Y. Huang, "Development of single sided flux couplers for contactless electric vehicle charging," IEEE Transactions On Industrial Electronics, vol 60., no 1., pp. 318-328, 2013.

5.3.2. PhD paper 5 – Experimental verification

This section similar to Section 5.2.3 provides experimental verification of corresponding paper {5}. The theory has been provided in paper {5} and this section will verify two main points introduced in the paper. First, it was provided that for given inverter current and switching frequency the emissions increase relatively lowers than the output power with changing load quality factor (denoted by added subscript 1, 2 and 3). Mathematically the last statement is provided as (42) and was proved in PhD paper {5} (Equation 15).

$$\frac{Q_2}{Q_1} > \frac{\sqrt{1+\left(\frac{K_s}{K_p}\frac{M}{L_s}Q_2\right)^2}}{\sqrt{1+\left(\frac{K_s}{K_p}\frac{M}{L_s}Q_1\right)^2}} \tag{42}$$

Secondly, proposed analytical emissions ratio (41) is verified with experimentally measured emissions ratio. The experimental results are presented at different quality factors for the four inductor configurations at constant primary current and switching frequency in Section 6.5.3.1 to 6.5.3.4. The analytical emissions ratio provided later in Table 9 to 14 is calculated using (41). It has inputs from the measured coil currents and space ratio equal to 1, 1, 0.9 and 1 (provided in Section 5.2.3) for the first, second, third and fourth inductor configuration for the calculation (41). The experimental space ratio on the other hand is calculated by dividing measured emissions in Matlab. This procedure is followed in experimental verification of other papers in Section 5.3.4, 5.4.2 and 5.5.3 and will not be provided again. The first quality factor (Q_{l1}) is taken as base quality factor for all configurations. Also, the capacitor combination is CC2 (Section 4.3) for Case 2 of Configuration 1 and 2 in Section 5.3.2.1.2 and 5.3.2.2.2 respectively. For remaining experiments, capacitor combination CC1 is used.

5.3.2.1. Configuration 1

Results are provided for this configuration for two switching frequencies of 21.8 kHz (Case 1) and 26.1 kHz (Case 2).

5.3.2.1.1. Case 1

The emissions, emissions ratio and electric quantities are presented at two different quality factors for both horizontal distances (H=0.3 m and 0.5 m) in Figure 24. The experimental and analytical calculations are provided in Table 9.

Table 9. Configuration 1 – Case 1 results

x	**R_{lx} (Ω)**	**Q_{lx}/Q_{l1}**	**P_l (W)**	**P_l ratio***	**Emissions ratio*, ****	**Analytical emissions ratio***
1	5.43	1	610.56	1	1	1
2	3.24	1.68	970.01	1.59	1.5	1.504

*@Q_{lx}/Q_{l1}

** Approximated central value using Figure 24

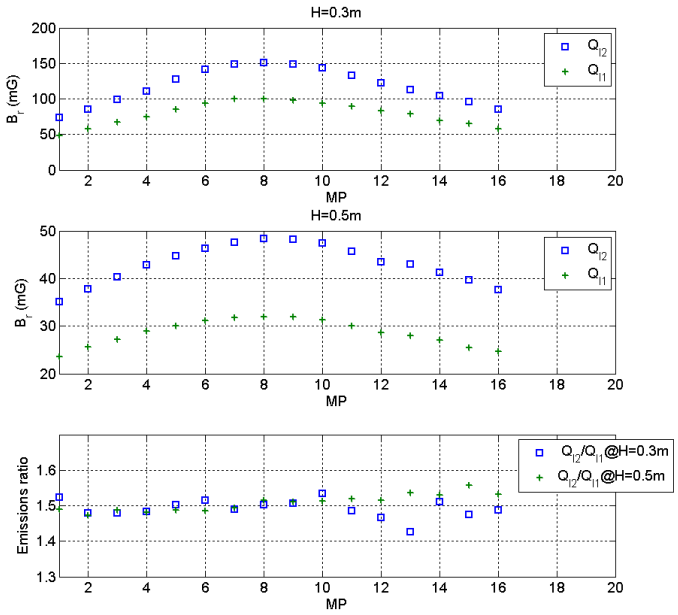

(a) Emissions and emissions ratio

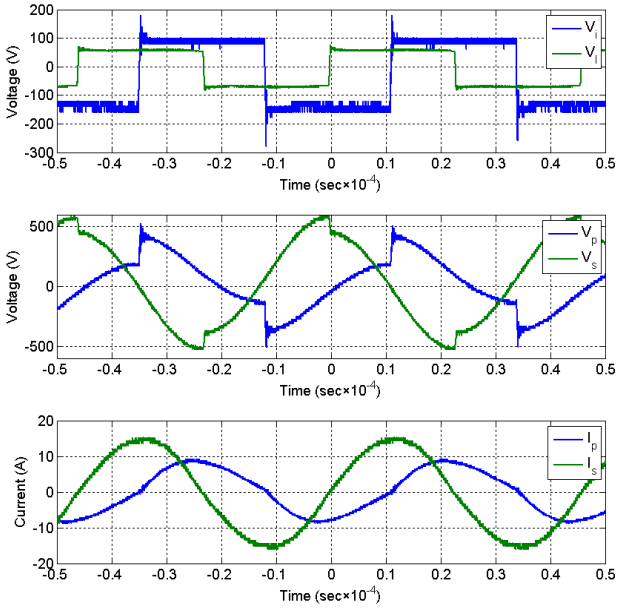

(b) Electrical quantities at Q_{l1}

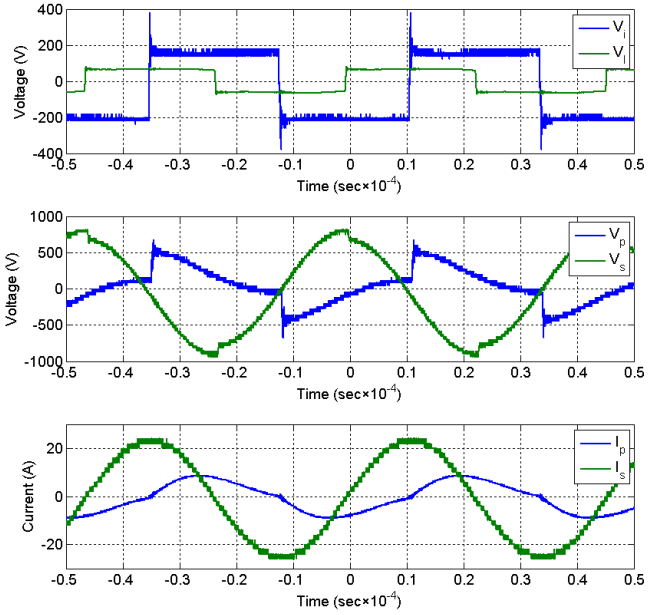

(c) Electrical quantities at Q_{l2}

Figure 24. Configuration 1 – Case 1 results

5.3.2.1.2. Case 2

The emissions, emissions ratio and electric quantities are presented at two different quality factors for horizontal distance (H=0.5 m) in Figure 25. The experimental and analytical calculations are provided in Table 10.

Table 10. Configuration 1 – Case 2 results

x	**R_{lx} (Ω)**	**Q_{lx}/Q_{l1}**	**P_l (W)**	**P_l ratio***	**Emissions ratio*, ****	**Analytical emissions ratio***
1	7.19	1	1490.40	1	1	1.00
2	5.22	1.38	1945.44	1.3	1.3	1.24

*@Q_{lx}/Q_{l1}

** Approximated central value using Figure 25

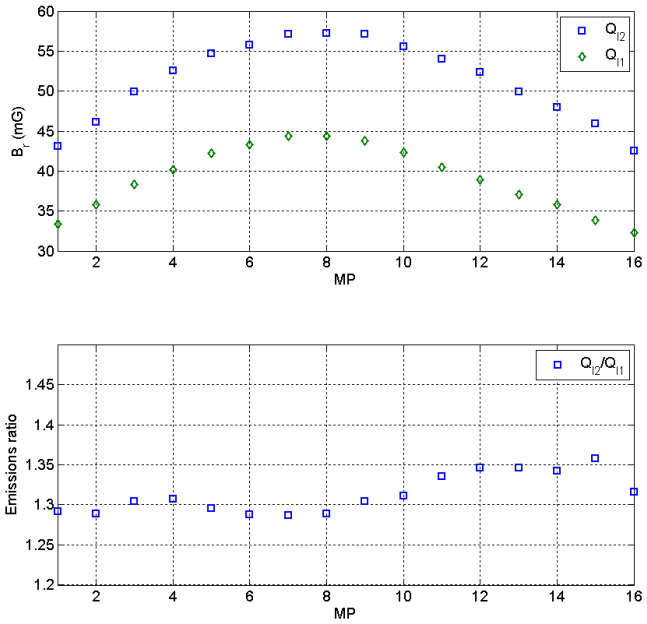

(a) Emissions and emissions ratio

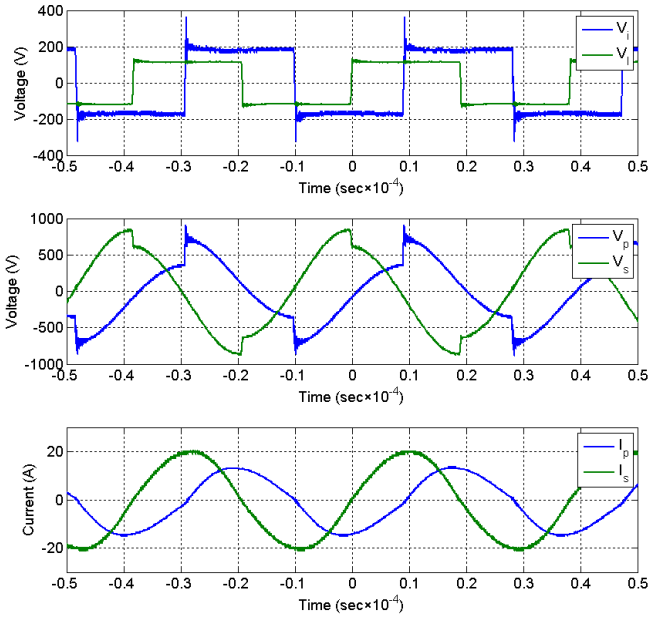

(b) Electrical quantities at Q_{l1}

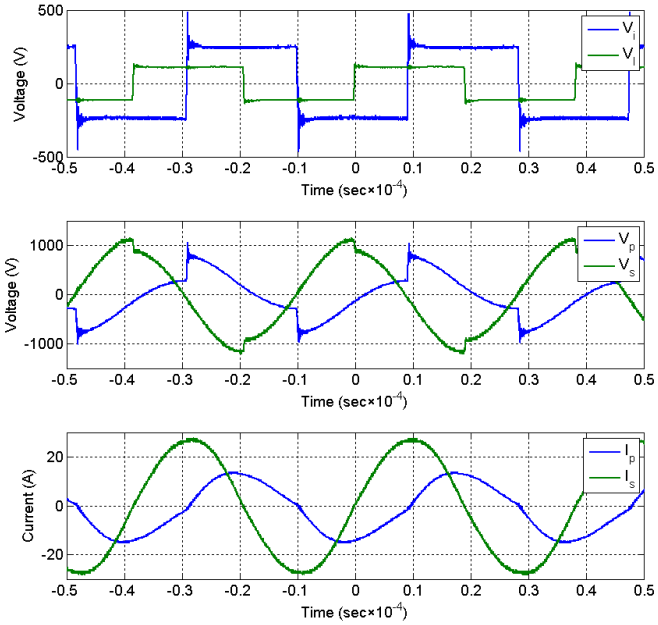

(c) Electrical quantities at Q_{l2}

Figure 25. Configuration1 – Case 2 results

5.3.2.2. Configuration 2

Results are provided for this configuration for two switching frequencies of 22 kHz (Case 1) and 26.3 kHz (Case 2).

5.3.2.2.1. Case 1

The emissions, emissions ratio and electric quantities are presented at three different quality factors for both horizontal distances (H=0.3 m and 0.5 m) in Figure 26. The experimental and analytical calculations are provided in Table 11.

Table 11. Configuration 2 – Case 1 results

x	**R_{lx} (Ω)**	**Q_{lx}/Q_{l1}**	**P_l (W)**	**P_l ratio***	**Emissions ratio*, ****	**Analytical emissions ratio***
1	5.23	1	221.13	1	1	1
2	4.33	1.21	254.39	1.15	1.05	1.04
3	3.08	1.70	352.46	1.59	1.24	1.23

*@Q_{lx}/Q_{l1}

** Approximated central value using Figure 26

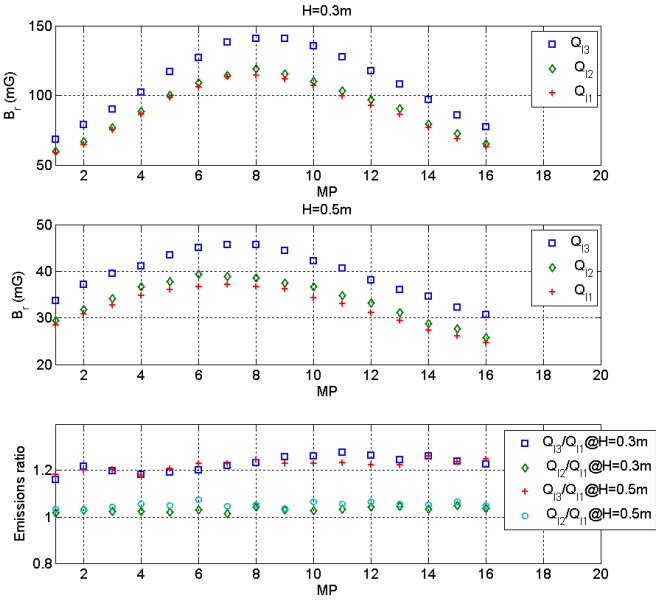

(a) Emissions and emissions ratio

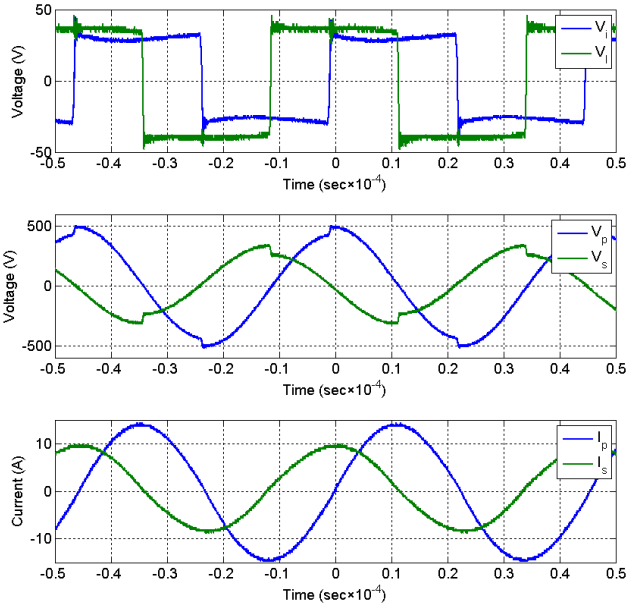

(b) Electrical quantities at Q_{l1}

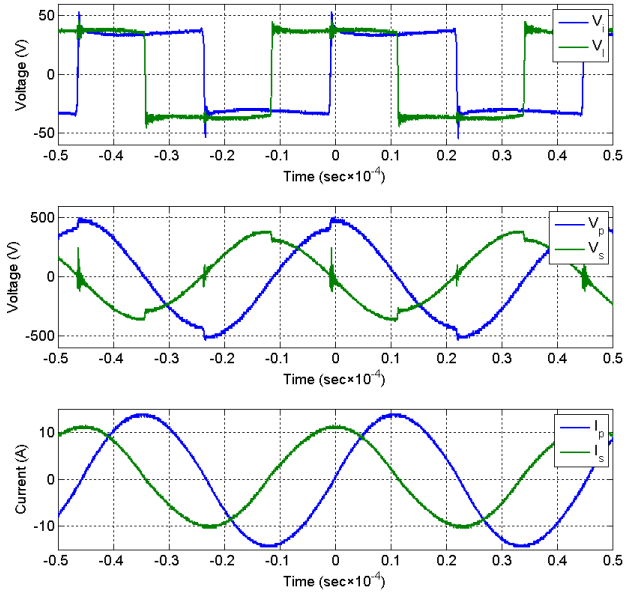

(c) Electrical quantities at Q_{l2}

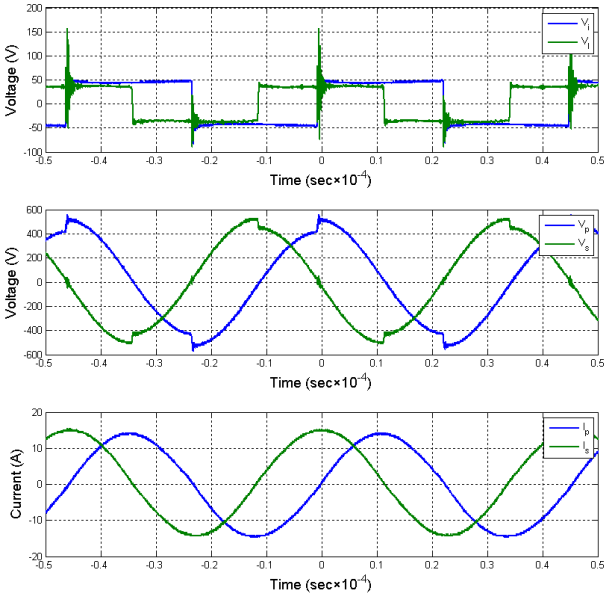

(d) Electrical quantities at Q_{l3}

Figure 26. Configuration 2 – Case 1 results

5.3.2.2.2. Case 2

The emissions, emissions ratio and electric quantities are presented at two different quality factors for horizontal distance (H=0.5 m) in Figure 27. The experimental and analytical calculations are provided in Table 12.

Table 12. Configuration 2 – Case 2 results

x	**R_{lx} (Ω)**	**Q_{lx}/Q_{l1}**	**P_l (W)**	**P_l ratio***	**Emissions ratio*, ****	**Analytical emissions ratio***
1	5.31	1	1010.99	1	1	1
2	4.22	1.26	1219.41	1.21	1.07	1.08

*@Q_{lx}/Q_{l1}

** Approximated central value using Figure 27

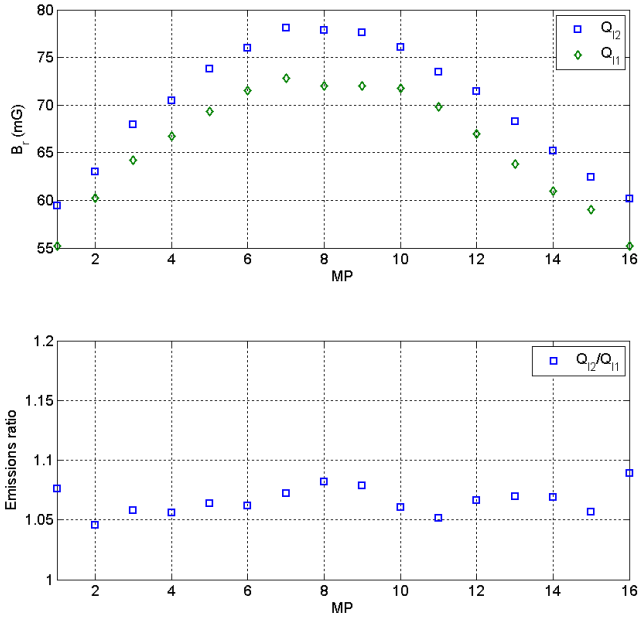

(a) Emissions and emissions ratio

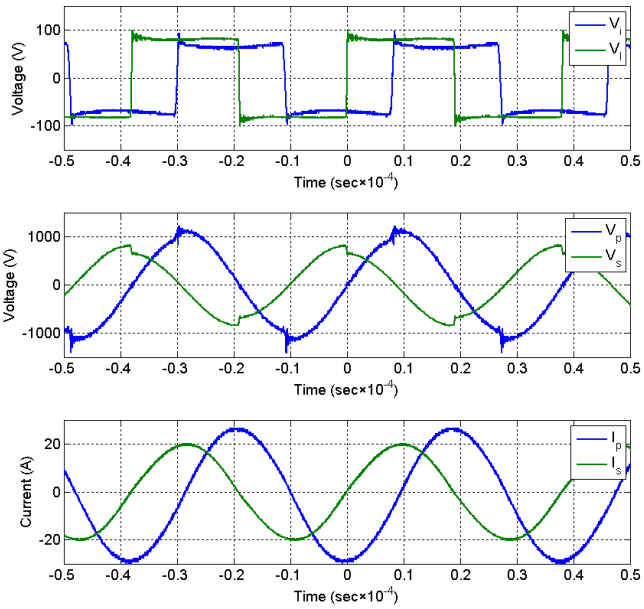

(b) Electrical quantities at Q_{l1}

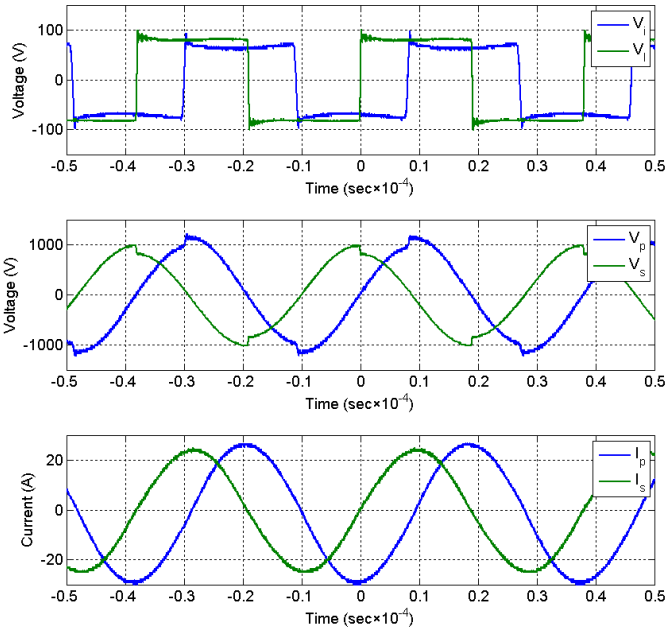

(c) Electrical quantities at Q_{l2}

Figure 27. Configuration 2 – Case 2 results

5.3.2.3. Configuration 3

Results are provided for this configuration at switching frequency of 21.7 kHz. The emissions, emissions ratio and electric quantities are presented at three different quality factors for both horizontal distances (H=0.3 m and 0.5 m) in Figure 28. The experimental and analytical calculations are provided in Table 13.

Table 13. Configuration 3 results

x	**R_{lx} (Ω)**	**Q_{lx}/Q_{l1}**	**P_l (W)**	**P_l ratio***	**Emissions ratio*, ****	**Analytical emissions ratio***
1	5.42	1	1	1	1	1
2	4.43	1.22	1.20	1.17	1.18	1.11
3	3.19	1.70	1.68	1.45	1.44	1.41

*@Q_{lx}/Q_{l1}

** Approximated central value using Figure 28

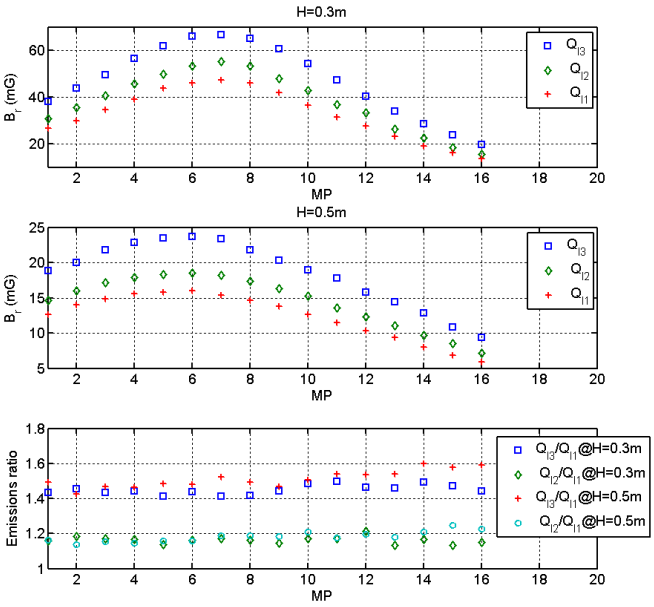

(a) Emissions and emissions ratio

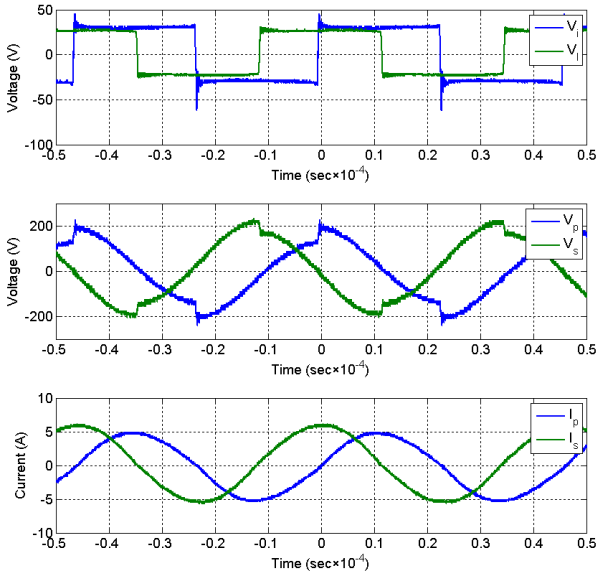

(b) Electrical quantities at Q_{l1}

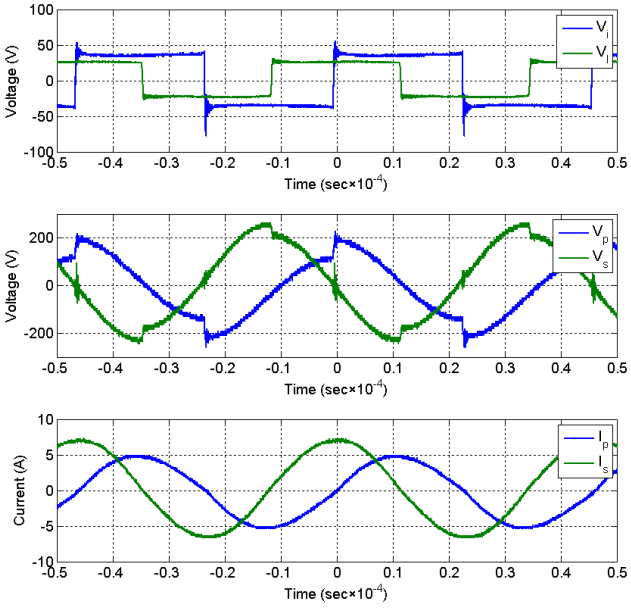

(c) Electrical quantities at Q_{l2}

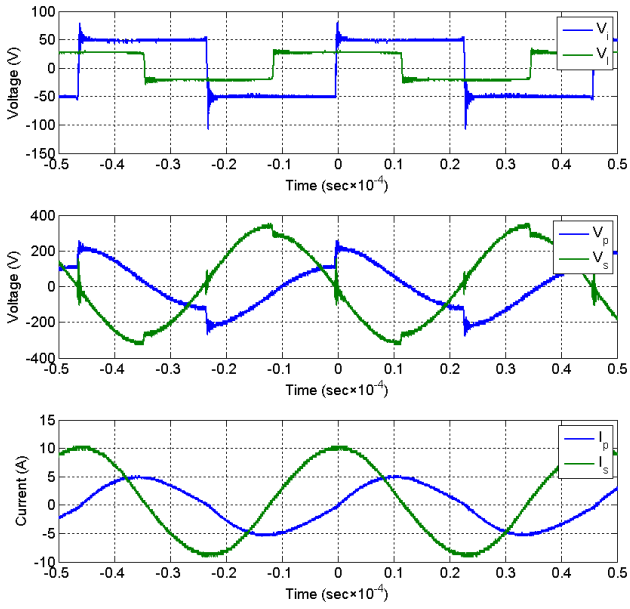

(d) Electrical quantities at Q_{l3}

Figure 28. Configuration 3 results

5.3.2.4. Configuration 4

Results are provided for this configuration at switching frequency of 21.7 kHz. The emissions, emissions ratio and electric quantities are presented for three different quality factors for both horizontal distances (H=0.3 m and 0.5 m) in Figure 29. The experimental and analytical calculations are provided in Table 14.

Table 14. Configuration 4

x	**R_{lx} (Ω)**	**Q_{lx}/Q_{l1}**	**P_l (W)**	**P_l ratio***	**Emissions ratio*, ****	**Analytical emissions ratio***
1	5.25	1	197.83	1	1	1
2	4.25	1.23	230.52	1.17	1.17	1.18
3	3.05	1.72	317.63	1.61	1.60	1.52

*@Q_{lx}/Q_{l1}

** Approximated central value using Figure 29

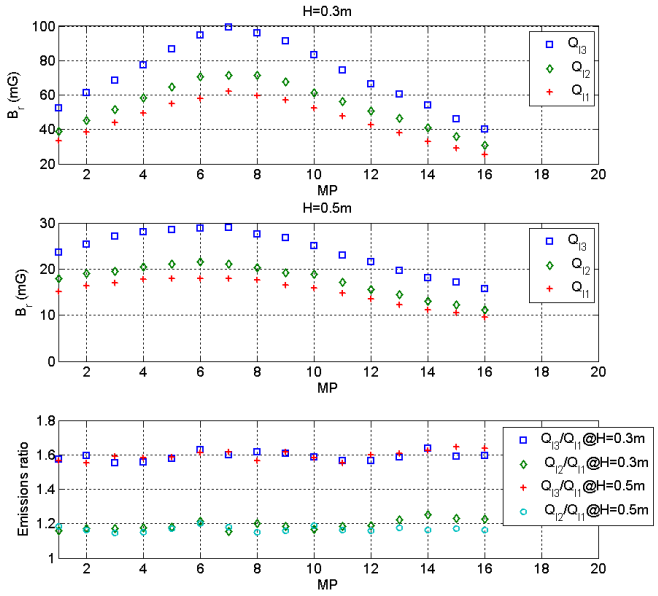

(a) Emissions and emissions ratio

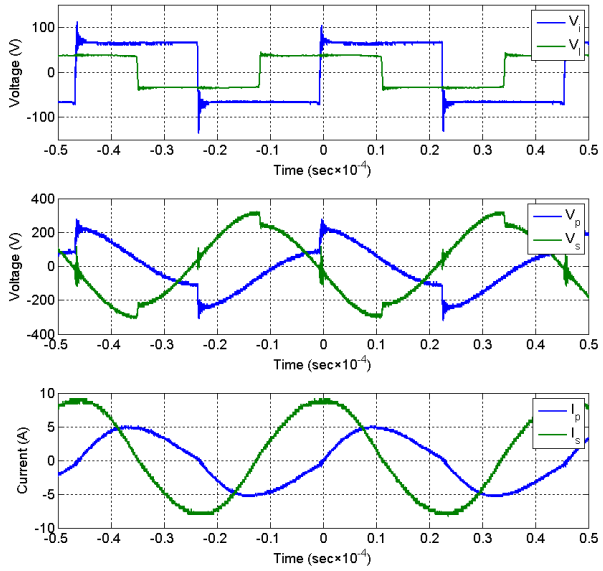

(b) Electrical quantities at Q_{l1}

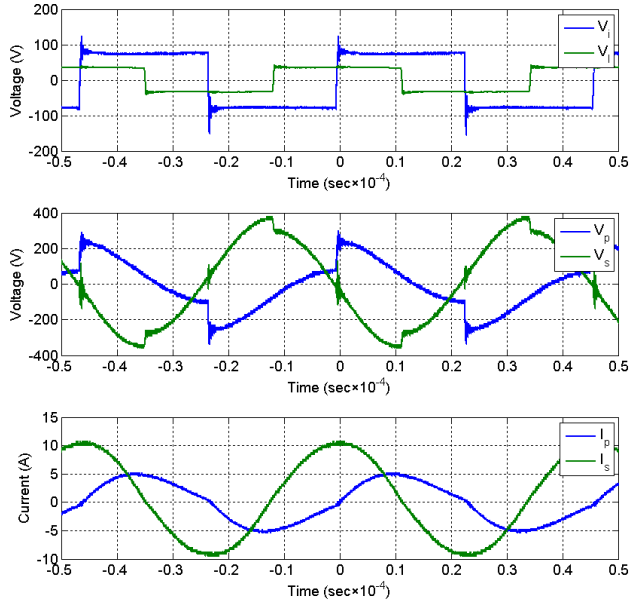

(c) Electrical quantities at Q_{l2}

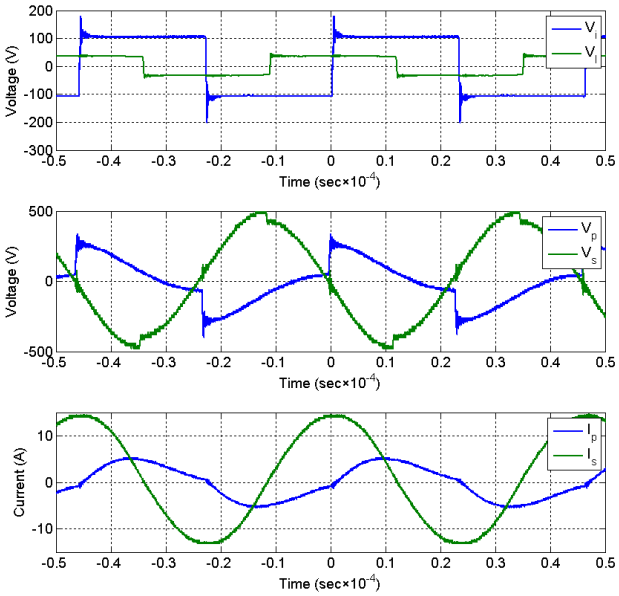

(d) Electrical quantities at Q_{l3}

Figure 29. Configuration 4 results

5.3.2.5. Discussion

The following observations are made from the results in Section 5.3.2.1 to 5.3.2.4.

1) Phase angle between the secondary current and inverter voltage w.r.t. primary current are close to 90˚ and 0˚ as provided in Figure 24 to 29. However in some cases (Figure 26 and 27), deviation in angle between the primary current and inverter voltage is slightly higher compared to others cases. But this can be ignored as purpose of the experiments is to verify the emissions ratio and its comparison with the output power. Both of which are dependent (4, 44) on the two currents magnitude and phase angle between them. As a result, the frequency is tuned in the experiments to provide resonance in the secondary side or phase angle between the two currents to be 90˚ as mentioned in theory for this application {5}. The small angle on the inverter side marginally increases inverter VA on account of reactive power and does not have influence on the measured quantities. Analogues statements are applicable for experiments conducted in Section 5.3.4, 5.4.2 and 5.5.3.

2) The experimental emissions ratio is in good compliance with analytical emissions ratio as provided in Table 9 to 14.

3) It was mentioned in the reference paper {5} that the output power increases linearly with the quality factor. However, results summarized in Table 9 to 14 show slightly lower increase in the output power compared to the quality factor. This is on account of the internal resistances which are active in the experimental results but were ignored in the reference paper {5}.

4) Increase in the emissions is much lower than increase in the output power for Configuration 2 as provided in Table 11 and 12. On the other hand, increase in the two quantities become nearly equal for Configuration 1, 3 and 4 provided in Table 9, 10, 13, 14. This behavior can be explained with help of (42). With increase in the coupling factor (Configuration 1, 3 and 4), second part of emission term become dominating and the emissions ratio value comes closer to quality factor ratio.

5) For Configuration 1 and 4, the reflected resistance is high or reflected quality factor is low on account of lower vertical gap (V=10 cm). This leads to comparable impedance for the first and third harmonic on the primary side and is visible in the primary current waveform in (b) and (c) parts of Figure 24 and 25 and (b), (c) and (d) parts of Figure 29.

5.3.3. PhD paper 6

This paper was originally published with following details.

{6} T. Batra, E. Schaltz, “Magnetic field emission comparison at different quality factors with series-parallel compensation network for inductive power transfer to vehicles", Proceedings of 4th International Electric Drives Production Conference (EDPC), pp 1-4, 2014.

Magnetic Field Emission Comparison at Different Quality Factors with Series-Parallel Compensation Network for Wireless Power Transfer to Vehicles

Tushar Batra and Erik Schaltz
Department of Energy Technology
Aalborg University
Aalborg, Denmark
tba@et.aau.dk, esc@et.aau.dk

***Abstract*— Input current of wireless power transfer system is limited by current rating of power converter on the primary side. Power rating of wireless power transfer system increases linearly with the quality factor for series-parallel topology of the system at a given primary current. Magnetic emissions to the surroundings also increase with increase in the quality factor. In this paper, first analytical expressions are developed for comparing magnetic emissions at different quality factors. Theoretical and simulation (Comsol) results show comparatively lower increase for the magnetic field emissions to the linear increase in the power rating with the quality factor. This paper signifies that at fixed primary current, operation of wireless power transfer system at higher quality factor is favorable with respect to the magnetic emissions.**

Keywords-Inductive Power Transfer, magnetic fields, resonance.

I. INTRODUCTION

Energy in the medium power range can be transferred without wires over a large air gap using different scientific principles [1]. The frontrunners in this power transfer are inductive coupling, resonant inductive coupling and capacitive coupling. The first two utilize same principle of electromagnetic induction for the power transfer but differ in size of the air gap and electrical circuitry. The last one on the other hand utilizes totally a different physics and is not under consideration. This paper is based on resonant induction coupling (RIPT) and hence the term wireless power transfer (WPT) is synonymous with RIPT. A simple block diagram of the system is provided below in Fig. 1.

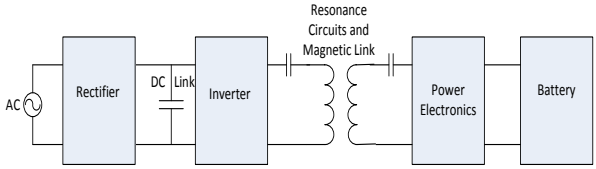

Fig. 1. Block diagram wireless power transfer [2]

Voltage source converter on the primary side rectifies the grid voltage and then inverts to produce square wave input voltage. Resonant circuits comprising of the primary capacitors and inductors allow the first harmonic currents of the switching frequency to prevail. The primary and secondary capacitors are designed to provide unity power factor and boost power transfer capability of the system at the resonant frequency.

Power electronics on the secondary side is used to control [3] flow of power to the battery of the vehicle by controlling the secondary side quality factor. The primary current is held constant for the power on the secondary side to be controlled linearly with the quality factor. Magnetic emissions [4] to surroundings are an important design criterion for WPT and do not change linearly with the quality factor. Firstly, theoretical expressions for variations in the magnetic emissions with the quality factor are developed in this paper. It is shown with help of theory and simulations that a higher quality factor is better from viewpoint of the magnetic emissions at constant primary current. A parallel publication discussing the same topic for series-series topology WPT was presented by the same authors in [5].

II. SAMPLE GEOMETRY

Sample geometry [2] [5] [6] used in the paper is provided in Fig. 2. Specifications for perfectly aligned identical inductors are provided in Table I.

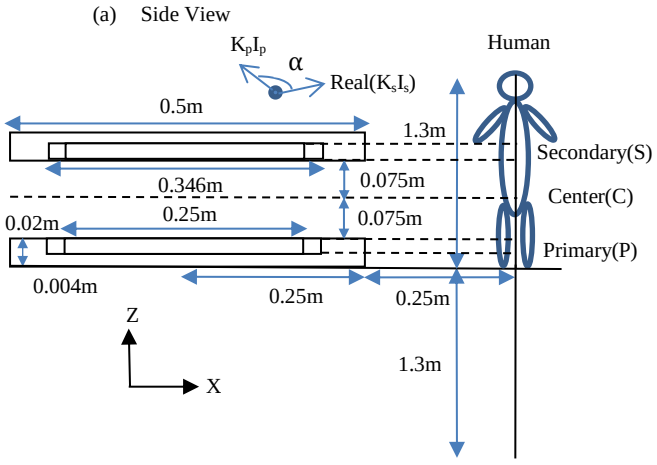

The work has financially been supported by The Danish Council for Strategic Research.

978-1-4799-5009-6/14/$31.00 ©2014 IEEE

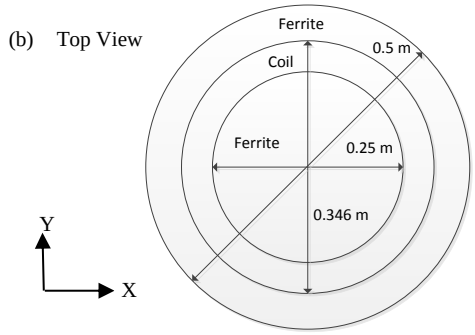

Fig. 2. Sample geometry [2] [5] [6]

TABLE I. INDUCTOR SPECIFICATION [5] [6]

Property	Value
Number of parallel conductors in each turn	810
Diameter of parallel conductor	0.1 mm
Outer diameter of coil	4 mm
Conductivity of conductor	6×10^7 (S/m)
Relative permeability of ferrite	2300

III. SERIES-PARALLEL COMPENSATION NETWORK

As mentioned in the introduction section that only the first harmonic currents are effective in the system, hence fundamental mode analysis [7] equivalent circuit is used and is provided in Fig. 3. The secondary side power electronics along with the load is approximated by a resistor. Moreover, the resistance of the coils and magnetic loss resistance are much smaller as compared to the load resistance and are neglected for the theoretical analysis.

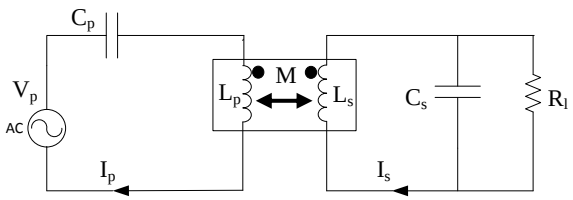

Fig. 3. Fundamental mode analysis equivalent circuit [6]

Symbols used in the paper are provided in Table II.

TABLE II. SYMBOLS [5]

Symbol	Name		Symbol	Name
I_p	Primary current		I_s	Secondary current
V_p	Primary voltage		M	Mutual inductance
L_p	Primary self-inductance		L_s	Secondary self-inductance
C_p	Primary capacitor		C_s	Secondary capacitor
R_l	Load resistance		Q	Quality factor
w	Angular frequency		w_r	Resonance angular frequency

Expressions for the voltage equations, resonance frequency, primary capacitor [8] and quality factor are provided in (1) to (5).

$$\left(jwL_p+\frac{1}{jwC_p}\right)I_p - jwMI_s = V_p \tag{1}$$

$$jwMI_p=\left(jwL_s+\frac{\frac{1}{jwC_s}R_p}{R_p+\frac{1}{jwC_s}}\right)I_{1s} \tag{2}$$

$$w_r=\frac{1}{\sqrt{L_sC_s}} \tag{3}$$

$$C_p=\frac{L_s}{(L_pL_s-M^2)w_r^2} \tag{4}$$

$$Q=\frac{R_l}{w_rL_s} \tag{5}$$

(1) and (2) using (3), (4) and (5) are modified to

$$V_p=\frac{w_rM^2}{L_s}QI_p \tag{6}$$

$$I_s=\frac{M}{L_s}(1+jQ)\,I_p. \tag{7}$$

Input power (P) of the system using (6) is

$$P=\frac{w_rM^2}{L_s}QI_p^2. \tag{8}$$

Due to the large air gap in WPT, operation is always in linear region [9] of B-H curve for ferrite. As a result for any point in the surroundings, coil magnetic fields ($B_{p,s}$) are proportional to their respective currents.

$$|B_{p,s}|=K_{p,s}|I_{p,s}| \tag{9}$$

$K_{p,s}$ are constants for a given point in the space for the primary and secondary coils. Rms magnetic field using (7), (9) and space angle α from Fig. 2 is given by

$$|B|=I_p\sqrt{\left[K_p{}^2+\left(K_s\frac{M}{L_s}\right)^2+2K_pK_s\frac{M}{L_s}\cos\alpha\right]+\left(K_s\frac{M}{L_S}Q\right)^2}\,. \tag{10}$$

$K_{p,s}$ varies for different points in space but their ratio is fairly constant and along with space angle is provided in the results section. This constant behavior can be used to obtain magnetic emissions ratio (K) of rms magnetic fields (B_a and B_b) using (10) at two different quality factors (Q_a and Q_b).

$$K=\frac{|B_a|}{|B_b|}=\frac{I_{pa}\sqrt{\left[1+\left(\frac{K_sM}{K_pL_s}\right)^2+2\frac{K_sM}{K_pL_s}\cos\alpha\right]+\left(\frac{K_sM}{K_pL_S}Q_a\right)^2}}{I_{pb}\sqrt{\left[1+\left(\frac{K_sM}{K_pL_s}\right)^2+2\frac{K_sM}{K_pL_s}\cos\alpha\right]+\left(\frac{K_sM}{K_pL_S}Q_b\right)^2}} \tag{11}$$

The currents are taken as equal as the study is based on constant primary current and hence (11) is modified to (12)

$$K=\frac{|B_a|}{|B_b|}=\frac{\sqrt{\left[1+\left(\frac{K_sM}{K_pL_s}\right)^2+2\frac{K_sM}{K_pL_s}\cos\alpha\right]+\left(\frac{K_sM}{K_pL_S}Q_a\right)^2}}{\sqrt{\left[1+\left(\frac{K_sM}{K_pL_s}\right)^2+2\frac{K_sM}{K_pL_s}\cos\alpha\right]+\left(\frac{K_sM}{K_pL_S}Q_b\right)^2}}. \tag{12}$$

Also, ratio of power (P_a and P_b) using (8) is

$$\frac{P_a}{P_b}=\frac{Q_a}{Q_b}. \tag{13}$$

An initial assumption is taken as

$$Q_a > Q_b. \tag{14}$$

Squaring both sides, first multiplying and then adding similar term on both sides and rearranging,

$$Q_a^2\left[1+\left(\frac{K_s M}{K_p L_s}\right)^2+2\frac{K_s}{K_p}\frac{M}{L_s}\cos\alpha\right]+\left(\frac{M K_s}{L_S K_p}Q_a Q_b\right)^2 >$$

$$Q_b^2\left[1+\left(\frac{K_s M}{K_p L_s}\right)^2+2\frac{K_s}{K_p}\frac{M}{L_s}\cos\alpha\right]+\left(\frac{M K_s}{L_S K_p}Q_a Q_b\right)^2. \tag{15}$$

$$\frac{Q_a}{Q_b} > \frac{\sqrt{\left[1+\left(\frac{K_s M}{K_p L_s}\right)^2+2\frac{K_s M}{K_p L_s}\cos\alpha\right]+\left(\frac{K_s M}{K_p L_S}Q_a\right)^2}}{\sqrt{\left[1+\left(\frac{K_s M}{K_p L_s}\right)^2+2\frac{K_s M}{K_p L_s}\cos\alpha\right]+\left(\frac{K_s M}{K_p L_S}Q_b\right)^2}}. \tag{16}$$

Comparing (12), (13) and (16),

$$\frac{P_a}{P_b} > \frac{|B_a|}{|B_b|}. \tag{17}$$

It can be seen in (17) that the linear increase of power is more than corresponding rise in the emissions for increasing quality factor.

IV. Results

A. Space angle α

Magnetic field directions for the set of inductors using Comsol are presented in Fig. 4.

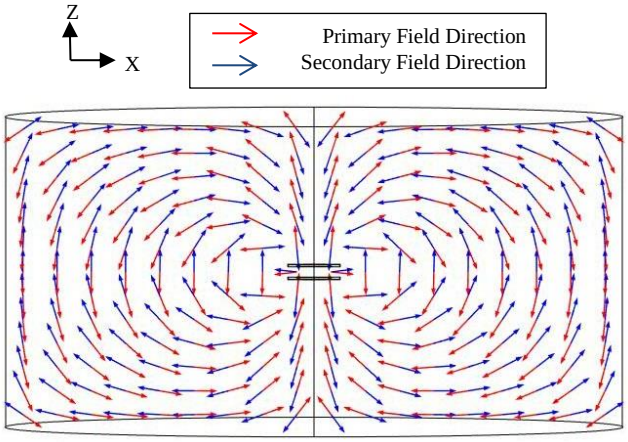

Fig. 4. Magnetic field directions [6]

The angle is 180° for nearly all points in the space. The value is different from this for points very close to the inductors as shown in Fig. 4 and is ignored for this study. (12) is modified to (18) using space angle equal to 180°.

$$K = \frac{\sqrt{\left(1-\frac{K_s M}{K_p L_s}\right)^2+\left(\frac{K_s M}{K_p L_S}Q_a\right)^2}}{\sqrt{\left(1-\frac{K_s M}{K_p L_s}\right)^2+\left(\frac{K_s M}{K_p L_S}Q_b\right)^2}} \tag{18}$$

B. Ratio K_s/K_p

Ratio K_s/K_p is provided in (19) and is obtained using (9).

$$\frac{K_s}{K_p} = \frac{|B_s|}{|B_p|} \tag{19}$$

No-load simulation tests [2] [5] [6] on Comsol with 23A rms at 20 kHz current are carried out and the results are provided in Fig. 5 and 6. Ferrite has an effect of displacing space maxima's and has already been discussed by the same authors in [2]. The ratio is fairly constant as one as visible in Fig. 6. Also K_s and K_p are proportional to number of primary and secondary turns and changing number of turns will change the ratio accordingly.

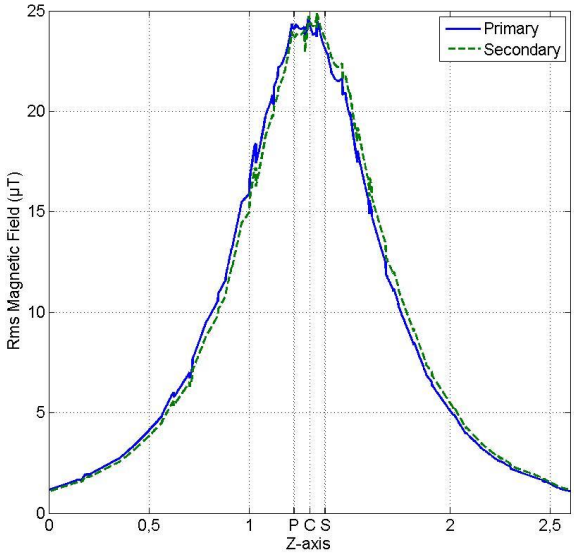

Fig. 5. Rms magnetic field (μT) versus Z-axis – No-load [5]

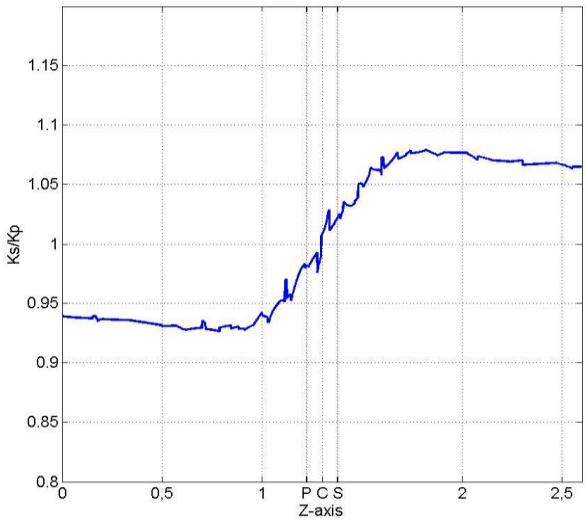

Fig. 6. Ratio Ks/K_p versus Z-axis – No-load [5]

C. Ratio K

On-load simulations are done on Comsol for quality factors from 4 to 10. The magnetic emissions for vertical line of Fig. 2(a) in matrix form are taken in Matlab. Simulated ratio K is obtained by dividing the magnetic emissions w.r.t base magnetic emissions at Q=4. Theoretical values of ratio K on the other hand are obtained from (18) using ratio K_s/K_p from Fig. 6. The two results for ratio K and rms magnetic field for simulations are provided in Fig. 7 and 8 respectively.

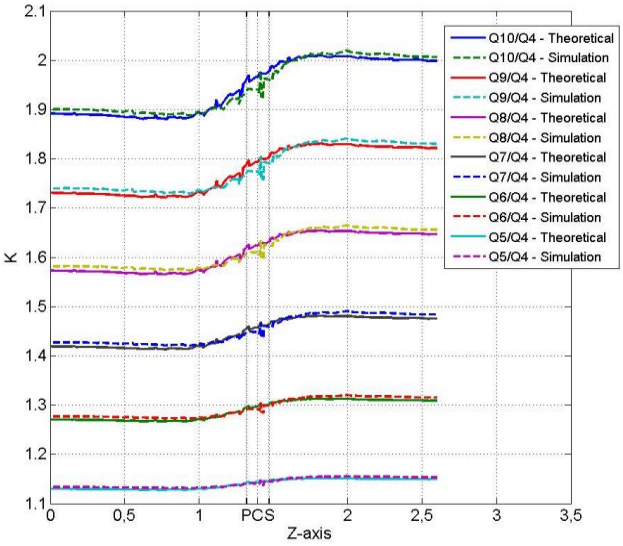

Fig. 7. Ratio K versus Z-axis – On-load

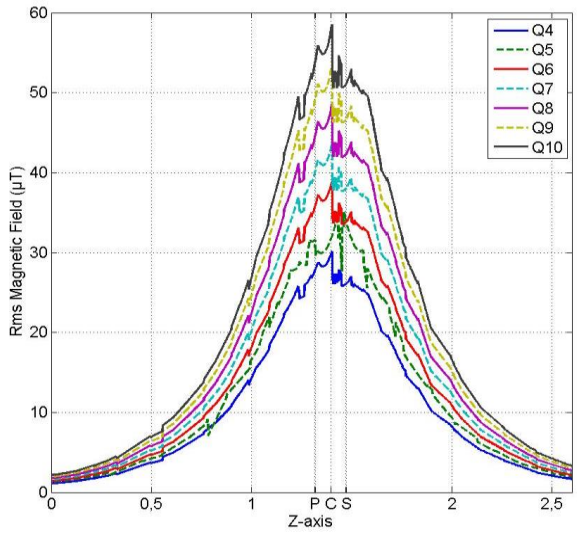

Fig. 8. Rms magnetic field (µT) verus Z-axis – On-load

Circuit parameters for on-load Comsol simulations are provided in Table III. The primary current is 23A rms at 20 kHz for all simulations.

TABLE III. CIRCUIT PARAMETERS

Q	I_s(A)	V_p(V)	P(W)=V_p*I_p
4	5.24+j20.12	82.84+j0.56	1905.32
5	5.36+j25.10	103.18+j0.06	2373.14
6	5.51+j30.07	123.44-j0.56	2839.12
7	5.69+j35.01	143.62-j1.30	3303.26
8	5.90+j39.94	163.73-j2.16	3765.79
9	6.14+j44.85	183.76-j3.13	4226.48
10	6.41+49.74	203.71-j4.23	4685.33

Ratio K has good compliment for the two results. Moreover, ratio K has small deviation on both sides from value at center (C). This deviation is reflected in ratio K from ratio K_s/K_p as visible in Fig. 6. If the deviation is ignored (K_s/K_p=1), ratio K can be calculated as a single number. This is a good advantage for initial system design and is most applicable to zone (at and close to C) of highest magnetic fields. Also the input power increases linearly with the quality factor as shown in Table III. Therefore for a constant primary current, the magnetic emissions have a comparatively lower increase as compared to the input power with the increasing quality factor.

V. CONCLUSION

Magnetic emissions are a significant design criterion for wireless power transfer systems. A higher quality factor operation enables more power to be transferred on the secondary side but also increases the magnetic emissions to the surroundings. In this paper, theoretical expressions for variations in the magnetic emissions with the quality factor are first developed and are later substantiated with simulations. Results show that the input power increases linearly with the quality factor whereas on the other hand magnetic emissions show a lower increase with the quality factor. Hence, higher quality factor operation is favorable from viewpoint of the magnetic emissions for constant primary current for series-parallel topology wireless power transfer system.

REFERENCES

[1] F. Musavi, M. Edington, and W. Eberle, "Wireless power transfer: A survey of EV battery charging technologies," Proceedings of Energy Conversion Congress and Exposition (ECCE 2012), pp. 1804-1810, 15-20 Sept. 2012.

[2] T. Batra, E. Schaltz, "Magnetic Field Emissions for Ferrite and Non-Ferrite Geometries for Wireless Power Transfer to Vehicles", Journal of Applied Physics, vol. 115, no. 17, pp. 17E715 - 17E715-3, 2014.

[3] G. A. Covic, J. T. Boys, "Modern Trends in Inductive Power Transfer for Transportation Applications," IEEE Journal of Emerging and Selected Topics in Power Electronics, vol 1., no 1., pp. 28-41, 2013.

[4] J. Kim, J. Kim, S. Kong, H. Kim, I. S. Suh, N. P. Suh, D. H. Sho, "et al." ,"Coil Design and Shielding Methods for MagneticResonant Wireless Po wer Transfer System", Proceedings of the IEEE , vol. 101, no. 6, pp. 1332-1342, 2013

[5] T. Batra, E. Schaltz, "Magnetic Field Emission Comparison at Different Quality Factors with Series-Series Compensation Network for Inductive Power Transfer to Vehicles", Proceedings of Wireless Power Transfer Conference (WPTC 2014) – In Press.

[6] T. Batra, E. Schaltz, "Magnetic Emissions Reduction by Varying Secondary Side Capacitor for Ferrite Geometry based Series-Parallel Topology Wireless Power Transfer to Vehicles", Proceedings of PCIM Europe Conference 2014 – In Press.

[7] M. G. Egan, D. L. O'Sullivan, J. G. Hayes, S. E. Schulz, J. T. Hall, "Power-Factor-Corrected Single-Stage Inductive Charger for Electric Vehicle Batteries," IEEE Transactions on Industrial Electronics, vol. 54, no. 2, pp. 1217-1226, 2007.

[8] W. Chwei-Sen, O. H. Stielau, and G. A. Covic, "Design considerations for a contactless electric vehicle battery charger," IEEE Transactions on Industrial Electronics, vol. 52, no. 5, pp. 1308-1314, 2005.

[9] M. Budhia, G. A. Covic, J. T. Boys, "Design and Optimization of Circular Magnetic Structures for Lumped Inductive Power Transfer Systems," IEEE Transactions On Power Electronics, vol 26., no 11., pp. 3096-3108, 2011.

5.3.4. PhD paper 6 – Experimental verification

This section provides experimental verification of paper {6}. This paper provides similar results for SP topology as are provided for SS topology in paper {5}. It has first been shown that for SP topology at given inverter current and switching frequency the emissions increase relatively lower than the output power with linearly increase load quality factor. The last statement has been proved mathematically as Equation (16, 18) in PhD paper {6} and the final result is provided here as (43).

$$\frac{Q_2}{Q_1} > \frac{\sqrt{\left(1-\frac{K_s}{K_p}\frac{M}{L_s}\right)^2+\left(\frac{K_s}{K_p}\frac{M}{L_s}Q_2\right)^2}}{\sqrt{\left(1-\frac{K_s}{K_p}\frac{M}{L_s}\right)^2+\left(\frac{K_s}{K_p}\frac{M}{L_s}Q_1\right)^2}} \tag{43}$$

The second objective of this section is to provide verification of the theoretical emissions ratio (41) with experimental calculated emissions ratio. The results are presented only for Configuration 2 at switching frequency of 26.3 kHz. The emissions, emissions ratio and electric quantities are presented at two different quality factors at horizontal distance (H=0.5 m) in Figure 30. The experimental and analytical calculations for this verification are provided in Table 15.

Table 15. Configuration 2 results

x	R_{lx} (Ω)	Q_{lx}/Q_{l1}	P_l (W)	P_l ratio*	Emissions ratio*, **	Analytical emissions ratio*
1	327.6	1	1215.31	1	1	1
2	418.8	1.28	1524.49	1.25	1.12	1.183

*@Q_{lx}/Q_{l1}

** Approximated central value using Figure 30

5.3.4.1. Discussion

The following observations are made from the results.

1) As required, the two currents are nearly 90˚ apart and input power factor is close to one as shown in Figure 30.

2) Both the objectives i.e. the two emissions ratios are in good compliment and increase in the output power is higher than increase in the emissions have been verified.

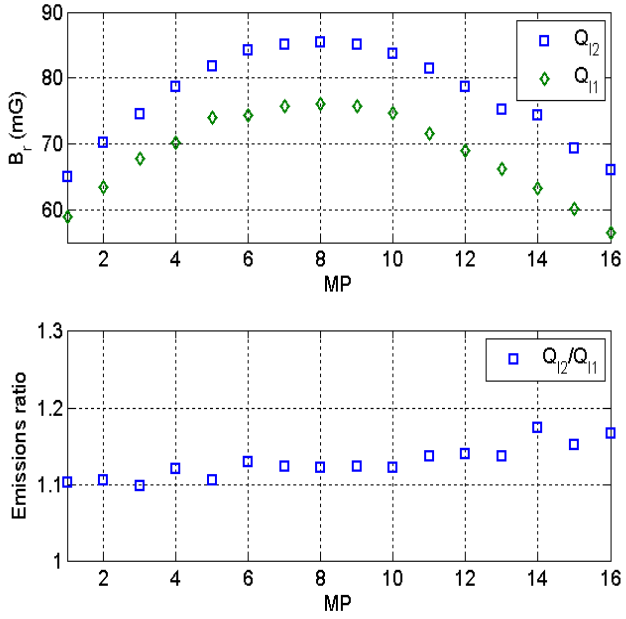

(a) Emissions and emissions ratio

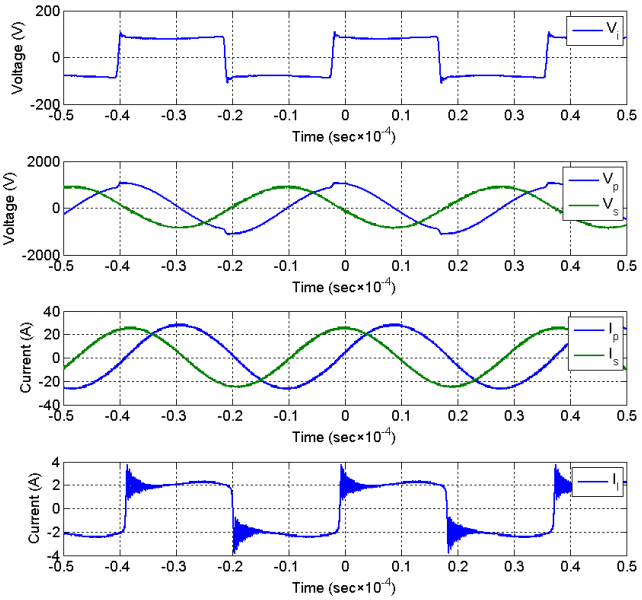

(b) Electrical quantities at Q_{l1}

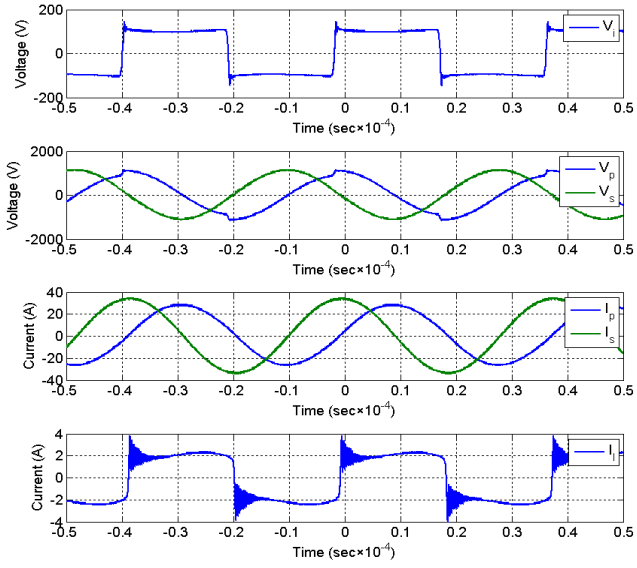

(c) Electrical quantities at Q_{l2}

Figure 30. Configuration 2 results

5.4. Application 2

Active shielding is used in addition to the passive shielding in the inductors to further suppress magnetic emissions in the surroundings. Traditionally in active shielding, an additional coil having separate power supply is used to generate magnetic field in phase opposition to one of the coil field of wireless charging inductors. This method was improved in [20] by removing requirement of additional power supply by powering the active shielding coil from the primary coil of wireless charging system. In this project, an improved version of this technology has been introduced by generating cancellation currents in the secondary coil rather than using an additional active shielding coil. The cancellation method is introduced in PhD papers {7} and {8} for SS and SP topologies in Section 5.4.1 and 5.4.3 respectively. The cancellation is made feasible by increasing the secondary capacitor value from resonance value and hence increasing value of the secondary circuit component in phase with the primary current. This increase leads to cancellation of the primary field by the secondary field as explained in detail with help of the semi-analytical method in papers {7} and {8}. The theory is supported with FEM results for the proposed cancellation method in the papers. Additionally, experimental verification of the method is provided for paper {7} in Section 5.4.2.

5.4.1. PhD paper 7

This paper was originally published with following details.

{7} T. Batra, E. Schaltz, S. Ahn, “Reduction of magnetic emission by increasing secondary side capacitor for ferrite geometry based series-series topology for wireless power transfer to vehicles", Proceedings of 16th European Conference on Power Electronics and Applications (EPE'14-ECCE Europe), pp 1-11, 2014.

Reduction of Magnetic Emission by Increasing Secondary Side Capacitor for Ferrite Geometry based Series-Series Topology for Wireless Power Transfer to Vehicles

Tushar Batra[1], Erik Schaltz[1] and Seungyoung Ahn[2]
Aalborg University[1] and Korea Advanced Institute of Science and Technology[2]
Pontoppidanstraede 101[1] and 373-1 Guseong-dong, Yuseong-gu[2]
Aalborg, Denmark[1] and Daejeon, South Korea[2]
Tel.: +45 – 9168.09.38.
E-Mail: tba@et.aau.dk, esc@et.aau.dk and sahn@kaist.ac.kr
URL: http://www.et.aau.dk/ and http://emc.kaist.ac.kr/

Acknowledgements

This work has financially been supported by The Danish Council for Strategic Research.

Keywords

« Wireless power transmission», « Resonant converter», « Electric vehicle ».

Abstract

Magnetic fields emitted by wireless power transfer to vehicles can potentially affect living organisms. As a result, minimizing the magnetic emissions without compromising with the power transferred is one of the most significant challenges in the success of this technology. Active and passive shielding methods are used for screening of the magnetic fields of this system. In this paper, a new active shielding design method for series-series topology of this technology has been presented. In this method, the secondary capacitor value is increased to reduce phase angle between the primary and secondary currents from the standard design. Therefore, a part of the secondary magnetic flux comes in phase opposition with the primary flux and the resultant field is reduced. Operation point is shifted with the new design from the maximum power transfer resonance point and hence the reflected resistance is reduced. In order to maintain the same power level, the primary current and voltage have to increased and decreased in the same proportion. Also, the primary capacitor needs to be increased for maintaining unity input power factor in the system. The above statements are provided first with help of analytical expressions and later substantiated with simulations. At the end, it is also shown that resonance in the system is still intact with this new design methodology.

Introduction

Wireless power transfer (WPT) in both stationary [1] and on-line [2] charging forms is set to revolutionize world of electric vehicles (EV). Charging without wires would be critical in solving problems of lower available energy in the battery of EV and uncomfortable hanging cables from the wired charging solution. But the wireless solution also has its set of problems mostly in the form of the magnetic field emissions to the surroundings that can harm living organisms. This paper is focused on the magnetic emissions of WPT and will be discussed after a brief description of the system. A block diagram of WPT system is provided below in Fig. 1.

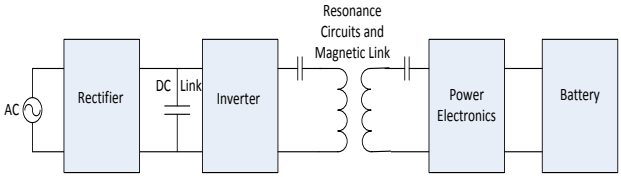

Fig. 1: Block diagram WPT system [3]

The supply voltage in the system is rectified and fed to the DC link capacitor of the resonant converter. This enables high frequency square waveform input voltage to the system. The resonant circuit filters the primary and secondary currents to sinusoidal of the fundamental component. Energy is transferred from the primary coil to the secondary coil in WPT using same principle of electromagnetic induction as in classical transformer. The major difference between the two systems is presence of a large air gap between the two coils of WPT. This large air gap results in high self-inductance for the two coils and hence capacitors are required on both sides for compensation. The primary side capacitor [4] is mainly responsible for unity input power factor operation and the secondary capacitor is used to boost the power transfer capability of the system. The secondary side compensation shifts the primary and secondary fluxes orthogonal to each other. And as a result there is no cancellation in phasor addition of the two coil fluxes.

Magnetic field shielding in the system is done by means of active and passive methods [5]. In passive shielding, the magnetic field is reduced by a combination of blocking properties of low resistivity metals like aluminum and low magnetic resistance path using magnetic materials like ferrite. Active shielding on the other hand is cancellation by introducing additional field in opposite direction to the main field. Major disadvantage with the active shielding is the requirement of additional components (power supply and third coil) in the system. Problem of additional power supply was solved by KAIST researchers by proposing Resonant Reactive Current Loop [6] method. But still this method requires an additional third coil for reducing the magnetic emissions.

In this paper a new design methodology for reducing the magnetic emissions of series-series topology WPT. Advantage of the proposed design is that it requires no additional components to be added to the system. In the new design, the secondary capacitor value is increased to lower phase angle between the primary and secondary currents from standard design [4] value. This enables a part of the secondary flux to oppose the primary flux and reduce the resultant field. The reduction first increases with the increasing secondary capacitor and then starts to decrease again. This offset from the secondary resonance point reduces the power transfer capability of the system. The primary current and voltage have to be increased and decreased in similar proportion to maintain same input power. Also an additional capacitive component is reflected on the primary side with the new design and hence the primary capacitor has to be increased to maintain unity power factor. As the primary capacitor and primary self-inductance are mainly responsible for the filter behavior of the system, the resonance in the system is maintained. Theoretical expressions are first presented in this paper for the above statements and are later supported with simulations. A similar new design methodology was also presented by the authors for series-parallel topology WPT in [7]. This new design can be used together with the existing active and passive shielding methods to reduce the magnetic emissions of the system.

Sample geometry

Sample geometry similar to one in [3] [7] is used in the paper. Top and side views of the geometry are provided in Fig. 2.

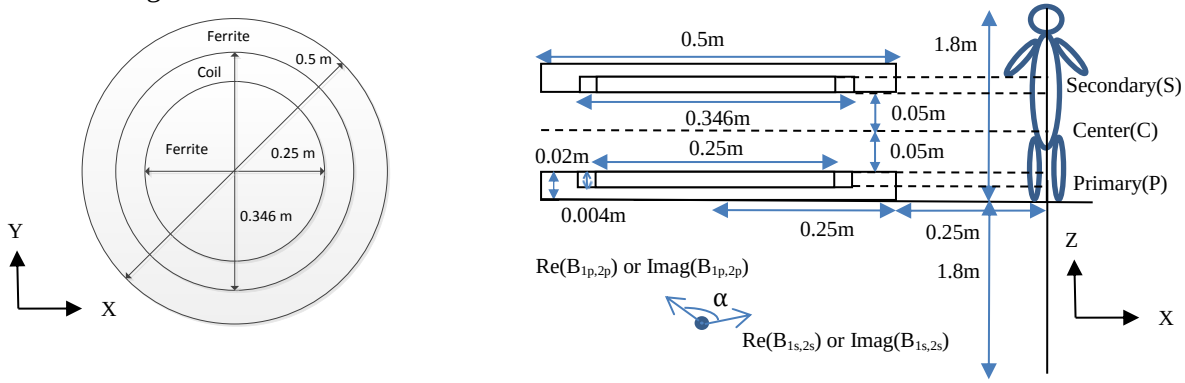

Fig. 2: Top and side views sample geometry [7]

The coil made of Litz wire is embedded in a ferrite disc. The two inductors are identical and centered (aligned case) at the same point. Results for another case (misaligned) where the upper inductor is shifted horizontally by 10 cm in the positive X-direction towards the human are also provided in the

paper. The self and mutual inductances for the aligned case are 157 µH and 60 µH. For the non-aligned case, value of the mutual inductance becomes 38 µH while the value of self-inductance practically remains unchanged. Detail of the inductor is provided below in Table I.

Table I: Details of inductor [8]

Property	Number of turns	Number of parallel conductor	Conductor diameter	Coil outer diameter	Conductor conductivity	Relative permeability ferrite
Value	12	810	0.1 mm	4 mm	6×10^7 (S/m)	2300

Theory

Standard design

Fundamental Mode Analysis (FMA) [9] equivalent circuit for the topology is provided in Fig. 3.

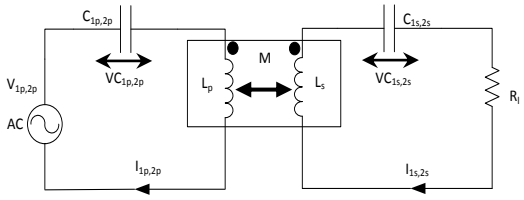

Fig. 3: FMA equivalent circuit series-series topology

The equivalent circuit is same for the two designs. Subscripts 1 and 2 are used to denote the standard and proposed designs. Also the subscripts p and s are used for denoting the primary and secondary sides of the system respectively. The inductors (L_p, L_s and M), load resistor (R_l) and quality factor (Q) are same for the two designs. The voltage equations, resonant frequency and Q for the system are provided in (1) to (4).

$$\left(j\omega L_p+\frac{1}{j\omega C_{1p,2p}}\right)I_{1p}-j\omega MI_{1s,2s}=V_{1p,2p} \tag{1}$$

$$\left(j\omega L_s+\frac{1}{j\omega C_{1s,2s}}\right)I_{1s,2s}+R_lI_{1s,2s}=j\omega MI_{1p,2p} \tag{2}$$

$$\omega_r=\frac{1}{\sqrt{L_pC_{1p}}}=\frac{1}{\sqrt{L_sC_{1s}}} \tag{3}$$

$$Q=\frac{\omega_rL_s}{R_l} \tag{4}$$

Inserting (3) and (4) into (1) and (2), (5) and (6) are obtained

$$V_{1p}=\frac{\omega_rM^2}{L_s}QI_{1p} \tag{5}$$

$$I_{1s}=j\frac{M}{L_s}Q\,I_{1p}. \tag{6}$$

The magnetic field path for WPT is dominantly air and hence maximum magnetic field strength in ferrite core is much lower than saturation value of ferrite. Hence the non-linear part of the B-H curve is not reached and the magnetic fields ($B_{1p,2p}$ and $B_{1s,2s}$) are proportional by the constants (K_p and K_s) to their respective coil currents. It can be expressed in equation form as

$$B_{1p,2p}=K_pI_{1p,2p} \tag{7}$$

$$B_{1s,2s}=K_sI_{1s,2s}. \tag{8}$$

Real (Re) and imaginary (Imag) parts of the resultant magnetic fields ($B_{1,2}$) is vector sum of the two coil fields with space angle α between them as shown in Fig.2 and is provided in (9) and (10).

$$\mathrm{Re}(B_{1,2}) = \sqrt{\left(\mathrm{Re}(B_{1p,2p})\right)^2 + \left(\mathrm{Re}(B_{1s,2s})\right)^2 + 2\mathrm{Re}(B_{1p,2p})\mathrm{Re}(B_{1s,2s})\cos\alpha} \quad (9)$$

$$\mathrm{Imag}(B_{1,2}) = \sqrt{\left(\mathrm{Imag}(B_{1p,2p})\right)^2 + \left(\mathrm{Imag}(B_{1s,2s})\right)^2 + 2\mathrm{Imag}(B_{1p,2p})\mathrm{Imag}(B_{1s,2s})\cos\alpha} \quad (10)$$

Magnitude of resultant magnetic field (B_1) using (6), (7), (8), (9), (10) and I_{1p} as reference phasor is

$$|B_1| = I_{1p}\sqrt{K_p{}^2 + \left(K_s Q \frac{M}{L_S}\right)^2}. \quad (11)$$

New proposed design

The secondary capacitor of the standard design is taken as b (constant) times the proposed design capacitor.

$$C_{1s} = bC_{2s} \quad (12)$$

Inserting (3), (4) and (12) in (1) and (2), we obtain

$$V_{2p} = \left(j\omega_r L_p + \frac{1}{j\omega_r C_{2p}}\right) I_{2p} + \frac{\omega_r M^2}{L_s} \frac{Q}{\left[1+Q^2(1-b)^2\right]} \left[1 - jQ(1-b)\right] I_{2p} \quad (13)$$

$$I_{2s} = \frac{M}{L_s} \frac{Q}{\left[1+Q^2(1-b)^2\right]} \left[Q(1-b) + j\right] I_{2p}. \quad (14)$$

In order to achieve unity power factor, value of the primary capacitor is calculated by equating imaginary part of (13) equal to zero. The values of primary capacitor and primary voltage are

$$C_{2p} = \frac{1}{\omega_r{}^2 L_p \left[1 - \frac{Q^2(1-b)M^2}{L_p L_s\left(1+Q^2(1-b)^2\right)}\right]} \quad (15)$$

$$V_{2p} = \frac{\omega_r M^2}{L_s} \frac{Q}{\left[1+Q^2(1-b)^2\right]} Q I_{2p}. \quad (16)$$

Magnitude of resultant magnetic field using (7), (8), (9), (10), (14) and I_{2p} as reference phasor is given by

$$|B_2| = I_{2p}\sqrt{\left[K_p{}^2 + \left(K_s \frac{M}{L_s} \frac{Q^2(1-b)}{1+Q^2(1-b)^2}\right)^2 + 2K_p K_s \frac{M}{L_s} \frac{Q^2(1-b)}{1+Q^2(1-b)^2}\cos\alpha\right] + \left[K_s \frac{M}{L_s} \frac{Q}{1+Q^2(1-b)^2}\right]^2}. \quad (17)$$

Theoretical comparison

The reflected impedance is lowered for the proposed design for b≠1 and hence the primary current has to be increased to maintain the same input power level. Using (5) and (16),

$$\frac{I_{2p}}{I_{1p}} = \sqrt{1+Q^2(1-b)^2}. \quad (18)$$

Ratio of the primary voltage is reciprocal of ratio for the primary current. Ratio of magnetic emissions (K) for the two designs using (11), (17) and (18) is

$$K = \frac{|B_1|}{|B_2|} = \frac{\sqrt{1+\left(\frac{K_s}{K_p}\frac{M}{L_s}Q\right)^2}}{\sqrt{1+Q^2(1-b)(1-b+2\frac{K_s}{K_p}\frac{M}{L_s}\cos\alpha)+\left(\frac{K_s}{K_p}\frac{M}{L_s}Q\right)^2}}. \quad (19)$$

In order to determine ratio K space angle α and ratio K_s/K_p are required. These are provided in next section with help of simulations. Ratio of the primary capacitors is also provided in (20).

$$\frac{C_{2p}}{C_{1p}} = \frac{1}{1 - \frac{M^2}{L_p L_s}\frac{Q^2(1-b)}{\left(1+Q^2(1-b)^2\right)}} \quad (20)$$

The cost of capacitors is dependent on their capacitance value and voltage rating. Hence, voltage stress on the capacitors is an important criterion for comparing the two designs. Ratio of the voltage stresses for the primary ($VC_{1p,\ 2p}$) and secondary ($VC_{1s,\ 2s}$) capacitor using (18) and (20) are provided in (21) and (22). The magnitude of secondary current is same for both due to constant output power as losses have been neglected in the theoretical comparison.

$$\frac{VC_{2p}}{VC_{1p}}=\frac{I_{2p}}{I_{1p}}\ \frac{C_{1p}}{C_{2p}}=\sqrt{1+Q^2(1-b)^2}\left[1-\frac{M^2}{L_pL_s}\frac{Q^2(1-b)}{\left(1+Q^2(1-b)^2\right)}\right] \tag{21}$$

$$\frac{VC_{2s}}{VC_{1s}}=\frac{I_{2s}}{I_{1s}}\ \frac{C_{1s}}{C_{2s}}=\frac{C_{1s}}{C_{2s}}=b \tag{22}$$

Simulations

Space angle α

As per law of electromagnetic induction, the secondary flux opposes the primary flux. Hence value of angle α is equal to 180° except for points close to the coils as shown in Fig. 4. Humans are not supposed to be very close to the inductors and hence angle α is taken as 180° in the paper. Comsol is used to plot the figure with the coils at the center and a cylinder of 3 m radius and 3 m height serving as magnetic zero potential.

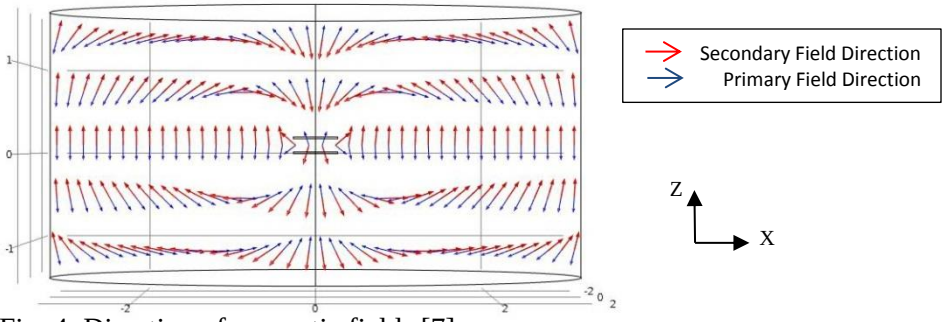

Fig. 4: Direction of magnetic fields [7]

Using angle α equal to 180°, (19) is modified to

$$K=\frac{\sqrt{1+\left(Q\frac{M}{L_S}\frac{K_s}{K_p}\right)^2}}{\sqrt{1+\left(Q^2(1-b)\left(1-b-2\frac{K_s}{K_p}\frac{M}{L_s}\right)+\left(Q\frac{K_s}{K_p}\frac{M}{L_s}\right)^2\right.}}. \tag{23}$$

Ratio K_s/K_p

Ratio K_s/K_p for the set of inductors can be obtained with help of no-load curves [3] [7] at same current (23A at 20 kHz). Using (7) and (8),

$$\frac{K_s}{K_p}=\frac{|B_s|}{|B_p|}. \tag{24}$$

The ratio K_s/K_p and rms magnetic fields for both the cases are provided in Fig. 5.

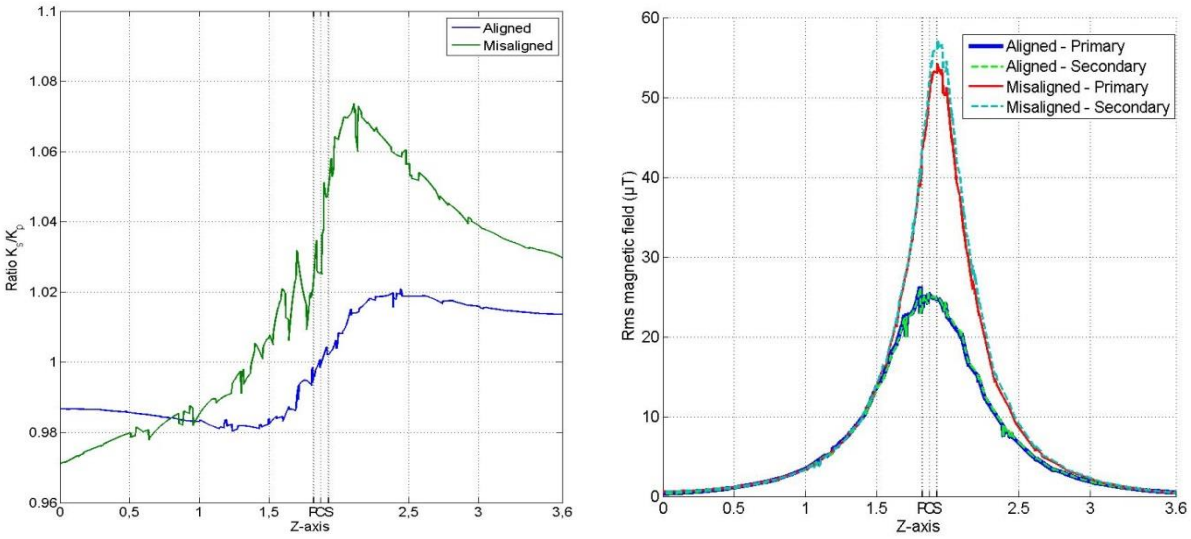

Fig. 5: Ratio K_s/K_p and rms magnetic field (μT) versus Z-axis

Ferrite has an effect of displacing space maxima's closer to each other as provided in [3]. Value of the ratio can be approximated as one for both the cases and ratio K can be calculated as a single number using (23). This is used later in section "Comparison" for calculating ratio K as a single number for given values of b.

Ratio K

Theoretical ratio K is calculated using ratio K_s/K_p from Fig. 5 and inserting in (23). On the other hand, simulated value of ratio K for the same system is obtained with help of on-load simulations on Comsol. Value of Q=6 is used for both the calculations. The frequency of operation is 20 kHz and the capacitors are calculated according to (3), (12) and (15). Firstly, values of circuit variables for the simulations are provided in Table II and III. Simulations are done using current (primary) source as input to the system. Magnitude of primary current (I_{2p}) for the proposed design is taken as constant (23 A rms) and current magnitude (I_{1p}) for standard design is calculated using (18). As an example, rms fields for standard and proposed design at b=1.42 in Fig. 8 corresponds to first row of Table III.

Table II: Circuit variables: Misaligned case

b	V_{1p}(V)	I_{1p} (A)	I_{1s} (A)	V_{2p} (V)	I_{2p} (A)	I_{2s} (A)
1.42	56.34+j0.29	8.33	-0.12+j11.82	21.31-j0.20	23	-11.09+j4.34
1.05	148.65+j0.79	21.93	-0.34+j31.18	141.14+j0.55	23	-9.58+j29.61
0.95	149.55+j0.79	22.11	-0.34+j31.39	145.15+j2.27	23	8.29+j30.45
0.769	91.05+j0.47	13.47	0.20+j19.11	55.12+j0.59	23	15.60+j11.47
0.5	49.16+j0.26	7.27	-0.11+j10.32	16.64+j0.18	23	9.91+j3.35

Table III: Circuit variables: Aligned case

b	V_{1p} (V)	I_{1p} (A)	I_{1s} (A)	V_{2p} (V)	I_{2p} (A)	I_{2s} (A)
1.42	142.71-j0.36	8.33	0.06+j18.85	53.49+j0.07	23	-17.75+j6.98
1.05	375.65-j0.95	21.93	0.15+j49.61	360.19-j2.74	23	-14.73+j47.56
0.95	378.78-j0.96	22.11	0.15+j50.03	364.89+j1.06	23	13.78+j48.19
0.769	230.64-j0.58	13.47	0.09+j30.46	137.10+j1.47	23	24.80+j18.04
0.5	124.52-j0.22	7.27	0.04+j16.45	40.76+j0.42	23	15.75+j5.30

(a) Misaligned case (b) Aligned case

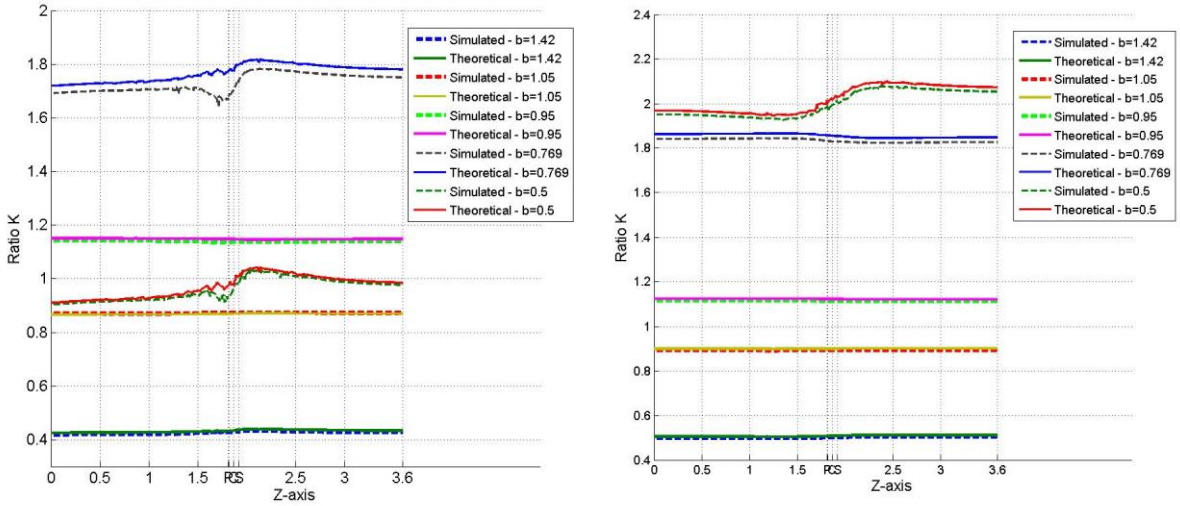

Fig. 6: Ratio K and versus Z-axis

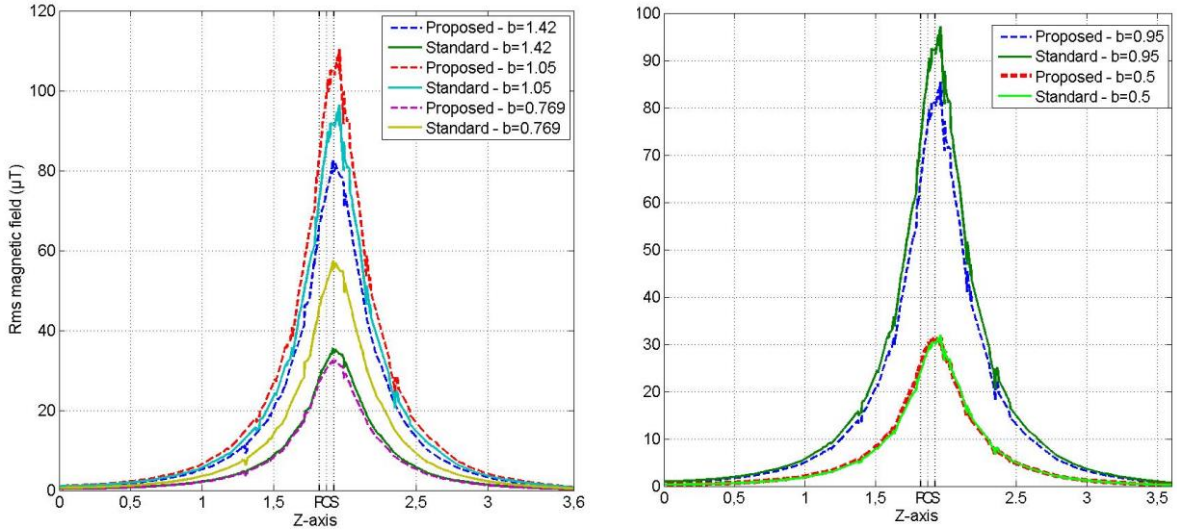

Fig. 7: Rms magnetic field (µT) versus Z-axis – Misaligned case

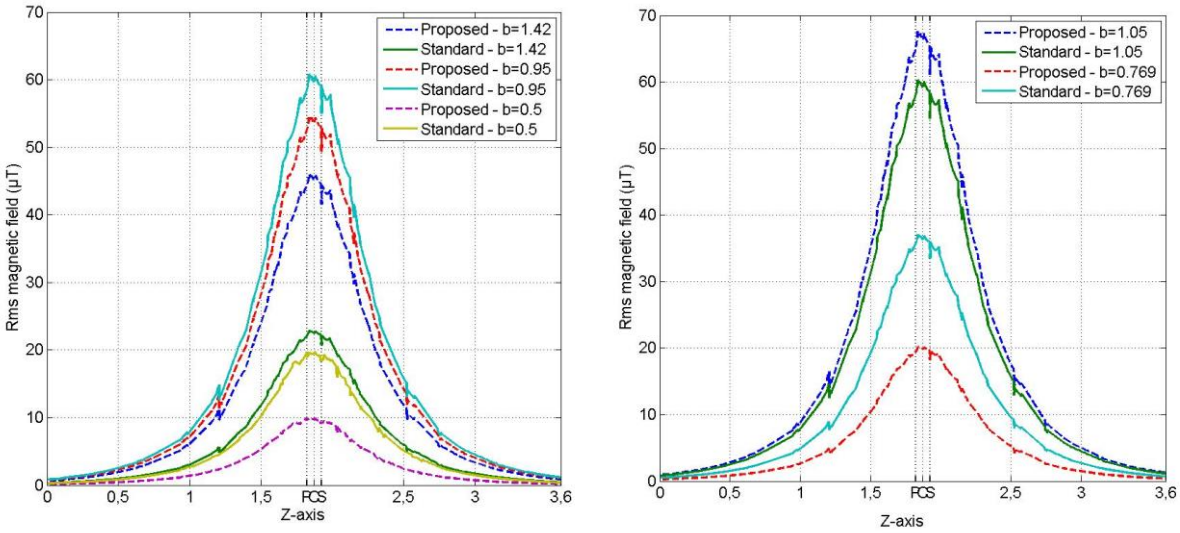

Fig. 8: Rms magnetic field (µT) versus Z-axis – Aligned case

The results for theoretical and simulated values of ratio K are in good agreement as shown in Fig. 6. Fig. 7 and 8 depict the same in terms of rms magnetic field values. The circuit variables in Table II and III are also compliant with analytical expressions provided in section "Theory".

Resonance

Resonance is maintained with the new proposed design and is shown with help of bode plots of the input impedance in Fig. 9 and 10. Using (1) and (2), the input impedance of the standard (Z_1) and proposed (Z_2) designs is provided in (25).

$$Z_{1,2}=j\omega L_p+\frac{1}{j\omega C_{1p,2p}}+\frac{\omega^2M^2}{j\omega L_s+\frac{1}{j\omega C_{1s,2s}}+R_l} \tag{25}$$

(a) (b)

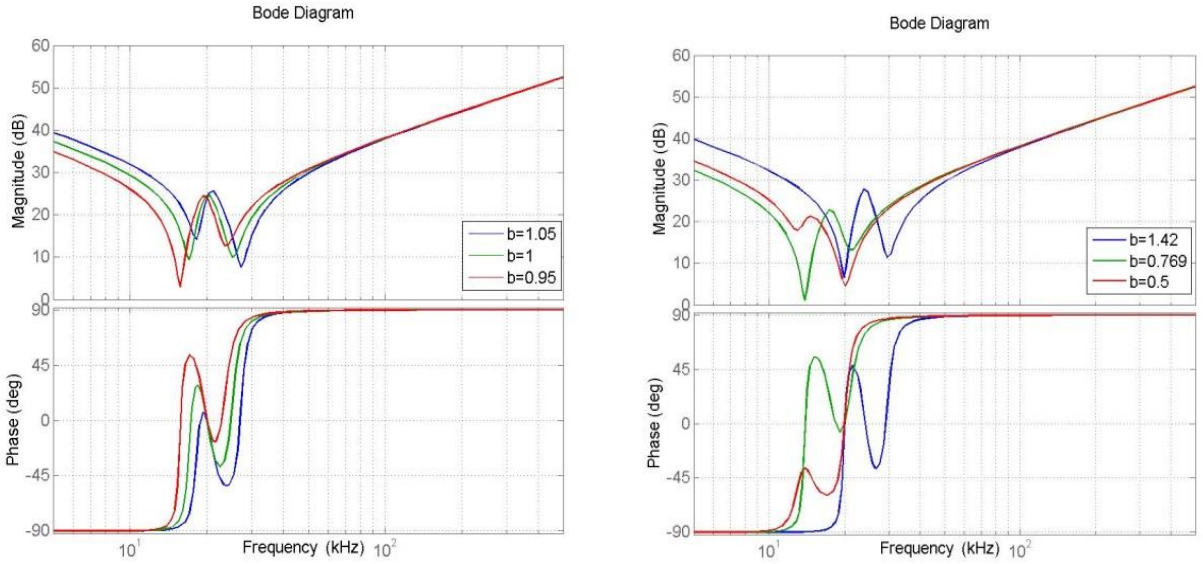

Fig. 9: Input Impedance Bode Plots – Aligned case

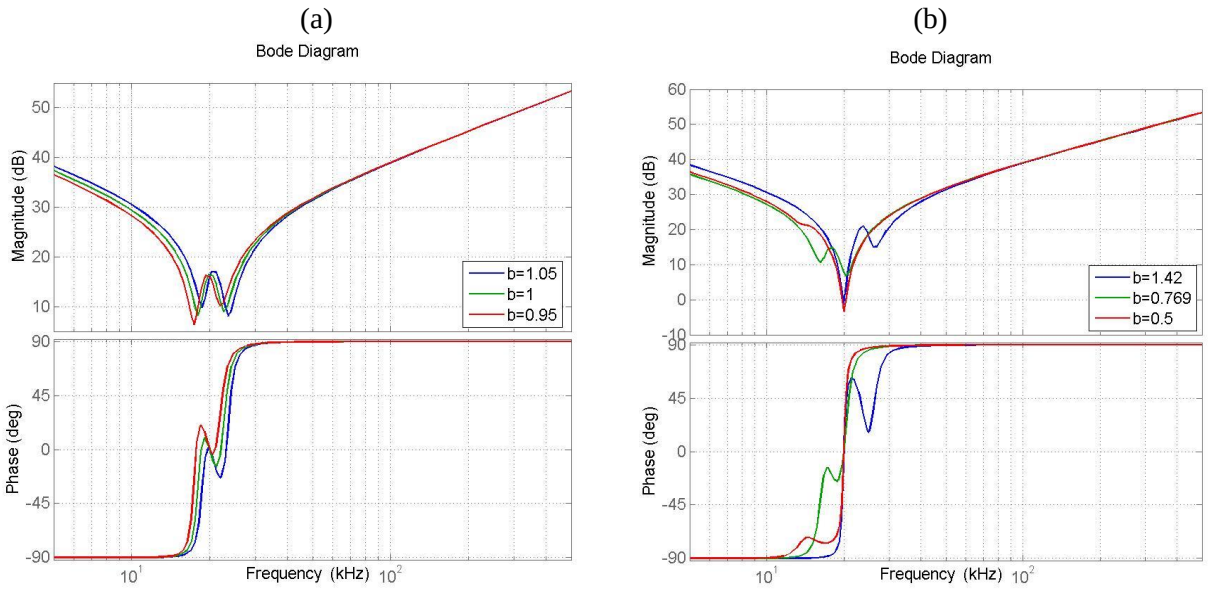

Fig. 10: Input Impedance Bode Plots – Misaligned case

The following observations are made from Fig. 9 and 10.

1) Phase angle for both the aligned and misaligned cases is zero degrees at the operational frequency (20 kHz).

2) Impedance to the higher frequencies is nearly same for different values of b for both the cases. Hence, the resonance is maintained in the system. The resonance is dominated by the primary capacitor and inductor and hence varying the secondary capacitor does not disturb the resonance of the system as proposed in the new design.

3) The new design shifts the operation from the secondary resonance point to another point. A careful examination of the (a) part of Fig. 9 and 10 shows that only for b=1, the local maximum in the magnitude plot is located exactly at the operational frequency.

Comparison

Theoretical ratios given by (18), (20), (21), (22) and (23) are plotted in Matlab to compare the two designs for b from 0 to 2. The primary current for the proposed design becomes very high beyond this range and hence this range has been selected. Results are provided for different combinations of K_s/K_p, M/L_s and Q in Fig. 11.

(a) M/L_s=0.38, K_s/K_p=1, Q=6

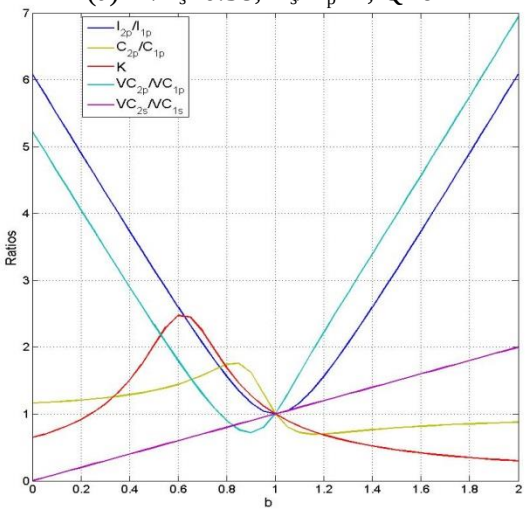

(b) M/L_s=0.21, K_s/K_p=1, Q=4

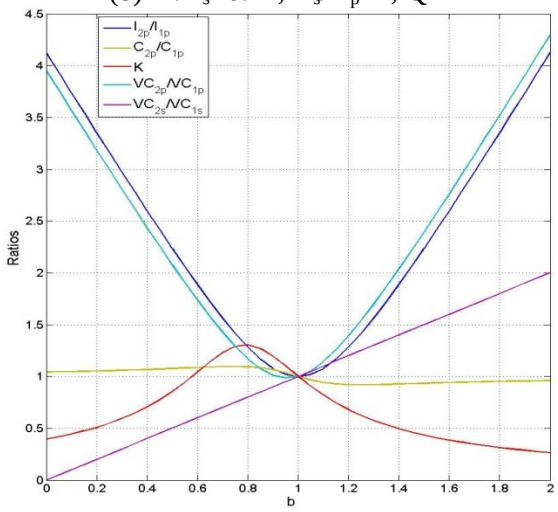

(c) M/L_s=0.19, K_s/K_p=2, Q=10

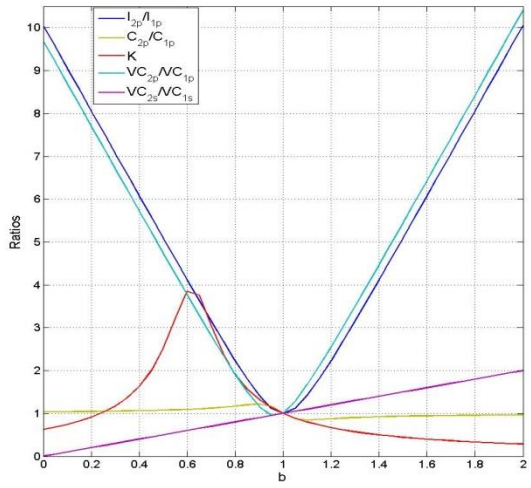

(d) M/L_s=0.19, K_s/K_p=2, Q=6

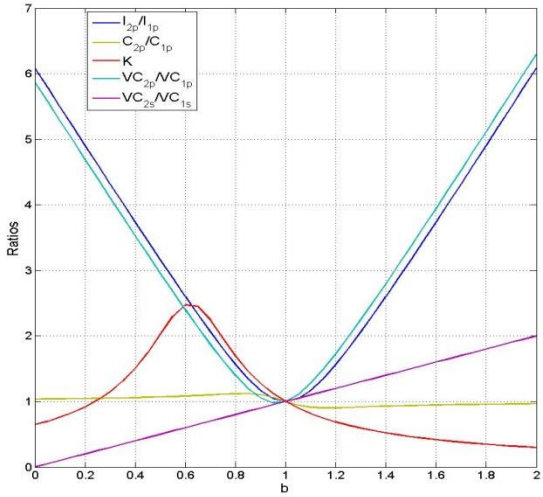

Fig. 11: Ratios for the two designs

The following points are to be noted from Fig. 11.

1) Ratio of the primary current is of parabolic nature centered at standard design (b=1). Hence if the secondary capacitor value is varied from the standard design, the primary current has to be increased to maintain the same power level. As the input power is constant, the primary voltage decreases in same proportion to the increase in the primary current.

2) The primary capacitor voltage stress ratio is product of the primary current ratio and inverse of the primary capacitor ratio as per (21). Hence, a bigger value of primary capacitor ratio than the primary current ratio ensures a lower voltage stress (VC_{2p}/VC_{1p}<1) for proposed design and vice versa. The lower voltage stress (0.8<b<1) is seen clearly shown in (a) part of Fig. 11. On the other hand, the secondary voltage stress is lower (b<1) for the proposed design as it changes linearly with b and is provided in (22).

3) Ratio K has maxima at value of b given by

$$b=1-\frac{K_s}{K_p}\frac{M}{L_s} \tag{26}$$

This can be found by differentiating (23) and equating it to zero. Point of maxima is same for (a), (c) and (d) parts as the product of K_s/K_p and M/L_s is same for them. Ratio K first increases till a maximum value and then start to decrease with the increasing secondary capacitor. Also increasing the secondary capacitor does not ensure decrease in the magnetic emissions for the proposed design as ratio K is lower than one on the left side in all parts of Fig. 11.

4) Ratio of the primary capacitor shows a similar behavior to ratio K. The maxima point can be found in a similar way using (20). It is dependent on the quality factor and is given by

$$b=1-\frac{1}{Q} \tag{27}$$

Conclusion

Secondary capacitor compensation in series-series wireless power transfer to vehicles is used to boost the power transfer capability of the system. But at the same time, it is the most favorable point for the phasor addition of the two coils magnetic fields. It is shown with help of theory and simulations that by increasing the secondary capacitor, the primary magnetic field can be cancelled to some extent by introducing an additional component in the secondary magnetic field and the resultant field can be reduced. The operation as a result shifts from the maximum power transfer point and the primary current has to be increased to maintain the same power level in the system. It is also shown that the resonance in the system is maintained with this design modification.

References

[1] Budhia M.: Design and Optimization of Circular Magnetic Structures for Lumped Inductive Power Transfer Systems, IEEE Transactions on Power Electronics, Vol. 26 no 11, pp 3096-3108

[2] Ahn S.: Magnetic Field Design for High Efficient and Low EMF Wireless Power Transfer in On-Line Electric Vehicle, EUCAP 2011, pp 3979-3982

[3] Batra T.: Magnetic Field Emissions for Ferrite and Non-Ferrite Geometries for Wireless Power Transfer to Vehicles, Journal of Applied Physics Vol. 115 no 17 pp 17E715 - 17E715-3

[4] Chwei-Sen W.: Design considerations for a contactless electric vehicle battery charger, IEEE Transactions on Industrial Electronics Vol. 52 no 5, pp 1308-1314

[5] Kim H.: Suppression of Leakage Magnetic Field from a Wireless Power Transfer System using Ferrimagnetic Material and Metallic Shielding, IEEE International Symposium on EMC 2012, pp 640-645

[6] Kim J.: Coil Design and Shielding Methods for Magnetic Resonant Wireless Power Transfer System, Proceedings of the IEEE Vol. 101 no 6, pp 1332-1342

[7] Batra T.: Magnetic Emissions Reduction by Varying Secondary Side Capacitor for Ferrite Geometry based Series-Parallel Topology Wireless Power Transfer to Vehicles, PCIM Europe 2014, In-Press

[8] Budhia M.: Development of single sided flux couplers for contactless electric vehicle charging, IEEE Transactions on Industrial Electronics, Vol. 60 no 1, pp 318-328

[9] Egan M.G.: Power-Factor-Corrected Single-Stage Inductive Charger for Electric Vehicle Batteries, IEEE Transactions on Industrial Electronics, Vol. 54 no 2, pp 1217-1226

5.4.2. PhD Paper 7 – Experimental verification

This section provides experimental verification of PhD paper {7} dealing with reduction of the emissions by increasing secondary side capacitor. The theory along with FEM simulations validation has been provided in paper {7}. In this section, experimental calculated emissions ratio is verified with proposed theoretical emissions ratio. There is a minor adjustment in the experimental verification compared to the paper {7}. The inverter current was increased in the paper to maintain constant output power with increasing secondary capacitor value. However in the experimental setup provided in Chapter 4, the inverter current is limited by DC power supplies and hence the experiments are conducted at constant inverter current and output power decreases with varying secondary capacitor. The experiments are conducted at four capacitance values other than the resonance capacitor value (152 nF) at switching frequency of 26.3 kHz for Configuration 2. The results are presented for two different values of load resistors (cases) in Section 5.4.2.1 and 5.4.2.2. The primary capacitor value has been adjusted to provide closet angle to unity power factor.

5.4.2.1. Case 1

The emissions, emissions ratio and electric quantities are presented for five secondary capacitance values (denoted by added subscript 1 to 5) at horizontal distance (H=0.5 m) in Figure 31. Exact value of the capacitors along with experimental and analytical calculations is provided in Table 16. Value of the load resistor for all the five experiments is approximately 4 Ω.

Table 16. Case 1 results

x	**C_{sx}**	**C_{px}**	**$b=C_{sx}/C_{s1}$**	**P_l (W)**	**P_l ratio***	**Emissions ratio*, ****	**Analytical emissions ratio***
1	152	152	1	1262.45	1	1	1.000
2	163	155	0.93	894.22	0.71	0.68	0.651
3	174	155	0.87	569.77	0.45	0.51	0.477
4	184	155	0.83	388.87	0.31	0.49	0.464
5	130	141	1.17	474.80	0.38	1.18	1.090

*@C_{sx}/C_{s1}

** Approximated central value using Figure 31

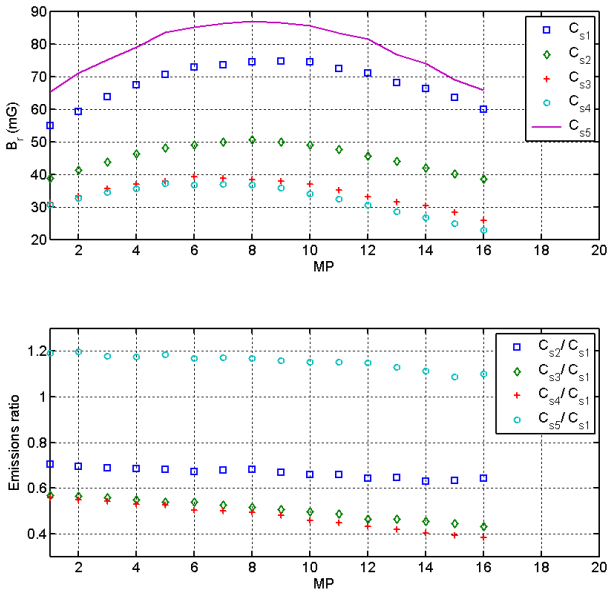

(a) Emissions and emissions ratio

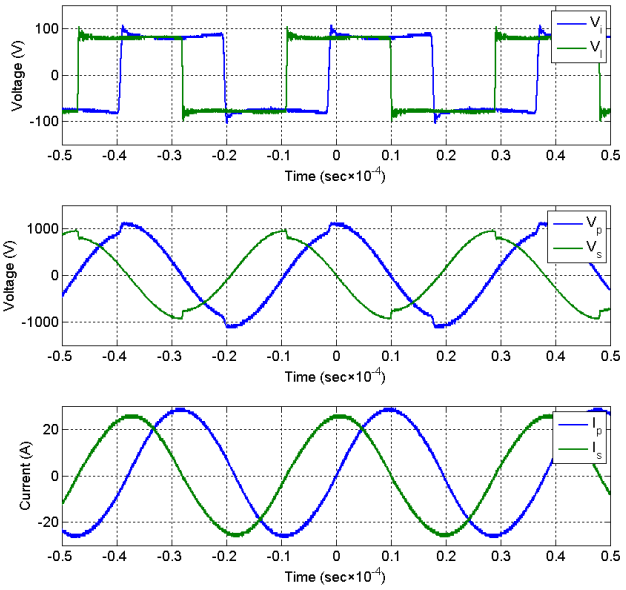

(b) Electrical quantities at C_{s1}

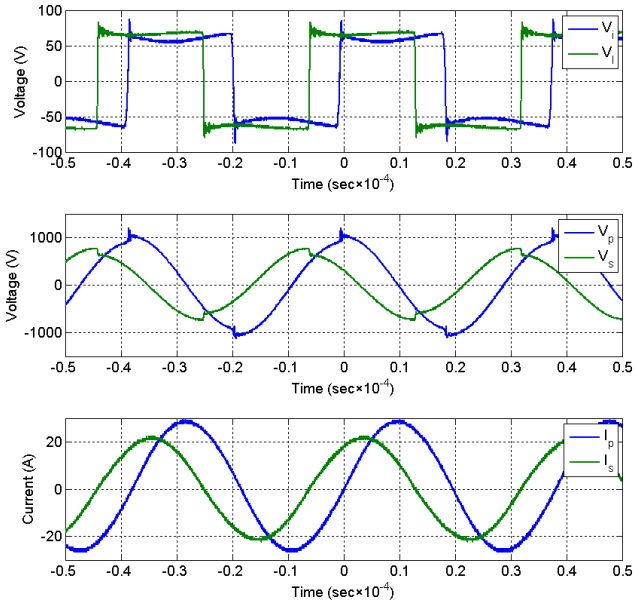

(c) Electrical quantities at C_{s2}

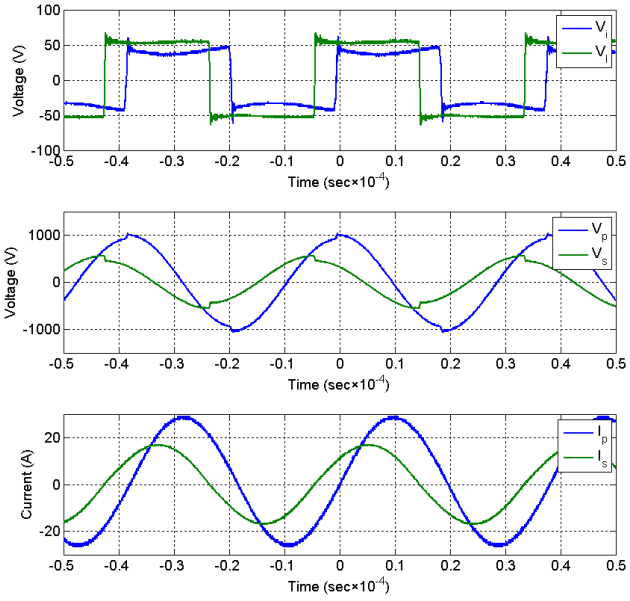

(d) Electrical quantities at C_{s3}

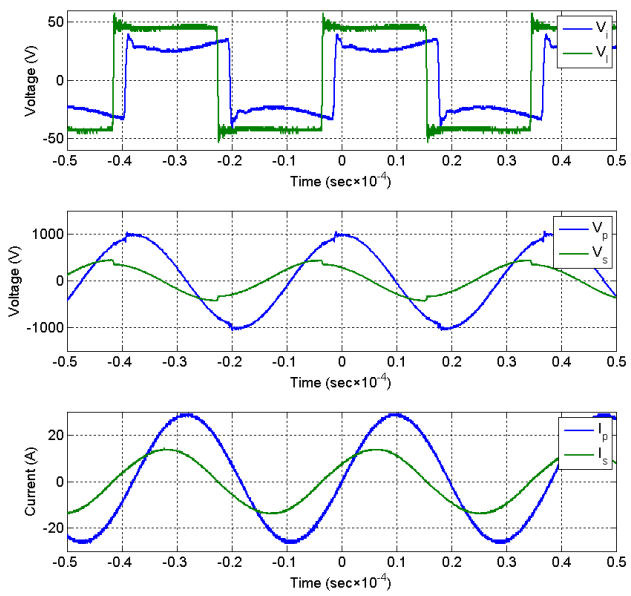

(e) Electrical quantities at C_{s4}

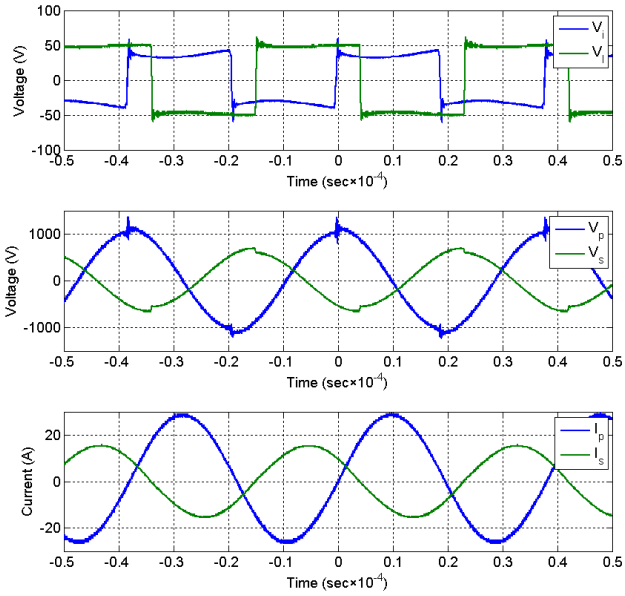

(f) Electrical quantities at C_{s5}

Figure 31. Case 1 results

5.4.2.2. Case 2

The emissions, emissions ratio and electric quantities are presented for five secondary capacitance values at horizontal distance (H=0.5 m) in Figure 32. The capacitors values are similar to the first case and are provided again in Table 17. Value of the output power, emissions ratio and analytical emissions ratio are also provided in the same table. Value of the load resistor is approximately 5.1 Ω for this case.

Table 17. Case 2 results

x	C_{sx}	C_{px}	C_{sx}/C_{s1}	P_l (W)	P_l ratio*	Emissions ratio*, **	Analytical emissions ratio*
1	152	152	1	995.80	1.00	1	1.000
2	163	152	0.93	795.71	0.80	0.78	0.775
3	174	152	0.87	580.99	0.58	0.6	0.591
4	184	152	0.83	413.78	0.42	0.57	0.574
5	130	141	1.17	495.94	0.50	1.18	1.124

*@C_{sx}/C_{s1}

** Approximated central value using Figure 32

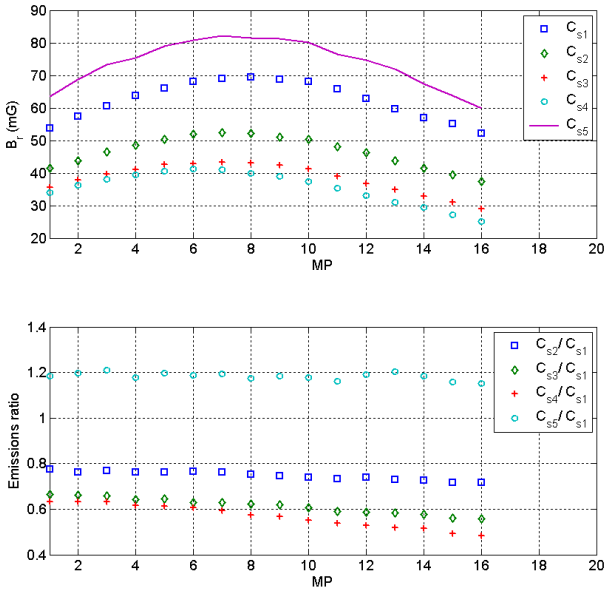

(a) Emissions and emissions ratio

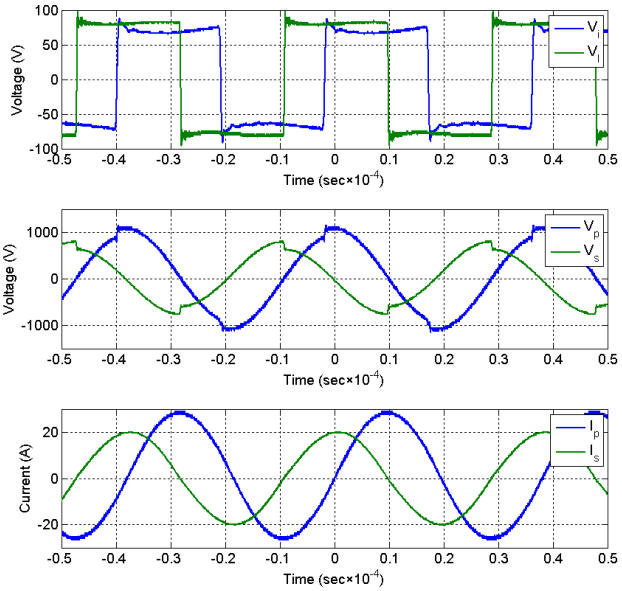

(b) Electrical quantities at C_{s1}

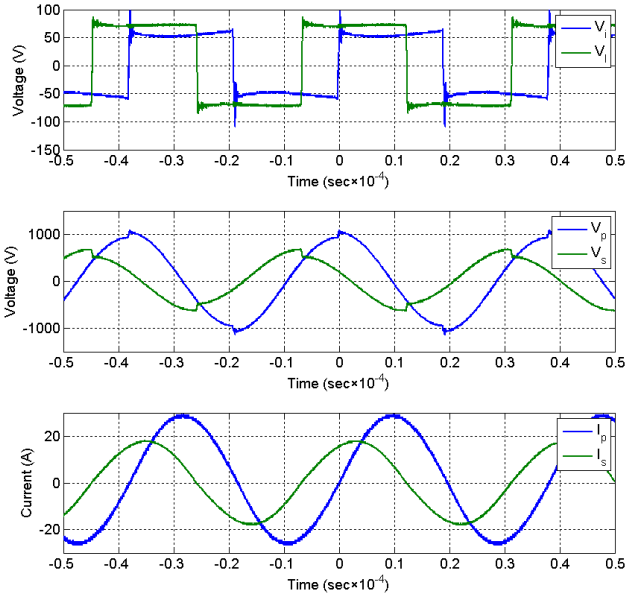

(c) Electrical quantities at C_{s2}

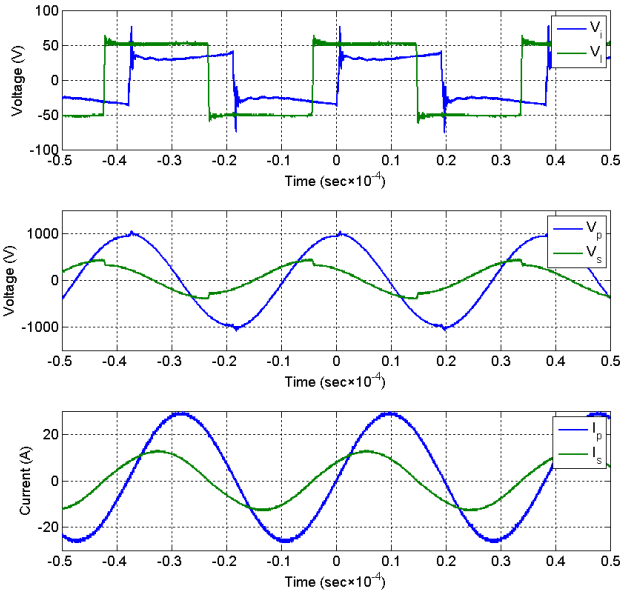

(d) Electrical quantities at C_{s3}

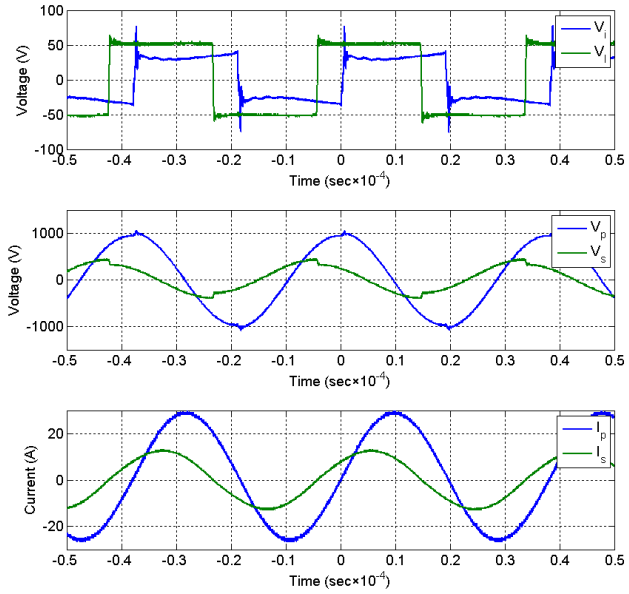

(e) Electrical quantities at C_{s4}

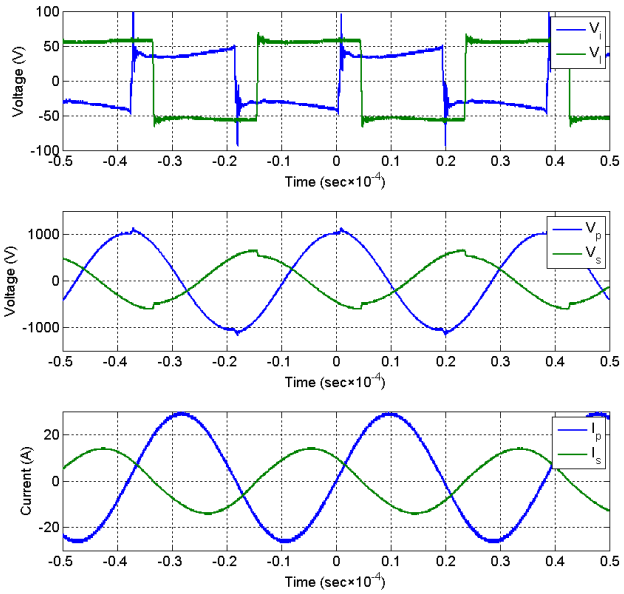

(d) Electrical quantities at C_{s5}

Figure 32. Case 2 results

5.4.2.3. Discussion

Main observations from results in Section 5.4.2.1 and 5.4.2.2 are as follows.

1) The system has input power factor close to one at all capacitor values for both cases in Figure 31 and 32.

2) Foremost point that is validated with the results is compliance of the experimental emissions ratio with the analytical emissions ratio as provided in Table 16 and 17.

3) With increase in the secondary capacitor (subscript 2, 3 and 4), the emission reduces from their resonance value (subscript 1) as provided in (a) parts of Figure 31 and 32 respectively. In other words, the emissions ratio becomes less than one at off-resonance value as provided in Table 16 and 17. This is on account of component of current that comes in phase with the primary current with increase in the secondary capacitor. This can be seen by comparing (c) to (e) with (b) parts of Figure 31 and 32 respectively. The two currents are orthogonal at resonant value of the secondary capacitor in (b) parts of Figure 31 and 32.

4) With reduction (subscript 5) in the secondary capacitor from the resonant value, the emissions increase or emissions ratio is above one as provided in Table 16 and 17. It is to be noted that the

secondary current is lower for C_5 compared to C_1. Hence for two coil currents, higher currents magnitude not necessarily stands for higher Rms emissions value. The phase angle is an important deciding factor in Rms emission value as provided by the semi-analytical method.

5) The output power and secondary current reduces with variation in the secondary capacitor as provided in Table 16 and 17.

5.4.3. PhD paper 8

This paper was first published at PCIM Europe Conference in 2014 with following details.

{8} T. Batra, E. Schaltz, “Magnetic Emissions Reduction by Varying Secondary Side Capacitor for Ferrite Geometry based Series-Parallel Topology Wireless Power Transfer to Vehicles", Proceedings of International Exhibition and Conference for Power Electronics, Intelligent Motion, Renewable Energy and Energy Management (PCIM Europe 2014), Publisher: VDE Verlag, Berlin Offenbach 2014, pp 1-9, 2014.
https://www.mesago.de/en/PCIM/home.htm?ovs_tnid=0

[1]Magnetic Emissions Reduction by Varying Secondary Side Capacitor for Ferrite Geometry based Series-Parallel Topology Wireless Power Transfer to Vehicles

Tushar, Batra, Aalborg University, Denmark, tba@et.aau.dk
Erik, Schaltz, Aalborg University, Denmark, esc@et.aau.dk

Abstract

Magnetic fields in surroundings of wireless power transfer system depends upon the two coil currents, distance from the coils and space angle between the two coil fields in steady state conditions. Increase in value of the secondary capacitor leads to a phase shift between the two currents and as a result magnetic emissions are reduced. But the side effect of this phase shift is reduction in the power transfer capability of the system. This paper proposes a new design method with help of theory and simulations which shows that it is possible to reduce the magnetic emissions and transmit the same power at unity power factor at expense of higher primary current and bigger capacitors on both sides. This reduction increases with increase in the secondary capacitor till a certain maximum point and then decreases. Hence this new design method can be very useful in reducing the magnetic emissions of series-parallel topology wireless power transfer to vehicles without compromising with the power transfer capability of the system.

1. Introduction

Wireless power transfer (WPT) system has been mostly used in the past for biomedical applications [1]. Application of this technology for charging electric vehicles is still in nascent stage. On one hand this system provides an automated and electrically safe system for charging but on the other hand the fields emitted by this system can have long term repercussions on living organisms [2]. Also, the emitted magnetic fields can interfere with the nearby equipment causing electromagnetic compatibility issues. A block diagram of WPT system is provided below in Fig. 1 followed by a brief description of the components.

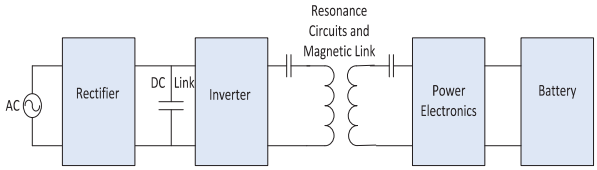

Fig. 1: Block diagram of wireless power transfer system

There are power electronic blocks on the primary (rectifier and inverter) and secondary sides for control of power and current on the two sides respectively. The two resonant circuits provide sinusoidal waveforms to the system. The two inductors are the energy transferring components in the system and are based on the principle of electromagnetic induction. Guidelines for the magnetic fields emitted by WPT system are based on rms values and a

[1] This work has financially been supported by The Danish Council for Strategic Research.

brief account of it can be found in [3]. Active and passive shielding [2] methods are used to minimize these emissions. Passive shielding [4] refers to use of ferrite and aluminum in the system for reducing magnetic fields in the surroundings. The proposed new design presented in this paper falls under category of active shielding and hence passive shielding will not be discussed further. Active shielding is technique of introducing a third coil in the system for magnetic field cancellation [5]. Disadvantage of this technique is requirement of an additional power source and extra space required for installing the third coil. Researchers from KAIST University were able to eliminate the first problem of additional power source by introducing reactive resonant current loop method [2]. But this method still requires switching capacitors for cancellation of magnetic field and the additional third coil. In the new proposed design, no extra components are required. The existing secondary capacitor is increased to reduce the phase angle difference between the two currents than the normal system design [6]. This phase shift strengthens component of the secondary magnetic flux which is in phase opposition with the primary magnetic flux. Extent of flux cancellation by this method depends on the increase in the value of the secondary capacitor, quality factor, coupling factor and distance from the coils. This cancellation increases with increase in the secondary capacitor up to a certain maximum value and then decreases. This increase also leads to increase and decrease in value of the reflected capacitance and resistance on the primary side respectively. The primary capacitor and primary current have to be increased in order to maintain unity power factor and equal power transfer capability in the system. Hence with these modifications the magnetic emissions of WPT can be reduced while transmitting the same power at unity power factor as illustrated in the paper with help of theory and simulations. This paper presents a new design methodology for WPT system with focus on magnetic emissions reduction and can be very useful for the future design of this system.

2. Theory

2.1. Sample geometry

The sample geometry [7] used in the paper is introduced in this section. Two views (top and side) of the geometry are presented below in Fig. 2.

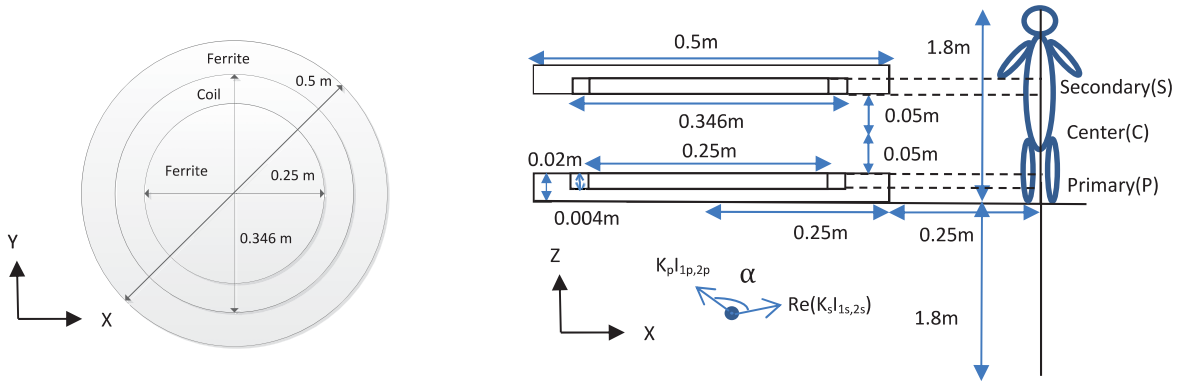

(a) Top view (b) Side view

Fig. 2: Sample geometry [7]

It consists of two perfectly aligned inductors, each having a coil embedded in a ferrite disc. The magnetic emissions are studied for vertical line at a horizontal distance of 0.5 m from the center of the inductors as shown in Fig. 2(b). The self and mutual inductance for the inductors are 157 and 60 µH respectively. Details of the coils and ferrite are provided in Table 1.

Property	Coil Wire	Numb -er of turns	Number of parallel conductor	Conductor diameter	Coil outer diameter	Conductor conductivity	Relative permeability ferrite
Type/Value	Litz	12	810	0.1 mm	4 mm	6×10^7 (S/m)	2300

Tab. 1: Coils and ferrite details [8]

2.2. Normal design

Fundamental mode analysis (FMA) equivalent circuit [9] for the series-parallel topology is same for both the designs and is provided in Fig. 3. The inductors (L_p, L_s and M) and load (R_p) are also same for both the designs. Subscript p, s and 1, 2 refer to the primary side, secondary side and normal design, new design respectively.

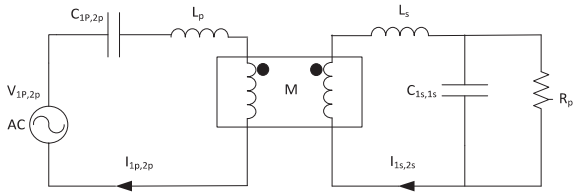

Fig. 3: FMA equivalent circuit series-parallel topology

The secondary capacitor is in resonance with the secondary coil and reflects a resistive and capacitive part on the primary side [6]. The primary capacitor is designed to compensate for both the self-inductance of the primary coil and the reflected capacitance. The voltage equations, resonant frequency (w_r), primary capacitor and quality factor (Q) of the system are provided in (1) to (5).

$$V_{1p,2p}=\left(jwL_p+\frac{1}{jwC_{1p,2p}}\right)I_{1p,2p}-jwMI_{1s,2s} \quad (1)$$

$$jwMI_{1p,2p}=\left(jwL_s+\frac{R_p\frac{1}{jwC_{1s,2s}}}{R_p+\frac{1}{jwC_{1s,2s}}}\right)I_{1s,2s} \quad (2)$$

$$w_r=\frac{1}{\sqrt{L_sC_{1s}}} \quad (3)$$

$$Q=\frac{R_p}{w_rL_s} \quad (4)$$

$$C_{1p}=\frac{1}{\left(1-\frac{M^2}{L_pL_s}\right)L_pw_r^2} \quad (5)$$

Inserting (3), (4) and (5) in (1) and (2), (6) and (7) are obtained. Also, input power (P_1) for the system is given by (8).

ISBN 978-3-8007-3603-4

$$V_{1p}=\frac{w_r M^2}{L_s} Q I_{1p} \tag{6}$$

$$I_{1s}=\frac{M}{L_s}(1+jQ) I_{1p} \tag{7}$$

$$P_1=\frac{w_r M^2}{L_s} Q I_{1p}^2 \tag{8}$$

Non-linear behavior of ferrite is ignored for WPT systems [3] as the saturation field is much higher than maximum magnetic field. Hence the magnetic fields (B_{1p} and B_{1s}) of the two coils at any point can be taken as proportional [7] to their respective currents. K_p and K_s are the proportionality constants for the point. The constants are identical for the two designs as the inductors and the surroundings are same for the designs.

$$B_{1p}=K_p I_{1p} \tag{9}$$

$$B_{1s}=K_s I_{1s} \tag{10}$$

The resultant magnetic field (B_1) using (7), (9), (10), space angle α from Fig. 2(b) and with the primary current (I_{1p}) as reference phasor (phase angle zero) can be written as

$$|B_1|=\sqrt{\left[(K_p I_{1p})^2+(\mathrm{Re}(K_s I_{1s}))^2+2\mathrm{Re}(K_s I_{1s}) K_p I_{1p}\cos\alpha\right]+\left[\mathrm{Imag}(K_s I_{1s})\right]^2}$$

$$|B_1|=I_{1p}\sqrt{\left[K_p{}^2+\left(K_s\frac{M}{L_s}\right)^2+2K_pK_s\frac{M}{L_s}\cos\alpha\right]+\left(\frac{M}{L_S}QK_s\right)^2}\,. \tag{11}$$

2.3. New design

The new design secondary capacitor is taken as constant multiple (a) of the normal design capacitor.

$$C_{2s}=aC_{1s} \tag{12}$$

Using (3), (4), (12) in (1) and (2), (13) and (14) are obtained.

$$V_{2p}=\left(jw_rL_p+\frac{1}{jw_rC_{2p}}\right)I_{2p}+\frac{w_rM^2}{L_s}\left[\frac{Q}{1+(a-1)^2Q^2}-j\frac{1+(a^2-a)Q^2}{1+(a-1)^2Q^2}\right]I_{2p} \tag{13}$$

$$I_{2s}=\frac{M}{L_s}\left[\frac{1+(a^2-a)Q^2}{1+(a-1)^2Q^2}+j\frac{Q}{1+(a-1)^2Q^2}\right]I_{2p} \tag{14}$$

For unity input power factor in (13), the primary capacitor value is

$$C_{2p}=\frac{1}{\left[1-\frac{M^2}{L_pL_s}\frac{1+Q^2(a^2-a)}{1+Q^2(a-1)^2}\right]L_pw_r{}^2}\,. \tag{15}$$

The primary voltage and input power (P_2) for the system using (13), (14) and (15) are

$$V_{2p}=\left(\frac{1}{1+(a-1)^2Q^2}\right)\frac{w_rM^2}{L_s}QI_{2p} \tag{16}$$

ISBN 978-3-8007-3603-4

$$P_2 = \left(\frac{1}{1+(a-1)^2Q^2}\right)\frac{w_r M^2}{L_s} Q I_{2p}^2. \quad (17)$$

The resultant magnetic field (B_2) using (9), (10), (14), space angle α from Fig. 2(b) and with the primary current (I_{2p}) as the reference phasor can be written as

$$|B_2| = I_{2p}\sqrt{\left[K_p^2 + \left(K_s\frac{M}{L_s}\frac{1+Q^2(a^2-a)}{1+Q^2(a-1)^2}\right)^2 + 2K_pK_s\frac{M}{L_s}\frac{1+Q^2(a^2-a)}{1+Q^2(a-1)^2}\cos\alpha\right] + \left[\frac{M}{L_s}\frac{Q}{1+Q^2(a-1)^2}K_s\right]^2}. \quad (18)$$

2.4. Comparison

The two topologies have the same input power when (8) and (17) are equal. Hence,

$$\frac{I_{2p}}{I_{1p}} = \sqrt{1+Q^2(a-1)^2}. \quad (19)$$

Ratio K for the magnetic emissions using (11), (18) and (19) can be expressed as

$$K = \frac{|B_1|}{|B_2|} = \frac{\sqrt{1+Q^2(a-1)^2}\sqrt{\left[K_p{}^2 + \left(K_s\frac{M}{L_s}\right)^2 + 2K_pK_s\frac{M}{L_s}\cos\alpha\right] + \left(\frac{M}{L_S}QK_s\right)^2}}{\sqrt{\left[\left(K_p\left(1+Q^2(a-1)^2\right)\right)^2 + \left(K_s\frac{M}{L_s}\left(1+Q^2(a^2-a)\right)\right)^2 + 2K_pK_s\frac{M}{L_s}\left(1+Q^2(a^2-a)\right)\left(1+Q^2(a-1)^2\right)\cos\alpha\right] + \left[\frac{M}{L_s}QK_s\right]^2}}. \quad (20)$$

In order to evaluate ratio K, ratio K_s/K_p and angle α are required. They are provided in the next section and afterwards ratio K is discussed. Also ratio of the secondary capacitors of the two designs using (5) and (15) is given by

$$\frac{C_{2p}}{C_{1p}} = \frac{1-\frac{M^2}{L_pL_s}}{1-\frac{M^2}{L_pL_s}\left[\frac{1+Q^2(a^2-a)}{1+Q^2(a-1)^2}\right]}. \quad (21)$$

3. Simulation results

3.1. Space angle α

Magnetic field direction for the two coils is shown on a normalized scale in Fig. 4. The space angle α as per law of electromagnetic induction has value of 180° except for points close to the coils as shown in Fig. 4. Livings beings are not supposed to be at such a close distance to the coils and hence this angle is taken as 180° in the paper.

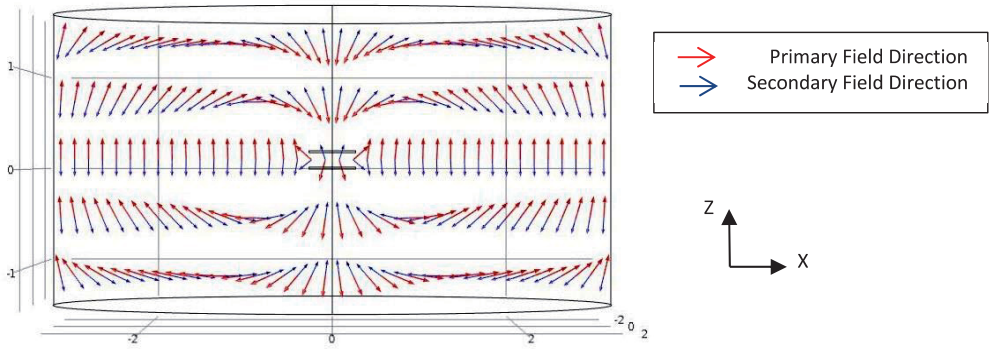

Fig. 4: Magnetic field direction for coils

3.2. Ratio K_s/K_p

Ratio K_s/K_p and associated rms magnetic field can be obtained by no-load curves [7] of the coils at same current (23A rms at 20kHz) and are provided in Fig. 5. Effect of ferrite on this ratio has already been discussed by the same authors in [7]. The magnetic field emitted by the two coils is nearly same at all points as shown in Fig. 5(b) and hence value of K_s/K_p can be approximated as one for all points in space as also shown in Fig. 5(a).

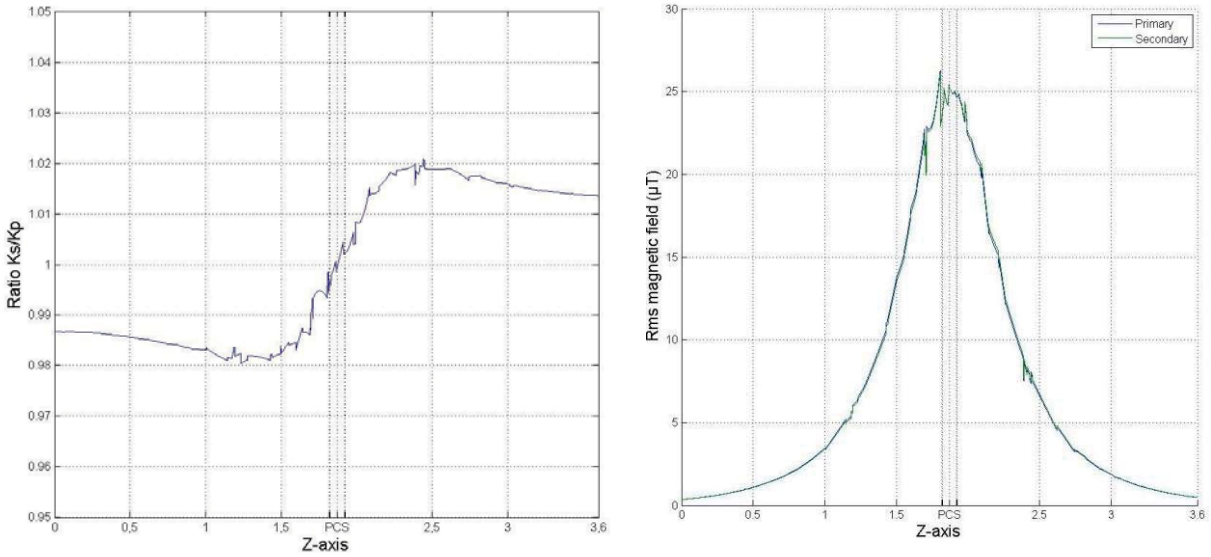

(a) Ratio K_s/K_p versus Z-axis (b) Rms magnetic field (µT) versus Z-axis

Fig. 5: No-load curves [7]

3.3. Ratio K

Ratio K using value of α as 180° (section 3.1) in (20) can be simplified to

$$K=\frac{\sqrt{1+Q^2(a-1)^2}\sqrt{\left(1-\frac{K_s M}{K_p L_s}\right)^2+\left(Q\frac{M K_s}{L_S K_p}\right)^2}}{\sqrt{\left[1-\frac{K_s M}{K_p L_s}+Q^2(a-1)\left(a-1-a\frac{K_s M}{K_p L_s}\right)\right]^2+\left[Q\frac{K_s M}{K_p L_s}\right]^2}}. \quad (22)$$

Ratio K can be theoretically calculated by taking value of K_s/K_p from Fig. 5(a) and applying in (22). Simulated values for same ratio K through on-load simulations on Comsol for five different values of constant a along with the theoretical ratios K are provided in Fig. 6(a). Rms magnetic fields for the same simulations are provided in Fig. 6(b). Values of M/L_s=0.38 and Q=6 are used for both the calculations. The currents and voltages rms values for the on-load simulations (20 kHz) are first provided in Table 2.

a	V_{2p} (V)	I_{2p} (A)	I_{2s} (A)	V_{1p} (V)	I_{1p} (A)	I_{1s} (A)
0.5	40.59+j0.16	23	-7.00+j5.27	124.71+j0.08	7.27	2.77+j16.47
0.9	291.72-j1.75	23	-14.18+j38.50	331.17+j0.23	19.72	7.50+j44.66
1.05	362.2+j2.42	23	22.95+j47.83	337.74+j0.26	22.03	8.39+j49.89
1.4	60.34+j0.98	23	27.34+j7.89	151.68+j0.10	8.85	3.37+j20.03
1.75	19.94+j0.43	23	19.87+j2.54	85.55+j0.06	4.99	1.90+j11.30

Tab. 2: Voltages and currents for on-load simulations

ISBN 978-3-8007-3603-4

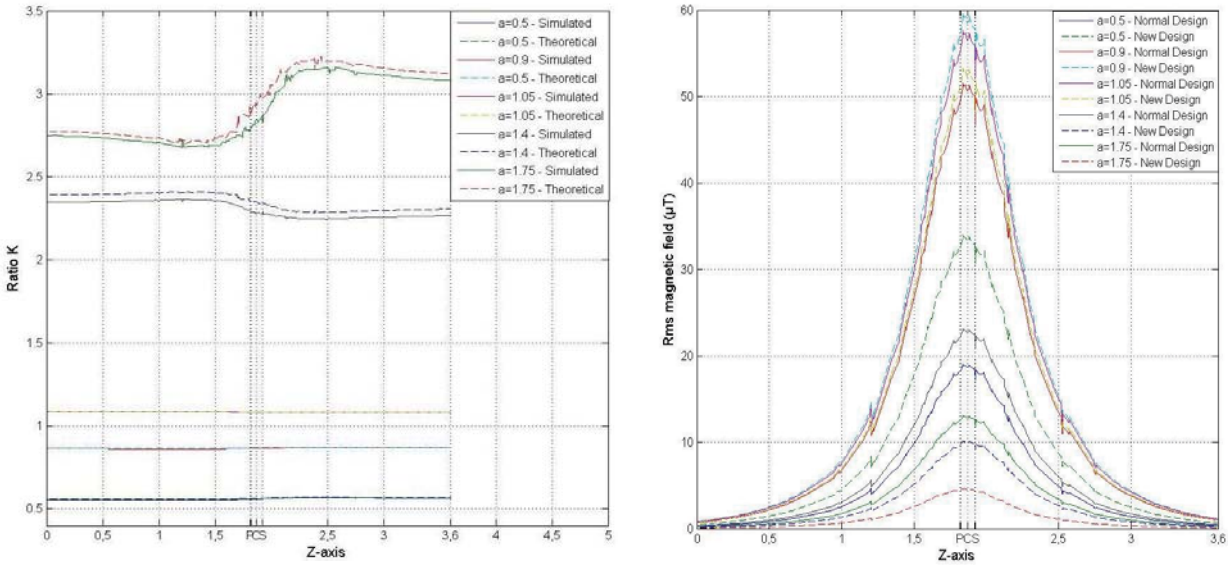

(a) Ratio K versus Z-axis (b) Rms magnetic field (µT) versus Z-axis

Fig. 6: Theoretical and simulated results

As shown in Fig. 6(a), the theoretical and simulated values for ratio K are in good agreement. Also ratio K in a similar way to ratio K_s/K_p (Fig. 5(a)) has a small deviation on both sides from its value at center (C). Ignoring this deviation gives advantage that ratio K can be defined by a single number for a given value of constant a. With this simplification, different ratios ((12), (19), (21) and (22)) for comparing the two designs are plotted on Matlab and are provided in Fig. 7(a). Results are also plotted for three other values of the system parameters (provided in captions) and are provided in Fig. 7(b) to 7(d). The primary capacitor ratios are algebraically modified for better representation and details are provided in the legend of the figures.

Following observations can be made from Fig. 7(a) to 7(d).

1) Ratio K increases with increase in value of constant a till a certain maximum point and then starts to decreases. The point of maximum is given by

$$a\text{-}1\text{-}a\frac{K_s}{K_p}\frac{M}{L_s}=0. \tag{23}$$

The left hand of (23) is present in the denominator of (20). Factor (K_s/K_p*M/L_s) and quality factor are same for parts (a) and (d) of Fig. 7 and hence the curves for ratio K are identical for these two parts.

2) An interesting observation from Fig. 7(b) is that increasing the secondary capacitor will not always reduce the emissions. In the figure, ratio K is less than one for an interval at the right hand side even when constant a is greater than one. Hence there can be a range for which the magnetic emissions cannot be reduced by increase in the value of secondary capacitor. This range can be investigated by plotting (22) for the parameters of that particular system.

ISBN 978-3-8007-3603-4

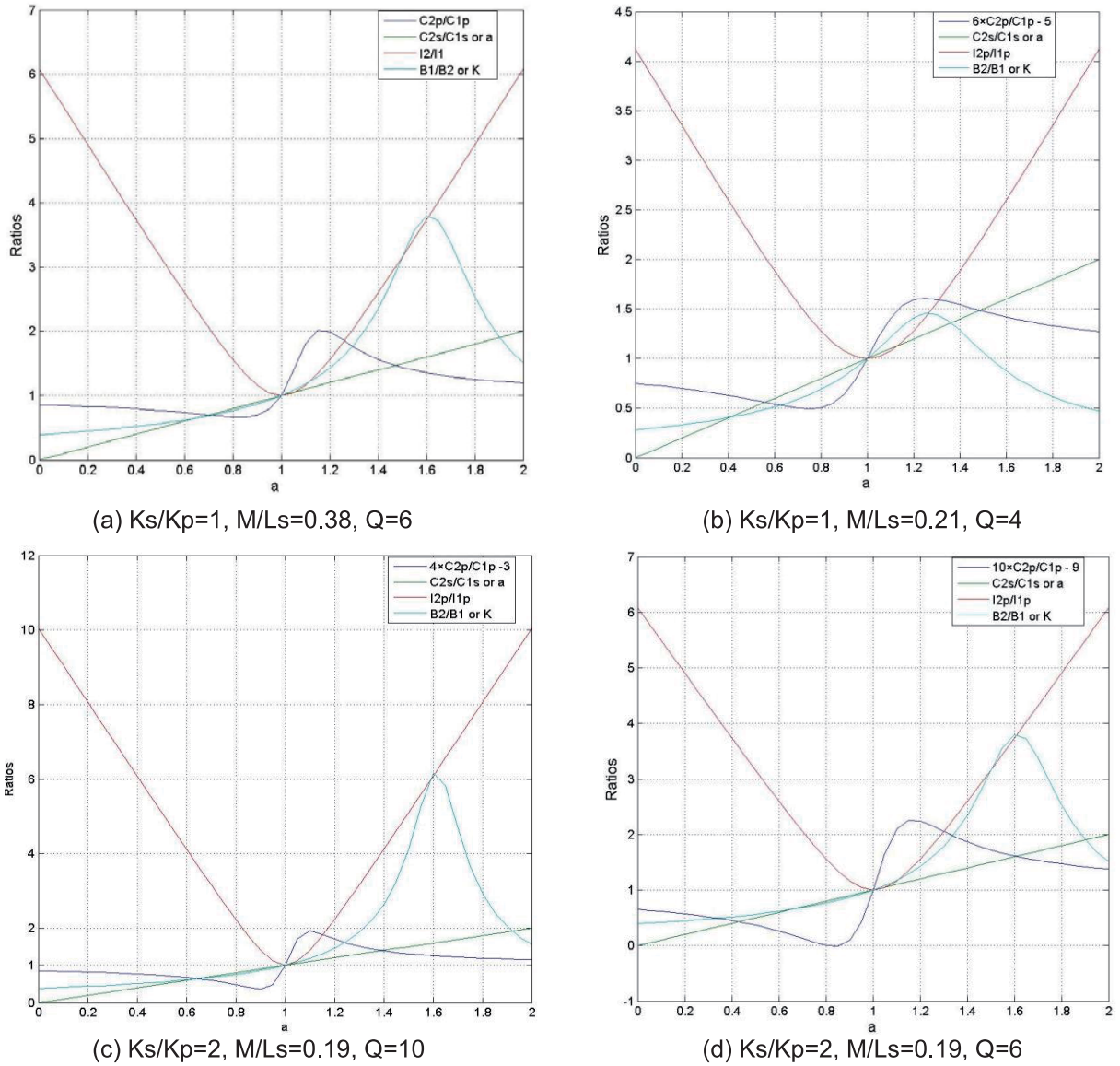

(a) Ks/Kp=1, M/Ls=0.38, Q=6

(b) Ks/Kp=1, M/Ls=0.21, Q=4

(c) Ks/Kp=2, M/Ls=0.19, Q=10

(d) Ks/Kp=2, M/Ls=0.19, Q=6

Fig. 7: Ratios of the two designs

3) Ratios of the primary capacitors show a similar behavior to ratio K but are always greater than one in the right half of the figures. Also the maximum of the primary capacitor ratio is determined by the quality factor the system. Term in the square bracket of (21) determines the maximum of this ratio as (M^2/L_sL_p) is very small compared to one. The squared term when differentiated and equated to zero to obtain maxima condition yields the following expression

$$a=1+\frac{1}{Q}. \qquad (24)$$

The maxima's in the figures are located at the points given by (24).

4) The primary current ratios shows the expected parabolic behavior with the minimum at resonance point (a=1). The primary voltage ratio (not provided) shows the opposite behavior (Table 2) as input power of the system is maintained constant at unity power factor.

ISBN 978-3-8007-3603-4

5) The last set of ratios for the secondary current are linear with respect to a as per its initial definition in (12).

4. Conclusion

In this paper a new design method for series-parallel topology wireless power transfer to vehicles has been presented. This design method reduces the magnetic field in the surroundings of the system by the increase in value of the secondary capacitor. This reduction depends upon system parameters namely quality factor, coupling factor and distance from the coils apart from the increase in the secondary capacitor value. Also bigger primary capacitor and higher input current are required than the state of the art design in order to achieve unity power factor and equal power transfer capability for the new design. Theoretical equations explaining this reduction are developed in this paper and are substantiated with simulations. Experimental verification of this work is in priority for future works.

5. References

[1] K. M. Silay, C. Dehollain, and M. Declercq, “Improvement of power efficiency of inductive links for implantable devices,” Research in Microelectronics and Electronics 2008, pp. 229-232, April 25 - June 22 2008.

[2] J. Kim, J. Kim, S. Kong, H. Kim, I. S. Suh, N. P. Suh, D. H. Sho, “et al.” ,“Coil Design and Shielding Methods for MagneticResonant Wireless Power Transfer Sys tem”, Proceedings of the IEEE , vol. 101, no. 6, pp. 1332-1342, 2013.

[3] M. Budhia, G. A. Covic, J. T. Boys, “Design and Optimization of Circular Magnetic Structures for Lumped Inductive Power Transfer Systems,” IEEE Transactions On Power Electronics, vol 26., no 11., pp. 3096-3108, 2011.

[4] H. Kim, J. Cho, S. Ahn, J. Kim, J. Kim, “Suppression of Leakage Magnetic Field from a Wireless Power Transfer System using Ferrimagnetic Material and Metallic Shielding”, IEEE International Symposium on EMC, Pittsburgh, USA, pp. 640-645, Aug. 06 2012 - Aug. 10 2012

[5] S. Ahn, J. Kim, “Magnetic Field Design for High Efficient and Low EMF Wireless Power Transfer in On-Line Electric Vehicle,” 5th European Conference on Antennas and Propagation - EUCAP 2011, pp. 3979-3982, 2011.

[6] W. Chwei-Sen, O. H. Stielau, and G. A. Covic, “Design considerations for a contactless electric vehicle battery charger,” IEEE Transactions on Industrial Electronics, vol. 52, no. 5, pp. 1308-1314, 2005.

[7] T. Batra, E. Schaltz, “Magnetic Field Emissions for Ferrite and Non-Ferrite Geometries for Wireless Power Transfer to Vehicles”, Journal of Applied Physics – Special Edition, in press.

[8] M. Budhia, G. A. Covic, J. T. Boys, C. Y. Huang, “Development of single sided flux couplers for contactless electric vehicle charging,” IEEE Transactions On Industrial Electronics, vol 60., no 1., pp. 318-328, 2013

[9] M. G. Egan, D. L. O'Sullivan, J. G. Hayes, S. E. Schulz, J. T. Hall, “Power-Factor-Corrected Single-Stage Inductive Charger for Electric Vehicle Batteries,” IEEE Transactions on Industrial Electronics, vol. 54, no. 2, pp. 1217-1226, 2007.

5.5. Application 3

Resonant topologies have been compared in terms of primary capacitor requirement, voltage and current stress, voltage or current source characteristic towards load etc. in literature [23, 27] and also reported in Section 2.4. However, the topologies have not been compared in terms of the magnetic emissions. SS and SP topologies are compared in term of the emissions for similar primary power electronics, load quality factor and hence equal output power rating in the third application. It is first derived using the semi-analytical method that SP topology with slightly inductive secondary circuit has minor edge in term of the emissions over SS topology having purely resistive circuit on the secondary side. Two PhD papers {9-10} explaining detailed theory of the comparison and validated with FEM results has been published during the project. Papers {9} and {10} are provided in Section 5.5.1 and 5.5.2 respectively followed by experimental verification in Section 5.5.3.

5.5.1. PhD paper 9

This was originally published with following details.

{9} T. Batra, E. Schaltz, “Magnetic field emission comparison for series-parallel and series-series wireless power transfer to vehicles – part 1/2", Proceedings of EVTEC and APE, pp 2014435, 2014.

20144035

MAGNETIC FIELD EMISSION COMPARISON FOR SERIES-PARALLEL AND SERIES-SERIES WIRELESS POWER TRANSFER TO VEHICLES – PART 1/2

Tushar Batra Erik Schaltz

Department of Energy Technology, Aalborg University
Pontoppidanstraede 101, Aalborg, Denmark (E-mail: tba@et.aau.dk)
(The work has financially been supported by The Danish Council for Strategic Research)

Presented at the EVTeC and APE Japan on May 22, 2014

ABSTRACT: Resonant circuits of wireless power transfer system can be designed in four possible ways by placing the primary and secondary capacitor in a series or parallel order with respect to the corresponding inductor. The two topologies series-parallel and series-series under investigation have been already compared in terms of their output behavior (current or voltage source) and reflection of the secondary impedance on the primary side. In this paper it is shown that for the same power rating series-parallel topology emits lesser magnetic fields to the surroundings than its series-series counterpart at steady state resonant operation. First of all analytical expressions for the above mentioned statement are presented and is later substantiated with simulations on a finite element solver (Comsol). Results for variation of the magnetic emissions ratio for the two topologies are presented in this paper for different gap distance between the two inductors, horizontal distance from the coils and turn ratio.

KEY WORDS: EV and HV systems, Wireless power transfer, Magnetic fields, Series-series topology, Series-parallel topology [A3]

1. Introduction

Wireless power transfer (WPT) system has lately gained momentum for vehicle applications due to their safety and automation. WPT is based on the same principle as that of a transformer. The major difference between the two is presence of a large air gap between the coils of WPT. This large air gap results in high self-inductance of the coils and hence capacitors are used on both sides for unity power factor operation and maximum power transfer [1] across the air gap. A block diagram of the system is provided below in Fig. 1.

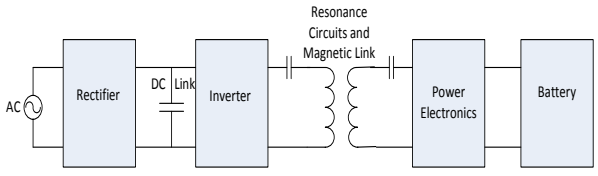

Fig. 1. Block diagram wireless power transfer.

The grid voltage is first rectified and then inverted for high frequency operation in the system. The squared output voltage of the inverter is fed to the resonant circuit and the currents as a result are of sinusoidal nature. The power electronics on the secondary side is used to control the power flow (either unidirectional [2] or bidirectional [3]) of the vehicle battery.

The self-inductance of the coils is compensated by capacitors on both sides by connecting the two in a series or parallel order. As a result four configurations [4] for the system can be made: series-series (SS), series-parallel (SP), parallel-series (PS) and parallel-parallel (PP). The primary capacitor for the latter two topologies (PS and PP) is dependent on the load and hence these topologies are not favored [4]. The other two topologies (SS and SP) have their own advantages and disadvantages [4]. SP topology has the advantage of having current source characteristics as compared to voltage characteristics of SS topology on the secondary side. SS topology on the other hand has the merit of no reflected impedance as compared to reactive coupling of SP topology towards the primary side.

In this paper, the two topologies (SS and SP) are compared for magnetic field emissions in the surroundings for the same input power. It is shown with help of analytical expressions and simulations that SP topology is more favorable from magnetic emissions point of view. This reduced magnetic field for SP topology comes from an additional component of secondary magnetic field which comes in phase opposition with the primary magnetic field. This paper is focused on this reduction behavior at different horizontal distance (from coils), vertical distance (between coils) and turn ratio. It is observed from the results that this reduction is practically constant in the surroundings except for points very close to the coils. The reduction deviates from the constant behavior as the horizontal and vertical distances are decreased and increased respectively. Also, variation in the number of secondary turns does not affect this reduction for the same primary current and quality factor. The decrease in the number of turns is compensated by the increase in the secondary current and vice versa.

2. Sample geometry

The sample geometry used in the paper is introduced in this section. Side and top views of the geometry are presented below in Fig. 2.

(a) Side view

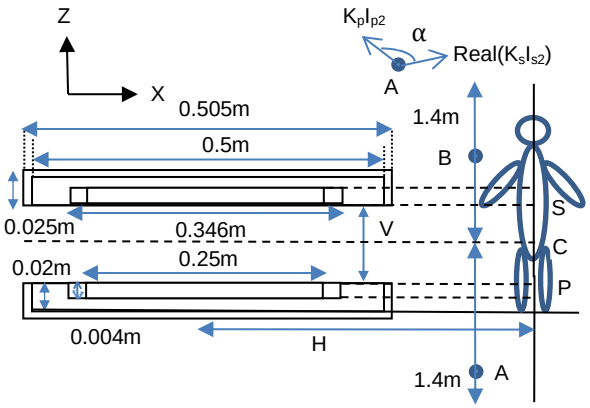

(b) Top view

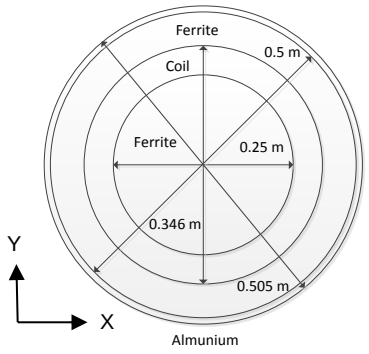

Fig. 2 Sample Geometry.

Ferrite and aluminum are used as passive shields [5, 6] in the system. Litz wire is used in both the coils. Results in this paper have been presented for two set of turn ratio (T) i.e. 12:12 and 12:6. A simplification for finite element simulations has been made that for the secondary inductor the space taken by the coil is same for both the turn ratio. Details of the coils [7] and shielding materials are provided in Table 1 below.

Table 1 Coils and shielding materials.

Property	Value
Number of parallel conductors in each turn	810
Diameter of parallel conductor	0.1 mm
Outer diameter of coil	4 mm
Conductivity of conductor	6×10^7 (S/m)
Relative permeability of ferrite	2300
Conductivity of aluminum	3.7×10^7 (S/m)

3. Theory

3.1. Nomenclature

The symbols used in the paper are first summarized in Table 2. The subscript letter '1' and '2' refer to SS and SP topology respectively. The inductors, secondary capacitor and resonance frequency are same for both the topologies. Value of the primary capacitor on the other hand is different [5] for the two topologies for maintaining unity power factor operation [4].

Table 2 Symbols.

Symbol	Name		Symbol	Name
I_{p1}, I_{p2}	Primary currents		I_{s1}, I_{s2}	Secondary currents
V_{p1}, V_{p2}	Primary voltages		P_1, P_2	Input Power
M	Mutual inductance		L_p, L_s	Primary and Secondary self-inductance
C_{p1}, C_{p2}	Primary capacitors		C_s	Secondary capacitor
R_1, R_2	Load resistance		Q_1, Q_2	Quality factor
w	Frequency		w_r	Resonance frequency

2.2. Series-series topology

Fundamental mode analysis (FMA) [8] equivalent circuit of the topology is provided below in Fig. 3.

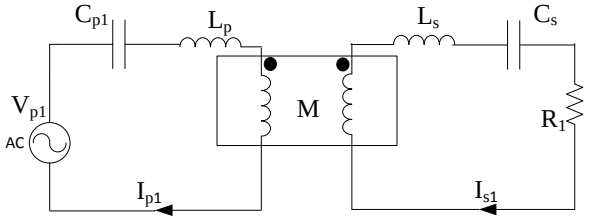

Fig. 3 FMA equivalent circuit series-series topology.

Expressions for the voltage equations, resonance frequency and quality factor of the system are provided below in (1) to (4)

$$\left(jwL_p+\frac{1}{jwC_{p1}}\right)I_{p1}-jwMI_{s1}=V_{p1} \quad (1)$$

$$\left(jwL_s+\frac{1}{jwC_s}\right)I_{s1}+R_1I_{s1}=jwMI_{p1} \quad (2)$$

$$w_r=\frac{1}{\sqrt{L_pC_{p1}}}=\frac{1}{\sqrt{L_sC_s}} \quad (3)$$

$$Q_1=\frac{w_rL_s}{R_1}. \quad (4)$$

At resonant operation, (3) will be valid. Using (3) and (4), (1) and (2) will be transformed to (5) and (6). The input power is given by (7).

$$V_{p1}=\frac{w_rM^2}{L_s}Q_1I_{p1} \quad (5)$$

$$I_{s1}=jM\frac{Q_1}{L_s}I_{p1}. \quad (6)$$

$$P_1=\frac{w_rM^2}{L_s}Q_1I_{p1}^2 \quad (7)$$

WPT systems use ferrite to reduce magnetic emissions and increase the power transfer capability of the system. But due to the presence of the large air gap, maximum magnetic field reached in ferrite cores of these systems is very less as compared to saturation magnetic field for ferrite. Hence, linear coefficient of permeability [9] is assumed for ferrite. Hence magnetic fields (B_{p1} and B_{s1}) at any point in the surroundings due to the primary and secondary coils can be written as follows

$$B_{p1}=K_pI_{p1} \quad (8)$$

$$B_{s1}=K_sI_{s1}. \quad (9)$$

K_p and K_s are corresponding constants for the primary and secondary coils for that point. As the inductors and the surroundings are identical for the two topologies, K_p and K_s are also same for the two. The number of turns for each coil is contained in the corresponding constant and is proportional to it. As the current for the two topologies are orthogonal to each other as shown in (6), hence the resultant field (B_1) at any point is

$$|B_1|=\sqrt{|I_{p1}K_p|^2+|I_{s1}K_s|^2} \quad (10)$$

Using (6), (10) can be transformed to

$$|B_1|=I_{p1}\sqrt{K_p{}^2+\left(K_sQ_1\frac{M}{L_S}\right)^2}. \quad (11)$$

2.3. Series-Parallel topology

FMA equivalent circuit for this topology is provided next in Fig. 4.

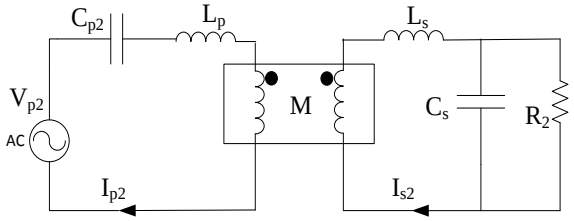

Fig. 4 FMA equivalent circuit series-parallel topology.

Expressions for the voltage equations, resonance frequency, primary capacitor and quality factor for the system are provided in (11) to (15)

$$\left(jwL_p+\frac{1}{jwC_{p2}}\right)I_{p2}-jwMI_{s2}=V_{p2} \quad (12)$$

$$jwMI_{p2}=\left(jwL_s+\frac{\frac{1}{jwC_s}R_2}{R_2+\frac{1}{jwC_s}}\right)I_{s2} \quad (13)$$

$$w_r=\frac{1}{\sqrt{L_sC_s}} \quad (14)$$

$$C_{p2}=\frac{L_s}{(L_pL_s-M^2)w_r^2} \quad (15)$$

$$Q_2=\frac{R_1}{w_rL_s} \quad (16)$$

At resonant operation, (14) will be valid. Using (14), (15) and (16), (12) and (13) will be transformed to (17) and (18). The input power for this topology is given by (19).

$$V_{p2}=\frac{w_rM^2}{L_s}Q_2I_{p2} \quad (17)$$

$$I_{s2}=M\left(\frac{1}{L_s}+j\frac{Q_2}{L_s}\right)I_{p2}. \quad (18)$$

$$P_2=\frac{w_rM^2}{L_s}Q_2I_{p2}^2 \quad (19)$$

The resultant magnetic field using (8), (9), (18) and space angle α between the fields in Fig. 2(a) and taking the primary current (I_{p2}) as reference phasor with phase angle zero is

$$|B_2|=\sqrt{\left[(K_pI_{p2})^2+(\text{Real}(K_sI_{s2}))^2+2\,\text{Real}(K_sI_{s2})\,K_pI_{p2}\cos\alpha\right]+\left[\text{Imaginary}(K_sI_{s2})\right]^2} \quad (20)$$

$$|B_2|=I_{p2}\sqrt{\left[K_p{}^2+\left(K_s\frac{M}{L_s}\right)^2+2K_pK_s\frac{M}{L_s}\cos\alpha\right]+\left(\frac{M}{L_S}Q_2K_s\right)^2} \quad (21)$$

2.4. Comparison

The two topologies have the same input power using (7) and (19) when

$$Q_1=Q_2=Q \quad \& \quad I_{p1}=I_{p2} \quad (22)$$

At this same power, ratio (K) of the magnetic fields using (11), (21) and (22)

$$K=\frac{|B_1|}{|B_2|}=\sqrt{\frac{1+\left(Q\frac{MK_s}{L_SK_p}\right)^2}{\left[1+\left(\frac{K_sM}{K_pL_s}\right)^2+2\frac{K_s}{K_p}\frac{M}{L_s}\cos\alpha\right]+\left(Q\frac{MK_s}{L_SK_p}\right)^2}} \quad (23)$$

The angle α is 180 degrees in the surroundings on account of principle of electromagnetic induction. Only very close to the inductor, the angle α has value other than 180 degrees and is explained in the next section. Hence as per (23), SP topology emits less magnetic fields as compared to SS topology for the same input power rating.

4. Results

4.1. Space angle α

The angle α can be seen with the help of Fig. 5. This figure is the arrow representation of the magnetic fields on a normalized scale. Outer cylinder has the magnetic potential zero and has dimensions of 3m diameter and 3m height. The coils are located at the center of the cylinder.

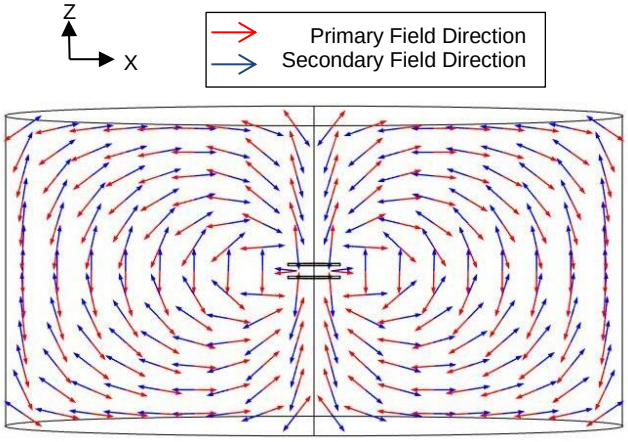

Fig. 5 Primary and secondary magnetic field directions.

As seen in Fig. 5, space angle is 180 degrees for nearly all points in the space and hence (23) is transformed to (24).

$$K=\frac{|B_1|}{|B_2|}=\sqrt{\frac{1+\left(Q\frac{M}{L_S}\frac{K_s}{K_p}\right)^2}{\left(1-\frac{M}{L_S}\frac{K_s}{K_p}\right)^2+\left(Q\frac{M}{L_S}\frac{K_s}{K_p}\right)^2}} \quad (24)$$

4.2. Ratio K_s/K_p

The ratio K_s/K_p can be investigated by plotting no-load curves [10, 11, 12] for the system at same current (23A at 20kHz). Using (8) and (9), ratio of magnetic fields of the two coils (B_s and B_p) at no-load conditions is equal to ratio K_s/K_p.

$$\frac{B_s}{B_p}=\frac{K_s}{K_p} \quad (25)$$

K_s/K_p curves and rms magnetic fields for the two coils at different horizontal distance (H), vertical distance (V) and turn ratio (T) are presented in Fig. 6 to 13.

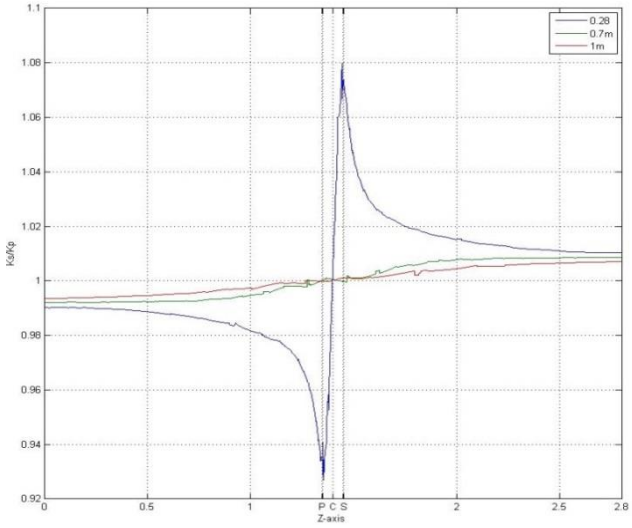

Fig. 6 Ratio K_s/K_p versus Z-axis at V=10cm, T=12:12.

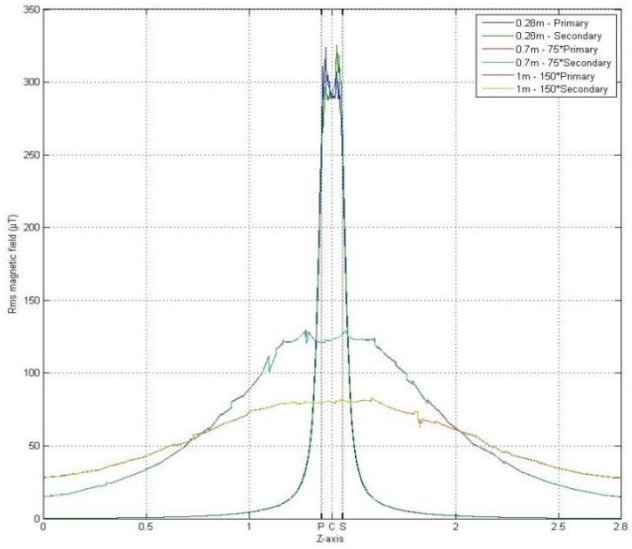

Fig. 7 No-load – Rms magnetic field (μT) versus Z-axis at V=10cm, T=12:12.

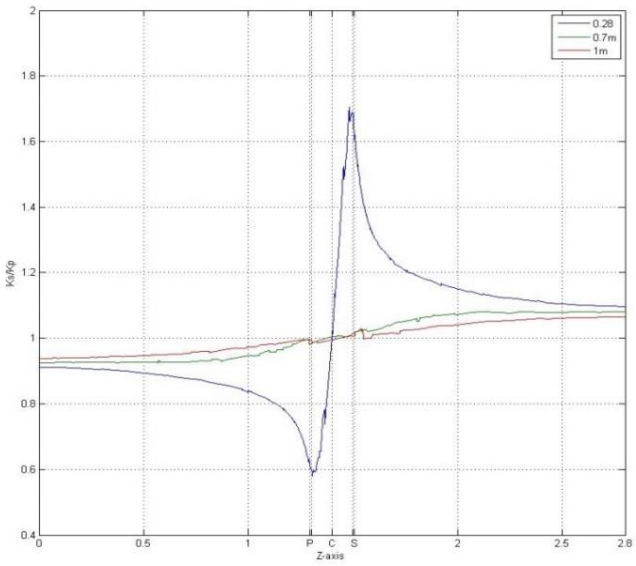

Fig. 8 Ratio K_s/K_p versus Z-axis at V=20cm, T=12:12.

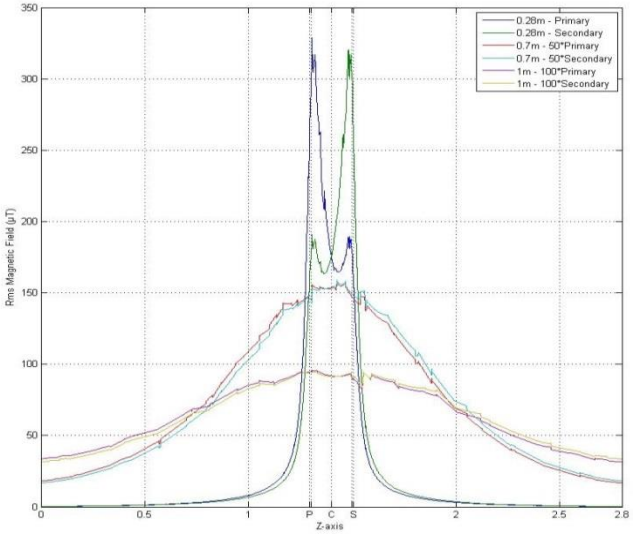

Fig. 9 No-load – Rms magnetic field (μT) versus Z-axis at V=20cm, T=12:12.

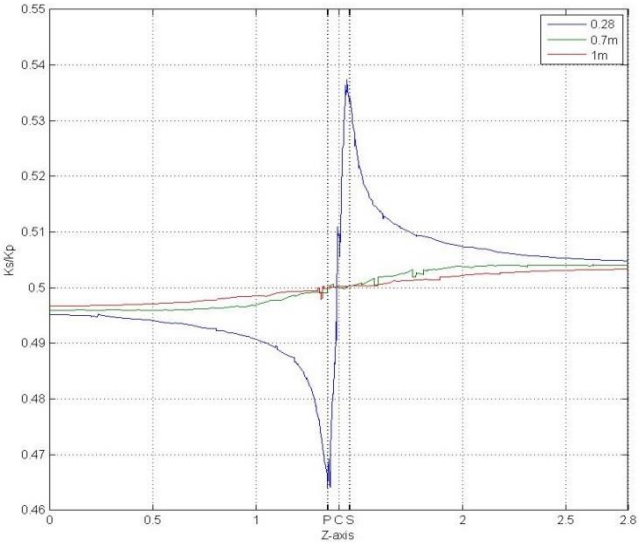

Fig. 10 Ratio K_s/K_p versus Z-axis at V=10cm, T=12:6.

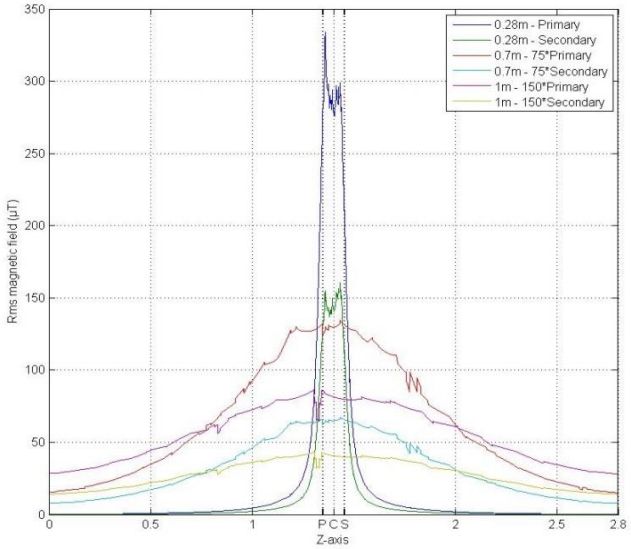

Fig. 11 No-load – Rms magnetic field (μT) versus Z-axis at V=10cm, T=12:6.

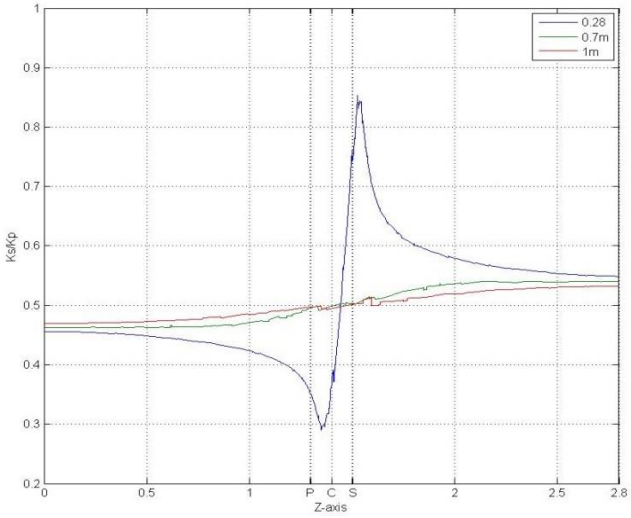

Fig. 12 Ratio K_s/K_p versus Z-axis at V=20cm, T=12:6.

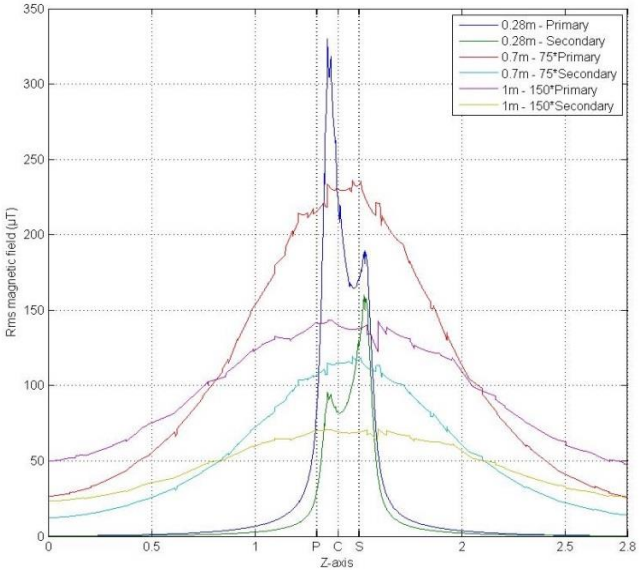

Fig. 13 No-load – Rms magnetic field (μT) versus Z-axis at V=20cm, T=12:6.

Following points are to be noted from Fig. 6 to 13. Points to left and right of center (C) on the Z-axis are termed as primary and secondary zone [10] points respectively in the paper.

1) As shown in Fig. 6, 8 and 10, 12 the value of ratio K_s/K_p is fairly equal to 1 and 0.5 except for points very close to the coils (between P and S for H=0.28m). Fig. 7, 9 and 11, 13 depict the same in terms of rms magnetic fields.

2) K_s and K_p are proportional to the number of turns for the corresponding coil. Therefore value of ratio K_s/K_p at C is half for T=12:6 (Fig. 10 and 12) as compared to the ratio for T=12:12 (Fig. 6 and 8).

3) With increase in V (Fig. 6, 8 and 10, 12) for any fixed point in the secondary zone for all H (0.28m, 0.7m and 1m), the ratio K_s/K_p also increases. On the other hand, increase in H for a constant V shows the opposite trend.

4) Aluminum and ferrite both have an effect on bringing space maxima's of the indivual coils closer to C as compared to geometries that do not have passive shielding. Details of the space profile curves have been discussed by the same authors in [10, 11, 12] and will not be provided here again.

4.3. Ratio K

Ratio K can be calculated theoretically by taking value of K_s/K_p from Fig. 6, 8, 10 and 12 and applying in (23). Simulated values for the same are obtained by on-load simulations on Comsol. The circuit parameters used for the calculations are provided in Table 3.

Table 3 Circuit Parameters.

T	Q	V(m)	L_p(μH)	L_s(μH)	M(μH)	M/L_s
12:12	4	0.1	147.09	147.09	49.59	0.34
12:6	4	0.1	147.09	36.77	24.80	0.67
12:12	4	0.2	138.69	138.69	14.21	0.10
12:6	4	0.2	138.69	34.67	7.10	0.20

The ratio K for both set of results and rms magnetic fields from on-load simulations are presented in Fig. 14 to 21.

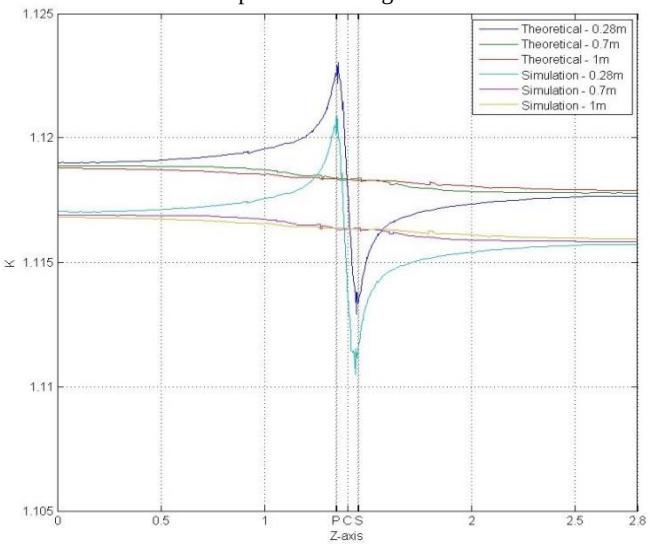

Fig. 14 Ratio K versus Z-axis at V=10cm, T=12:12.

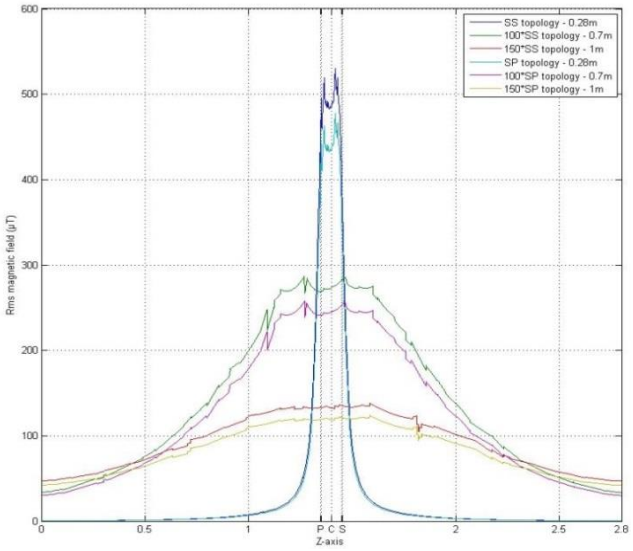

Fig. 15 On-load – Rms magnetic field (μT) versus Z-axis at V=10cm, T=12:12.

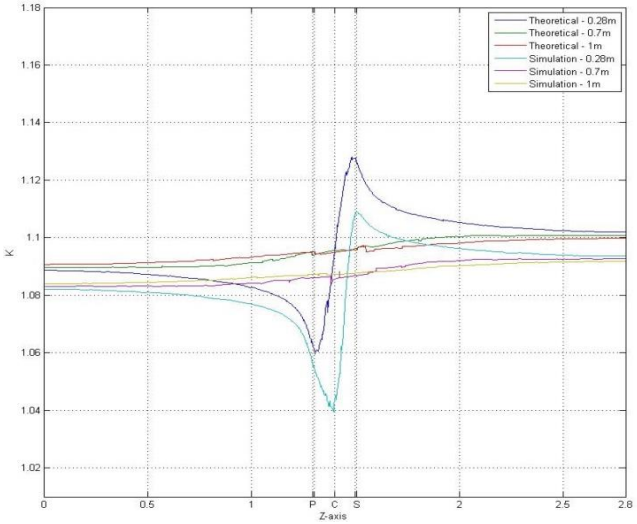

Fig. 16 Ratio K versus Z-axis at V=20cm, T=12:12.

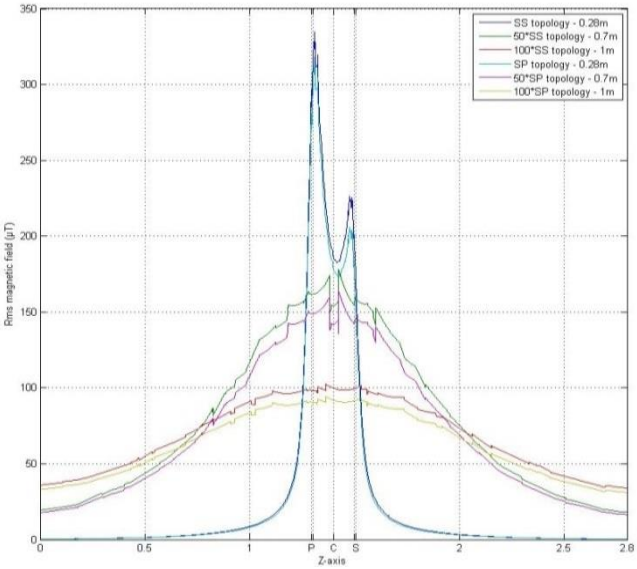

Fig. 17 On-load – Rms magnetic field (μT) versus Z-axis at V=20cm, T=12:12.

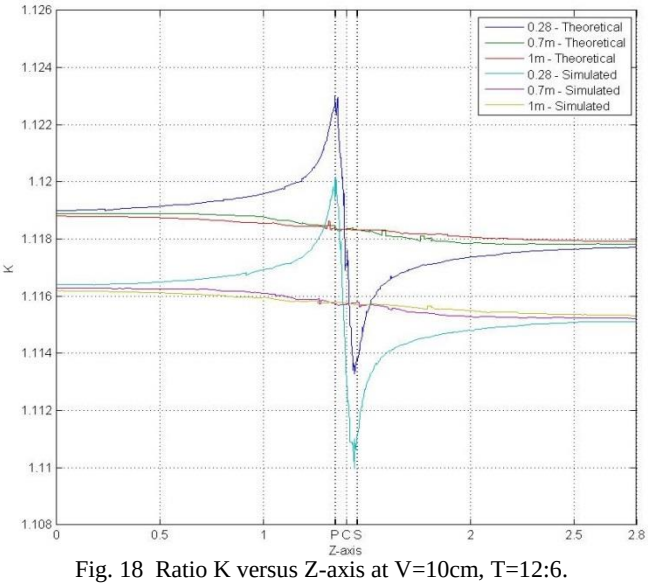

Fig. 18 Ratio K versus Z-axis at V=10cm, T=12:6.

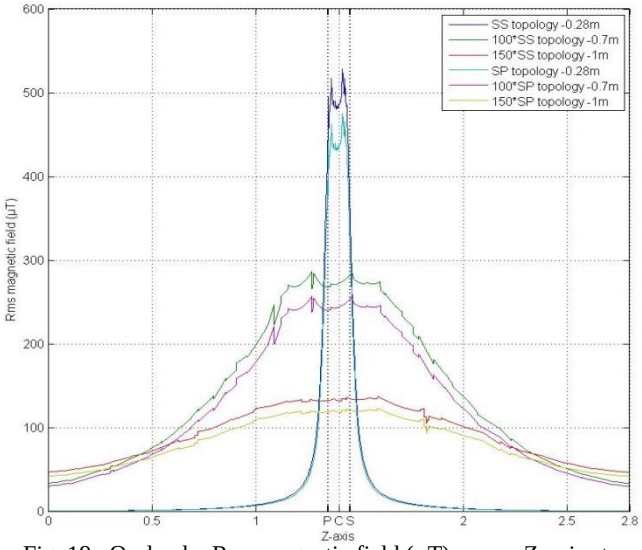

Fig. 19 On-load – Rms magnetic field (μT) versus Z-axis at V=10cm, T=12:6.

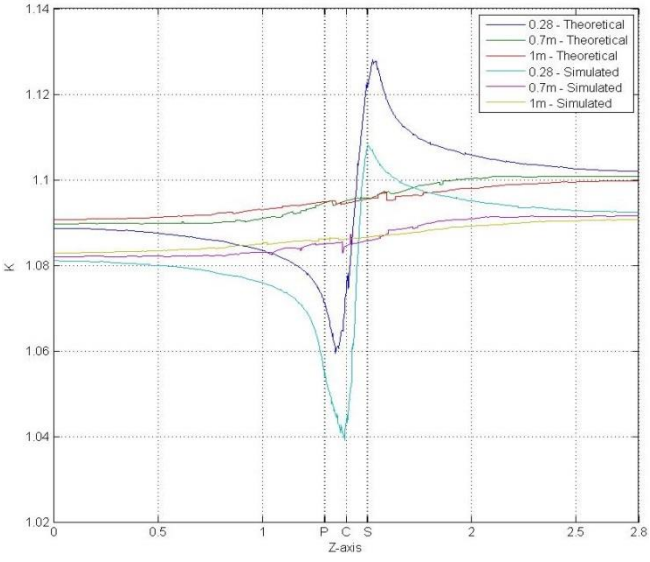

Fig. 20 Ratio K versus Z-axis at V=20cm, T=12:6.

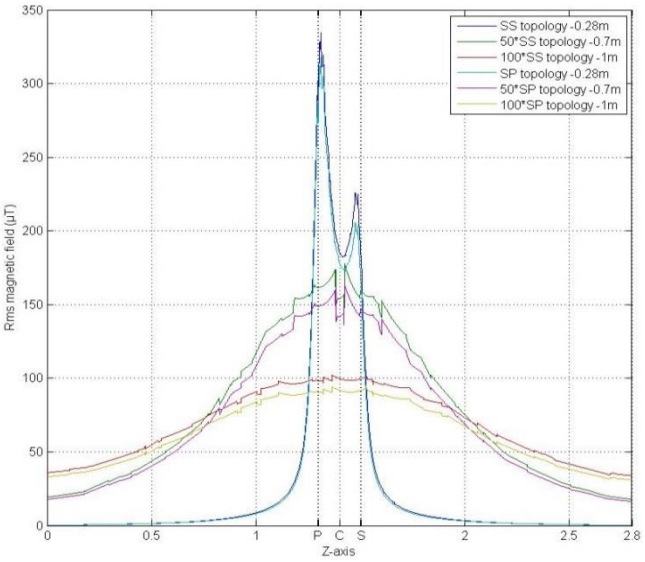

Fig. 21 On-load – Rms magnetic field (μT) versus Z-axis at V=20cm, T=12:6.

Fig. 14 to 21 provides the following information about the magnetic field emissions for the two topologies.

1) Ratio K is always greater than one in Fig. 14, 16. 18 and 20. The same can be seen with help of rms curves of Fig. 15, 17, 19 and 21. SP topology curves are lower than their corresponding SS topology curves in the figures.

2) The theoretical calculated values (24) with this assumption of space angle α equal to 180 degrees shows good compliance with the simulated results in Fig. 14, 16, 18 and 20.

3) Ratio K is identical for Fig. 14, 18 and 16, 20. Ratio K_s/K_p is half for T=12:6 as compared to the ratio for T=12:12 as provided in section 4.2. But on the other hand ratio M/L_s for T=12:6 is two times this ratio for T=12:12 as shown in Table 3. Hence as per (24), the two ratios are identical. This is also visible in terms of rms fields in Fig. 15, 19 and 17, 21.

4) For any H (0.28m, 0.7m or 1m), K has more deviation from the value at C with increase in V as seen by comparing Fig. 14, 16 and 18, 20.

5) For a constant V (Fig. 14, 16, 18 and 20), ratio K shows lesser deviation from value at C with increase in H.

6) Humans are not supposed to be very close (H = 0.28m) to the inductors and hence ratio K can be taken as constant. Using value of K_s/K_p as one, ratio K can be given a simple number by its value at C.

The rms value of voltages and currents for the on-load simulations are presented at last in Table 4. The primary current is 23A rms for 20kHz for all the on-load simulations.

Table 4 Voltages and currents.

T	V (m)	V_{p1} (V)	I_{s1} (A)	V_{p2} (V)	I_{s2} (A)
12:12	0.1	192.40 – j 1.30	0.12 + j 30.67	192.23 – j 0.23	7.71 + j 30.67
12:12	0.2	17.04 – j 0.13	0.05 + j 8.96	17.65 – j 0.05	2.36 + j 9.32
12:6	0.1	191.29 - j 1.29	0.24 + j 60.96	191.11 + j 0.38	15.21+ j 60.98
12:6	0.2	16.94 – j 0.13	0.10 + j 17.81	17.55 – j 0.001	4.66 + j 18.52

5. Conclusion

Series-parallel topology for wireless power transfer system performs better in terms of magnetic flux emissions than its series-series topology counterpart for the same power rating. In very simple words, presence of a part of the secondary magnetic flux which is in phase opposition with the primary flux for series-parallel topology is the reason for the reduced magnetic fields for this topology. Theoretical equations describing the above statement are presented in this paper and are supported by simulations. Ratio of magnetic emissions of the two topologies is practically constant in the surroundings and can be represented by a single number. Also, it is shown that for the same primary current and quality factor, the magnetic emission ratio remains unchanged with varying turn ratio. The experimental verification of this paper would be included in future works.

References

(1) U. K. Madawala, and D. J. Thrimawithana：Current sourced bi-directional inductive power transfer system: IET Power Electronics, vol. 4, p. 471-480 (2011).

(2) A. Neves, D. M. Sousa, A. Roque, J. M. Terras: Analysis of an inductive charging system for a commercial electric vehicle: 14th European Conference on Power Electronics and Applications (EPE 2011), p. 1-10, Aug. 30 2011-Sept. 1 (2011).

(3) U. K. Madawala, and D. J. Thrimawithana：A Bidirectional Inductive Power Interface for Electric Vehicles in V2G Systems: IEEE Transactions on Industrial Electronics,, vol. 58, no. 10, p. 4789-4796 (2011).

(4) W. Chwei-Sen, O. H. Stielau, and G. A. Covic: Design considerations for a contactless electric vehicle battery charger: IEEE Transactions on Industrial Electronics, vol. 52, no. 5, p. 1308-1314 (2005).

(5) H. Kim, J. Cho, S. Ahn, J. Kim, J. Kim：Suppression of Leakage Magnetic Field from a Wireless Power Transfer System using Ferrimagnetic Material and Metallic Shielding: IEEE International Symposium on EMC, Pittsburgh, USA, pp. 640-645 (2012).

(6) J. Kim, J. Kim, S. Kong, H. Kim, I. S. Suh, et al：Coil Design and Shielding Methods for Magnetic Resonant Wireless Power Transfer System: Proceedings of the IEEE , vol. 101, no. 6, p. 1332-1342 (2013).

(7) M. Budhia, G. A. Covic, J. T. Boys, C. Y. Huang：Development of single sided flux couplers for contactless electric vehicle charging: IEEE Transactions On Industrial Electronics, vol 60., no 1., p. 318-328 (2013).

(8) M. G. Egan, D. L. O'Sullivan, J. G. Hayes, S. E. Schulz, J. T. Hall：Power-Factor-Corrected Single-Stage Inductive Charger for Electric Vehicle Batteries: IEEE Transactions on Industrial Electronics, vol. 54, no. 2, p. 1217-1226, (2007).

(9) M. Budhia, G. A. Covic, J. T. Boys：Design and Optimization of Circular Magnetic Structures for Lumped Inductive Power Transfer Systems: IEEE Transactions On Power Electronics, vol 26., no 11., p. 3096-3108, (2011).

(10) T. Batra, E. Schaltz：Magnetic Field Emissions for Ferrite and Non-Ferrite Geometries for Wireless Power Transfer to Vehicles: Journal of Applied Physics – Special Edition, in press.

(11) T. Batra, E. Schaltz：Space Profile of Magnetic Fields for Wireless Power Transfer to Vehicles: IEEE Energy Conversion Congress and Expo. 2014 – Submitted.

(12) T. Batra, E. Schaltz：Magnetic Emissions Space Profile of for Ferrite and Non-Ferrite based Geometries for Wireless Power Transfer to Vehicles: Intermag Conference 2014 – Accepted.

5.5.2. PhD paper 10

This was originally published with following details.

{10} T. Batra, E. Schaltz, “Magnetic field emission comparison for series-parallel and series-series wireless power transfer to vehicles – part 2/2", Proceedings of EVTEC and APE, pp 2014436, 2014.

20144036

MAGNETIC FIELD EMISSION COMPARISON FOR SERIES-PARALLEL AND SERIES-SERIES WIRELESS POWER TRANSFER TO VEHICLES – PART 2/2

Tushar Batra Erik Schaltz

Department of Energy Technology, Aalborg University
Pontoppidanstraede 101, Aalborg, Denmark (E-mail: tba@et.aau.dk)
(The work has financially been supported by The Danish Council for Strategic Research)

Presented at the EVTeC and APE Japan on May 22, 2014

ABSTRACT: Series-series and series-parallel topologies are the most favored topologies for design of wireless power transfer system for vehicle applications. The series-series topology has the advantage of reflecting only the resistive part on the primary side. On the other hand, the current source output characteristics of the series-parallel topology are more suited for the battery of the vehicle. This paper compares the two topologies in terms of magnetic emissions to the surroundings for the same input power, primary current, quality factor and inductors. Theoretical and simulation results show that the series-parallel topology emits lesser magnetic field to the surroundings as compared to its series-series counterpart. The results have been provided for ratio of the magnetic emissions for the two topologies at different quality factor, vertical distance between the inductors and turn ratio of the coils.

KEY WORDS: EV and HV systems, Wireless power transfer, Magnetic fields, Series-series topology, Series-parallel topology [A3]

1. Introduction

Electromagnetic induction is the foundation principle of electrical machines. Researchers of today are interested in both stationary and on-line wireless charging [(1)] of electric vehicles using this principle. The concept of wireless power transfer (WPT) is not new and has been used in applications for a considerable time in the bio-medical industry [(2)]. A block diagram of WPT system is provided below in Fig. 1.

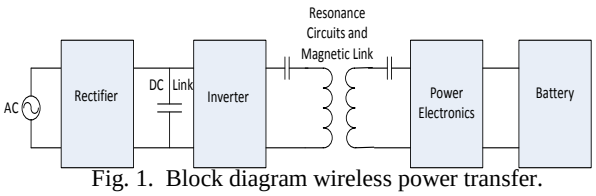

Fig. 1. Block diagram wireless power transfer.

The grid voltage in this system is first rectified to feed the DC-link capacitor which in turn feeds the inverter [(3)]. Power is transferred from the primary coil to the secondary coil by means of magnetic fields. An air-gap of 10 cm to 20 cm is present between the two inductors of WPT for vehicle applications. The magnetic field path as a result is dominantly air for this system. These fields can potentially harm nearby human beings and equipment and are required to comply with the guidelines [(4)]. Active and passive shielding [(1)] are used in the design of inductors to reduce the magnitude of the fields in the surroundings.

Power electronics on the secondary side is used to control flow of power and current into the battery of vehicle. Capacitors are required on the primary and secondary sides for unity power factor operation and to boost the power transfer capability of the system. The capacitors are connected in series or parallel order to the corresponding inductors. The four topologies [(5)] as a result for the system are series-series (SS), series-parallel (SP), parallel-series (PS) and parallel-parallel (PP). The magnetic emissions of the first two topologies are under investigation in this paper. SP topology having current source output characteristics is favored for the battery over the voltage source output characteristics of SS topology. On the other hand, SS topology has the advantage of having only resistive reflection on the primary side as compared to resistive and capacitive reflection for SP topology.

This paper compares the magnetic emissions of the two topologies for similar input power, primary current, quality factor and inductors. Theoretical and simulations show that SP topology emits lesser magnetic fields to the surroundings as compared to SS topology. The two currents in SS topology are orthogonal to each other whereas the phase angle between the two currents is lower than ninety degrees in SP topology. This leads to reduction of the primary magnetic flux by a component of the secondary magnetic flux in SP topology. This reduction depends on the quality factor, coupling factor, turn ratio and ratio of distance of the coils from the measurement point. In a parallel publication, variation in the emissions reduction for the two topologies were discussed for different horizontal distance, turn ratio and coupling factor by the same authors. This is the second part of the same paper and in this part; variation in the reduction is provided for different quality factor, coupling factor and turn ratio. First of all it is shown in the paper that this reduction decreases with increase in the quality factor of the system. It is also observed from the results that for system having equal number of coil turns and lower coupling factor the maximum reduction point occurs at higher quality factor operation and vice versa.

2. Sample geometry

The sample geometry used in the paper is introduced in this section. Side and top views of the geometry are presented below in Fig. 2.

(a) Side view

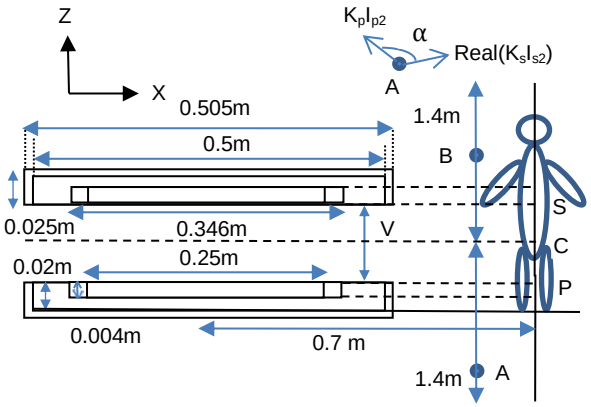

(b) Top view

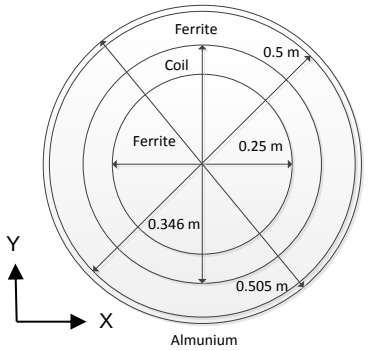

Fig. 2 Sample Geometry.

Ferrite and aluminum are used as passive shields [1, 6] in the system. Litz wire is used in both the coils. Results in this paper have been presented for two set of turn ratio (T) i.e. 12:12 and 12:6. A simplification for finite element simulations has been made that for the secondary inductor the space taken by the coil is same for both the turn ratio. Details of the coils [4] and shielding materials are provided in Table 1 below.

Table 1 Coils and shielding materials.

Property	Value
Number of parallel conductors in each turn	810
Diameter of parallel conductor	0.1 mm
Outer diameter of coil	4 mm
Conductivity of conductor	6×10^7 (S/m)
Relative permeability of ferrite	2300
Conductivity of aluminum	3.7×10^7 (S/m)

3. Theory

3.1. Nomenclature

The symbols used in the paper are first summarized in Table 2. The subscript letter '1' and '2' refer to SS and SP topology respectively. The inductors, secondary capacitor and resonance frequency are same for both the topologies. Value of the primary capacitor on the other hand is different [5] for the two topologies for maintaining unity power factor operation [5].

Table 2 Symbols.

Symbol	Name		Symbol	Name
I_{p1}, I_{p2}	Primary currents		I_{s1}, I_{s2}	Secondary currents
V_{p1}, V_{p2}	Primary voltages		P_1, P_2	Input Power
M	Mutual inductance		L_p, L_s	Primary and Secondary self-inductance
C_{p1}, C_{p2}	Primary capacitors		C_s	Secondary capacitor
R_1, R_2	Load resistance		Q_1, Q_2	Quality factor
w	Frequency		w_r	Resonance frequency

2.2. Series-series topology

Fundamental mode analysis (FMA) [7] equivalent circuit of the topology is provided below in Fig. 3.

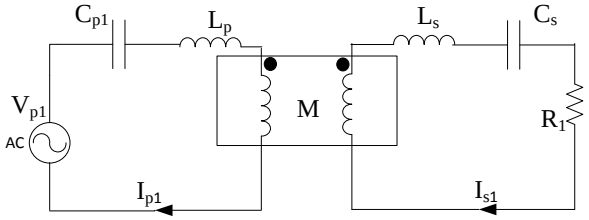

Fig. 3 FMA equivalent circuit series-series topology.

Expressions for the voltage equations, resonance frequency and quality factor of the system are provided below in (1) to (4)

$$\left(jwL_p+\frac{1}{jwC_{p1}}\right)I_{p1}-jwMI_{s1}=V_{p1} \quad (1)$$

$$\left(jwL_s+\frac{1}{jwC_s}\right)I_{s1}+R_1I_{s1}=jwMI_{p1} \quad (2)$$

$$w_r=\frac{1}{\sqrt{L_pC_{p1}}}=\frac{1}{\sqrt{L_sC_s}} \quad (3)$$

$$Q_1=\frac{w_rL_s}{R_1}. \quad (4)$$

At resonant operation, (3) will be valid. Using (3) and (4), (1) and (2) will be transformed to (5) and (6). The input power is given by (7).

$$V_{p1}=\frac{w_rM^2}{L_s}Q_1I_{p1} \quad (5)$$

$$I_{s1}=jM\frac{Q_1}{L_s}I_{p1}. \quad (6)$$

$$P_1=\frac{w_rM^2}{L_s}Q_1I_{p1}^2 \quad (7)$$

WPT systems use ferrite to reduce magnetic emissions and increase the power transfer capability of the system. But due to the presence of the large air gap, maximum magnetic field reached in ferrite cores of these systems is very less as compared to saturation magnetic field for ferrite. Hence, linear coefficient of permeability [8] is assumed for ferrite. Hence magnetic fields (B_{p1} and B_{s1}) at any point in the surroundings due to the primary and secondary coils can be written as follows

$$B_{p1}=K_pI_{p1} \quad (8)$$

$$B_{s1}=K_sI_{s1}. \quad (9)$$

K_p and K_s are corresponding constants for the primary and secondary coils for that point. As the inductors and the surroundings are identical for the two topologies, K_p and K_s are also same for the two. The number of turns for each coil is contained in the corresponding constant and is proportional to it. As the current for the two topologies are orthogonal to each other as shown in (6), hence the resultant field (B_1) at any point is

$$|B_1|=\sqrt{|I_{p1}K_p|^2+|I_{s1}K_s|^2} \quad (10)$$

Using (6), (10) can be transformed to

$$|B_1|=I_{p1}\sqrt{K_p{}^2+\left(K_sQ_1\frac{M}{L_S}\right)^2}. \quad (11)$$

2.3. Series-Parallel topology

FMA equivalent circuit for this topology is provided next in Fig. 4.

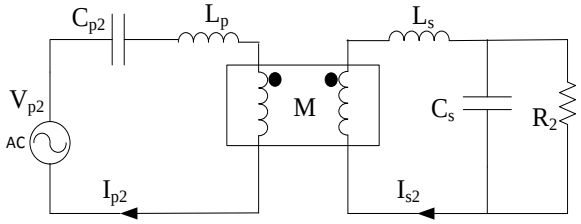

Fig. 4 FMA equivalent circuit series-parallel topology.

Expressions for the voltage equations, resonance frequency, primary capacitor and quality factor for the system are provided in (11) to (15)

$$\left(jwL_p+\frac{1}{jwC_{p2}}\right)I_{p2}-jwMI_{s2}=V_{p2} \quad (12)$$

$$jwMI_{p2}=\left(jwL_s+\frac{\frac{1}{jwC_s}R_2}{R_2+\frac{1}{jwC_s}}\right)I_{s2} \quad (13)$$

$$w_r=\frac{1}{\sqrt{L_sC_s}} \quad (14)$$

$$C_{p2}=\frac{L_s}{(L_pL_s-M^2)w_r^2} \quad (15)$$

$$Q_2=\frac{R_1}{w_rL_s} \quad (16)$$

At resonant operation, (14) will be valid. Using (14), (15) and (16), (12) and (13) will be transformed to (17) and (18). The input power for this topology is given by (19).

$$V_{p2}=\frac{w_rM^2}{L_s}Q_2I_{p2} \quad (17)$$

$$I_{s2}=M\left(\frac{1}{L_s}+j\frac{Q_2}{L_s}\right)I_{p2}. \quad (18)$$

$$P_2=\frac{w_rM^2}{L_s}Q_2I_{p2}^2 \quad (19)$$

The resultant magnetic field using (8), (9), (18) and space angle α between the fields in Fig. 2(a) and taking the primary current (I_{p2}) as reference phasor with phase angle zero is

$$|B_2|=\sqrt{\left[(K_pI_{p2})^2+(\text{Real}(K_sI_{s2}))^2+2\,\text{Real}(K_sI_{s2})\,K_pI_{p2}\cos\alpha\right]+\left[\text{Imaginary}(K_sI_{s2})\right]^2} \quad (20)$$

$$|B_2|=I_{p2}\sqrt{\left[K_p{}^2+\left(K_s\frac{M}{L_s}\right)^2+2K_pK_s\frac{M}{L_s}\cos\alpha\right]+\left(\frac{M}{L_S}Q_2K_s\right)^2} \quad (21)$$

2.4. Comparison

The two topologies have the same input power using (7) and (19) when

$$Q_1=Q_2=Q \quad \& \quad I_{p1}=I_{p2} \quad (22)$$

At this same power, ratio (K) of the magnetic fields using (11), (21) and (22)

$$K=\frac{|B_1|}{|B_2|}=\sqrt{\frac{1+\left(Q\frac{MK_s}{L_SK_p}\right)^2}{\left[1+\left(\frac{K_sM}{K_pL_s}\right)^2+2\frac{K_s}{K_p}\frac{M}{L_s}\cos\alpha\right]+\left(Q\frac{MK_s}{L_SK_p}\right)^2}} \quad (23)$$

The angle α is 180 degrees in the surroundings on account of principle of electromagnetic induction. Only very close to the inductor, the angle α has value other than 180 degrees and is explained in the next section. Hence as per (23), SP topology emits less magnetic fields as compared to SS topology for the same input power rating.

4. Results

4.1. Space angle α

The angle α can be seen with the help of Fig. 5. This figure is the arrow representation of the magnetic fields on a normalized scale. Outer cylinder has the magnetic potential zero and has dimensions of 3m diameter and 3m height. The coils are located at the center of the cylinder.

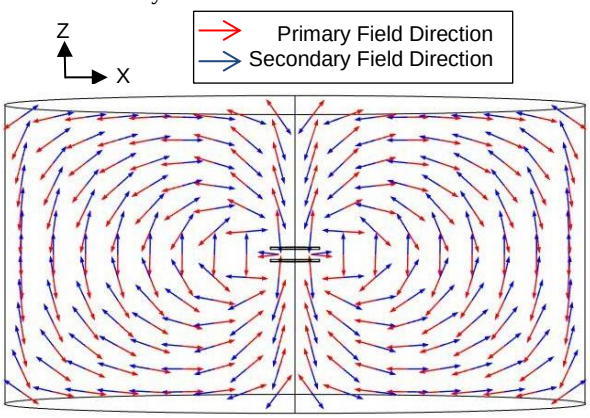

Fig. 5 Primary and secondary magnetic field directions.

As seen in Fig. 5, space angle is 180 degrees for nearly all points in the space and hence (23) is transformed to (24).

$$K=\frac{|B_1|}{|B_2|}=\sqrt{\frac{1+\left(Q\frac{M K_s}{L_S K_p}\right)^2}{\left(1-\frac{M K_s}{L_S K_p}\right)^2+\left(Q\frac{M K_s}{L_S K_p}\right)^2}} \quad (24)$$

4.2. Ratio K_s/K_p

Ratio K_s/K_p can be found by plotting no-load curves [9, 10, 11] for the system at same current (23A at 20kHz). Using (8) and (9), ratio of the magnetic fields of the two coils (B_s and B_p) at no-load conditions is equal to ratio K_s/K_p.

$$\frac{B_s}{B_p}=\frac{K_s}{K_p} \quad (25)$$

K_s/K_p curves and rms magnetic fields for the two coils at different quality factor (Q), vertical distance (V) and turn ratio (T) are presented in Fig. 6 to 13.

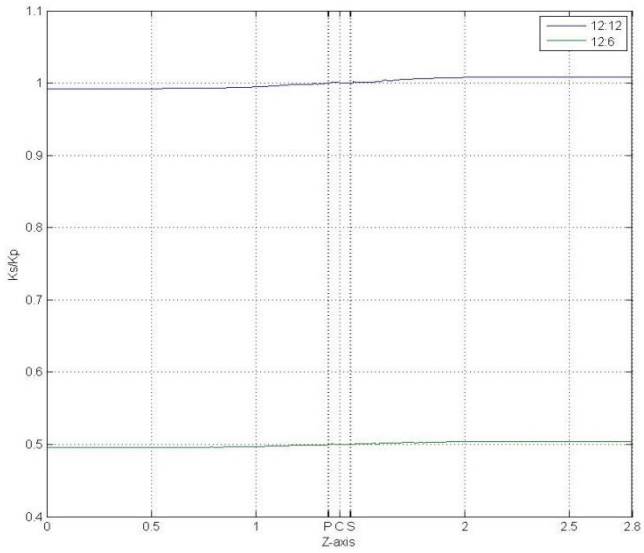

Fig. 6 Ratio K_s/K_p versus Z-axis at V=10cm.

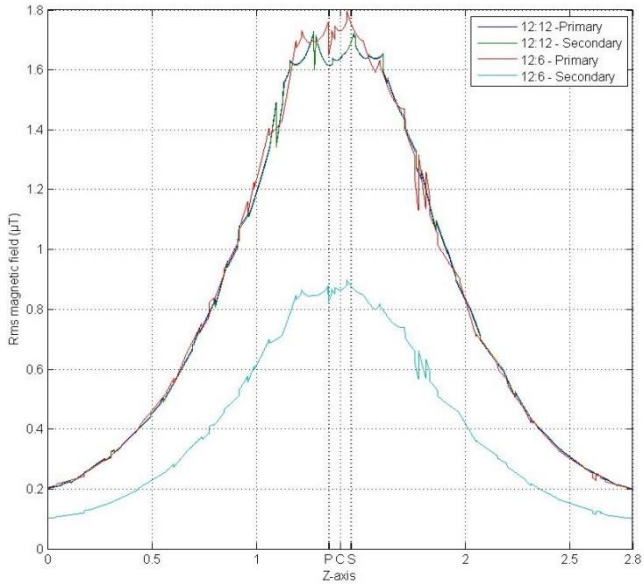

Fig. 7 No-load – Rms magnetic field (μT) versus Z-axis at V=10cm.

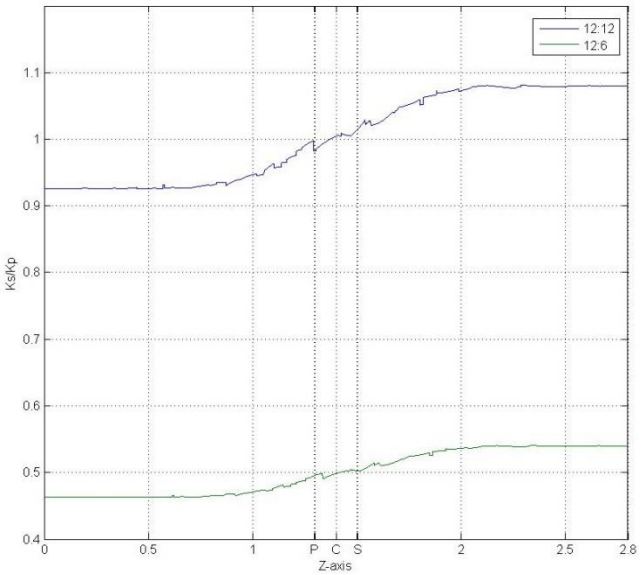

Fig. 8 Ratio K_s/K_p versus Z-axis at V=20cm.

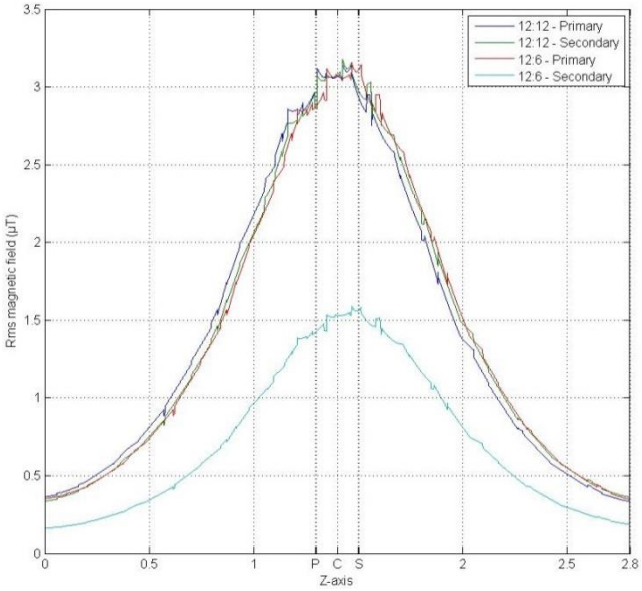

Fig. 9 No-load – Rms magnetic field (μT) versus Z-axis at V=20cm.

Following points are observed from Fig. 6 to 9. Primary and secondary zones [9] are defined as points to the left and right of center (C) in the paper.

1) Value of ratio K_s/K_p is equal to one and half as shown in Fig. 6 and 8. There is a small deviation from its value at C but for practical purposes can be ignored. Fig. 7 and 9 provide the same information in terms of rms magnetic fields.

2) K_s and K_p are proportional to the number of turns for the corresponding coil. Therefore value of ratio K_s/K_p at C is half for T=12:6 as compared to the ratio for T=12:12 in Fig. 6 and 8.

3) With increase in V for any fixed point in the secondary zone, ratio K_s/K_p increases for both T in Fig. 6 and 8.

4) Aluminum and ferrite both have an effect on bringing space maxima's of the indivual coils closer to C as compared to geometries that do not have passive shielding. Details of the space profile curves have been discussed by the same authors in [9, 10, 11] and will not be provided here again.

4.3. Ratio K

Quality factors of 4 to 10 are used for designing these systems. Theoretical ratio K can be calculated by using value of ratio K_s/K_p from Fig. 6 and 8 and applying in (24). The remaining parameters used for the calculation are provided in Table 3.

Table 3 Circuit Parameters.

T	V(m)	L_p(μH)	L_s(μH)	M(μH)	M/L_s
12:12	0.1	147.09	147.09	49.59	0.34
12:6	0.1	147.09	36.77	24.80	0.67
12:12	0.2	138.69	138.69	14.21	0.10
12:6	0.2	138.69	34.67	7.10	0.20

Simulated value of this ratio is obtained from on-load simulations on Comsol. Rms magnetic field for the two topologies from on-load simulations and their ratio K for both set of results at different Q, V and T are presented in Fig. 10 to 17.

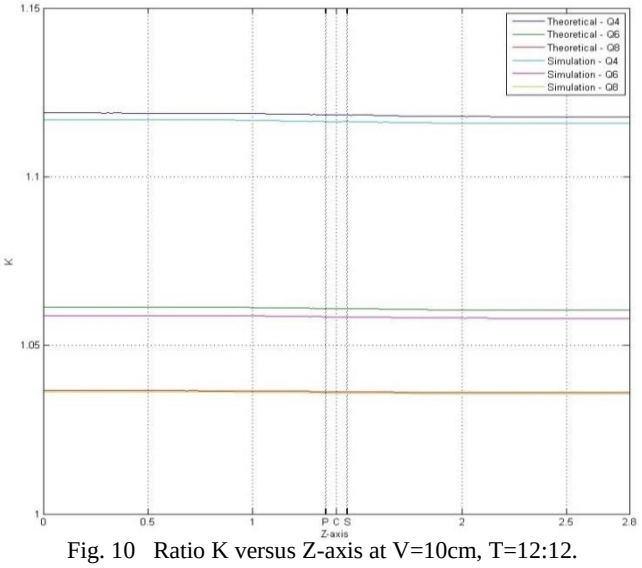

Fig. 10 Ratio K versus Z-axis at V=10cm, T=12:12.

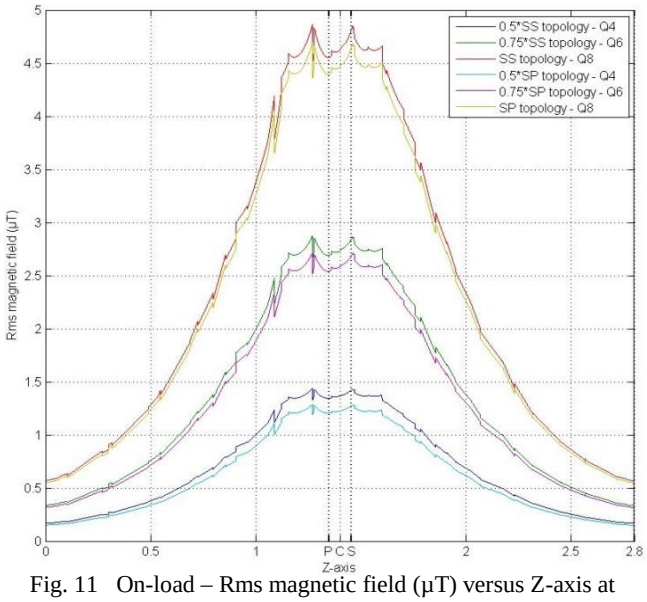

Fig. 11 On-load – Rms magnetic field (μT) versus Z-axis at V=10cm, T=12:12.

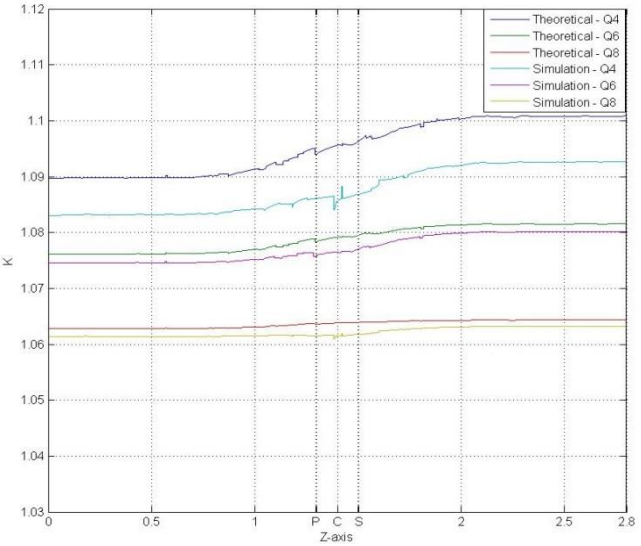

Fig. 12 Ratio K versus Z-axis at V=20cm, T=12:12.

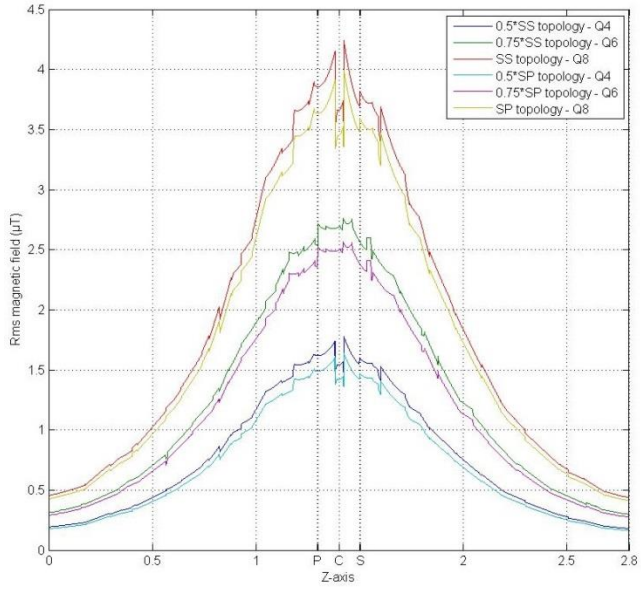

Fig. 13 On-load – Rms magnetic field (μT) versus Z-axis at V=20cm, T=12:12.

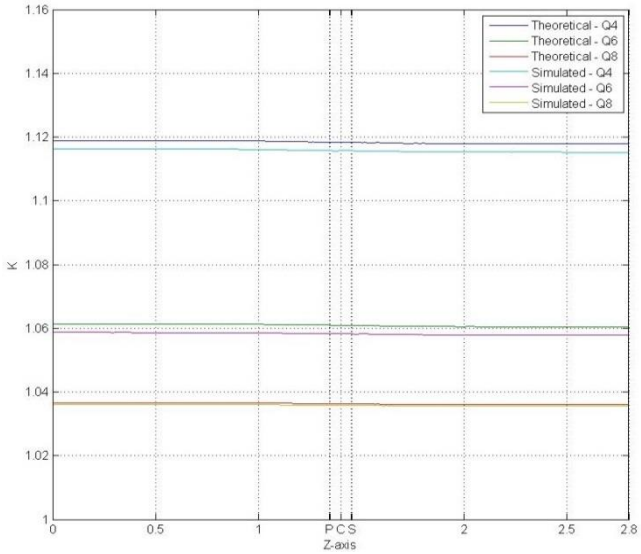

Fig. 14 Ratio K versus Z-axis at V=10cm, T=12:6.

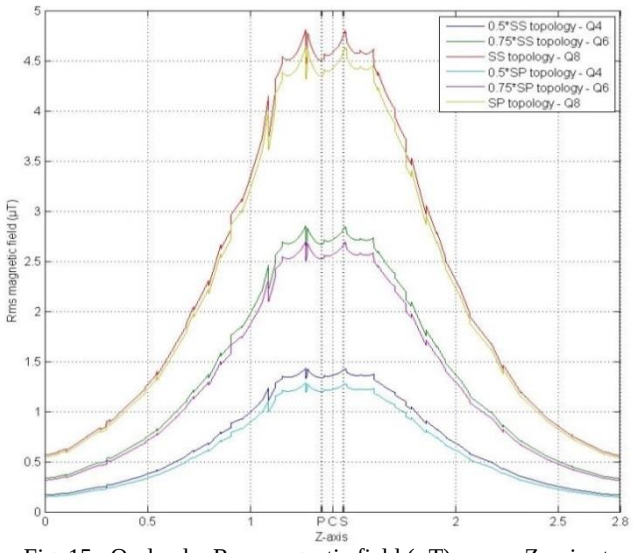

Fig. 15 On-load – Rms magnetic field (μT) versus Z-axis at V=10cm, T=12:6.

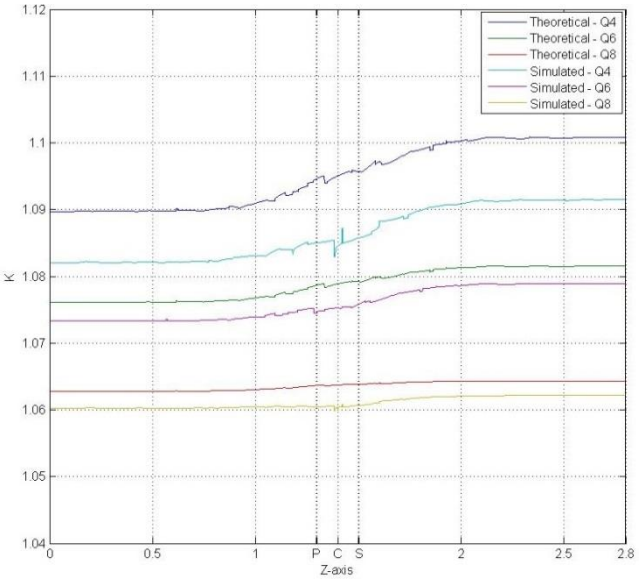

Fig. 16 Ratio K versus Z-axis at V=20cm, T=12:6.

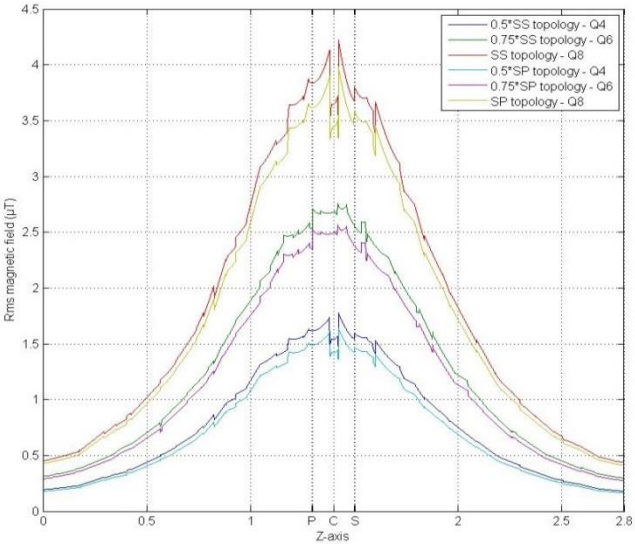

Fig. 17 On-load – Rms magnetic field (μT) versus Z-axis at V=20cm, T=12:6.

The observations from Fig. 10 to 17 are provided below.

1) Ratio K is always greater than one in Fig. 10, 12, 14 and 16. The same can be seen with help of rms curves of Fig. 11, 13, 15 and 17. SP topology curves are lower than their corresponding SS topology curves in the figures.

2) The theoretical calculated values (24) with this assumption of space angle α equal to 180 degrees shows good compliance with the simulated results in Fig. 10, 12, 14 and 16.

3) Ratio K has small deviation on both sides from its value at C as shown in Fig. 10, 12, 14 and 16. By neglecting the deviation, ratio K can be calculated using (24) as a single number and can be used to investigate the difference in magnetic emissions for the two topologies at same input power for a given combination of (K_s /K_p), (M/L_s) and Q.

3) For higher coupling factor (Q8), ratio K increases with V as shown in Fig. 10, 12 and 14, 16. On the other hand, ratio K for the other two quality factors (Q6 and Q4) shows the opposite trend. But this is a specific observation for the given set of parameters. For general analysis, ratio K in (24) is plotted against $K_s/K_p*M/L_s$ for different quality factor as provided in Fig. 18.

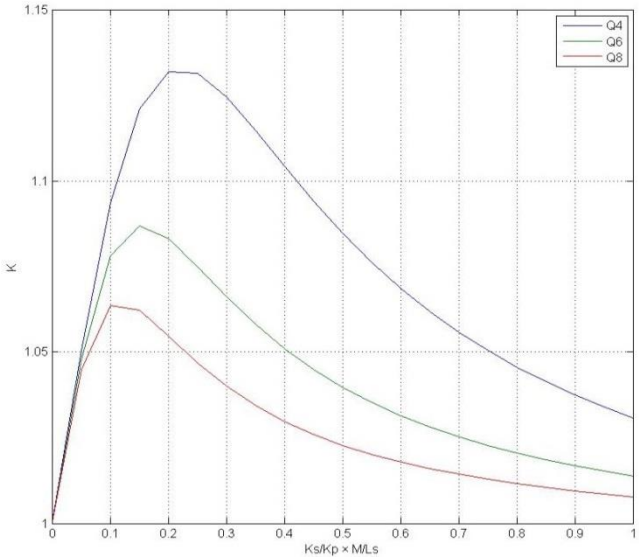

Fig. 18 Ratio K versus ratio $K_s/K_p*M/L_s$.

For obtaining the point of maxima in Fig. 18, (24) is differentiated w.r.t. ratio $K_s/K_p*M/L_s$ and is equated to zero. The value of ratio $K_s/K_p*M/L_s$ for which maxima exists is given by (26).

$$\left(\frac{K_s}{K_p}\frac{M}{L_s}\right)_{max} = \frac{-1+\sqrt{1+4Q^2}}{2Q^2} \quad (26)$$

As factor $4Q^2$ is very greater than one, hence (26) can be simplified to (27).

$$\left(\frac{K_s}{K_p}\frac{M}{L_s}\right)_{max} = \frac{-1+2Q}{2Q^2} \quad (27)$$

Horizontal coordinates of maxima's in Fig. 18 are in agreement with (27). Hence, it can be concluded that for a higher quality factor, the maximum ratio K is at a lower value of ratio $K_s/K_p*M/L_s$ and vice versa. If number of turns are equal for the two coils, ratio K_s/K_p is equal to one and the last statement is valid for coupling factor (M/L_s).

4) Rms magnetic fields in Fig. 11 and 13 are identical to the corresponding field values in Fig. 15 and 17. The secondary turns are half for the second set of figures. But the secondary current becomes double (Table 4 and 5) to compensate for reduction in the number of secondary turns and hence the secondary magneto motive force remains constant. The secondary current becomes double on account of two times increase in value of coupling ratio (M/L_s – Table 3). Ratio K on the same lines is identical for the two sets of T in Fig. 10, 14 and 12, 16.

5) Ratio K decreases with increase in the quality factor in Fig. 10, 12, 14 and 16. The second term in numerator and denominator of (24) becomes dominant with the increasing quality factor. Hence the ratio approaches unity with the increasing quality factor.

At last, the rms values of voltages and currents for the on-load simulations are presented in Table 4 and 5. The primary current is 23A rms for 20kHz for all the on-load simulations.

Table 4 Voltages and currents – T=12:12.

Q	V (m)	V_{p1} (V)	I_{s1} (A)	V_{p2} (V)	I_{s2} (A)
4	0.1	192.40 – j 1.30	0.12 + j 30.67	192.23 – j 0.23	7.71 + j 30.67
6	0.1	285. 87 – j 2.07	0.19 + j 45.66	286.10 – j 0.45	7.68 + j 45.73
8	0.1	379.44 – j 2.88	0.27 + j 60.66	378.98 – j 0.73	7.68 + j 60.62
4	0.2	17.04 – j 0.13	0.05 + j 8.96	17.65 – j 0.05	2.36 + j 9.32
6	0.2	25.92 – j 0.25	0.06 + j 13.93	25.86 – j 0.13	2.37 + j 13.19
8	0.2	34.00 – j 0.34	0.11 + j 18.46	33.97 – j 0. 17	2.38 + j 18.45

Table 5 Voltages and currents – T=12:6.

Q	V (m)	V_{p1} (V)	I_{s1} (A)	V_{p2} (V)	I_{s2} (A)
4	0.1	191.29 - j 1.29	0.24 + j 60.96	191.11 + j 0.38	15.21+ j 60.98
6	0.1	283. 23 – j 2.05	0.38 + j 90.48	283.52 + j 0.44	15.10 + j 90.62
8	0.1	374.69 – j 2.84	0.54 + j 119.83	374.40 + j 0.44	14.99 + j 119.78
4	0.2	16.94 – j 0.13	0.10 + j 17.81	17.55 – j 0.001	4.66 + j 18.52
6	0.2	25.65 – j 0.25	0.16 + j 27.57	25.62 – j 0.04	4.64 + j 27.56
8	0.2	33.58 – j 0.33	0.23 + j 36.45	33.54 – j 0. 06	4.63 + j 36.43

5. Conclusion

Series-parallel and series-series compensation networks are actively used for design of wireless power transfer system for vehicles. The two topologies have their own set of advantages and disadvantages. But in this paper it is shown that the series-parallel topology has reduced magnetic emissions than the series-series topology for same input power, primary current, inductors and quality factor. The first outcome of the paper is that with increase in the quality factor the reduction becomes less. With help of analytical expressions and simulations it is also shown that a system having lower coupling factor and equal number of turns has a reduction peak at a higher coupling factor and vice versa.

References

(1) J. Kim, J. Kim, S. Kong, H. Kim, I. S. Suh, et al：Coil Design and Shielding Methods for Magnetic Resonant Wireless Power Transfer System: Proceedings of the IEEE , vol. 101, no. 6, p. 1332-1342 (2013).

(2) K. M. Silay, C. Dehollain, and M. Declercq：Improvement of power efficiency of inductive links for implantable devices: Research in Microelectronics and Electronics 2008, pp. 229-232, April 25 - June 22 2008.2

(3) U. K. Madawala, and D. J. Thrimawithana：Current sourced bi-directional inductive power transfer system: IET Power Electronics, vol. 4, p. 471-480 (2011).

(4) M. Budhia, G. A. Covic, J. T. Boys, C. Y. Hu4ng：Development of single sided flux couplers for contactless electric vehicle charging: IEEE Transactions On Industrial Electronics, vol 60., no 1., p. 318-328 (2013).

(5) W. Chwei-Sen, O. H. Stielau, and G. A. Covic: Design considerations for a contactless electric vehicle battery charger: IEEE Transactions on Industrial Electronics, vol. 52, no. 5, p. 1308-1314 (2005).

(6) H. Kim, J. Cho, S. Ahn, J. Kim, J. Kim：Suppression of Leakage Magnetic Field from a Wireless Power Transfer System using Ferrimagnetic Material and Metallic Shielding: IEEE International Symposium on EMC, Pittsburgh, USA, pp. 640-645 (2012).

(7) M. G. Egan, D. L. O'Sullivan, J. G. Hayes, S. E. Schulz, J. T. Hall：Power-Factor-Corrected Single-Stage Inductive Charger for Electric Vehicle Batteries: IEEE Transactions on Industrial Electronics, vol. 54, no. 2, p. 1217-1226, (2007).

(8) M. Budhia, G. A. Covic, J. T. Boys：Design and Optimization of Circular Magnetic Structures for Lumped Inductive Power Transfer Systems: IEEE Transactions On Power Electronics, vol 26., no 11., p. 3096-3108, (2011).

(9) T. Batra, E. Schaltz：Magnetic Field Emissions for Ferrite and Non-Ferrite Geometries for Wireless Power Transfer to Vehicles: Journal of Applied Physics – Special Edition, in press.

(10) T. Batra, E. Schaltz：Space Profile of Magnetic Fields for Wireless Power Transfer to Vehicles: IEEE Energy Conversion Congress and Expo. 2014 – Submitted.

(11) T. Batra, E. Schaltz：Magnetic Emissions Space Profile of for Ferrite and Non-Ferrite based Geometries for Wireless Power Transfer to Vehicles: Intermag Conference 2014 – Accepted.

6. Conclusion and scientific contributions

Resonant inductive wireless charging is a promising technology and has capability to enable mass deployment of electric vehicles. This technology has been around for a long time but is still immature from application point of view. This thesis is summary of research work conducted by PhD student Tushar Batra at Department of Energy Technology, Aalborg University on this subject. The first result achieved during the project is that the design process has been improved by adding reflected quality factor to existing design blocks. Addition of this extra block converts the system into an equivalent power source along with the transmission and load. Also, system design parameters of output power, voltage stress and efficiency can be defined as simple functions of existing and added design block. A special focus has been given to the inductor design by first generalizing the design in terms of usage of components. Afterwards two investigations have been made for passive shielding usage optimization with respect to various design parameters, i.e. coupling factor, emissions, weight, dimensions and cost. Results from the first investigation suggest that additional ferrite should be added in center of the inductors as this provides highest increase in the coupling factor per unit weight added. The ferrite and aluminum thickness are reduced in the secondary investigation and results show that reduction in weight and dimensions are much higher than decrease and increase in the power transfer and losses respectively. For cost reduction of the inductors, commonly used high and expensive grade of ferrite is compared with lower and cheaper grade. The results show that there is minor decrease in the output power and efficiency with usage of the lower grade compared to the higher grade. The last result obtained from this project is a semi-analytic method for comparison of magnetic emissions at different value of the coil currents. This method will help in including the emissions in design of the primary and secondary power electronics apart from the inductor design. The semi-analytical method is based on constant ratio of secondary to primary magnetic emissions in far region in the surroundings. This ratio has been termed as space ratio and its constant nature is validated with help of theory, simulations and experiments. With verification of the semi-analytical method, three applications have been addressed in the project. In the first application, it is shown that selection of higher load quality provides comparably lower increase in the emissions than increase in the output power for similar output power, inverter current and switching frequency. The first application has been provided for SS and SP topologies. An active shielding method has been developed in the second application. In the proposed method, the secondary capacitor value is increased from the resonance value and hence component of the secondary current in phase with the primary current is increased. This leads to cancellation of the primary field and reduction in Rms value of the field. This application has been validated with FEM simulations and experiments for SS topology and only with FEM simulations for SP topology. The final application deals with comparing the emissions of SS and SP topologies at similar input and output conditions. Lower emissions for SP topology compared to SS topology derived using the semi-analytical method is verified with FEM simulations and experiments for this application.

7. Future works

At the end, the following areas on wireless charging have been shortlisted for further research in future projects.

1) Development of less computational intensive methods for calculation of coil internal resistance.

2) Optimization of passive shielding usage in the inductor design w.r.t. coupling factor, losses, emissions, weight, dimensions and cost.

3) Investigation on optimal operational frequency w.r.t. output power, efficiency, emissions, weight, dimensions and cost.

4) Investigating second form of this technology: dynamic wireless charging solution for electric vehicles.

References

[1] N. Tesla, “Apparatus for Transmission of Electrical Energy”, US Patent No. 649,576, 1900.

[2] N. Tesla, “System of Transmission of Electrical Energy”, US Patent No. 649,621, 1900.

[3] K. M. Silay, C. Dehollain, and M. Declercq, “Improvement of power efficiency of inductive links for implantable devices”, Research in Microelectronics and Electronics 2008, pp. 229-232, April 25 - June 22 2008.

[4] P. T. Theilmann, P. M. Asbeck, "An Analytical Model for Inductively Coupled Implantable Biomedical Devices with Ferrite Rods", IEEE Transactions on Biomedical Circuits and Systems, vol.3, no.1, pp.43-52, Feb. 2009.

[5] R. R. Harrison, "Designing Efficient Inductive Power Links for Implantable Devices", IEEE International Symposium on Circuits and Systems (ISCAS) 2007, vol., no., pp.2080-2083, 27-30 May 2007.

[6] S. Dieckerhoff, M. J. Ruan, R. W. De Doncker, "Design of an IGBT-based LCL-resonant inverter for high-frequency induction heating", Conference Record of IEEE Industry Applications Conference 1999, Thirty-Fourth IAS Annual Meeting, vol.3, no., pp.2039-2045, 1999.

[7] U. Schwarzer, R. W. De Doncker, "Power losses of IGBTs in an inverter prototype for high frequency inductive heating applications," 27th Annual Conference of IEEE Industrial Electronics Society (IECON) 2001, vol.2, no., pp.793-798 vol.2, 2001.

[8] S. E. Shladover, ‘‘Highway electrification and automation’’, California PATH Program, Univ. California Berkeley, Berkeley, CA, USA, UCB-ITS-PRR-92-17, 1992.

[9] Roadway powered electric vehicle project track construction and testing program phase 3D, Univ. California Berkeley, Berkeley, CA, USA, PATH Res. Rep., UCB-ITS-PRR-94-07,Mar. 1994.

[10] O. H. Stielau, G. A. Covic, "Design of loosely coupled inductive power transfer systems", International Conference on Power System Technology (PowerCon) 2000, vol.1, no., pp.85-90 vol.1, 2000.

[11] H. Sakamoto, K. Harada, S. Washimiya, K. Takehara, Y. Matsuo, F. Nakao, “Large air-gap coupler for inductive charger [for electric vehicles]”, IEEE Transactions on Magnetics, vol. 35, no. 5, pp. 3526-3528, 1999.

[12] A. Kurs, A. Karalis, R. Moffatt, J. D. Joannopoulos, P. Fisher, and M. Soljacic, “Wireless Power Transfer via Strongly Coupled Magnetic Resonances”, Science, 317, 5834, pp. 83-86, 2007.

[13] http://www.ikea.com/us/en/catalog/categories/departments/wireless_charging/30611/

[14] https://www.pluglesspower.com/shop/

[15] F. Musavi, M. Edington, and W. Eberle, “Wireless power transfer: A survey of EV battery charging technologies”, Energy Conversion Congress and Exposition (ECCE) 2012, pp. 1804-1810, 15-20 Sept. 2012.

[16] S. Ahn, J. Kim, “Magnetic Field Design for High Efficient and Low EMF Wireless Power Transfer in On-Line Electric Vehicle”, Proceedings of 5th European Conference on Antennas and Propagation - EUCAP 2011, pp. 3979-3982, 2011.

[17] J. Shin, S. Shin, Y. Kim, S. Ahn, S. Lee, G. Jung, S. Jeon; D. Cho, "Design and Implementation of Shaped Magnetic-Resonance-Based Wireless Power Transfer System for Roadway-Powered Moving Electric Vehicles", IEEE Transactions on Industrial Electronics, vol.61, no.3, pp.1179-1192, March 2014.

[18] Y. J. Jang, Y. D. Ko, S. Jeong, "Optimal design of the wireless charging electric vehicle", IEEE International Electric Vehicle Conference (IEVC) 2012, vol., no., pp.1-5, 4-8 March 2012.

[19] G. A. Covic, J. T. Boys, M. L. G. Kissin, H. G. Lu, "A Three-Phase Inductive Power Transfer System for Roadway-Powered Vehicles", IEEE Transactions on Industrial Electronics, vol.54, no.6, pp.3370-3378, Dec. 2007.

[20] J. Kim, J. Kim, S. Kong, H. Kim, I. S. Suh, N. P. Suh, D. H. Sho, J. Kim, S. Ahn, ”Coil Design and Shielding Methods for a Magnetic Resonant Wireless Power Transfer System”, Proceedings of the IEEE , vol. 101, no. 6, pp. 1332-1342, 2013.

[21] A. Neves, D. M. Sousa, A. Roque, J. M. Terras, “Analysis of an inductive charging system for a commercial electric vehicle”, 14th European Conference on Power Electronics and Applications (EPE 2011), pp. 1-10, Aug. 30 2011-Sept. 1 2011.

[22] M. G. Egan, D. L. O'Sullivan, J. G. Hayes, M. J. Willers, C. P. Henze, “Power-Factor-Corrected Single-Stage Inductive Charger for Electric Vehicle Batteries”, IEEE Transactions on Industrial Electronics, vol. 54, no. 2, pp. 1217-1226, 2007.

[23] W.Chwei-Sen, O.H.Stielau, and G.A.Covic, “Design considerations for a contactless electric vehicle battery charger”, IEEE Transactions on Industrial Electronics, vol. 52, no. 5, pp. 1308-1314, 2005.

[24] U. K. Madawala, D. J. Thrimawithana, "Modular-based inductive power transfer system for high-power applications", IET Power Electronics, vol.5, no.7, pp.1119-1126, August 2012.

[25] M. Budhia, G. A. Covic, J. T. Boys, “Design and Optimization of Circular Magnetic Structures for Lumped Inductive Power Transfer Systems”, IEEE Transactions On Power Electronics, vol 26., no 11., pp. 3096-3108, 2011.

[26] M. Budhia, G. A. Covic, J. T. Boys, “Development of single sided flux couplers for contactless electric vehicle charging”, IEEE Transactions On Industrial Electronics, vol 60., no 1., pp. 318-328, 2013.

[27] M. Budhia, G. A. Covic, J. T. Boys, Chang-Yu Hwang, “Development and evaluation of single sided flux couplers for contactless electric vehicle charging”, Energy Conversion Congress and Exposition (ECCE) 2011, vol., no., pp. 614-621, 2011.

[28] W. Chwei-Sen, O. H. Stielau, and G. A. Covic, “Design considerations for a contactless electric vehicle battery charger”, IEEE Transactions on Industrial Electronics, vol. 52, no. 5, pp. 1308-1314, 2005.

[29] Y. J. Jang, Y. D. Ko, "System architecture and mathematical model of public transportation system utilizing wireless charging electric vehicles", 15th International IEEE Conference on Intelligent Transportation Systems (ITSC) 2012, vol., no., pp.1055-1060, 16-19 Sept. 2012.

[30] D. J. Thrimawithana, U. K. Madawala, "Current sourced bi-directional inductive power transfer system", IET Power Electronics, vol. 4, no. 4, pp. 471-480, 2011.

[31] D. J. Thrimawithana, U. K. Madawala, "A Bidirectional Inductive Power Interface for Electric Vehicles in V2G Systems", IEEE Transactions on Industrial Electronics,, vol. 58, no. 10, pp. 4789-4796, 2011.

[32] D. J. Thrimawithana, U. K. Madawala, "A primary side controller for inductive power transfer systems", IEEE International Conference on Industrial Technology (ICIT) 2010, vol., no., pp.661-666, 14-17 March 2010.

[33] C. Wang, G. A. Covic, O. H. Stielau, "Investigating an LCL load resonant inverter for inductive power transfer applications", IEEE Transactions on Power Electronics, vol.19, no.4, pp.995-1002, July 2004.

[34] U. K. Madawala, D. J. Thrimawithana, A. Francis, M. Neath, "Magnetic modeling of a high-power three phase bi-directional IPT system", 37th Annual Conference on IEEE Industrial Electronics Society (IECON) 2011, vol., no., pp.1414-1419, 7-10 Nov. 2011.

[35] T. Diekhans, F. Stewing, G. Engelmann, H. Van Hoek, R. W. De Doncker, "A systematic comparison of hard- and soft-switching topologies for inductive power transfer systems", 4th International Electric Drives Production Conference (EDPC) 2014, vol., no., pp.1-8, Sept. 30-Oct. 1 2014.

[36] H. Moon, S. Kim, H. Ho Park, S. Ahn, "Design of a Resonant Reactive Shield With Double Coils and a Phase Shifter for Wireless Charging of Electric Vehicles", IEEE Transactions on Magnetics, vol.51, no.3, pp.1-4, March 2015.

[37] J. M. Miller, C. P. White, O. C. Onar, P. M. Ryan, "Grid side regulation of wireless power charging of plug-in electric vehicles", Energy Conversion Congress and Exposition (ECCE), pp. 261-268, 15-20 Sept. 2012.

[38] J. D. Heebl, E. M. Thomas, R. P. Penno, A. Grbic, "Comprehensive Analysis and Measurement of Frequency-Tuned and Impedance-Tuned Wireless Non-Radiative Power-Transfer Systems", IEEE Antennas and Propagation Magazine, vol. 56, no. 4, pp. 44-60, 2014.

[39] G. A. Covic, J. T. Boys, "Modern Trends in Inductive Power Transfer for Transportation Applications", IEEE Journal of Emerging and Selected Topics in Power Electronics, vol.1, no.1, pp.28-41, March 2013.

[40] D. J. Wilcox, M. Conlon, W. G. Hurley, "Calculation of self and mutual impedances for coils on ferromagnetic cores", Physical Science, Measurement and Instrumentation, Management and Education - Reviews, IEE Proceedings A , vol.135, no.7, pp.470,476, Sep 1988.

[41] W. G. Hurley, M. C. Duffy, "Calculation of self and mutual impedances in planar magnetic structures", IEEE Transactions on Magnetics, vol.31, no.4, pp.2416-2422, Jul 1995.

[42] S. Kong, C. Hwang, K. Kim, H. Kim, L. Park, U. Park, J. Kim, J. Kim, "Analytical model for predicting the electromagnetic fields intensity in wireless power transfer systems", IEEE Electrical Design of Advanced Packaging and Systems Symposium (EDAPS) 2011, vol., no., pp.1-4, 12-14 Dec. 2011.

[43] A. Rosskopf, E. Bar, C. Joffe, "Calculation of ohmic losses in litz wires by coupling analytical and numerical methods," 4th International Electric Drives Production Conference (EDPC) 2014, vol., no., pp.1-6, Sept. 30 2014-Oct. 1 2014.

[44] A. Rosskopf, E. Bar, C. Joffe, "Influence of Inner Skin and Proximity Effects on Conduction in Litz Wires", IEEE Transactions on Power Electronics, vol.29, no.10, pp.5454-5461, Oct. 2014.

[45] J. A. Ferreira, "Improved analytical modeling of conductive losses in magnetic components", IEEE Transactions on Power Electronics, vol.9, no.1, pp.127-131, Jan 1994.

[46] M. Etemadrezaei, S. M. Lukic, "Equivalent complex permeability and conductivity of Litz wire in wireless power transfer systems", IEEE Energy Conversion Congress and Exposition (ECCE) 2012, vol., no., pp.3833-3840, 15-20 Sept. 2012.

[47] M. Bartoli, N. Noferi, A. Reatti, M. K. Kazimierczuk, "Modeling Litz-wire winding losses in high-frequency power inductors", 27th Annual IEEE Power Electronics Specialists Conference (PESC) 1996, vol.2, no., pp.1690-1696 vol.2, 23-27 Jun 1996.

[48] http://www.icnirp.org/cms/upload/publications/ICNIRPemfgdl.pdf

[49] https://www.trifield.com/UserFiles/UHS%202012(1).pdf

[50] C. M. Zierhofer, E. S. Hochmair, "Geometric approach for coupling enhancement of magnetically coupled coils", IEEE Transactions on Biomedical Engineering, vol. 43, no. 7, pp. 708-714, 1996.

[51] S. Kim, D. H. Jung, J. J. Kim, B. Bae, S. Kong; C. Song; J. Kim, "Modeling of electromagnetic interference shielding materials in wireless power transfer for board-to-board level interconnections", in Wireless Power Transfer Conference (WPTC), 2014 IEEE , vol., no., pp.273-276, 8-9 May 2014.

[52] H. Kim, J. Cho, S. Ahn, J. Kim, J. Kim, "Suppression of Leakage Magnetic Field from a Wireless Power Transfer System using Ferrimagnetic Material and Metallic Shielding", Proceedings of IEEE International Symposium on EMC, Pittsburgh, USA, pp. 640-645, 2012.

[53] H. Kim, C. Song, J. Kim, J. Kim, J. Kim, "Shielded coil structure suppressing leakage magnetic field from 100W-class wireless power transfer system with higher efficiency", IEEE MTT-S International Microwave Workshop Series on Innovative Wireless Power Transmission: Technologies, Systems, and Applications (IMWS), 2012, vol., no., pp.83-86, 10-11 May 2012.

[54] M. G. Egan, J. M. D. Murphy, J. G. Hayes, S. E. Schulz, J. T. Hall, "Wide-load-range resonant converter supplying the SAE J-1773 electric vehicle inductive charging interface", IEEE Transactions on Industrial Electronics, vol. 35, no. 4, pp. 884-895, 1999.

[55] M. Kiani, U. M. Jow, M. Ghovanloo, “Design and Optimization of a 3-Coil Inductive Link for Efficient Wireless Power Transmission”, IEEE Transactions on Biomedical Circuits and Systems, vol 5., no 6., pp. 579-591, 2011.

[56] R. Laouamer, M. Brunello, J. P. Ferrieux, O. Normand, N. Buchheit, “A multi resonant conver ter for non contact charging with electromagnetic coupling”, 23rd International Conference on Industrial Electronics, Control and Instrumentation (IECON) 1997 , vol. 2, pp. 792-797, 1995.

[57] D. Yinliang, S. Yuanmao, G. Yougang, "Design of coil structure achieving uniform magnetic field distribution for wireless charging platform", 24th International Conference on Power Electronics Systems and Applications (PESA) 2011, vol., no., pp.1-5, 8-10 June 2011.

[58] E. I. Zountouridou, G. C. Kiokes, N. D. Hatziargyriou, N. K. Uzunoglu, "An evaluation study of wireless access technologies for V2G communications", 16th International Conference on Intelligent System Application to Power Systems (ISAP) 2011, vol., no., pp.1-7, 25-28 Sept. 2011.

[59] M. Catrysse, B. Hermans, R. Puers, “An inductive power system with integrated bi-directional data-transmission”, Sensors and Actuators A: Physical, vol. 115, pp. 221-229, 2004.

[60] Z. N. Low, R. A. Chinga, R. Tseng, J. Lin, "Design and Test of a High-Power High-Efficiency Loosely Coupled Planar Wireless Power Transfer System", IEEE Transactions on Industrial Electronics, vol.56, no.5, pp.1801-1812, May 2009.

[61] K. Lee, Z. Pantic, S. M. Lukic, "Reflexive Field Containment in Dynamic Inductive Power Transfer Systems", IEEE Transactions on Power Electronics, vol.29, no.9, pp.4592-4602, Sept. 2014.

[62] Y. Sakaki, "An approach estimating the number of domain walls and eddy current losses in grain-oriented 3% Si-Fe tape wound cores", IEEE Transactions on Magnetics, vol.16, no.4, pp.569-572, July 1980.

[63] R. Tasnim, S. Khan, M. Mohamed, A. Arshad, N. Saquib, "Analyzing hysteresis loops via coupling factors for inductive sensing technique", International Conference on Computer and Communication Engineering (ICCCE) 2012, vol., no., pp.574-577, 3-5 July 2012.

[64] E. Bou, E. Alarcon, R. Sedwick, P. Fisher, "Interference analysis on Resonant Inductive Coupled Wireless Power Transfer links", IEEE International Symposium on Circuits and Systems (ISCAS), 2013, vol., no., pp.2783-2786, 19-23 May 2013.

[65] J. Wang, J. Li, S. L. Ho, W. N. Fu, Y. Li, H. Yu, M. Sun, "Lateral and Angular Misalignments Analysis of a New PCB Circular Spiral Resonant Wireless Charger", IEEE Transactions on Magnetics, vol.48, no.11, pp.4522-4525, Nov. 2012.

[66] M. Yilmaz, P. T. Krein, "Review of the Impact of Vehicle-to-Grid Technologies on Distribution Systems and Utility Interfaces", IEEE Transactions on Power Electronics, vol.28, no.12, pp.5673-5689, Dec. 2013.

[67] A. Christ, M. G. Douglas, J. M. Roman, E. B. Cooper, A. P. Sample, B. H. Waters, J. R. Smith, N. Kuster, "Evaluation of Wireless Resonant Power Transfer Systems With Human

Electromagnetic Exposure Limits", IEEE Transactions on Electromagnetic Compatibility, vol.55, no.2, pp.265-274, April 2013.

[68] T. Sato, Y. Sakaki, "Physical meaning of equivalent loss resistance of magnetic cores", IEEE Transactions on Magnetics, vol.26, no.5, pp.2894-2897, Sep 1990.

[69] G. Hrkac, M. Kirschner, F. Dorfbauer, D. Suess, O. Ertl, J. Fidler, T. Schrefl, "Three-dimensional micromagnetic finite element simulations including eddy currents", Journal of Applied Physics, vol.97, pp.10E3111-3, 2005.

[70] Y. Zhang, M. C. Cheng, P. Pillay, "A Novel Hysteresis Core Loss Model for Magnetic Laminations", IEEE Transactions on Energy Conversion, vol.26, no.4, pp.993-999, Dec. 2011.

[71] P. Nakmahachalasint, K. D. T. Ngo, L. Vu-Quoc, "A behavioral model for frequency-dependent hysteresis in power ferrites", IEEE Transactions on Magnetics, vol.40, no.4, pp.1784-1790, July 2004.

[72] M. C. Rodriguez, C. Sanz, "Simple Frequency Domain Model for Hysteresis and Eddy Currents in Cylindrical and Parallelepipedal Cores", IEEE Transactions on Magnetics, vol.43, no.5, pp.1912-1919, May 2007.

[73] J. Cale, S. D. Sudhoff, R. R. Chan, "A Field-Extrema Hysteresis Loss Model for High-Frequency Ferrimagnetic Materials", IEEE Transactions on Magnetics, vol.44, no.7, pp.1728-1736, July 2008.

[74] D. C. Jiles, D. L. Atherton, "Theory of ferromagnetic hysteresis (invited)", Journal of Applied Physics, vol.55, pp.2115-2120, 1984.

[75] S. Lizon-Martinez, B. Tellini, R. Giannetti, G. Robles, "Measurement of Asymmetric Minor Loops in Soft Ferrites Up to Medium Frequencies", IEEE Transactions on Instrumentation and Measurement, vol.58, no.2, pp.423-428, Feb. 2009.

[76] J. Reinert, A. Brockmeyer, R. W. De Doncker, "Calculation of losses in ferro- and ferrimagnetic materials based on the modified Steinmetz equation", IEEE Transactions on Industry Applications,, vol.37, no.4, pp.1055-1061, Jul/Aug 2001.

[77] A. V. D. Bossche, V. C. Valchev, G. B. Georgiev, "Measurement and loss model of ferrites with non-sinusoidal waveforms", IEEE 35th Annual Power Electronics Specialists Conference (PESC) 2004, vol.6, no., pp.4814-4818 Vol.6, 20-25 June 2004.

[78] M. Kiani, M. Ghovanloo, "A Figure-of-Merit for Designing High-Performance Inductive Power Transmission Links", IEEE Transactions on Industrial Electronics, vol.60, no.11, pp.5292-5305, Nov. 2013.

[79] C. Wang, G. A. Covic, O. H. Stielau, "General stability criterions for zero phase angle controlled loosely coupled inductive power transfer systems", IEEE 27th Annual Conference of Industrial Electronics Society (IECON) 2001 , vol.2, no., pp.1049-1054 vol.2, 2001.

[80] S. Krishnan, S. Bhuyan, V. P. Kumar, W. Wang; J. A. Afif, K. S. Lim, "Frequency agile resonance-based wireless charging system for Electric Vehicles", IEEE International Electric Vehicle Conference (IEVC) 2012, vol., no., pp.1-4, 4-8 March 2012.

[81] T. Imura, H. Okabe, Y. Hori, "Basic experimental study on helical antennas of wireless power transfer for Electric Vehicles by using magnetic resonant couplings", IEEE Vehicle Power and Propulsion Conference (VPPC) 2009, vol., no., pp.936-940, 7-10 Sept. 2009.

[82] Y. Kubo, N. Shinohara, T. Mitani, "Development of a kW class microwave wireless power supply system to a vehicle roof", IEEE MTT-S International Microwave Workshop Series on Innovative Wireless Power Transmission: Technologies, Systems, and Applications (IMWS) 2012 , vol., no., pp.205-208, 10-11 May 2012.